# Investigation of the Radial Ionization Distribution of Heavy Ions with an Optical Particle Track Chamber and Monte-Carlo Simulations

Dissertation
zur Erlangung des Doktorgrades
der Naturwissenschaften

vorgelegt beim Fachbereich Physik
der Johann Wolfgang Goethe-Universität
in Frankfurt am Main

von
Gábor Laczkó
aus Budapest

Frankfurt 2006

vom Fachbereich Physik der Johann Wolfgang Goethe-Universität als Dissertation angenommen.

Dekan:                      Prof. Dr. Wolf Aßmus

Gutachter:                 Prof. Dr. Horst Schmidt-Böcking,
                                Prof. Dr. Gerhard Kraft

Datum der Disputation:

Diese Arbeit möchte ich meinem Vater widmen, der mir die Begeisterung für die Naturwissenschaften vermittelt  hat, den Abschluss der Arbeit jedoch nicht mehr erleben durfte.

# Content

# 1 Introduction

Beams of charged particles like protons or heavy ions (ions heavier than protons are termed heavy ions in the usual terminology of radiobiology) represent a superior radiotherapeutic alternative for the treatment of deep-seated tumors compared to conventional photon beams. Ion beams have an inverted depth dose profile: In contrast to the exponential dose deposition of conventional photon beams, the absorbed dose of ions increases with the penetration depth and shows a steep maximum (Bragg peak) and a sharp drop behind it. In addition, the relative biological effectiveness, RBE (see equation (2.1)), of ions is higher than that of sparsely ionizing radiation, especially in the stopping region at the Bragg peak. Hence, the deposited energy and - even more pronounced due to the increased biological effectiveness – the cell killing effect have their maximum values not on the skin but in a deepness in the body that can be adjusted by varying the ion energy. This property of charged particles allows for an outstanding conformity and effectiveness of the applied radiation dose, if appropriate techniques of beam application and treatment planning are applied.

At one of the most advanced experimental therapy units worldwide, at GSI, energy and intensity modulated beams of carbon ions are provided by a fully active beam shaping system. Active beam shaping means that the prescribed dose is achieved in an extended (typically 100 - 200 $cm^3$) target volume by superposition of many (thousands or tens of thousands) narrow pencil beams. The lateral deflection, the ion energy (i.e. penetration depth in tissue) and the intensity of the individual pencil beams can be adjusted precisely to deliver a predefined dose to each tumor voxel according to the treatment plan. The small lateral scattering of heavy ions as well as the steep decrease in dose beyond the Bragg maximum are essential for the success of this raster scan method. The selection of carbon ions for the therapy is a result of an optimization: carbon ions have increased RBE (see chapter 2.7) and smaller lateral scattering and range straggling than e.g. protons [Tob79]. On the other hand, the impact of heavier ions than carbon would result in a strong focusing of dose in the central ion track core (see "overkill" effect in chapter 2.7) and a significant dose contribution behind the Bragg peak due to nuclear fragmentation of the original ions. Nuclear fragmentation of carbon ions into smaller ions or neutrons (see chapter 3.1) results in a small tail of dose beyond the Bragg maximum, either. Nevertheless, while this phenomenon does not affect radiation quality strongly in the case of the less heavy carbon ions, it enables the online PET analysis of the spatial distribution of the positron-emitting $^{11}C$ and $^{10}C$ fragments inside the patient [Eng81]. These isotopes have approximately the same ranges as the original $^{12}C$ ions; hence measuring the distribution of the $^{11}C$ and $^{10}C$ fragments by PET methods allows for a verification of the calculated range distribution and thus indirectly of the dose distribution in the irradiated volume. For detailed information on the therapy method see [Kra00] and for the medical summary of the results after the therapy in 152 patients see [Scz04].

The basis of any successful therapy is the uniform and strong irradiation of the tumor volume together with the sparing of the surrounding healthy tissues. Although the achievable irradiation field is much more tumor-conform with heavy ions than with photons, this advantage can only be optimally utilized, if a delicate, radiobiology-based treatment planning is applied. The treatment planning has to deal with a complex mixed irradiation field as a part of the carbon ions degrade into fragments with different atomic numbers, energies and penetration depths. Furthermore, irradiation of the tumor has to be uniform in cell survival probability (or biological effective dose) rather than in dose. Figure 1.1 illustrates, that the spatial distribution of the applied dose with carbon ions differs significantly from that of the resulting biological effect. This is due to the higher biological effectiveness of the ions towards the end of their path (Bragg peak).
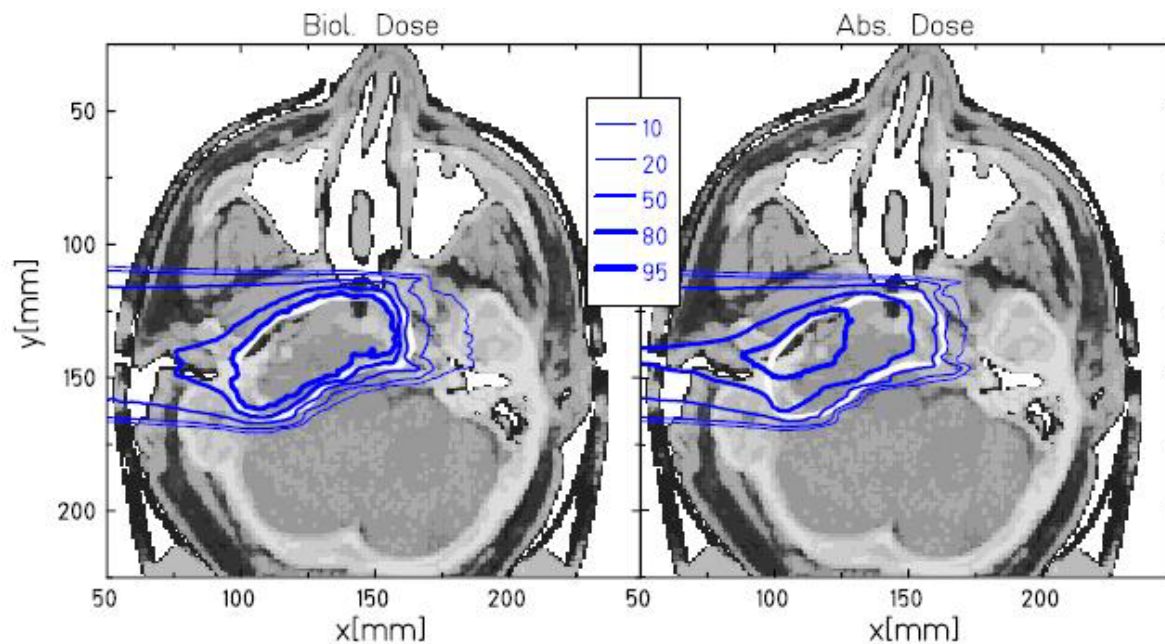
Figure 1.1: *Simulated dose distributions due to the irradiation of a tumor with carbon ions in the base of the scull [Krm00b]. The beam reaches the target from the left side of the image. The increasing biological effectiveness towards the right end of the target volume, where most of the dose is delivered by Bragg peaks of carbon ions, is illustrated well by the different spatial distributions in the dose (right image) and the biological effective dose (left image).*

The example of Figure 1.1 demonstrates, that the absorbed dose alone cannot describe the biological effect of the irradiation. Ionizing radiation deposits energy in discrete packages that are distributed non-uniformly in the irradiated volume. The spatial pattern of the ionizations (ionizations are the most relevant energy transfer points regarding the biological effects of radiation) at a given absorbed dose level influences greatly the effect of the radiation on biological structures. In general, sparsely ionizing radiation (like photons) causes mostly single lesions in the DNA of a cell, which can be fixed by biochemical repair mechanisms. Densely ionizing radiation (e.g. in the Bragg peak region of carbon ions), on the other hand, causes frequently large ionization clusters along the path of the ionizing particle. Ionization cluster denotes for an agglomeration of ionizations within a volume of a few cubic nanometer. These clusters may result in irreparable complex lesions of the DNA result with a high probability. This leads to mutation, malfunction or death of the affected cell.

To quantify the biological effect in therapy with heavy ions relative to the classical treatment with photons, the local effect model (LEM) was developed at GSI [Sch94], [Sch96]. The LEM assumes that instead of an averaged macroscopic dose, the "local" dose inside a very small, biologically relevant volume (e.g. few $nm^3$) of the cell nucleus determines the expectable biological effect (see definitions of local dose and local effect in chapter 2.7.3). I.e. on the nanometric scale the nature of the radiation, which delivers the dose, does not matter – with other words, ion radiation may be replaced by e.g. X - rays and the local radiation effect due to ions is equal to the local effect due to X – rays provided that both radiation types delivered an identical dose to the nanometric volume. Furthermore, the model assumes that the radiation effect on a cell can be determined as a simple addition of the local effect contributions to the nanometric volumes which constitute in their sum the cell nucleus. This assumption implies that interactions of so called sublethal events over large distances of the order of micrometers can be neglected.

The assumptions of the model can be justified by theoretical and experimental results. It is the most successful biophysical model so far in predicting survival curves due to heavy ion

irradiation. The successful application of LEM in the framework of treatment planning for carbon-ion cancer therapy at GSI [Scz04] is a great evidence for its capabilities. However, the required precision can only be guaranteed if the input parameters used by the model reflect the reality well.

The predictions of the LEM are based on two biological parameters:
1. size and shape of the nucleus of the irradiated cell type,
2. survival curve of the irradiated cell type due to X - ray irradiation.

Furthermore, two physical parameters:
3. expectable amount (flux, density) and type (atomic number and energy) of the ions which deposit energy in an arbitrary selected cell nucleus in the irradiated volume,
4. radial dose distribution, $d(r)$, around the tracks of the propagating ions.

The fourth parameter, $d(r)$ is a deterministic quantity and it describes the mean local dose value ($dE / dm$) at a radial distance of $r$ from the core of the ion track (where $E$ is the deposited energy in the small volume with a mass of $dm$). Based on the $d(r)$ contributions of the ion tracks, the local dose and thus the local effect can be determined in each nanometric volume segment of the cell nucleus. And finally the survival rate of the arbitrary selected cell or the RBE of the irradiation can be acquired. A detailed description of the LEM and a brief overview of several other biophysical models are given in chapter 2. The focus of the present work is put onto the experimental determination of $d(r)$.

Beside experiments there are basically two possibilities to examine the $d(r)$ function around ion tracks; in the framework of analytical models and by means of Monte Carlo (MC) simulations. The analytical models, such as the track structure model of Katz et al. [Kat72], the core-penumbra model of Chatterjee and Schäfer [Cha76] and the models of Kiefer et al. [Kie86] and Xapsos et al. [Xap94], derive closed equations for $d(r)$ based on different assumptions and simplifications in the collision processes. An overview of the most important analytical models is not presented in this work, it can be found in the thesis of Ramm [Ram94] and in that of Schmollack [Scm95]. According to all models, a $1/r^2$-dependence for $d(r)$ is a good approximation in a wide range of $r$ (see Figure 2.3), but the differences in the fine structure of the different approaches are significant especially at small and large $r$.

In the practical application, MC simulations are the most common methods because of their capability to describe the full complexity and stochastics of ion transport in matter, however, only as far as the cross sections are available. There is a summary table in [Krm95] about the different simulation codes. The present work is motivated by the request for an experimental benchmarking tool to test the simulated results and predictions of such models concerning the spatial radiation pattern and namely the radial dose distribution, $d(r)$. The simulation method and the computer code, TRAX, used at GSI to study track structure and to obtain or benchmark crucial input parameters for the therapy planning, was developed by Kraemer et al. [Krm94] at GSI. In the past years of extended application, the TRAX code turned out to be a very successful particle transport code, at least for particles (e.g. carbon ions) and energy regions (moderate energies), which are relevant for ion therapy. This is the main motivation for choosing TRAX as the code to be benchmarked by our experiments. Furthermore, a straight forward adaptation of TRAX for the comparison with experiments with our particle tracking detector could be obtained. A detailed description of the physical processes, which are simulated and neglected in TRAX, will be presented in chapter 3.

Direct measurements of $d(r)$ in dense materials like tissue or water are not possible. The required resolution of the order of nanometers up to several micrometers is not achievable with present technology. Instead, gas chambers or cloud chambers can be used to measure the corresponding quantity at much lower matter density. The length scale is than multiplied by

the ratio of the gas and tissue densities. The possible consequences of the neglected solid state effects due to this measurement concept are pointed out in chapter 4.1.

Some of the very few existing measurement systems that are capable to produce $d(r)$ data in volume sites significantly below the micrometer order of magnitude ([Met88], [Win76]), [Var77]) are briefly described in chapter 4. The experimental investigations in this work were performed with the Optically read out PArticle track Chamber, OPAC. A comprehensive report on the detector can be found in [Tit98] and [Titt99]. Based on this work and a proposal by Dangendorf [Dan01] the project was continued in the framework of the present PHD work.

The principle of OPAC is an optically read out time projection chamber (TPC) with a parallel-drift field and one or several electron and light amplification stages. The two dimensional projection of the three dimensional ionization pattern - caused by the ionizing particle passing through the chamber - is read out by an image intensified CCD camera. The pressure of the filling gas was adjusted to 4, 10 and 40 hPa in the measurements presented in this work. The gas pressure and the width of the drifting region determine the extent of electron diffusion in the chamber which is the major limiting parameter of the spatial resolution of OPAC. The lower limit of the radial range, where the measurement data is not affected significantly by the diffusion is about 100 nm (at a gas pressure of 4 hPA). The upper limit of the measured radial range is 6 μm (at a gas pressure of 40 hPA) and the best resolution amounts to 33 nm - the data are scaled to water density. Detailed description of the experimental system and the improvements compared to its original status, described in [Tit98], is given in chapter 5.

The raw images, captured by OPAC, illustrate qualitatively the properties of the track of ionizing particles very well. However, an extensive data analysis is needed to achieve the quantitative information for the derivation of the searched $d(r)$ function. E.g. the image is the two dimensional projection of the original track, i.e. the distance of a certain ionization location in the image (a small peak in e.g. Figure 7.1) from the track core does not correspond unambiguously to the corresponding distance in the chamber, because the relative "deepness" of the event (the third coordinate) is not known. Therefore, an unfolding method is necessary to derive the $d(r)$ function from the images. The data analysis methods and algorithms to recover hidden information from the measured tracks are described in chapter 6.

Finally, the results of the measurements which were performed with OPAC at the ion accelerator at GSI are shown in chapter 7. Systematic measurements of carbon ion track structures were performed at various carbon ion energies from 400 MeV/u down to Bragg peak energies. The comparison of the measurement results (i.e. $d(r)$ functions) with the corresponding simulated data shows an excellent agreement. The agreement between measured and simulated data is still reasonable but significantly worse if heavier ions are applied instead of carbon. Nevertheless, the expected discrepancies between the ionization patterns of ions of different atomic number but same deposited energy (i.e. same LET) could be shown in the measurements.

It is obvious, that the application range of OPAC cannot be restricted to the measurement of $d(r)$ functions of ions. Due to the very detailed information from the ionization pattern of ionizing particles, delivered by OPAC, the achieved images can be used to derive various quantities of microdosimetry or nanodosimetry. These quantities can be not only of deterministic but also of stochastic nature (e.g. proximity functions or cluster size distributions – for definitions see chapter 2). Furthermore, OPAC can be applied in other fields of radiation physics not exclusively in radiation biophysics. Recently the method is further developed to an application in nuclear astrophysics [Mos05], [Wei06].

# 2 Biophysical models of radiation action

The widespread application of ionizing radiation and the effective radiation protection require further efforts to fill the gap between physics of radiation action in matter, and the wide variety of facts described in terms of biology, biochemistry and medicine. First of all, proper selection of quantitative terms with respect to both the acting physical agent (radiation) and the radio-biological effect is needed for theoretical considerations and model building. Radiation dose (D), defined as the average absorbed energy per unit mass, is the standard physical quantity to measure radiation effect on matter. The main reason for this choice is that it can be readily defined and measured for each sort of ionizing radiation. Although the absorbed dose is an important determinant of the biological effect, much more detailed physical and biological information is needed to predict the reaction of a living biological system with radiation. Some of the physical and biological factors that have to be taken into account for the model building and parameter selection efforts are listed below:

1. *Endpoint selection:* The measure of the radiation effect can be different for different biological endpoints under consideration, like structural changes in certain targets (e.g. single- and double DNA strand breaks, clustered DNA damages or chromosomal aberrations) or inactivation of a certain biological function (e.g. cell death (apoptosis), enzyme inactivation, mutation, immunomodulation, or at organism level, carcinogenesis). In the case of radiotherapy the desired endpoint is cell killing in the target volume, as well as avoiding of late effects in normal tissue.

2. *Stochastics of energy deposition and biological response:* Both the physical and biological processes are of stochastic nature [Hug66]. Physical stochastics means, that despite specified dose and radiation type, the pattern of the radiation energy deposition differs from track to track. But even identical patterns of energy deposition induce different reactions in "identical" biological objects (biological stochastics).

3. *Spatial ionization pattern:* Ionizing radiation deposits energy in discrete packages that are distributed non-uniformly in the irradiated volume. The spatial pattern of the energy transfer points at a given absorbed dose level influences greatly the effect of the radiation on biological structures. Figure 2.1 shows a comparison of measured survival curve of 250 kV X-rays, 1 GeV/u $^{56}$Fe ions and 2.4 MeV $^4$He ions. Note the typical shouldered shape of the X-ray curve (initial shallow slope followed by a continuously bending curve at higher doses.) In contrast, densely ionizing ion radiation has a simple exponential survival curve. However, even the dose effect curves of the two described ions have different slopes despite their similar LET values (~ 150 keV/μm).

4. *Time scale:* The time scale of the relevant processes ranges from $10^{-14}$ s (atomic interactions) to several decades (late effects, e.g. carcinogenesis).

5. *Target selection:* Ionizing radiation triggers a chain of events on the atomic, molecular, cellular levels, and can have prompt or long term consequences on the affected tissue, organ and ultimately on the whole organism. Many models treat cells as targets of radiation, and assume them to be independent from each other (neglecting for example the presently intensively investigated bystander effects ([Nag92], [Saw01] and [Azz04]) or e.g. immune response of the whole organism in the case of late effects.)
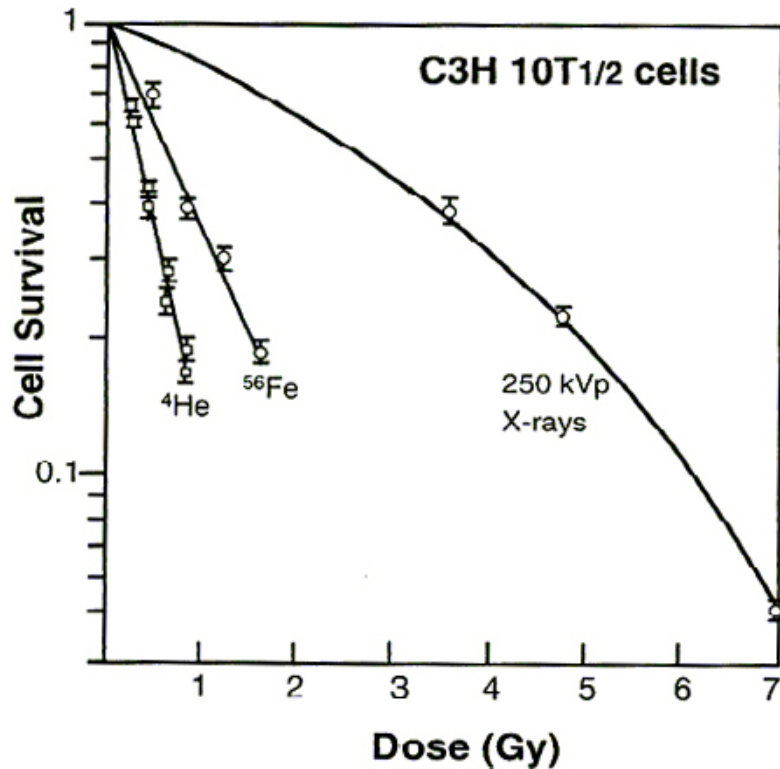
Figure 2.1: *Cell survival curve for C3H 10T1/2 cells exposed to 250 kV X-rays, 1 GeV/u $^{56}$Fe ions and 2.4 MeV $^4$He ions. The LET of both the $^{56}$Fe and $^4$He ions was 150 keV/μm [Ric98].*

6. *Target size:* Related to the points above, an obvious question concerns the dimensions of the sites (sites can be identified with entities, like e.g. nucleus, nucleosoms or DNA) in which the energy concentration is critical regarding biological effectiveness. It seems to be well established, that there are at least two domains of importance. [Ros94] The cell nucleus with dimensions of the order of micrometers and compact DNA segments with dimensions of less than ten nanometers. Others [Gro02b] put their emphasis exclusively on the nanometer site.

7. *Direct and indirect effects:* Assuming the DNA to be the relevant target, complex physical, chemical, biological processes have to be taken into account. Radiation damage to cellular DNA is assumed to be caused by direct ionization of the DNA and by successive chemical reactions with reactive species, produced by ionization of surrounding molecules (mainly produced by radiolysis of water, resulting in $H^+$ and $OH^-$ radicals).

8. *Damage complexity-reparability:* Some of the DNA damages (lesions) can be repaired by enzymatic repair mechanisms. The complexity of the damage correlates directly to its reparability. This is the main reason why the relative biological effectiveness (RBE) of different radiation types with different ionization densities can vary on a large scale.

9. *Temporal aspects:* The radiation effect depends on the temporal function of dose application. Many cellular effects (especially at high dose of low LET radiation) are caused by two independent tracks hitting the same cell nucleus which necessarily occur at different times. In the case of temporary extended exposure with low dose or fractionated irradiation the damage produced by the first track may be repaired before the second one causes an additional damage. This phenomenon reduces the efficiency of protracted irradiation, but to a different extent for different radiation types (e.g. low or high LET

6

radiation) depending mainly on the overall importance of the repair processes following the irradiation.

10. *Radiation sensitivity of tissue, the role of oxygen content and cell cycle:* Different cell types can react differently on the same radiation, depending on their cell-specific radiation sensitivity. Radiotherapy e.g. has to take special care of the protection of particularly radiosensitive healthy tissues (e.g. brain stem and spinal cord in the brain) in the neighborhood of the target volume. The amount of oxygen present in the target region present can affect the radiosensitivity too. Some tumors contain hypoxic cells that are up to three times more radioresistant than the corresponding oxygenated cells. Furthermore, cell survival is also a function of the cell cycle stage at which exposure occurs. It is most strongly affected during mitosis and least affected during the so called G1 and S phases of the cell cycle.

11. *Mixed radiation fields:* One of the most ambitious modeling purposes is the prediction of biological radiation action in modern ion radiotherapy (e.g. at GSI [Kra00]). At each point in the irradiated volume a mixed radiation field exists consisting of high- and low-LET primary ions as well as their nuclear fragmentation products.

As already mentioned in the introduction, appropriate selection of physical and biological parameters (well measurable parameters, if possible) are essential requirements of any model building. The most commonly used physical parameters (besides dose) aiming to describe some of the above mentioned relevant physical properties of radiation are: projectile energy, $E$ [MeV or MeV/u for ions]; particle fluence, $\Phi$ [cm$^{-2}$]; various cross sections, $\sigma$ [m$^2$ or barn], determining the probability of a certain interaction between projectile and matter (ionization, excitation, scattering, total); *LET* (will be exactly defined in chapter 2.1); radial dose $d(r)$ [Gy] (exact definition later, in chapter 2.7) and quantities, established by microdosimetry and nanodosimetry, like specific energy, $z$, lineal energy $y$ or cluster size distribution (definition later, in chapter 2.2).

The most important quantitative measures of biological response in use are the survival curve, *S(D)* which indicates the proportion of well defined biological units, that do not show a certain reaction, as a function of the average dose; the relative biological effectiveness, *RBE*, which is defined as a ratio of doses, that produce the same biological effect,

$$RBE = \frac{D_L}{D_H} \tag{2.1}$$

where $D_H$ refers to the radiation in question and $D_L$ is the reference radiation dose (e.g. 250 kV X-rays, $^{60}$Co gamma or therapeutic photon radiation). Also cross sections or yield specifications are frequently used for cell inactivation or DNA lesions.

Numerous models were developed in radiation biophysics, but there is still no closed, generally accepted, quantitative description that fully incorporates all the parameters mentioned above. Nevertheless, many of the more sophisticated models are able to predict the response of some biological systems under certain circumstances and endpoint requirements with satisfactory accuracy. Radiation protection, for instance deals with relatively low dose levels and the endpoint under consideration is a possible late effect. When defining exposure levels, different radiation quality of e. g. photons and neutrons has to be taken into account. For this purpose a weighting factor is given by a quality factor, *Q*, mostly independent from atomic number or energy. The accuracy of the resulting biological effective dose is sufficient in radiation protection to define upper limits fixed by law. In contrast, radiation therapy has a much higher demand on precision and the endpoint in the target volume is cell death, whereas

it is late effect in healthy tissue. A brief overview of the past model development lines and present trends is presented in the following chapters.

# 2.1 Historical biophysical concepts

## 2.1.1 Classical target theory

The earliest radiobiological model, the target theory, was based on two observations; on the discontinuous, quantum-like energy absorption by matter and on the shape of survival curves. The gradually decreasing behavior of $S(D)$ (often purely exponential: $S(D) = e^{-\alpha D}$) was attributed to the stochastic occurrence of hits in critical targets [Lea56], [Des64]. It was assumed, that a few, independent hits were necessary to induce a biological effect, hence Poisson statistics was applied. The number of hits and targets was assumed to determine exclusively whether the object does or does not react (neglecting e.g. biological stochastics or repair effects). One of the most common simple variants is the single-target-multi-hit model, assuming, that $m$ hits are necessary and sufficient for the effect to be produced. The dose-survival curve is than given by:

$$S(D) = \sum_{k=0}^{m-1} \frac{(\alpha D)^k}{k!} e^{-\alpha D} \tag{2.2}$$

where $\alpha$ corresponds to the hit probability (normalized to dose). Another basic approach is the multi-target-single-hit model, which assumes that $n$ targets are hit by one single projectile:

$$S(D) = 1 - (1 - e^{-\alpha D})^n \tag{2.3}$$

Target theory can deliver satisfactory results for very small biological objects (like viruses) which show a pure exponential dose-effect behavior for every radiation ($m = 1$ or $n = 1$ in equations (2.2) and (2.3), respectively). But for most targets and endpoints of interest, survival curves are shouldered ($m>1$ or $n>1$) for X-ray radiation and change their shape, getting more nearly exponential for high-LET radiation (see chapter 2.7.1). Classical target theory cannot treat this, unless $m$ and $n$ are allowed to be different depending on radiation (i.e. hits cannot be identical physical events for each radiation). This fact hinders the development of a systematic theory of RBE [Gun83] in the framework of classical target theories.

## 2.1.2 The LET concept

The most frequently used non-stochastic quantity, characteristic for ionization density of a radiation, the linear energy transfer (LET) was firstly implemented by Zirkle in 1953 [Zir53].

$$\text{LET} = \frac{dE}{dx} \tag{2.4}$$

where $dx$ is the distance propagated by the projectile and $dE$ is the mean energy deposited locally by the projectile and its $\delta$-electrons. The energy restricted linear energy transfer, $L_\Delta$, excludes $\delta$-electrons beyond a cut-off kinetic energy of $\Delta$. This definition sets an upper limit for the projectile track radius (maximal range of the $\delta$-electrons, with an energy of $\Delta$), and $\delta$-electrons with higher energies must be taken into account as separate particles. In this work the term LET accounts for the unrestricted linear energy transfer ($\text{LET}_\infty$), also called stopping power.

As mentioned in the introduction, the biological effect of the radiation depends strongly on the pattern of ionization. However, LET does not describe this pattern unambiguously, if plotting RBE versus LET, essentially two types of correlations can be found. RBE(LET) decreasing monotonously if the endpoint is e.g. virus inactivation or gene mutation, where *S(D)* shows a clear exponential characteristics for each type of radiation. For the most typical cases of chromosome aberrations or mammalian cell killing (shouldered gamma response), RBE(LET) first increases, forms a maximum in the LET region of about 25 to several hundred keV/μm and decreases above that. A more detailed description and explanation of this behavior follows in chapter 2.7.

Various attempts have been made to standardize the measured RBE(LET) functions for particular classes of objects and effects [Nak67], [Ang67], starting mostly with the determination of RBE from experimental data for mono-LET radiations, and trying to predict RBE for radiations with broad LET spectra by weighting like:

$$RBE = \frac{\int\limits_0^\infty d(\text{LET})\text{RBE}(\text{LET})\text{dLET}}{\int\limits_0^\infty \text{dLET}} \tag{2.5}$$

where *d*(LET) is the normalized dose spectrum. Such efforts have led to some achievements in the field of radiation protection [ICR66], but the LET concept cannot be regarded as a general theory of RBE, and this weakness has several reasons. Although the RBE(LET) relationship exists, it is not known a priori for all kinds of radiation and thus can be derived only from experiments with the biological system under consideration. The additivity of the biological effects of the single LET components, as implied in equation (2.5), is not applicable for mammalian cells, where cumulative action of sublesions is needed to trigger an irreparable DNA-damage. The survival curve shape depends on LET in these cases, and this fact results in an RBE(LET) function, that also depends on the considered effect. Bewley in 1968 [Bew68] found great deviations between measured survival curves and calculated ones based on equation (2.5) for fast neutrons. He concluded in his analysis, that the main reason for the failure is the fact, that different particles of same LET produce different δ-electron spectra, i.e. LET cannot be the only parameter to specify the microstructure of ionization patterns.

## 2.2 Microdosimetry

Microdosimetry has now grown into a well established field of modern biophysical research. It was introduced and developed by Rossi and his co-workers [Ros59], [Ros60], [Bia63], [Ros68] as a system of concepts as well as of physical quantities and their measurement. Its main emphasis is put on the description and measurement of stochastical physical parameters in microscopic volumes (typically 1 μm).

### 2.2.1 Microdosimetric quantities

Consider a small volume, *V*, of spherical or any other shape in a uniformly irradiated medium. The volume is filled with matter of mass *m* and the radiation delivers a dose, *D* in this volume. The energy, *η* imparted to the matter in that volume is a stochastic quantity despite the fixed dose. The specific energy is defined as the ratio:

$$z = \frac{\eta}{m} \qquad (2.6)$$

The unit of $z$ is Gy = J/kg. Specific energy is considered to be a continuous random variable, despite the fact, that $z$ is measured or calculated on the basis of a limited number of discrete values (i.e. ionizations). $f(z;D)$ is the probability density function (spectrum) of $z$ at a fixed dose value, $D$. The notation shows explicitly the dose-dependency of the spectrum shape. The expectation value of $f(z;D)$ is just the dose itself:

$$\bar{z} = \int_0^\infty z f(z;D)dz = D \qquad (2.7)$$

Very important to note, that $\eta$ can be deposited in one or more events. The term, event, is used for the penetration with all the resulting interactions of one incident particle. Therefore, the terms, absorption events or deposition events, correspond to different incident particles that are statistically independent from each other. The single event microdosimetric spectrum, $f_1(z)$ denotes the probability density function of $z$ conditioned by the circumstance that one and only one event took place in $V$ volume. The expectation value of $f_1(z)$ is called frequency average:

$$z_F = \int_0^\infty z f_1(z)dz \qquad (2.8)$$

The mean number of events, $n$, in the volume, $V$ is obviously $n = D/z_F$. The second moment of $f_1(z)$ is also of great importance. The so called dose average is the ratio of the second and first moments:

$$z_D = \int_0^\infty z d_1(z)dz = \frac{1}{z_F}\int_0^\infty z^2 f_1(z)dz \qquad (2.9)$$

where $d_1(z)$ is the dose probability density; the fraction of absorbed dose per event delivered by energy deposition events of specific energy in the interval $[z,z+dz]$, $(d_1(z) = f_1(z)z/z_F)$. The dose average is related to the variance of the distribution $f_1(z)$.

It can be shown [Ros96], that the second moment of the specific energy density function, $\overline{z^2}$, can be expressed with $D$ and $z_D$:

$$\overline{z^2} = z_D D + D^2 \qquad (2.10)$$

For the representation of single event distribution and experimental data, it is common to use lineal energy, $y$, rather than the specific energy. If $l$ refers to the mean chord length of the volume (its value is $l = 4V/A$ for a convex volume, where $A$ is the surface area of the volume), the lineal energy can be expressed as with $l$ and $\eta$, imparted energy:

$$y = \frac{\eta}{l} \qquad (2.11)$$

Similarly to the specific energy, lineal energy is a stochastic quantity and its density function, $f(y)$, and moments can be defined [Ros96]. It should be mentioned, that despite the specific energy can be treated as the stochastic analogon of the absorbed dose, the relation between the lineal energy and the somewhat similar non-stochastic quantity with the same unit, the LET, is not a simple analogy.

Distributions of specific energy and lineal energy are not capable to account for all aspects of the energy transfer pattern of a particle track. However, the whole information, including the spatial coordinates and types of every interaction and the whole characteristics of each particle leaving the interaction location, would be very exhaustive and not even needed for most purposes. It is generally necessary to condense this information and summarize it in some way in order to use it in the analysis of biological effects. It depends largely on the biophysical model used, which aspects of the track structure can be ignored. One of the most established parameters used by microdosimetry with great relevance on biophysical effects is the proximity function, proposed by Kellerer and coworkers [Kel75]. The integral proximity function, $T(x)$ is the energy deposited within spheres with a radius of $x$ centered at a randomly chosen energy transfer point. The concept ignores the details of the interactions, and considers only energy deposited in an averaged way. The differential proximity function, $t(x)$ evaluates the total energy deposited at transfer points in the shell at distance $x$ to $x+dx$ from the randomly selected energy transfer point.

## 2.2.2 Gross sensitive volume

The most direct implication of microdosimetry is the fact that the survival curve of a single cellular object is determined by the specific energy rather than the macroscopic expectation value, $D$. Hence $S(D)$ should be the expectation value of a $z$-dependent survival function, $S_0(D)$:

$$S(D) = \int_0^\infty S_0(z) f(z;D) dz \qquad (2.12)$$

The volume, which z and f(z;D) refer to, is called gross sensitive volume (GSV). In this model GSV must be large enough to ensure, that energy deposition outside it does not contribute to the effect [Ros64] (the most common choice is the cell nucleus). If $S_0(z)$ is not allowed to depend on radiation quality, this model turns out to be unable to deliver a satisfactory theory of RBE, e.g. it cannot yield RBE values greater than unity at large doses [Gun83]. The reason for this is the different spatial ionization pattern of different types of radiation inside the GSV (rather uniform at low LET, and more clustered at high LET), that is not reflected by $f(z;D)$. Hence, it is necessary to define other sites, smaller than the GSV, at which energy concentration is relevant.

## 2.2.3 Site model formalism for theory of dual radiation action (TDRA)

The development of this model was motivated by the observation [Ros70], that the RBE of neutrons of moderate energies (between 100 keV and a few MeV) relative to X-ray radiation depends on $D_H$, the absorbed dose of neutrons. The basic assumption expressed by the term "dual" is that radiation induces primarily sublesions, that have negligible probability of causing the biological effect under consideration incoherently, but they can interact and build lesions. A lesion is a cellular injury (e.g. double strand break) that can cause the effect independently of the presence of other lesions with a certain probability. The first formulation of the TDRA, the site model, does not go further, but according to distance model of TDRA (see next section) lesions can also act coherently and form compound lesions that have another effect probability. The term, compound lesion, is used in [Ros96] for combination of lesions in larger regions (micrometer domain). Exchange aberrations, i.e. hardly repairable misjoining of broken chromosomes are mentioned as an example.

The site model assumes that the rate of lesion formation is proportional to the square of the number of sublesions that are produced in a site which may be considered to be the average volume in which combination occurs. The number of sublesions in this site is proportional to the specific energy, $z$, in that volume. Thus, the mean value for the number of lesions:

$$\varepsilon(z) = cz^2 \tag{2.13}$$

where the constant, $c$, corresponds to the probability of combination of sublesions to lesions. In the first formulation (the site formulation) of the TDRA [Kel72], the mean number of lesions, as a function of absorbed dose, $\varepsilon(D)$, is obtained by averaging the specific energy spectrum according to the $f(z,D)$:

$$\varepsilon(D) = \int_0^\infty cz^2 f(z,D)dz = c\overline{z^2} = c(z_D D + D^2) \tag{2.14}$$

where the result (2.10) is used to express the second moment of specific energy with its dose average. (2.14) is the central equation of the site model formulation of TDRA which describes the average yield of lesions. Since the site model assumes, that this quantity is the only one on which biological response depends, RBE values for radiations of higher LET can be derived from equations (2.1) and (2.14) and the fact that effects are the same, if $\varepsilon(D_L) = \varepsilon(D_H)$.

The site model can serve as introduction into the field of microdosimetric radiobiological theories. Although it can deliver more or less reliable results for RBE in some benchmark cases (e.g. low dose limit), the site model can only be regarded as first approximation. The model has several limitations: The volume of the site is considered to be the average volume in which sublesion combination occurs. Geometric sublesion distribution inside the sites or interactions between formations of sublesions in adjacent sites are not taken into account. Furthermore, the response of the cell depends on what has happened in the entire GSV, in all sites simultaneously (e.g. role of compound lesions). The model cannot deal with energy transported by reactive species, i.e. indirect damages. The yield of sublesions is assumed to be the same for the same dose but different LET. As a consequence of this simplification, saturation effects are neglected. Some of these effects can be taken into account by adequate modifications (e.g. by adding of a linear component to the quadratic term in equation (2.13)).

The coefficient, $c$, should be constant if nothing but the total energy imparted to a site determines the kinetics of sublesion formation. However, as the submicroscopic structure of energy deposition in particle tracks inside the site also plays a role, $k$ has to involve an additional dependence on radiation quality, but there is no way to evaluate this dependence by means of microdosimetry.

Many efforts were made in the framework of microdosimetry to establish a model, which can predict the biological output (e.g. RBW, $S(D)$ or $\varepsilon(D)$) on the basis of measured microdosimetric (physical) quantities (see chapter 2.2.1) and theoretical considerations. However, all models that reproduce the biological response with a sufficient precision implement coefficients or weighting functions that have to be derived from biological measurements. Furthermore, such weighting functions have no "universal validity", but have different values under different circumstances. For example, it is often necessary to determine the weighting functions by measurements for each endpoint and dose level independently.

## 2.3  Molecular theory of cell survival (α/β models)

The molecular theory of cell survival [Cha73],[Cha81] assumes that double strand breaks of DNA (DSB) result in cell death with probability, $p$. DSB are postulated to be produced by both single particle passage event (inter-track action) and combinations of two single strand breaks (SSB), induced by two independent particle passage events (intra-track action). Hence, $N$, the number of DSB per cell has a linear-quadratic dose dependence:

$$N = \alpha D + \beta D^2 \tag{2.15}$$

where $\alpha$ relates to an irreversible lethal effect (produced merely by a single particle passage, what is typical for $\alpha$-radiation) and $\beta$ is related to DSB production by accumulating SSB damages. To derive the survival curve, DSB are postulated to affect the cell in a non-cumulative way, thus Poisson statistics can be applied. Survival is determined by the probability of no lethal event i.e. $x = 0$, where $x$ is the random variable for the yield of lethal DSB in the cell, and $pN$ product is its mean value:

$$S(0) = \frac{(pN)^0}{0!} e^{-pN} = e^{-p(\alpha D + \beta D^2)} = S(D) \tag{2.16}$$

The molecular theory is closely related to the TDRA in the respect that only a differently interpreted linear-quadratic mean yield of lesions is derived and determines the effect. Of course the possibility to fit survival cures by linear-quadratic models is not a sufficient criterion of these concepts which should be predictive for all type of irradiation. Many assumptions of molecular theory, however, can be questioned. The usage of Poisson distribution cannot be justified for high-LET radiation because one traversal is often enough or more than enough (saturation effect) to kill a cell. Besides, the quadratic component starts to dominate the measured X-ray survival curves of mammalian cells even at dose levels of several Gy. Mean distances of SSBs are estimated to be millions of DNA base pairs at such dose levels (measured data sets for SSB distances are compared (figure 6.5 in Gun83)). Conversely, non-linear dose effect relations indicate that biological effects could be the result of multiple events within micrometer distances, rather than DNA base pair dimensions. The other possibility is that the quadratic component should be attributed to other phenomena (e.g. repair; see chapter 2.5) rather than to inter-track actions.

## 2.4  Phenomenological description of survival curves

There are numerous models that ensure a relatively good fit for any measured survival curves with missing or questionable attempt to find a physical-biological concept behind. The two–component theory [Ben62] was e.g. originally derived from the multi-target model (section 2.1), extended by an exponential factor and giving up its original interpretation. The three-lambda model [Dou76] was developed because the linear-quadratic model failed to produce a good fit to the data derived from mouse skin survival experiments. The cubic survival equation was created by adding a third order term to the linear-quadratic expression for the purpose of quantitative comparison of various biophysical models [Tob85].

## 2.5   Models based on biological assumptions

Without engaging in details or critical examination of the validity of this group of models, some aspects are pointed out here to give a feeling for the huge spectrum of possible alternative interpretations of radiobiological effects and the processes leading to them.

In contrary to the models in the previous sections, the repair-misrepair model [Tob85] assumes that the initial yield of the so called uncommited lesions is proportional to the dose and a linear-self-repair and a quadratic-misrepair process compete in determining the probabilities of survival. Tobias shows, that at low doses, the survival curve of TDRA (section 2.2) and that of the molecular theory (section 2.3) can be translated to the repair-misrepair model despite the conceptually different assumptions.

The saturable repair model [Goo85] assumes that repairable radiation lesions are produced locally by one track action, hence the initial number of lesions is linear to the absorbed dose. Some of these lesions are repaired by a system whose efficiency decreases with increasing dose due to partial saturation of the repair kinetics, e.g. the limited number of repair enzymes can be reduced by radiation (some of the models include recycling of injured enzymes). After a certain time (e.g. according to cell cycle) lesions become no longer repairable. In addition, radiation may produce not repairable lesions too. Goodhead claims that most of the common phenomena which have been used as the basis for biophysical models can equally well be explained in terms of saturable repair (no need for e.g. sublesions).

Many other biology-based models are briefly described in [Tob85] and [Goo85], like the "cybernetic" model [Kap72] or the lethal-potentially lethal model.

## 2.6   DNA-lesion theory, nanodosimetry

The DNA lesion theory is based on the assumption that a theory of RBE for cell killing should include information about lesions at both molecular and cellular level. Models of RBE must imply a higher effectiveness if a definite energy imparted to the GSV is more concentrated in a smaller part of it [Gun83]. Numerous experimental investigations concerning the induction of SSB and DSB in cellular DNA have shown that the yield is proportional to dose up to several tens of Gy (e.g. [Tau96]). This means that intra-track interactions do not play a significant role in producing DNA lesions (at usual dose levels), thus the relevant site for DNA lesion production must be at nanometer order of magnitude. Simmons and Watt extend this statement even for a wider spectrum of endpoints [Sim99]. This finding suggests a target-model description for SSB and DSB production, using the conceptual equivalence: DNA = target, lesion = hit (for various sorts of lesions). The quantity, $s$, represents the average number of lesions per unit molecular weight of DNA and per unit specific energy. The following expression is suggested in [Gun77]:

$$s = \frac{1}{z_F} \sum_{j=0}^{\infty} \lambda_j f_1(j) \tag{2.17}$$

where $f_1(j)$ is the single event nanodosimetric spectrum in terms of ionization number, $j$, rather than specific energy. It refers to a target volume associated with the filamentous double-strand DNA. Its diameter is supposed to be similar to that of the DNA (2 nm). Indirect damages are not taken into account separately. $\lambda_j$ denotes the probability that an event of $j$ ionizations results in a lesion.

On the micrometer level the yield and distribution of these DNA-lesions is taken into account to determine the probability that an increment of specific energy in the GSV does not inactivate the cell. The $f(z;D)$ spectrum in the GSV is further needed to determine the survival curve. The resulting $S(D)$ survival curve contains three parameters that depend on the biological system only and one radiation-dependent parameter. For practical applications of this theory, the first three parameters can be determined for a reference radiation, say $^{60}$Co $\gamma$ - rays. Once these parameters have been fixed, the survival probability depends only on $f_1(j)$, $\lambda_j$ and $r$, where the latter is the relative efficiency for producing a lesion with high-LET particles compared to low-LET particles at the same dose. A detailed description ([Gun83]) and evaluation of this model is beyond the scope of the present work.

Numerous recent works focus on the nanometer site and assume that early damage to cells is initiated by radiation damage to cellular DNA. DSB and clustered lesions of DNA caused by clustered ionization by single particle tracks in sizes of DNA fractions (2-3 nm) [Gro02a], [Gro02b] [Gar04] or in chromatin fiber segments (25 nm in diameter) [Nar02] are considered to be responsible for biological effects. The quantity measured and simulated in these works, called cluster size distribution, is equivalent to $f_1(j)$, single event nanodosimetric spectrum of the lesion model (for the same or slightly bigger sites). In [Gar04] Garty describe a novel nanodosimeter to measure the cluster size distribution in gas, simulating short, nanometric segments of DNA. A simple biophysical model was developed in order to use the achieved cluster size distribution to assume the expectable yield of SSB, DSB and clustered lesions in these DNA segments (equivalent quantities to $s$ of the lesion model). In-vitro measurement of the same lesion yields was performed simultaneously, using plasmid-extract. Reasonable agreement between the predicted and measured yields of DSB but significant discrepancies in the case of SSB and clustered lesions were observed.

Such measurements and models deliver important information for the understanding of radiation action in living matter. However, it is not yet clear, if it is possible to establish a generally acceptable biophysical model which describes the correlation between the yields of different DNA damages and the observable cellular effects (namely survival curves or RBE values).

# 2.7  Amorphous track models, local effect model

## 2.7.1 Biological effects of ion radiation

The explanation (or even prediction) of ion survival curves is especially challenging for most of the described models. However, the recent development and future potential of ion radiotherapy facilities [Kra00] requires the precise determination of biological effects for different ions in various types of tissue in a broad energy range at various dose levels. As discussed in section 2.1, LET can not determine the biological efficiency alone, different ions have different RBE values at the same LET [Kra87] (see Figure 2.2b). The maximum of RBE was measured to be at 25 keV/μm for $^1$H, [Bel89], at 100 keV/μm for $^4$He or $^2$H [Bar63] and at 200 keV/μm for $^{12}$C beams [Tod65]. The maximum is located at even higher LET values for heavier ions [Kra87]. Simultaneously, the value of the corresponding RBE maximum decreases with increasing atomic number ($Z$).

The shape of a selected curve at a given (not too high) $Z$ in Figure 2.2 can be explained according to [Kra99b] in the following way.: The RBE is around unity at low LET because the ionization density is relatively low, therefore the resulting damages are mostly less

complex, often repairable. In the region of the RBE maximum, the local ionization densities along the ion tracks are high, causing clustered and thus less repairable DNA lesions. A single track passing a cell nucleus can kill the cell with considerable probability. As this probability tends to unity with increasing LET, the deposited energy in the affected cells increases further, but the killing probability cannot exceed unity. An increasing part of the dose is "wasted", this phenomena is termed overkill [But67]. Additionally, apart from the low energy region behind the Bragg peak (e.g. below 100 keV for protons), ions are slower at high LET (Figure 2.2a). Slower ions produce slower $\delta$-electrons with shorter ranges. This results in a decreasing track radius (it will be quantified in equation (2.32)). Hence, the average ionization density in nanometer sites along the track increases even faster than the LET making the overkill effect even more pronounced.

Heavier ions are faster than lighter ions at the same LET (Figure 2.2); hence the energy is distributed wider by the faster $\delta$-electrons. The most efficient ionization density level is reached at higher LET, which is the reason for the shifted maximum positions. Let us now compare the biological efficiency of two (not too heavy) different ion beams, if both are at their individual RBE-maximum (at different energy and LET). The ions of higher $Z$ have higher LET, therefore the particle fluence needed to deposit the same dose is lower. Although the track radius of the heavier ion is larger hence the inactivation cross section of a single ion is larger, this fact obviously cannot fully compensate the reduction in fluence: the total inactivation cross section of correspondingly lighter ions is still higher - lower survival level can be observed at the same dose. This is the main reason, why the maximum RBE values are lower for ions of higher $Z$.
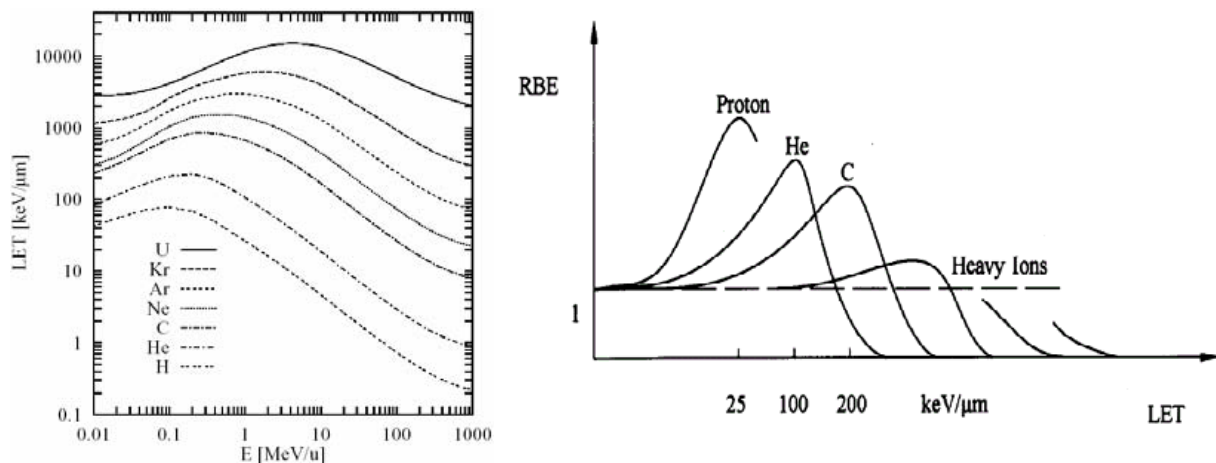


Figure 2.2: *Physical and biological properties of different ions in matter ($\rho = 1$ g/cm$^3$)*
a) *LET of different ions as a function of energy, calculated with ATIMA [Scw91].*
b) *Schematic RBE-LET dependency of ions of different Z. The RBE reaches its lower maximum at higher LET, for increasing Z. (LET of $^1$H cannot be higher, than ~85 keV/µm (Bragg peak), while LET of $^{238}$U cannot be below ~1700 keV/µm). [Kra99a].*

Beside the complex $Z$-dependency, RBE of ions depends on the biological system, where the most important properties are the repair capacity [Kra99b] and the oxygen content. The dose dependent steepness ratio of the ion and X-ray survival curves has the consequence that the RBE of a given cell depends strongly on the survival level under consideration.

None of the models mentioned in the previous chapters has proved its ability to explain all these features of ion survival curves in a predictive manner with the accuracy, needed for heavy ion therapy planning [Kra99a]. Many of the models, developed primarily e.g. for radiation protection purposes and being optimized for X-ray or neutron radiation do not handle the overkill phenomenon. Especially the reproduction of the $Z$-dependent location and

value of RBE maxima (see Figure 2.2b) is problematic for all the models. However, the track structure approach [But67] was found to be able to reproduce the mentioned features of ion RBE if a certain set of parameters (concerning mainly the response of the given cells to X-ray radiation) is given.

## 2.7.2 The track structure theory of RBE

The track structure theory, developed by Butts and Katz [But67], [Kat71] addresses the RBE problem directly. The survival curve, $S_\gamma(D)$, for photon radiation is considered to be well known, and an attempt is made to reduce the action of single heavy charged particles to $S_\gamma(D)$. The model treats the ion track as nothing but a blurred shower of $\delta$-electrons which have the same quality as photon-produced electrons. The model distinguishes between two action modalities "ion-kill" and "$\gamma$-kill". Intra-track effects can be neglected at low fluence, the damage is due to single ion transits (only ion-kill plays a role). There is an additional contribution at high fluence, where $\delta$-electrons of several ions can overlap in space and determine the effect ($\gamma$-kill).

The probability of killing a cell by one traversal through its sensitive volume is assigned with $P$. In a general case the model assumes, that the fraction $P$ of the dose, $D$, is delivered in the ion-kill mode and the remaining $(1-P)$ in the $\gamma$-kill mode. $P$ can be expressed as the ratio:

$$P = \sigma / \sigma_0 \qquad (2.18)$$

where $\sigma$ is the inactivation cross section of the cell for a certain particle in ion-kill mode, and $\sigma_0$ is the saturation cross section, therefore it determines the response to very-high LET radiation. Let us assume an ion that passes in the distance $r$ from the center of a selected sensitive site. The mean dose, $\overline{D}(r)$, is the mean energy deposited in the sensitive volume according to the radial dose distribution along the ion track. $E(r)$, effect probability is assumed to be determined by $\overline{D}(r)$ in that way, as if the whole neighborhood of the site was affected by $\gamma$-rays delivering the same dose, i.e. according to $S_\gamma(D)$, $\gamma$-survival curve. $\sigma$ is evaluated formally by summing up the $E(r)2\pi r dr$ weighted elementary ring areas:

$$\sigma = 2\pi \int_0^\infty t\left[1 - S_\gamma\left(\overline{D}(t)\right)\right]dt \qquad (2.19)$$

If $F$ denotes the particle fluence, and the initial cell population is $N_0$, the expected number of cells surviving ion-kill, $N'$, can be expressed as follows:

$$N' = N_0 e^{-\sigma F} \qquad (2.20)$$

The remaining $N'$ population is assumed to be the initial population for the $\gamma$-kill which delivers the remaining $(1-P)D$ dose and affect the cells again according the $\gamma$-ray survival curve. Hence, the resulting survival curve can be written in the following form:

$$S(D) = \frac{N'}{N_0}S_\gamma\left((1-P)D\right) = e^{-\sigma F}S_\gamma\left((1-P)D\right) \qquad (2.21)$$

The explicit evaluation of $S_\gamma$ is carried out by using the pure m-target-1-hit model (see chapter 2.1) for the sensitive site of the cell:

$$S_\gamma(D) = 1 - (1 - e^{D/D_0})^m \qquad (2.22)$$

After collecting the equations (2.18), (2.21) and (2.22) and using D = F*LET, the formulation takes the form of the three-parameter two-component model (chapter 2.4):

$$S(D) = e^{-\sigma_0 P \frac{D}{LET}} \left[ 1 - \left( 1 - e^{-\frac{(1-P)D}{D_0}} \right)^m \right]$$

(2.23)

For the practical application, P is derived from (2.18) and (2.19), where the numerically calculated result of the integral is approximated by an analytical expression of the ion velocity, its effective charge, $m$ and a fourth parameter, $\kappa$ which combines size and radiosensitivity [Kat03]. The parameters $D_0$ and $m$ are obtained from fitting the $\gamma$-sensitivity curves only, by the expression (2.22). $\sigma_0$ and $\kappa$ are derived from different LET curves.

The amorphous track model of Katz turned out to be well suited to reproduce the general features of the cell-survival RBE including the $Z$-dependent characteristics of the RBE-LET function and the decrease in RBE at the end of the tracks due to overkill effects. However, as pointed out by several authors [Gun83], [Pag01] and [Sch04], good agreements with experimental results can not be achieved in each case (weak prediction for fast neutrons [Gun83] or for slow very heavy ions [Sch04]) and in some other cases the agreement is due to rather arbitrary adjustable parameters (like $\kappa$) or inconsistencies between application and interpretation of various facts or assumptions (e.g. regarding to target size or ion-kill to $\gamma$-kill ratio). The main deficiency of the approach is due to the averaging of dose inside the sensitive site (similar to the GSV concept discussed on the basis of equation (2.12)). This simplification has the most severe consequences for light and slow ions, where the very high local dose along the ion track cannot be taken into account due to the averaging over the extended site. It was shown in [Pag01] and in [Sch04] that only an approximating formula (see equation (5) in [Kat71]) used instead of the (2.19) integral leads to satisfactory results in this case. Thus this "approximating" form and some other assumptions (e.g. multi-hit model, size of the sensitive volume, distinguishing between the two killing modalities) have questionable theoretical justification or biological motivation, the theory has to be treated as a largely formal, mathematical construction, nevertheless, still successful and with predictive power in many cases.

## 2.7.3 The local effect model

Motivated by the success of the amorphous track model, Scholz and Kraft developed a new version of the models based on track structure, the local effect model (LEM) [Sch94], [Sch96]. Besides the limitations of the Katz model mentioned above, the need for adjusted parameters based on experimental data with low- and high-LET particles was not satisfactory for the purposes of high-LET therapy planning. The concept of LEM keeps some of the basic ideas of the Katz model, but makes a successful attempt to modify it in order to make it more universal on a solid biophysical basis and based on an unambiguous experimental data-set.

Similar to the track structure model, LEM does not make an attempt to describe in detail the chain of physical, chemical and biological processes that follows an irradiation of biological systems. However, many of the aspects, described in the introduction of chapter 2, can be regarded to be implemented through the $X$-ray survival curve. The sensitive site (GSV) is assumed to be the cell nucleus and based on the work of Barendsen [Bar90] and others, it is further assumed, that the sensitivity of the cell nucleus has no spatial variation across the nucleus. However, the cell reacts not according to the average dose, integrated for the entire GSV, like in the Katz model. Based on the investigations of Goodhead and co-workers [Goo79] it is rather assumed, that cell inactivation can be attributed to at least one local lethal event inside the nucleus (e.g. not repaired complex DNA lesion). Investigations with ultrasoft $X$-rays [Goo79] indicate that in order to form a lethal lesion, ionization density in very small subvolumes with dimensions in the order of several nm is decisive (the same result was

achieved in [Sim99]). I.e. interactions of sublethal events over large distances of the order of micrometers can be neglected (in contrast to findings, like in [Kel80] about two dominating interaction domains - see chapter 2.2). LEM assumes, that for inducing a lethal lesion in subvolume, $V$, of the cell nucleus, the probability is completely determined by the local dose in $V$. In the formal description the size of $V$ is infinitely small. For practical application and numerical calculations a discretization of the cell nucleus into still very small regions is appropriate. This discretization plays a role only in the very central region of the ion track cores, where the local dose gradient is significant. The consequence of the finite size of $V$ *is* an averaging of the effects over $V$, which to some extent accounts for the diffusion of the radiation-induced reactive species. This is not included in the track structure models used so far. It was shown in systematic sensitivity studies, that the exact size of the nanometric sized discrete regions do not affect the resulting RBE values strongly [Sch04].

The central quantity in the LEM, the local dose, $d$, is the expectation value of the deposited energy in $V$ for a given set of incoming particles. LEM assumes, that for the radiation effect in $V$ only $d$ matters, regardless of what kind of particles are responsible for the local dose deposition. This central assumption of the LEM can be formulated as follows (e.g. for ions compared to X-ray radiation):

$$v_{Ion}(d) = v_X(d) \tag{2.24}$$

where $v_{Ion}(d)$ and $v_X(d)$ are the lethal event densities in $V$, at the local dose level, $d$ for ion and X-ray radiation, respectively.

It is important to note, that the local dose is an expectation value in both cases. For X-rays the spatial distribution of $d$ and thus of $v_X(d)$ are assumed to be homogenous even down to nanometer volumes ($d = D$), i.e. the physical stochastics of the secondary electrons produced by the photons is neglected. This assumption is definitely justified at higher dose levels where many independent primary photons contribute to the dose in small volumes, than in the low-dose limit. In the case of particle radiation, the ion tracks are treated individually and the spatial distribution of the local dose, $d(x,y,z)$ is determined as a sum of the radial doses of the tracks at $(x,y,z)$. The radial dose, $d(r)$, is defined as the expectation value of the deposited energy as a function of the distance from an ion track axis. This is also a deterministic quantity, i.e. it has a single value on a whole cylindrical surface around the ion track. Although the position of each single track is simulated by Monte Carlo calculations, therefore the resulting $d(x,y,z)$ for ions is neither constant nor deterministic, it still does not account for the stochastics due to the $\delta$-electrons. However, the role of stochastics is not absolutely eliminated by the LEM. The ionization patterns, spatial fluctuations according to secondary electrons originating from X-rays and from $\delta$-electrons around ion tracks are not very different at the same local dose level. Therefore, if the density and energy spectrum of the both secondary electron populations do not differ very much at a given local dose level, the role of stochastics should be similar in the both cases, hence $v_{Ion}(d)$ and $v_X(d)$ could be already affected by inherent stochastics in a similar manner This anticipation should be investigated further.

According to the constant spatial distribution of lethal events after X-ray radiation, $v_X(d)$ can be expressed as a ratio of the dose-dependent expectation value of lethal event yield in one cell, $\overline{N_X(D)}$, and the volume of the cell nucleus, $V_{Nucl}$:

$$v_X(d) = v_X(D) = \frac{\overline{N_X(D)}}{V_{Nucl}} \tag{2.25}$$

$S_X$ survival at a given dose represents the fraction of cells with no lethal events. The pattern of energy deposition due to X-rays is sufficiently homogenous to assume, that the distribution of lethal events among individual cells obeys Poisson statistics, hence, according to the same argumentation as in chapter 2.3 for equation (2.16), $S_X$ can be expressed with $\overline{N_X(D)}$ :

$$S_X = e^{-\overline{N_X}} \tag{2.26}$$

From equations (2.25) and (2.26) follows:

$$v_X(D) = \frac{-\ln S_X(D)}{V_{Nucl}} \tag{2.27}$$

The expected number of lethal events in a cell after ion radiation, $\overline{N_{Ion}(D)}$, can be calculated by integrating $v_{Ion}(d)$ over the whole volume of the nucleus:

$$\overline{N_{Ion}(D)} = \int_{V_{Nucl}} v_{Ion}[d(x,y,z)] dV \tag{2.28}$$

Now, after application of (2.25) for $v_{Ion}[d(x,y,z)]$ the result of (2.27) can be written in (2.28):

$$\overline{N_{Ion}(D)} = \int_{V_{Nucl}} v_X[d(x,y,z)] dV = \int_{V_{Nucl}} \frac{-\ln S_X[d(x,y,z)]}{V_{Nucl}} dV \tag{2.29}$$

Result (2.29) introduces the central input parameters needed to apply the model and Figure 2.3 illustrates this schematically. As already mentioned above, $d(x,y,z)$ is obtained in practice as the sum of the radial dose contributions of that tracks, which contain the position $(x,y,z)$ inside their $\delta$-electron range. The particle trajectory positions are determined by random sampling according to the macroscopic dose and the particle LET. The local effects are than determined from the X-ray survival curve. The local effects have to be integrated over the nucleus volume, hence the third crucial input parameter (besides $d(r)$ and $S_X(D)$) is the radius of the cell nucleus.
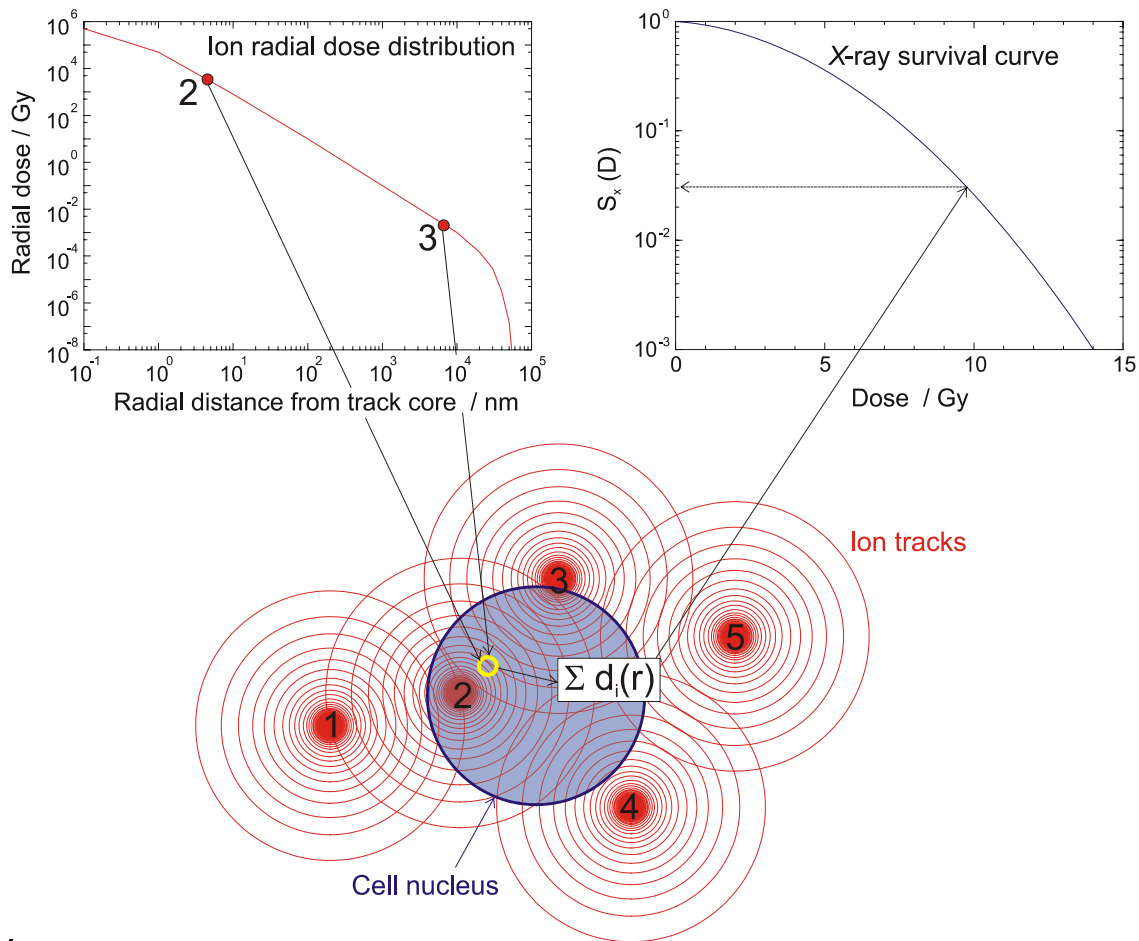
Figure 2.3: *Schematic representation of the required input parameter set and the way of proceeding for the application of the LEM. The local dose at a certain location is acquired as the sum of the radial doses around the tracks (the red circles represent iso-dose surfaces). The local effect is than calculated according to the X-ray surviving curve. The whole cell reacts to the integral of these local effect contributions, rather than to the integral dose.*

Figure 2.4 demonstrates that LEM is capable to achieve satisfactory agreement with measured survival data. The assumptions of the model can be justified by theoretical and experimental results. The model works effectively in the whole practically interesting energy region of any ion. It is the only biophysical model so far, that can predict both the *Z*-dependent shift of RBE-maximum and the decline of its value with a sufficient precision (see introduction of chapter 2.7). Although the construction of the model was motivated by charged particles, the validity of it is not restricted to ion radiation; LEM calculations show similar agreement with experiments for neutrons (see Figure 2.4c). Without the introduction of different inactivation modes (see comments on Katz model), LEM can predict the transition from the shouldered *X*-ray survival curves to exponential ones depending on the size and repair capability of the biological object. However, the validity of the assumptions still requires further confirmations. Particularly the neglected role of long-distance lesion-interactions and stochastics (see comments above) as well, as the local effect equivalence due to *X*-rays and particle beams. The model was primarily constructed for application in radiotherapy or space research rather than for radiation protection; its validity at low dose levels is limited. Nevertheless, the successful application of LEM in the framework of treatment planning for carbon-ion cancer therapy at GSI, Darmstadt, Germany [Kra00], [Scz04] is a great evidence for the potency of the LEM as a theory of biological effect. Besides, measured cross sections for single- and double-strand break induction in SV40 plasmid DNA after high-LET

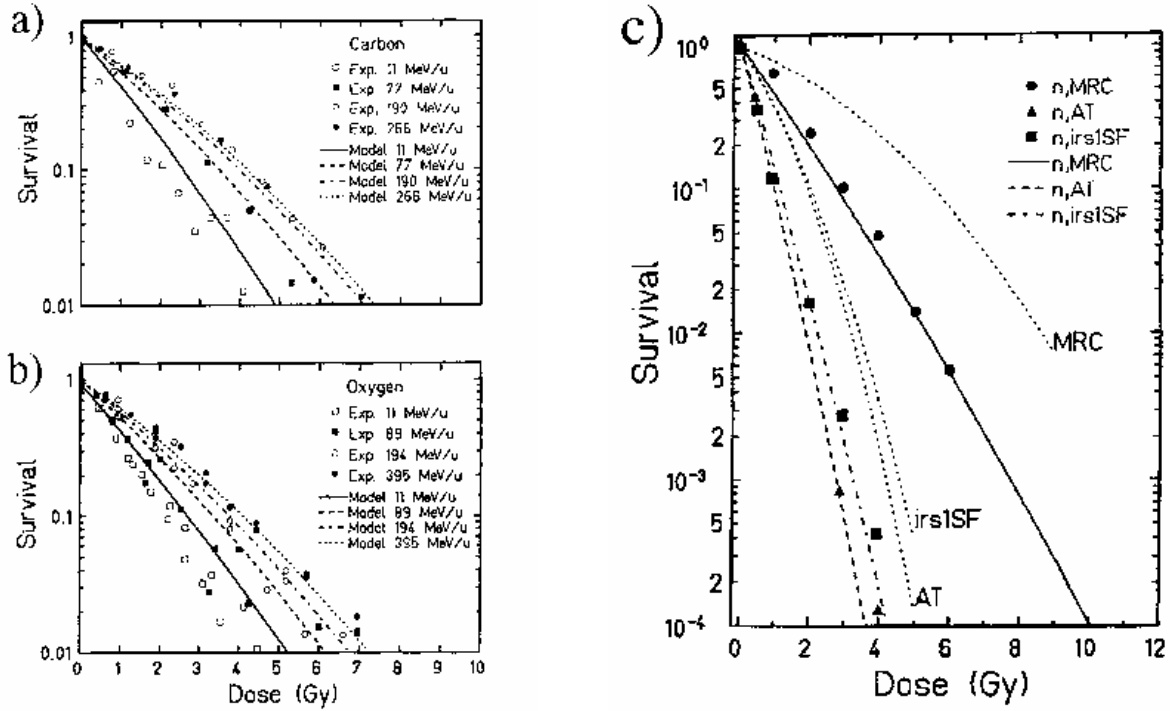irradiation can be reproduced well by a model based on the same considerations, as used for LEM [Bro03].



Figure 2.4: *Comparison of measured simulated (with LEM) survival curves. a),b) Measured (symbols) and simulated (lines) survival curves for carbon and oxygen beam lines at different energies interacting with CHO cell. (measurements: Kraft-Weyrather et al., unpublished). c) Measured [Egu96] and simulated survival curves. Three different cell lines (AT and MRC human; irs1FS Chinese hamster) were irradiated by ~14 MeV neutron. The dotted lines represent the X-ray survival curves for the corresponding cell lines. Mainly due to the different repair capability of the different cell lines the X-ray sensitivities are largely different, which is reflected in the different neutron sensitivities. This is predicted rather well by the LEM.*

Equation (2.29) is the most general formulation of the LEM. For the practical application (e.g. therapy planning at GSI [Kra00], [Krm00a]) some further concretions and approximations are adopted. Details about simplifications and description of an iterative algorithm to calculate RBE values fast under realistic circumstances (e.g. different tissues, mixed radiation fields) can be found in [Sch97] and [Krm00b]. Here, we just mention, that in the practical application the cells are e.g. assumed to be cylindrical with their axis parallel to the projectiles. The X-ray survival curves are parameterized in a modified linear-quadratic manner [Sch96]. Finally, for the radial dose distribution in practical applications [Sch96] LEM often applies the following approximation:

$$d(r) = \begin{cases} \lambda LET / r_{min}^2 & : r < r_{min} \\ \lambda LET / r^2 & : r_{min} < r < r_{max} \\ 0 & : r > r_{max} \end{cases} \qquad (2.30)$$

where the normalization constant, $\lambda$, is adjusted according to:

$$LET = \int_{0}^{r_{max}} d(r)\mathrm{d}r \qquad\qquad (2.31)$$

$r_{max}$ is the range of the fastest $\delta$-electrons produced by the primary particle and it is determined by the specific energy (energy divided by the particle mass) of the incoming ion:

$$r_{max} = \gamma E^{\delta} \qquad\qquad \text{where } \delta \approx 1{,}7 \qquad\qquad (2.32)$$

And $\gamma$ scaling constant depends on the material. This approximate formula shows a nearly quadratic dependency between the specific energy and the track radius. For radii below $r_{min}$ is a constant dose assumed, where $r_{min}$ is usually selected to be ~10 nm. The role of this parameter and its biophysical motivation was already explained above in connection with the discretization of the nucleus volume.

# 3 Ion transport in matter

The present work is focused on the investigation of the ionization pattern (mainly the radial ionization distribution) in matter due to ion penetration. For the successful measurement and simulation of the physical parameters, relevant in the biophysics, it is essential to have a broad insight into the physical processes that take place when an ion passes through a matter. Heavy charged particles traversing matter lose energy through successive interactions with the atoms and molecules of the material. A possible classification of the interactions is made according to the interacting partner of the projectile: it can be a whole molecule (resulting in the dissociation of it), an atomic nucleus (nuclear stopping or nuclear reactions see chapter 3.1), but most of the projectile energy is deposited via interactions between the projectile and single electrons of a target atom (see chapter 3.2) or molecule. The biological effect is dominated by the consequences of the latter interaction form and particularly by that of ionizations (see chapter 2).

## 3.1 Nuclear stopping, nuclear reactions

The interactions of the projectile with an atomic nucleus result in the nuclear stopping of the projectile. The most probable interactions are elastic or inelastic scattering in the Coulomb field of the nucleus. In solid matter, at low collision energies, nuclear stopping can lead to a displacement of atoms in the crystal structure or to phonon excitations in the target. In the case of elastic scattering the projectile is simply deflected by target atoms without any change of their internal structure. While the internal quantum state of one or both of the participating particles due to an inelastic scattering process undergoes a change (e.g. excitation of the nucleus material: Coulomb excitation). The overall contribution of nuclear stopping to the energy loss of the projectile is negligible above ion energies of several tens of keV (see Figure 3.1), thus there is no need to take it into consideration in the present work.
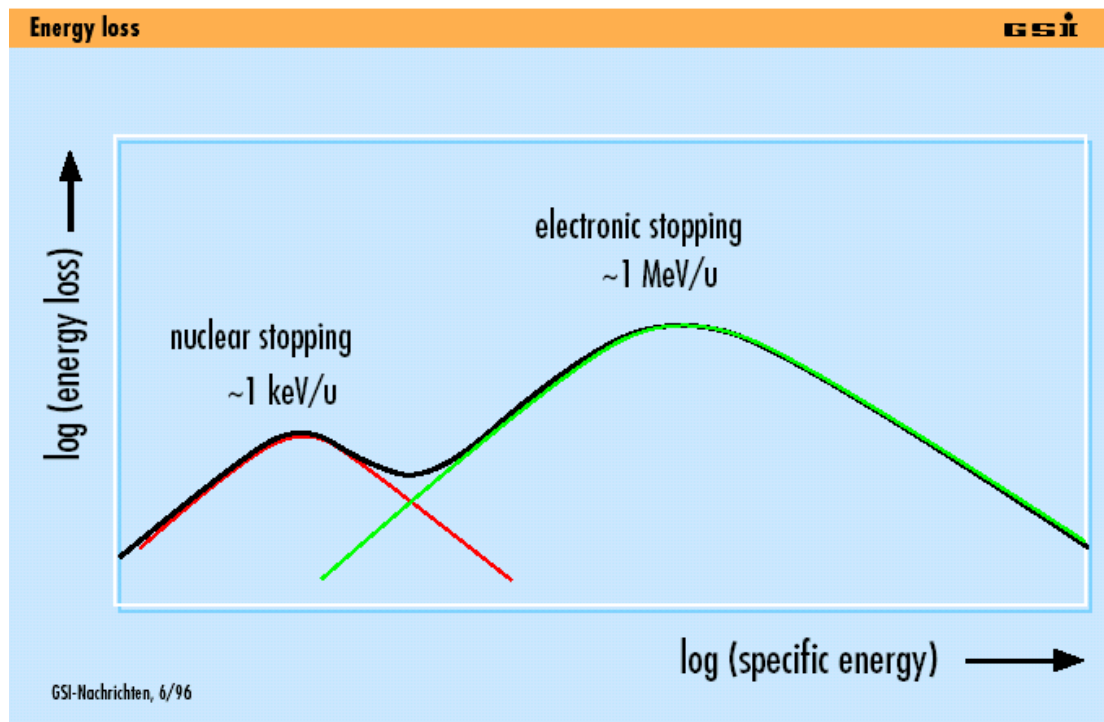
Figure 3.1: *Schematic curves of nuclear (red curve) and electronic (green curve) stopping of an ion in matter as a function of its specific energy. The nuclear stopping is dominant only at very low energies (far below the Bragg peak).*

Besides elastic and inelastic scattering there are other interactions: nuclear reactions, where at least one of the participating atomic nuclei undergoes a transformation into another nucleus (e.g. emission of neutron, proton or another particle or more of them). This process is called fragmentation. The first systematic investigation of the fragmentation of $^{12}C$ ions in $H_2$, He and C targets was described by Webber et al. [Web90]. An investigation of the heavy ion fragmentation in water target was performed by Schardt et al. [Sdt96]. An overview of the literature about fragmentation issues can be found in the dissertation of Gunzert-Marx [Kon04], which contains also a summary of the fragmentation properties of carbon ions in water.

The phenomenon of fragmentation has certain consequences for the experiments with OPAC, where different ions of diefferent energies were used as projectiles. At high ion energy the ion energy was defined directly by the accelerator, but for energies below about 100 MeV/u a water column was used as energy degrader. Along their path through the water column some of the original ions undergo fragmentation, thus not only original ions reach OPAC, but also various fragments, i.e. lighter ions.

It can be concluded, that the role of fragmentation behind the energy degrader used in the measurements with OPAC is immense. E.g. if using primarily 676 AMeV $^{12}C$ ions, more than two third of them are fragmented behind a water column of 25 cm thickness [Sdt96]. The study of fragmentation is not an issue of the present work. All the quantitative examinations with OPAC are restricted to the investigation of the ionization pattern of the original ions that reach the sensitive volume without nuclear reactions. Some of the smaller fragments are also detected by OPAC and their contribution needs to be rejected by the analysis software. This can be achieved by selecting the particles according to LET. For practical details about the method of the fragment elimination see chapter 7.2.

# 3.2 Electronic stopping, primary electron production

Most of the ion energy is deposited in interactions with the electron shell (electronic stopping). Furthermore, about 2/3 of the energy loss of the ion is transferred into kinetic energy of the $\delta$-electrons ([Gro80], p. 81). The purpose of the present work is to describe the ionization pattern at a certain ion energy. The stopping process of the ions itself is not studied in this work. The energy of the ions, passing through the sensitive volume, can be treated as constant under most of the measurement conditions. Only qualitative measurement results will be shown at energies below or slightly above the Bragg peak, where the energy loss of the ions inside the chamber is not negligible compared to their absolute energy. A description of the most important processes that are accompanied by electron production will be specified in this chapter in more detail. Other processes, resulting in energy loss of the incident ion (like excitation or molecular dissociation) will not be treated here. The most established model, that treats the cumulative energy loss of ions, was introduced by Bethe and Bloch. They used the first Born approximation [Bet30] at relativistic energies [Blo33]. The most relevant results concerning the LET-energy function are summarized by Titt (see p. 6 in [Tit99].

The present work concentrates on the spatial distribution of ionization locations inside the matter, caused by an ion penetration. The ionization pattern arises as a result of primary ionization events (the penetrating ion directly ionizes the matter) and secondary ionization events (the energetic free electrons, produced by the ion or another electron, ionize the matter). Therefore it is not enough to determine the primary ionization locations, the emission energies and angles of the emitted electrons and their further transport an ionization pattern are also needed. To illustrate the various processes of ion induced electron emission, Figure 3.2 displays the two dimensional momentum distribution of the electrons emitted in collisions of 5,88 AMeV $U^{29+}$ with $C_3F_8$. The image was taken by Bechthold et al. [Bec97] at GSI with a toroidal spectrometer, developed by Hagmann [Hag93], based on the revolutionary spectrometer technology, established by Engelhardt et al. [Eng81]. The electron distribution is presented in the momentum space, where the abscissa corresponds to the beam direction ($p_{\parallel}$) and the point, ($p_p$,0) represents the projectile velocity, $v_p$, being about 15 atomic units (15 a.u.) in the presented case. The momentum of an emitted electron (a single black dot in Figure 3.2) is proportional to its distance from the origin. The angle of the momentum, $\vartheta$, is measured with respect to the beam direction. Since the image is axial symmetric to the beam axis, $\vartheta$, which varies between 0° (forward scattering) and 180° (backward scattering), contains the entire physical relevant information. In Figure 3.2 ringlike structures can be recognized. These ridges are characteristic for certain electron emission processes, which are specified in Figure 3.2 with letters and briefly described in the following sections of this chapter.
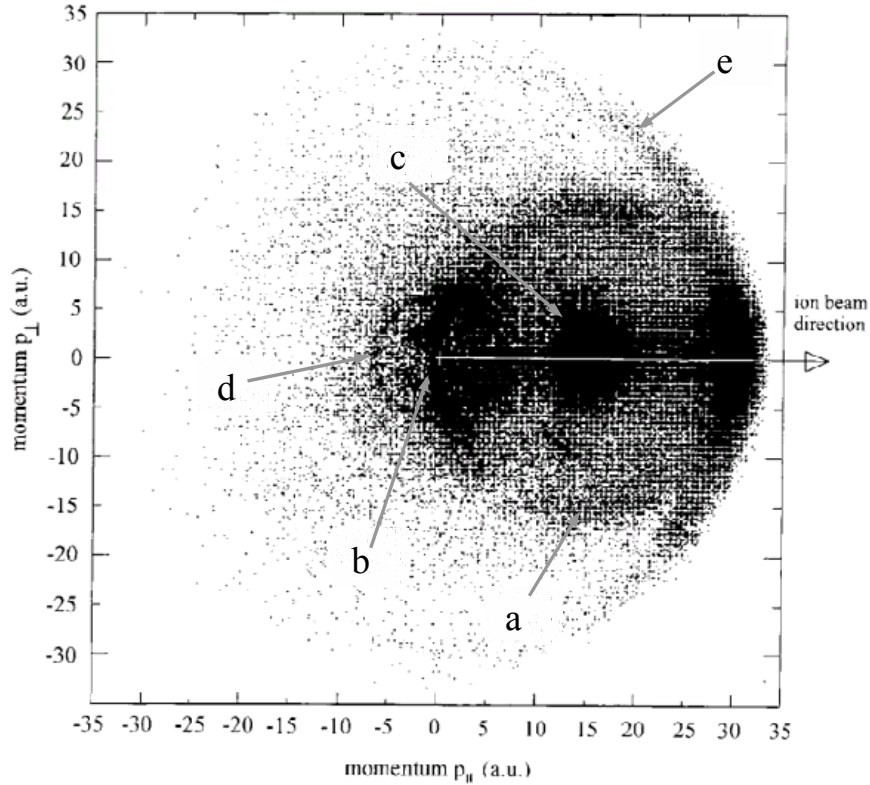
Figure 3.2: *Experimental momentum distribution for electrons emitted in collisions of 5,88 AMeV $U^{29+}$ with $C_3F_8$ (source: [Bec97]). Ringlike structures, characteristic for different emission processes can be observed with different centers and radii ($p_r$).*

a) *Binary encounter electrons, center: ($p_p$,0), $p_r = p_p$*
b) *Target electrons from peripherical collisions, center: (0,0), $p_r << p_p$*
c) *Loss electrons (of the projectile), center: (0,0), radius: $p_r = p_p$; predominantly around ($p_p$,0): Cusp peak*
d) *Target Auger electrons, center: (0,0), $p_r < p_p$; $p_r = 0,43 \, p_p$ in the given example (fluorine KLL Auger)*
e) *Double scattered target electrons: center: (0,0), radius: $p_r = 2p_p$*

It is important to note, that Figure 3.2 reflects the momentum distribution of the $\delta$-electrons induced by the passage of heavy ions in a gas. Similar measurements were performed by Hagmann at Kansas State University, using solid targets from carbon and aluminium were used instead of the $C_3F_8$ gas as interaction medium [Zae02]. In these measurements a sharp and very narrow ridge (like an electron jet) appears along the ion beam axis in forward direction (some measurements show a ridge in backward direction as well). The toroidal spectrometer has a good angular resolution and the capability of recording the entire angular distribution of the $\delta$-electrons in a single run. These features of the measurement device made it possible, to observe the described electron jets. More details on this subject are given in chapter 4.1.

## 3.2.1 Binary encounter (BE) electrons

The main contribution to the electron emission is the BE process around the projectile emission system $(0,p_p)$. Its dominance is even more pronounced, if the focus is on $\delta$-electrons of higher momentum at larger angles. Thus, BE electrons play the most crucial role for energy transfer further away from the track core and thus in the forming of the radial ionization distribution. BE electrons are produced in hard, knock-on collisions between the ion and an

electron of a target atom. The impact parameter for the BE collisions is small, thus the transferred energy is high compared to the binding energy of the electron to the nucleus. The presence of the surrounding atoms is also negligible. Hence, the interaction can be treated as a classical two-body collision of a point-like projectile and a free (or quasi free) electron (Rutherford scattering). Quasi free implies, that the target electrons are handled as free for the determination of the transfer energies or scattering cross sections, but the resulting electron energy is the energy transfer reduced by the binding energy of the ejected electron to its target nucleus
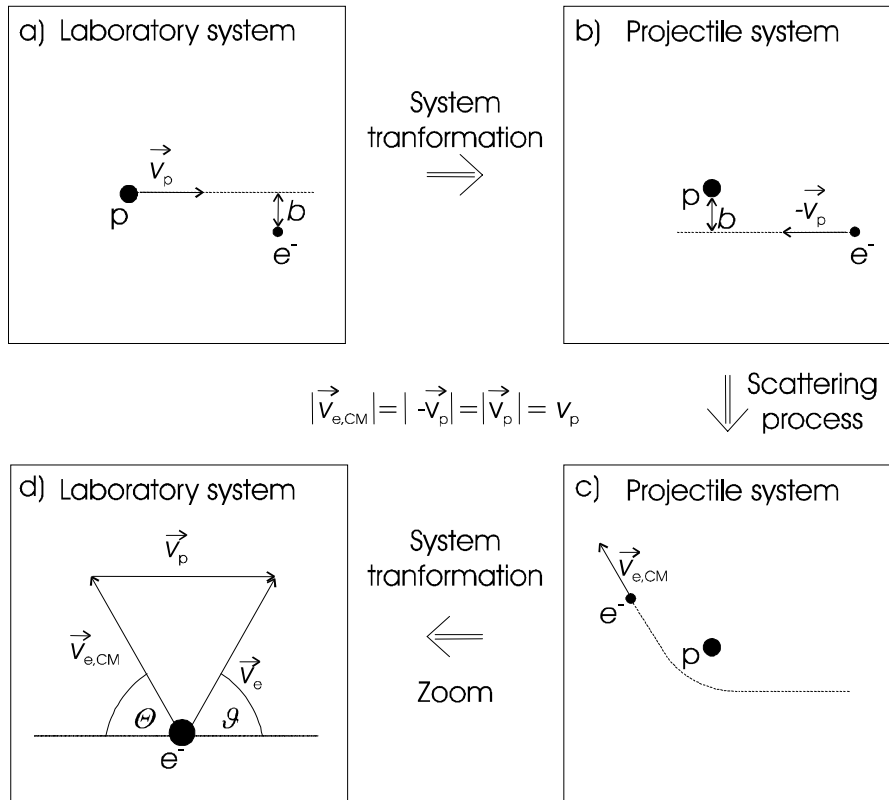


Figure 3.3: *Demonstration of the kinematics of the binary encounter electron production. a) The projectile, p, approaches a (quasi)steady, (quasi)free electron with a velocity of $\vec{v}_p$ and an impact parameter of b, b) shows the same situation from the projectile system, i.e. approximately the center of mass system, c) illustrates schematically the path of the electron and its velocity, $\vec{v}_{e,CM}$, after the scattering in the projectile system, d) demonstrates the back-transformation to the laboratory system, where the electron velocity is $\vec{v}_e$ after the interaction. The scattering is elastic, therefore $\left|\vec{v}_{e,CM}\right| \approx \left|\vec{v}_p\right|$ ($m_e << m_p$). Thus, the scattering angle in the projectile system, $\Theta$ and in the laboratory system, $\vartheta$, underlie the relationship: $\Theta + 2\vartheta = 180°$.*

It is useful to treat this problem in the center of mass system which can be treated as equivalent with the projectile system due to the mass difference between the projectile and the interacting electron. Figure 3.3 demonstrates the initial situation, the transformation into the projectile system, the scattering, observed from the projectile system and the back-transformation to the laboratory system. The projectile ion with mass, $m_p$, atomic number, $Z_p$, initial speed, $v_p$, and energy, $E_p$ reaches the electron with the impact parameter, *b*, (Figure 3.3 a). The projectile is (nearly) at rest in the center of mass system, and the electron with the

mass, $m_e$, approaches the projectile with a velocity of $-v_p$ (Figure 3.3 b). After the elastic scattering the absolute value of its velocity remains approximately the same, while its direction changes by the angle, $\Theta$ in the projectile system (Figure 3.3 c). After the back-transformation (Figure 3.3 d), the scattering angle in the laboratory system, $\vartheta$, can be expressed with $\Theta$ as follows:

$$\vartheta = \frac{180° - \Theta}{2} \tag{3.1}$$

The absolute value of the velocity, $|\vec{v}_e|$, of the emitted electron in the laboratory system:

$$v_e = |\vec{v}_e| = 2v_p \cos \vartheta \tag{3.2}$$

Thus, there is an unambiguous correlation between the emission angle and the energy transfer to the BE electron, $\Delta E$, for a fixed projectile energy and mass:

$$\Delta E = 4 \frac{m_e}{m_p} E_p \cos^2 \vartheta \tag{3.3}$$

The maximal BE electron energy can be achieved in forward scattering ($\vartheta = 0°$, hence $\Theta = 180°$). In this case $v_e = 2v_p$, and for the maximal $\delta$-electron energy we obtain:

$$\Delta E_{max} \approx 4 \frac{m_e}{m_p} E_p \approx \frac{1}{500 Z_p} E_p \tag{3.4}$$

According to the equation (3.2), all BE electrons should appear in Figure 3.2 along a well defined single circle, but a broad distribution can be observed in the reality. This discrepancy between the basic theory above and the observations is due to the assumption that the target electrons are at rest before the interaction. The broadening of the spectra is due to the superposition of the initial momentum distribution of the bounded electron (Compton profile) and the momentum distribution from the BE collision. The binary encounter approximation (BEA) supplements the Rutherford model by accounting for the Compton profile of the ejected BE electrons. The validity and limitations of the BEA will be described in chapter 3.3.3.

By applying the conservation laws for energy, momentum and angular momentum to the electron scattering in the Coulomb potential of the projectile, the angular differential cross section in the center of mass system can be determined as follows:

$$\left[\frac{d\sigma}{d\Omega}\right]_{CM}^{BE} = \frac{q_{eff}^2 e^4}{16 E_{e,CM}^2 \sin^4 \Theta/2} \tag{3.5}$$

where $e$ is the electron charge, $E_{e,CM}$ is the energy of the ejected electron in the center of mass system and $q_{eff}$ is the effective projectile charge. The quadratic scaling of the Rutherford cross sections with the effective charge of the projectile is an important feature of this result. After traversing any matter with sufficient thickness, projectiles keep only electrons with orbital velocities above the propagation velocity of the projectile. The resulting equilibrium charge state is called effective charge. The effective charge equals the atomic number of the projectile, if the ion is light and fast. Heckmann et. al. [Hec60] have found a semi-empirical formula (Barkas formula) to derive the effective charge for heavy ions as a function of the atomic number and the relative velocity of the projectile ($\beta$):

$$q_{\mathrm{eff}} = Z_{\mathrm{p}}\left[1 - \exp\left(-125\beta Z_{\mathrm{p}}^{-\frac{2}{3}}\right)\right] \tag{3.6}$$

## 3.2.2 Electrons from peripheral collisions

If the impact parameter of the projectile with respect to a target electron is comparable with the distance of this electron and the target nucleus, then the problem has to be treated as a three body collision. The target atom is ionized by the projectile ion but the emitted electron is scattered in the potential field of the target nucleus before leaving the interaction location. These electrons have low energies (typically below 100 eV), and their angular distribution is nearly isotropic in the laboratory system.

## 3.2.3 Loss electrons, cusp electrons

If the projectile is not a bare ion, a projectile electron can be raised into continuum state by a Rutherford-scattering in the Compton field of a target nucleus (loss electrons). The kinetic energy of a loss electron is not affected by the elastic scattering, therefore its velocity preserves the $v_{\mathrm{p}}$, projectile velocity modified slightly by the initial Compton-profile of the projectile electron. The double differential cross section for loss electron production decreases with increasing emission angle radically. It is also possible, that a target electron is captured into a high Rydberg state of the projectile. These electrons appear together with the loss electrons under $\vartheta = 0°$ in a "cusp"-shaped peak. In the Figure 3.2 the peak at $(p_{\mathrm{p}},0)$ can be attributed to loss, rather than to capture electrons, because the charge of the projectile ions (+29) is far below the equilibrium charge state at the given projectile energy.

## 3.2.4 Auger electrons

If an inner shell ionization of a target atom is induced by the projectile, the atom deexcites by emitting a photon or another electron (Auger electron). The energy of the Auger electron can be derived from the binding energies of the contributing electrons in their initial and final states. For a given target material one or few Auger transitions and thus one or few discrete Auger electron energies are characteristic. Therefore the energy of the Auger electrons is constant and the emission cross section is nearly constant independently of the emission angle (circle centered in the origin, with a radius of about 5 a.u. in Figure 3.2). The projectile can emit Auger electrons as well. The angular energy and cross section functions of the emitted electrons are transformed by the initial $v_{\mathrm{p}}$ velocity and the Doppler effect in this case. The contribution of Auger electrons to the whole $\delta$-electron emission is small, especially that of the projectile Auger electrons.

## 3.2.5 Double scattered electrons

A ridge of high energy electrons can be observed in Figure 3.2 in $2v_{\mathrm{p}}$ distance around the origin. It is not discernible from the BE ridge for small angles, but observable up to scattering angles of about 135°. This $\delta$-electron contribution is attributed in [Bec97] to BE electrons that were produced in extreme forward angles and subsequently scattered by the potential field of the target atom ("ternary encounter electrons"). This ridge gets significant only in the case of very heavy target atoms (scattering cross sections depend on $Z^2$).

The detailed description and analysis of the processes, briefly described above, with experimental confirmation is presented in the dissertation of Bechthold [Bec96]. A more detailed description of the BE approximation follows in the next chapter.

# 3.3  The Monte Carlo (MC) code, TRAX

A very important benefit of OPAC is its capability to serve as a benchmarking tool for verification of models, which are applied to describe the transport of charged particle through matter. The present work is motivated by the request for an experimental benchmarking tool to test the simulated results and predictions of such models concerning the spatial radiation pattern and namely the radial dose distribution, $d(r)$. $d(r)$ is the crucial physical input parameter required by the LEM (see chapter 2.7) biophysical model for the determination of biological effects of heavy ion impact in tissue. The simulation method and the computer code, TRAX, used at GSI to study track structure, and to obtain or benchmark crucial input parameters for the therapy planning, was developed by Kraemer et al. [Krm94] at GSI. In the past years of extended application the TRAX code turned out to be a very successful particle transport code, at least for particles (e.g. carbon ions) and energy regions (moderate energies), which are relevant for ion therapy. This is the main motivation for choosing TRAX as the code to be benchmarked by the experiments. Furthermore, a straight forward adaptation of TRAX for the experiment with OPAC could be obtained.

## 3.3.1 The MC method

Triggered by the explosive development in computational speed in the past decades, the Monte-Carlo (MC) method has grown out to be the preferred strategy to study the details of ionization pattern. (For details on the method see [Lan00].) The analytical solution of some complex problems is often not suitable or only at the price of questionable assumptions and disregards. The MC method can treat any geometry of any size or complexity. Due to the capability of handling the single interactions individually, it can account for stochastics and the limitation in spatial resolution is only given by the location uncertainty of the target particles. Thus, modeling at molecular level is possible, e.g. $d(r)$ can be determined very close to the center of the track (at $r < 1$ nm). The recent computers allow for a fast reduction of the random error in most of the cases. The only, even though serious limitation of the method is the fact, that the precision and validity of the results is totally based on the precise knowledge of cross sections for all the interactions, which play a role during the transport. Nevertheless, in general cross sections, due to their fundamental characteristics, still provide the most precise and detailed information that exists on single interactions of particles with matter.

## 3.3.2 Calculation strategy

The TRAX code uses the MC method to simulate the production and transport of $\delta$-electrons after heavy ion impact. The heavy ion ionizes the matter with an average spatial frequency of its mean free path which is derived from the total ionization cross section. The ejected electrons are treated individually. Emission energy ($E_e$) and angle ($\vartheta$) are sampled for each $\delta$-electron from the appropriate double differential cross section table. The produced $\delta$-electrons are then transported from collision to collision, whereas each interaction is treated individually. The interactions under consideration are elastic scattering, ionization and excitation, which are treated in a similar way, as by authors like Paretzke, Breger or Grosswendt ([Ber63], [Par78] and [Gro78]). However, Paretzke has optimized the treatment

31

for low energy electrons [Par88], and in the case of TRAX the inaccuracy of the heavy ion track structure is dominated by the improperly known ionization cross sections for ions in any case.

The various cross sections, needed for the ion and electron transport are based on a mixture of theoretical considerations, experimental data and semiempirical fits. All the cross section data are derived for water vapor as target medium. Water is the most important component in human tissues. This fact and the relatively high amount and accuracy of cross section data and experience available for water vapor have motivated this choice. It will be shown in chapter 4.1, that the filling gas of OPAC, triethylamin, also can be simulated with water after an appropriate scaling.

### 3.3.3 Simulation of the *δ*-electron production

The locations for ionizing interaction of a projectile ion with the target atoms in the medium are sampled from an exponential distribution with a mean free path according to the total $\delta$-electron production cross section. The double differential cross sections are then determined according to the binary encounter approximation (BEA).

### 3.3.4 The binary encounter approximation (BEA)

The BEA is a semiclassical model based on the Rutherford theory (see chapter 0). The broad energy distribution at a given angle (see Figure 3.2) can be explained in the framework of the BEA. The model is semiclassical, because the momentum distribution is determined from the original wave function of the target electron, while treating the motion of the projectile classically. The development of the BE theory has a long history. The first efforts of Thomas [Tho12] were developed further by Gryzinsky [Gry59]. The idea was improved to a successful theory by authors like Brugges [Bru64], Garcia [Gar69], Bonsen and Vriens [Bon69].

The first step is the application of the conservation rules, like for the deduction of the Rutherford single-differential cross section (see equation (3.5) If taking into account the initial velocity of the electron, $v_{e0}$, the result of the consideration is a triple-differential cross section for the $\delta$-electron production: $\dfrac{\mathrm{d}^3\sigma}{\mathrm{d}\Delta E\,\mathrm{d}\Omega\,\mathrm{d}v_{e0}}(\Delta E, v_p, v_{e0}, \vartheta)$. The double-differential cross section can be determined by folding with the initial velocity distribution, $f(v_{e0})$, of the bound electron:

$$\frac{\mathrm{d}^2\sigma}{\mathrm{d}\Delta E\,\mathrm{d}\Omega}(\Delta E, v_p, \vartheta) = n \int_0^{v_{max}} \frac{\mathrm{d}^3\sigma}{\mathrm{d}\Delta E\,\mathrm{d}\Omega\,\mathrm{d}v_{e0}} f(v_{e0})\,\mathrm{d}v_{e0}$$

$$\text{with } \int_0^{v_{max}} f(v_{e0})\,\mathrm{d}v_{e0} = 1$$

(3.7)

where $v_{max}$ is determined from equation (3.2) and $n$ is the number of electrons in the shell with the velocity distribution, $f(v_{e0})$. There exists an analytical expression for the $f(v_{e0})$ distribution of 1s hydrogenic electrons:

$$f(v_{e0}) = \frac{32 v_{e0}^2 v_0^5}{\pi (v_{e0}^2 + v_0^2)^2}$$

(3.8)

where $v_0$ is the mean velocity of the bound electrons:

$$v_0 = \int_0^{v_{max}} v_{e0} f(v_{e0}) \mathrm{d}v_{e0} \qquad (3.9)$$

It was shown by Bonsen and Vriens [Bon70], that the distribution (3.8) can also be applied for other light target atoms, like for helium. Although the equations (3.7) and (3.8) were originally intended for use with atomic s shells only, in its present version TRAX applies them also for the water molecule.

### 3.3.4.1 Mean velocity of the bound electrons - Virial theorem, Slater rules

The mean velocity of the bound electrons, $v_0$, can be estimated by means of the Virial theorem. In general, the Virial theorem holds both, classical- and quantum mechanics, and relates the average kinetic and average potential energies of a system of particles with arbitrary potential interactions in their pure energy states. The most general form of the theorem in one dimension:

$$\overline{K} = \frac{1}{2}\overline{\left[r\frac{\partial U}{\partial r}\right]} \qquad (3.10)$$

If an electron is bound in the Coulomb potential field, $U$, of an atom ($Z$) and has a kinetic energy of $K$, and an average velocity of $v_0$, $K$ and $U$ are given:

$$K = \frac{1}{2}m_e v_0^2 \qquad (3.11.a)$$

$$U = -\frac{Ze^2}{4\pi\varepsilon_0 r} \qquad (3.11.a)$$

The application of the Virial theorem, (3.10), for the electron in the Coulomb potential results in:

$$\overline{K} = \frac{1}{2}m_e v_0^2 = -\frac{1}{2}\overline{U} \qquad (3.12)$$

$v_0$ could be determined based on the binding energy, $E_b$, values, which are relatively well known from experiments. The binding energy of an electron is the energy needed to set the bound electron free. This can be expressed with the following equation:

$$E_b = -\left(\overline{K} + \overline{U}\right) = \overline{K} = \frac{1}{2}m_e v_0^2 \qquad (3.13)$$

Ramm shows a comparison of measured [Sdt87] and calculated [Krm91] double differential cross sections (see Figure 2.11 in [Ram94]). If the curves are calculated with BEA using $v_0$ values from (3.13), then the agreement with the measured data is poor. Despite, fair agreement is observable, if the $v_0$ input parameter for the BEA calculation is determined directly from (3.12) using the following approximation for $\overline{U}$ :

$$\overline{U} = R\left(\frac{Z - s_{nl}}{n}\right)^2 \qquad (3.14)$$

where $R = 13{,}6$ eV is the Rydberg energy, $n$ is the principal quantum number and $s_{nl}$ shielding constants depend on the principal and azimuthal quantum numbers of the target electron. The (3.14) expression obeys the Slater rules [Sla60]. TRAX applies the BEA (the equations (3.7) and (3.8)) for water molecule together with (3.14) and the Slater rules. The $H_2O$ molecule has

five weakly bound electron pairs of "oxygenic nature" having 1s, 2s and 2p character. The application of the Slater rules yields $\overline{K} = 806$ eV for the 1s electrons and $\overline{K} = 70,4$ eV for the eight L-shell electrons (reference in [Krm94], p. 8).

### 3.3.4.2  Validity and limitations of the BEA

In [Krm94] a detailed overview about the applicability of the BEA is given. Sufficient agreement between measurements and experiments were found in such cases, where the projectile was a proton, an α-particle (see Figure 3.4) or another relatively light ion. The TRAX code applies the BEA to determine double differential cross sections for proton projectiles, and the results are than scaled by $q_{eff}^2$ (see equation (3.5)) to the ion type and velocity under consideration, where $q_{eff}^2$ is determined according to the Barkas formula (3.6).
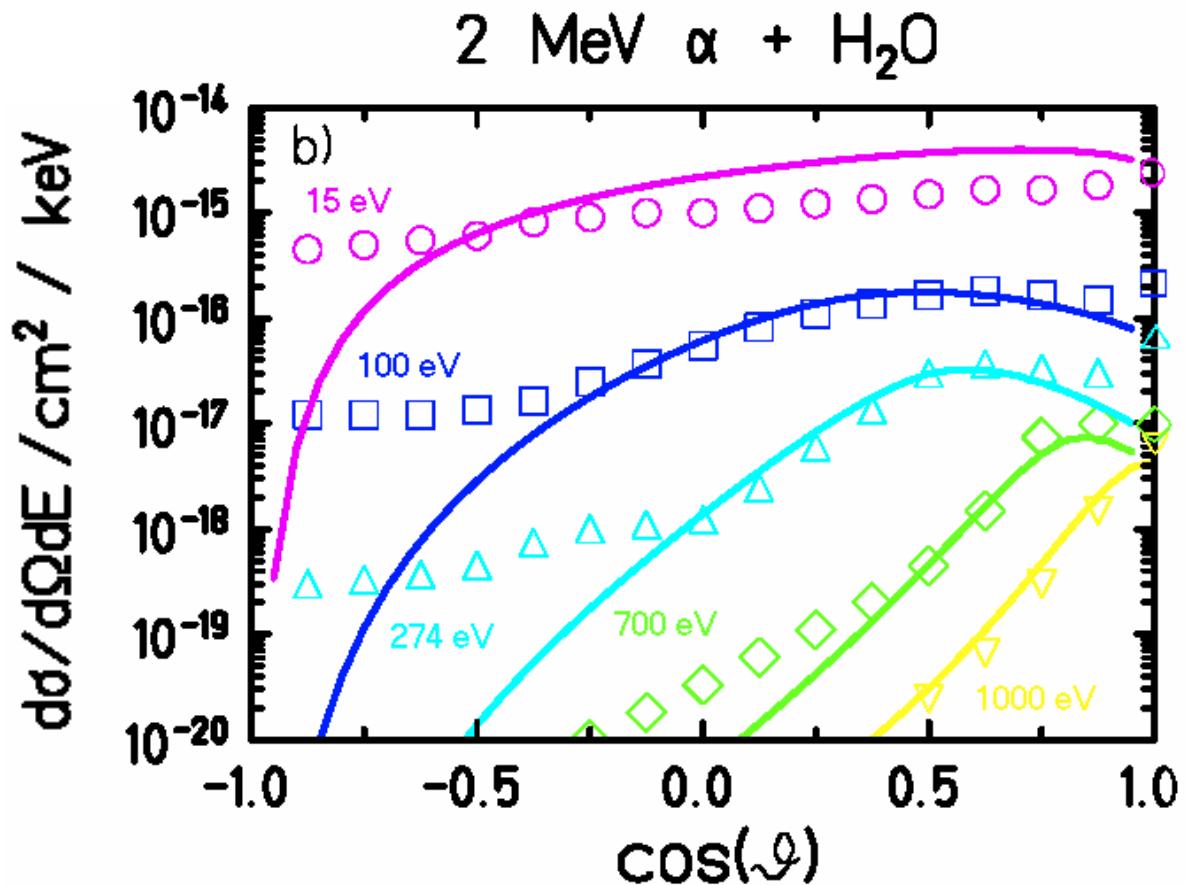


Figure 3.4: *Angular distribution of δ-electrons of selected energies ejected from the collision of 2 MeV α-particles on water vapor. The symbols represent measured results [Ton80] and the curves are BEA calculations [Krm94], where the initial velocity distribution of the interacting electron is determined according to Virial theorem and the Slater rules ([Krm94] and [Ton80]).*

The most pronounced discrepancies between BEA simulations and experimental results (see Figure 3.4) were found at backward angles. The reason for this is evident: BEA results in backward scattered electrons only if $\Theta$ (in equation (3.1)) is small, therefore $\Delta E$ (see equation (3.3)) is small, and the projection of the initial velocity of the electron into the laboratory system accounts for the resultant backward velocity. The BEA does not account for the δ-electrons produced in other than the electron emission processes (see chapter 3.2). In Figure 3.4 the cusp peak from the continuum charge transfer processes are well identifiable at

moderate energies and at strongly forward angles in the measured data, while it cannot be reproduced by the BEA simulations. The contribution of the electrons from peripheral collisions results in an almost isotropic $\delta$-electron distribution at 15 eV electron energy in the measurements, while the BEA anticipates a sharp decline in backward directions (see Figure 3.4). Also the contribution of the target Auger electrons enhances the electron yield in backward directions at moderate $\delta$-electron energies, which is of course not attributed for in the BEA.

Nevertheless, the agreement between measurements and BEA simulations are quite good for protons (see Figure 5 in [Krm94]), $\alpha$-particles or other light and structureless projectiles. The basic assumptions of the BEA are ideally fulfilled; so that the double differential cross sections for the dominating BE electrons can be derived with sufficient precision. However, for heavy or structured projectiles the pure BEA is not capable to describe satisfactory the scattering of the bound electrons. The assumptions of the BEA about a collision of a pure Coulomb field with a quasi-free electron, originating from an unperturbed target shell are not fulfilled. The high charge state of the projectile perturbs the electron cloud of the target resulting in modified initial electron velocities. Furthermore, if the projectile is not fully stripped, its effective charge cannot be determined reliably through the Barkas formula (equation (3.6)). The effective charge depends not only on the atomic number and velocity of the projectile but also on the impact parameter, if the projectile has bound electrons. If the impact parameter, $b$, is very small, $q_{eff}$ can be close or equal to $Z_p$. If $b$ is comparable with the radii of the bound projectile electrons, the potential field of the projectile cannot be treated as a Coulomb field. The radial gradient of the potential field in the region of the remaining electron shells is much higher, than it would be for a bare ion with the same $Z_p$. As the energy transfer is proportional with the potential gradient, the modified potential field has the consequence that the impact parameter region, where the energy transfer is around its maximum, is extended. The result is a strongly increased cross section for forward scattering. On the other hand, if the impact parameter is significantly above the electron shell radii of the projectile, its potential field can be approximated by a Coulomb field with an electric charge, approximated by the Barkas formula.

Numerous experiments confirmed the increased $\delta$-electron yield for not fully stripped projectiles in forward direction. Bechthold defines an enhancement factor to express the ratio between the measured and the expected (according to the BEA) forward scattering ($\vartheta = 0°$) cross sections (see page 101-107 in [Bec96]). The value of the enhancement factor is around 2 for $Xe^{40+}$ and 10 for $U^{29+}$ projectiles. This phenomenon exists for relatively light, but not fully stripped ions as well. Richard et al. measured BE electrons emitted under $\vartheta = 0°$ after collisions of fluorine ions in $H_2$ or He target matter. The charge state of the fluorine ions was varied from +3 until +9 (bare). The cross section for the forward scattered was found to decline with increasing charge state, instead of rising with it quadratically [Ric90]. The enhancement factor for $F^{3+}$ reaches 13.

Despite its limited validation, TRAX applies the BEA to determine the primary $\delta$-electron distribution for any projectile ion. This relative simple model is indeed sufficient for the simulation of the ionization pattern of carbon ions, especially regarding that features of the ion tracks, which are important for the therapy (e.g. radial dose distribution). Furthermore, the model is typically used to simulate tracks at energies well above the Bragg peak. If the energy of the carbon ion exceeds the level of about 2 AMeV, it is probably fully stripped according to the Barkas formula (3.6). The scaling as $Z_p^2 = q_{eff}^2$ for bare ions works well, if the necessary criterions for applying first order perturbation theories, which predict $Z_p^2$ scaling, are fulfilled (page 54 in [ICR96]). The essential criterion for applying first order perturbation theories, such as the Born approximation [Bet30], is that the ionization probabilities must be small.

Otherwise, if ionization probabilities can approach unity, so the cross section saturate at values smaller than those predicted by $Z_p^2$ scaling. Large ionization probabilities also result in an enhanced importance of multiple ionization, which does not scale as $Z_p^2$. The criterion of relatively low ionization probabilities is fulfilled for light and fast projectiles. Nevertheless, the comparison of measured (with OPAC) and simulated (with TRAX) tracks of very heavy ions have to be made in consideration of the significant discrepancies from the applied $Z_p^2$ scaling, especially if the simulated ion is not bare.

It is beyond the scope of the present experimental work to describe more delicate models for δ-electron production, which are not being applied by TRAX. Generally, cross section data can be obtained in there basic manners:

1.  Theoretical models use only fundamental constants, but have restricted ranges of validity due to the simplifications required in order to obtain practical solutions.

2.  Semi-empirical models are simple to apply, but the knowledge of adjustable fitting parameters is generally required.

3.  Tables of experimental data can be used directly but are sparse and often require extrapolation or interpolation for missing data.

A brief description of many of the most widely established models together with some fitting parameters and a list of experimental reports can be found in the ICRU report 55 [ICR96]. The PHD thesis of Ramm [Ram94] and that of Bechthold [Bec96] put their focus on the experimental investigation of the δ-electron production following an ion penetration in matter. A more detailed description of some useful models can be found in these works, such as the n-Body-Classical-Trajectory-MC method (CTMC) ([Bec96] page 38). The Semi-Classical Approximation (SCA) is a quantummechanical time-dependent first order perturbation theory ([Bec96], page 40). The MC simulations in the works of Grosswendt and Garty (see [Gro78], [Gro02a], [Gro02b], [Gar02] and [Gar04]) are based on the analytical functions and experimentally based fitting parameters of Rudd et al. [Rud85] for the determination of the total ionization cross section of protons. At the ionization locations, determined according to the Rudd cross sections, Grosswendt and Garty use the semi-empirical Hansen-Kocbach-Stolterfoht (HKS) model (see page 51 in [ICR96]) in order to sample the emission energy and angle of the produced δ-electrons. The first experimental results with OPAC were compared with MC simulations in the PHD thesis of Titt (see page 61 in [Tit99]). The author used the ionization cross sections according to Rudd as well. Then he determined the initial energy and angle of the δ-electrons according to the BEA cross sections.

After determining the ionization locations according to the total electron emission cross section, TRAX samples the initial energy and polar angle of the electrons (relative to the propagation direction of the projectile ion) at each ionization location individually in the described way. The azimuthal angle of the initial velocity of the δ-electron is sampled to be uniformly distributed between 0 and $2\pi$. The resulting location and velocity vectors for the δ-electrons are than used as input parameters for the individual MC transport of each δ-electron. The cross section data, used for the electron transport, are briefly described in the following chapter.

## 3.3.5 Transport of δ-electrons in matter

According to the Rudd model (see Figure 2.5 in [Tit99]) or the binary encounter approximation (see the previous paragraphs), the single differential cross section for the

$\delta$-electron emission, $\dfrac{\mathrm{d}\sigma}{\mathrm{d}E}$, has a maximum at low energy and decreases towards higher energies rapidly. The maximum of the initial $\delta$-electron energy is typically of the order of tens or hundreds of keV, determined by the BE kinematics (3.4). The mean value of the initial emission energy depends on the ion energy, but it is in the order of hundreds of eV in the ion energy region of interest in the present work. There exists no comprehensive theory for the precise treatment of the low energy electron transport in matter.

The three basic processes, which have to be taken into account, are elastic scattering in the Coulomb field of an atomic nucleus, ionization of a target atom (molecule) and excitation of target electrons. The ultimate purpose of the measurements and simulations is to determine the ionization density distribution in the matter and the locations of excitation and elastic scattering interactions are not directly of interest. But for the electron transport they have to be included in the simulation. An electron interacts with a particle of identical (electron) or much higher (atomic nucleus) mass and thus scattering angles are often large. This results in a track that is very tortuous compared to the nearly straight path of a heavy charged particle. Therefore, elastic scattering locations and scattering angles affect the resulting spatial ionization pattern strongly. The electrons with energies below several keV can be fully stopped inside the sensitive volume of OPAC at a pressure of 10 hPa. Most of the $\delta$-electrons have energies below this level, but the faster electrons also undergo a significant slow-down inside the sensitive volume. Thus, the simulation of excitation events is necessary to be able to account for the electron energy along the electron path. Other processes, like bremsstrahlung or relativistic effects play only a minor role at the energies under consideration, therefore such interactions are not handled by TRAX.

The cross sections for the three basic electron-electron interactions are shown in Figure 3.5. The curves are mainly semi-empirical fits on experimental data. TRAX samples the mean electron free paths according to the curves in Figure 3.5

### 3.3.5.1 Elastic scattering

According to Figure 3.5, the total elastic scattering cross section increases monotonously with decreasing energy, being the most probable interaction type below an electron energy of 300 eV. Kraemer distinguishes two regimes of energy for the TRAX simulations. For high electron energies ($T > 0{,}5$ keV) the Rutherford cross section with screening correction is applied (as by Berger and Grosswendt [Ber63] and [Gro78]):

$$\frac{\mathrm{d}\sigma_e}{\mathrm{d}\Omega} = \frac{Z^2 e^4}{4T^2 \left(1 - \cos\vartheta + 2\eta\right)^2} \tag{3.15}$$

Taking into account, that $\sin^4(\vartheta/2) = (1 - \cos\vartheta)^2 / 4$, the only deviation of (3.15) from (3.5) is characterized by the screening parameter, $\eta$, which increases with increasing $Z$ and decreasing $T$ according to the Molière theory [Mol48].

For electron energies below 0,5 keV all existing theoretical considerations are of limited validity and precision. E.g. backward scattering is underestimated by the screened Rutherford cross section for low electron energies. The cross sections, used by TRAX in this energy regime, are based on experimental data. Besides the few data on water vapor [Kif71], [Tra83], additional data are derived from $H_2$ and $O_2$ cross sections according to the additive rule:

$$\sigma_{H_2O} = \sigma_{H_2} + \frac{1}{2}\sigma_{O_2} \tag{3.16}$$

(3.16) is true for appropriate cross sections of any kind (total, double differential) approximately [Krm94]. TRAX applies a fitted function on the available experimental data, where the weighting parameters of Legendre polynomials of the order of zero and two are responsible for the increased backward scattering (see equation (4) in [Krm94]).
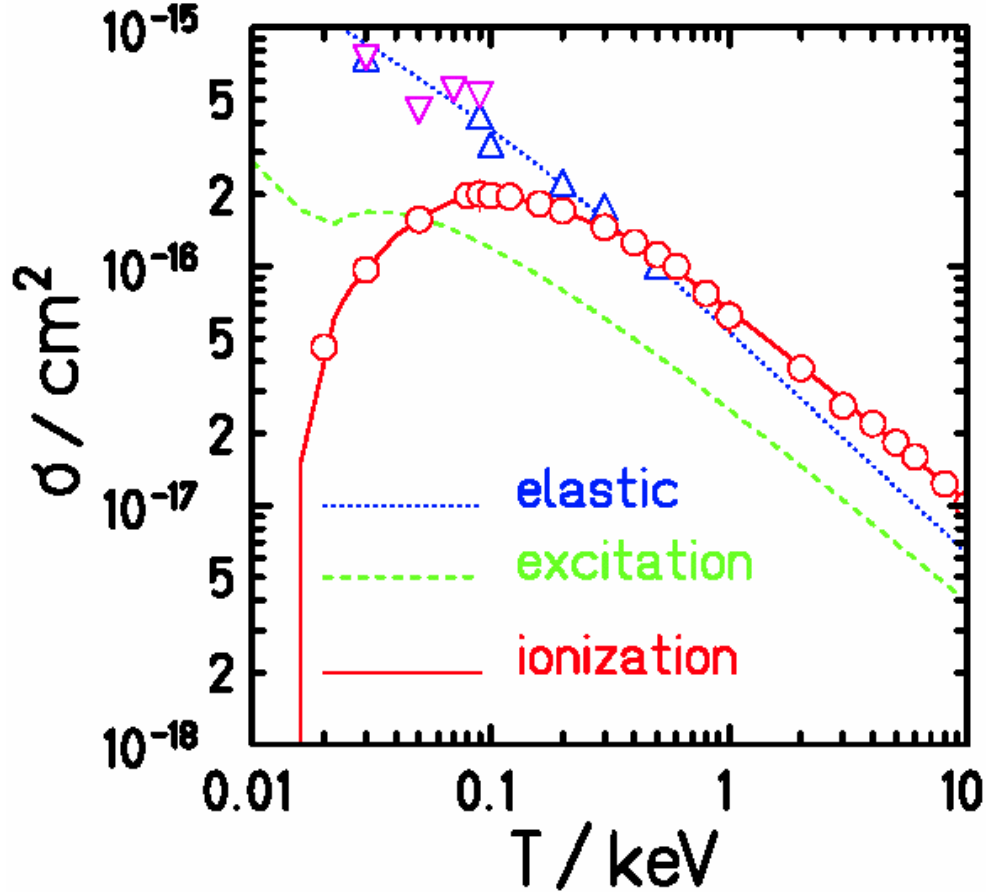


Figure 3.5: *The electron cross sections, used by TRAX, to simulate the δ-electron transport in matter (curves). The symbols represent experimental data in water vapor. (△[Tra83] and ▽ [Kif71] are data for elastic scattering and ○ [Scn66] is measured ionization cross section data at different electron energies. The curves are semi-empirical fits on experimental data. (T is the kinetic energy of electrons).*

### 3.3.5.2 Ionization

The simulation of ionization by δ-electron impact is carried out by TRAX in the following steps:

1. *Threshold energy:* The principal condition of an ionization event is that the energy of the δ-electron, hitting a molecule of the medium ($H_2O$ in TRAX) has to be above the binding energy, $E_b$ of the affected molecular electron. If an ionization occurs, the same energy is needed to be transferred to the secondary electron to get it free from the bound state. Paretzke and Berger (see Figure 3 in [Par78]) provide data for the fractional contributions of the five electron shells of the water molecule to the total ionization cross section. Instead of sampling the interacting electron shell and thus $E_b$ from these functions, TRAX derives $E_b$ from the mean $\overline{E_b}(T)$ function, also given in [Par78]. $\overline{E_b}(T)$ increases with

38

increasing $T$ from 12,7 eV to about 16,7 eV monotonously according to the empirical formula given in page 6 in [Krm94]. Hence, the history of any primary or secondary $\delta$-electron (higher order $\delta$-electrons are also termed as secondary $\delta$-electrons) can be terminated if the electron energy drops below 12,7 eV, because no further ionization can take place. TRAX finishes the tracking of electrons at this threshold level.

2. *Total ionization cross section:* The total ionization cross sections for electron impact (see red curve in Figure 3.5) were measured by Schutten et al. [Scn66]. For energies, higher than 0,3 keV, the measured data can be fitted well by the following simplified formulation of the Bethe-Bloch cross section [Bet30]:

$$\frac{d\sigma_i}{dT} = \frac{4\pi a_0^2 R}{T} M_i^2 \ln\left(\frac{T}{c_i}\right) \tag{3.17}$$

where $a_0$ is the Bohr radius and $R$ is the Rydberg energy. $M_i^2$, oscillator strength is chosen to be 3,14 for a good fit of the experimental data and the $c_i$ constant is 12,7 eV, the minimum value of $\overline{E_b}(T)$. For energies below 0,3 keV TRAX interpolates with the experimental data.

3. *Simple differential cross section regarding the secondary electron energy:* After an ionization location has been determined, the velocity and propagation direction of both the incoming and emitted electrons have to be calculated. As a first step, TRAX samples the energy of the secondary electron, $T_{sec}$, according to the following semiempirical formula:

$$\frac{d\sigma}{dT_{sec}} \approx \left(1 + \left(\frac{T_{sec}}{\Gamma}\right)^2\right)^{-1} \tag{3.18}$$

The cross section, above, depends theoretically on the energy of the primary electron, $T$, in some extent, hence the parameter, $\Gamma$, depends on $T$ as well. However, the study of the data, given by Opal et al. [Opa72], leads to the result, that a constant value of $\Gamma = 11,4$ eV is sufficient. If $T_{sec}$ is already chosen, the energy of the incident electron after the interaction, $T'$, can be determined:

$$T' = T - E_b - T_{sec} \tag{3.19}$$

4. *Emission angles:* There are neither analytical, semiempirical relations nor extensive experimental data for the angle dependency of the double differential cross sections. TRAX chooses the emission angles of the two interacting electrons according to the suggestions given by Grosswendt et al. [Gro78].

After the determination of the emission energies (see par. 3) and angles (see par. 4), the histories of the both electrons are simulated further, until their energy fall below the threshold (see par. 1).

### 3.3.5.3 Excitation

Data on electronic excitation is even scarcer than that for the elastic scattering and ionization processes. TRAX takes the total electronic excitation cross section data from [Par78] and parameterizes it according to the equation (3.17), with $M_x^2 = 1,194$ oscillator strength and $c_x = 8,2$ eV. The mean energy loss of the incident electron, $T-T'$, rises from 8 eV if $T$ is small, to 13 eV at $T = 100$ eV, and has the constant value of 13 eV for higher incident energies (see page 5 in [Krm94]). TRAX assumes further, that the incident electron keeps its propagation direction after the excitation process. This assumption is based on measured angular

distribution data after electronic excitation of $N_2$ molecules, which is strongly peaked forward [Tra83].

# 4 Measurement methods

The following chapter gives a brief overview about the various experimental methods that were developed to measure characteristic properties of the spatial distribution of ionizing radiation around particle tracks. The measurement of the track structure with a resolution of several nm or several tens of nm is not feasible directly in tissue or in solid or liquid matter. Instead, nanodosimetry simulates the microscopical volume of tissue by replacing it by a much larger cavity filled with tissue-equivalent (TE) gas of much lower density (simulation principle). In the gas volume the same processes occur at much larger distances. The simulation principle was established by the experimental microdosimetry.

## 4.1 Simulation of a nanometric target size in low pressure gases

For the following discussion a spherical volume is assumed. Similar considerations, however, are valid for volumes of different shapes. For experimental microdosimetry the pressure of the filling gas has to be modified in such manner, that the energy loss of passing charged particles is identical in the gas sphere and in the tissue sphere of microscopic dimensions. If the mean energy losses are $\Delta E_t$ in a tissue sphere of diameter $d_t$ and $\Delta E_g$ in the gas sphere of diameter $d_g$, the condition is:

$$\Delta E_t = \left(\frac{S}{\rho}\right)_t \rho_t d_t = \left(\frac{S}{\rho}\right)_g \rho_g d_g = \Delta E_g \tag{4.1}$$

where $\rho_t$ and $\rho_g$ are the densities, and $\left(\dfrac{S}{\rho}\right)_t$ and $\left(\dfrac{S}{\rho}\right)_g$ are the mass stopping powers of the tissue and the filling gas of the detector cavity, respectively. The equation has been written for particles crossing a diameter, but it holds for any equivalent trajectories. However, the (4.1) condition is not sufficient if one is interested not only in the expectation value of the energy loss, but also in the entire ionization distribution.

According to (4.1), if the mass stopping powers of the tissue and that of the gas cavity are the same, the searched condition can be written as follows:

$$\rho_t d_t = \rho_g d_g \tag{4.2}$$

Therefore, the mean energy loss of charged particles is equal in both spheres if the diameter of the simulated tissue sphere equals that of the gas sphere scaled by the ratio of the density of the gas to the density of the tissue. (4.2) is the basic equation of this so called "simulation principle".

The remaining condition, that $\left(\dfrac{S}{\rho}\right)_t$ should equal $\left(\dfrac{S}{\rho}\right)_g$ is fulfilled, if the atomic composition of the tissue and the gas are identical and if the mass stopping powers are independent from the density. Most microdosimetric studies assume that the mass stopping powers are independent from the density despite the fact, that the tissue in condensed phase is simulated by a material in gas phase. This assumption turns out to be applicable in most cases.

However, as already pointed out in chapter 3.2, new experimental results provide clear evidences on discrepancies between the interactions of heavy ions passing through gases and solid matter. Double differential momentum distributions of $\delta$-electrons, induced by ions penetrating a thin foil were measured with the toroidal electron spectrometer [Bec96]. In measurements with fluorine ion beams $(1,5-2\,\mathrm{MeV/u})$, passing through thin carbon, aluminium or gold target foils, a steep and very narrow electron jet was observed along the ion beam axis in forward direction [Zae02]. This observation can be explained physically by the strong screening of the projectiles nuclear potencial in solid matter. The electric field potential around the projectile in a gas has the typical characteristics of $1/r$ where $r$ is the radial distance from the projectile. In solid matter the potential of the projectile is screened strongly by the surrounding atoms. Due to this screening effect the potential drops faster than $1/r$ around the projectile in this case. This results in larger forces between the projectile and the interacting electrons. As a consequence, the ratio of hard forward scattered $\delta$-electrons could be higher than in ion-gas interactions. Thus, the momentum distribution of the primary $\delta$-electrons is different in gas and tissue, and $\left(\dfrac{S}{\rho}\right)_t$ is possibly higher than $\left(\dfrac{S}{\rho}\right)_g$, as the energy dissipation increases with increasing scattering angle (in the projectile system) according to equation (3.3).

It has to be noted, that the additional $\delta$-electrons, scattered in forward direction were observed only up to the projectile velocity (in the momentum space) [Zae02], i.e. no enhancement of the BE peak could be demonstrated so far – neither with the toroidal spectrometer, nor by others. On the other hand, some of the measurements detected an enhancement in the $\delta$-electron yield in the backward direction as well [Zae02]. A possible physical explanation of these phenomena may be that the potential field of the nuclear track "channels" $\delta$-electrons, emitted below certain emission energies and angles (both in forward and in backward directions), back into the track (plasma focussing). The ongoing investigations at GSI, Darmstadt [Hag06] could clarify the open questions.

Furthermore, condensed phase effects can also become significant, if the projectile energy is so low, that electrons cannot be treated as quasi-free. Another example for the density effects on mass stopping power is the possible increase of the effective charge of a non-bare projectile ion at high densities. Successive excitations of projectile electrons at a higher rate can result in a higher ionization level of the projectile. It was also shown, that the stopping power is lower in gas relative to condensed phase if the projectile is a relativistic electron [ICR83].

Nevertheless, at present, no other measurement method exists to study the spatial dose distribution in tissue experimentally than the measurement in a gas. The principal instrument of microdosimetry is the tissue equivalent proportional counter (TEPC), which applies so called tissue equivalent materials for the walls and the gas cavities of the counters to ensure a very similar atomic composition to tissue. The principle of the TEPC will be briefly described in chapter 4.2.

As it was recognized, that the biological effects are strongly related to local DNA-damage clusters in regions with dimensions of a few and a few tens of nanometer, it became evident, that the measured quantities in the framework of microdosimetry (e.g. measured with TEPCs) cannot fully describe all the physical parameters which determine the radiobiological effect (see chapter 2.2). Nevertheless, in addition to providing an insight into many radiobiologically relevant aspects of radiation action in matter, the tools and quantities, established by microdosimetry also act as a base for the nanodosimetry and for high

resolution track structure studies. The need for the application of the simulation principle is even more pronounced if the target volume becomes smaller.

However, in contrary to TEPCs, the interacting gas is not tissue equivalent in many measurement concepts in nanodosimetry. The need for a very high spatial resolution and the requirement, that the gaseous interaction medium is also the amplification medium for a proportional counter predestinate the choice of special gases in some of the concepts. The other typical reason for the usage of gases other than TE ones is the fact, that no extensive cross section tables are available for TE gases. Therefore, the capability to compare the results with Monte Carlo simulations is limited. The experience shows, however, that the exact atomic composition of the detector filling gases does not influence the results strongly, if an appropriate scaling is applied. Many authors apply a simple scaling with the ratio of the densities according to equation (4.2).

Toburen and Wilson [Ton77] present experimental evidences for the scalability and additivity of cross sections. The authors found that for proton impact (0,3 MeV $< E_p <$1,5 MeV) both the double and the single differential cross sections of water vapor can be constructed as the sum of the corresponding cross sections of the molecular $H_2$ and the half of that of the molecular $O_2$ (additivity). The cross sections of the $H_2$ and $O_2$ molecules themselves are also comparable with the corresponding cross sections of $H_2O$, if the molecular cross sections are simply divided by the number (per unit of volume) of "weakly" bound electrons in the molecule. Weakly bound electrons are identified in light atoms or molecules as all electrons except K-shell electrons. The corresponding cross sections of methane, other hydrocarbons and different amines were also scaled in the described way. The scaled double differential electron emission cross sections of the different molecules show a good agreement with the only exception of the $H_2$ molecule. Hydrogen cross sections were found to exhibit a much more peaked angular distribution near the binary encounter peak than the other molecules. The discrepancies for both scaling and additivity were found to increase for electron energies below 100 eV and for decreasing ion energy. This phenomenon can be explained by the increasing role of the molecular structure at low energies. In the cited paper, the authors do not examine to what extent the same scaling and additivity is valid for the electron impact cross sections.

Other authors prefer different scaling methods. Budd and Marshal [Bud83a], [Bud83b] use a tissue equivalent gas in the low pressure cloud chamber, which will be briefly introduced in chapter 4.5. The authors scale the results to those which would be expected in liquid water using a slightly different scaling factor. It was derived by calculating the theoretical track lengths in the cloud chamber gas mixture and water using a modified Bethe-Bloch method [Mar80] and taking the ratio of the results. A further small scaling factor was included for the slight differences in W value between the two materials. In a later work with the same chamber [Sto93a], [Sto93b] the tissue equivalent gas was replaced by water vapor. Among other advantages an enhanced spatial resolution was achievable by using water vapor as filling gas.

Grosswendt [Gro04] derives from theoretical considerations, that the scaling by the density ratio (see equation (4.2)) should be corrected by the ratio of the mean free path of the traversing ions with respect to ionization in the gas to that in liquid water (or tissue). This correction would lead to the same mean cluster size (see chapter 2.6) and to the same variance of it in the gas cavity and in the simulated "nanoscopic" volume. The crucial assumption of this scaling rule is that the contribution of secondary electrons to cluster-size formation is negligible. This assumption can be made only if the ion hits the target gas cavity in its center and if the diameter and height of the target volume are much smaller than the mean free path

of the δ-electrons (simulated dimensions not larger than a few nm at $\rho_t$). Grosswendt applies the scaling for nanodosimeters, filled with nitrogen and propane gases (see chapter 4.3).

The filling gas in the presented tracking chamber, OPAC, is triethylamin, (TEA, $(H_5C_2)_3N$). About the reasons of the gas selection see chapter 5.1, [Tit98] and [Tit99]. The preferred strategy for scaling the relevant distances in OPAC, for instance the distance between two ionization locations, is the scaling with the density of weakly bound electrons according to Toburen et al. [Ton77] (described above). This scaling can be justified by the fact, that similarly to water, TEA contains only light elements and the hydrogen content is also close to each other. Let us assume that the distance between two events is $d_g$ in OPAC. To achieve the corresponding distance, $d_t$ in the simulated liquid water target (which is a substitute to a sub-cellular biological target), the scaling according to equation (4.2) has to be modified in a way which accounts for the density of weakly bound electrons instead of the mass density:

$$d_t = d_g \frac{N_g^{we} \rho_g / M_g}{N_t^{we} \rho_t / M_t} \tag{4.3}$$

where the molar weight of water, $M_t$, is: $M_t = 18$ g/mol and that of TEA is $M_g = 10118$ g/mol. The number of weakly bound electrons per mol is $N_t^{we} = 8$ in water and $N_g^{we} = 44$ in TEA. With these numbers:

$$d_t = 0{,}98 \frac{\rho_g}{\rho_t} d_g \tag{4.4}$$

Comparing to the uncertainties of the model and to the overall uncertainties of the measurement, the factor of 0,98 can be substituted by 1 in the practice. Hence, in the later data analysis a simple scaling with the gas density is applied. In the experiment the chamber was used at various gas pressure values. TEA is treated as ideal gas. Therefore a change of the gas pressure by a given factor means a corresponding change of its density and therefore a change in the magnification of the simulated $d_t$ distance by the same factor.

## 4.2  Tissue equivalent proportional counters (TEPC)

Numerous different TEPC detectors have been developed since the middle of the past century (see e.g. review in [Ros96]). The photo and the schematic view in Figure 4.1. depict one of the first TEPCs, which was used by Rossi and co-workers at Columbia University nearly 50 years ago. A conventional TEPC is a proportional counter with a spherical cavity containing a central anode wire. It is filled with a tissue equivalent counting gas at low pressure. The wall of the counter is commonly made of conductive tissue equivalent material and is used as cathode. Typical for the operation of proportional counters is the gas multiplication which relies on the condition that the electric field within the counter is sufficiently high to allow for an electron multiplication by secondary ionization proportional to the amount of the primary ionization. TEPCs are operated in pulse mode and the pulse-height spectrum is collected. The physical quantity actually measured by a proportional counter is a charge that is proportional to the number of ion pairs created by traversing particles. The W-value provides the quantitative correlation between the number of ion pairs created and energy imparted. Thus, the knowledge of the W-value is necessary to convert the pulse-height spectrum converted into e.g. lineal energy spectrum (see chapter 2.2).
The spherical shape of the chamber in Figure 4.1 was chosen so that its response would be more or less independent from the direction of the radiation. However, using a wire as the

anode complicates this because the electric field can become distorted towards the ends of the anode where the latter gets close to the cathode. Because of this distorted field, gas multiplication is position dependent along the wire. To prevent this, and create a cylindrical electric field along the length of the anode wire, the latter is surrounded by a fine helical wire. Unfortunately, this helix is susceptible to vibration and such vibration can result in microphonic noise, i.e., spurious counts.
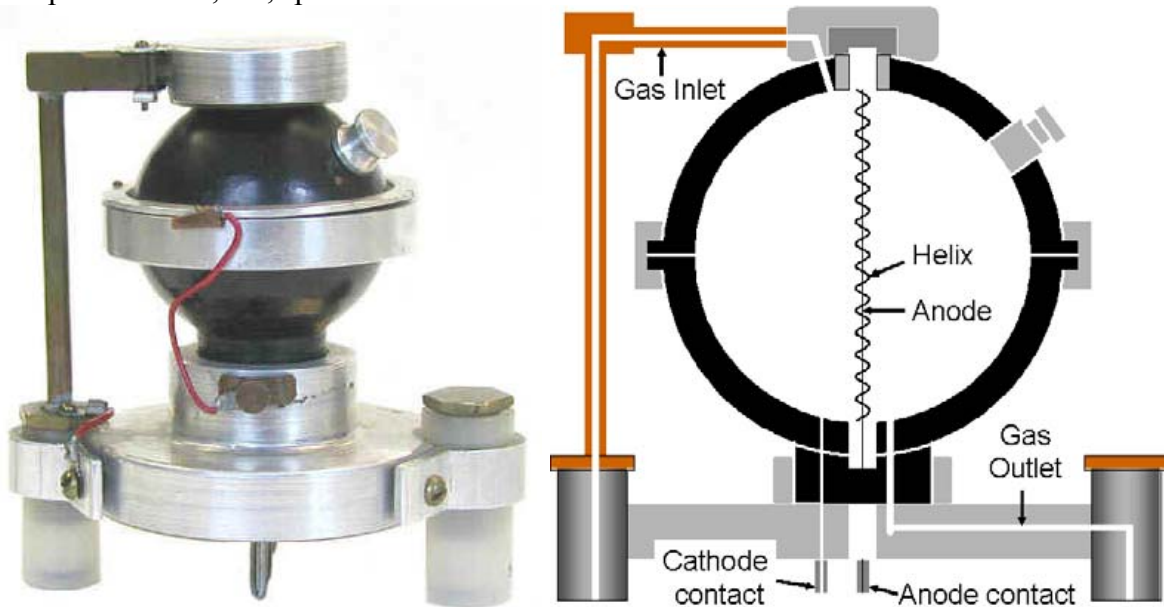


Figure 4.1: *Photo and schematic section of one of the first TEPCs used by Rossi at Columbia University (ca. 1960). The spherical chamber is surrounded by tissue equivalent walls and filled by tissue equivalent gas [Oak99].*

The density difference between the cavity and the surrounding wall can lead to distortions of experimental microdosimetric distributions (chapter 2.2). These "wall effects" (recognized by Rossi [Ros67], treated theoretically by Kellerer [Kel71]) are due to the fact that energy deposition is not along straight lines, but particles may scatter and their tracks have branches of secondaries and tertiaries. For radiations where distortions of the measured distribution cannot be ignored, so called "wall-less" counters have been built. A wide spectrum of different walled and wall-less TEPCs is presented in [ICR83] and [Ros96].

The length scale in measurements with TEPCs is typically at micrometer level (see also chapter 2.2). However, already early TEPCs appeared to work satisfactory in simulation of sites down to diameters of 0,25 μm. But there are fundamental reasons, why adequate accuracy cannot be attained for smaller sites with conventional TEPCs [Ros96]. If the pressure in the cavity is reduced too far, the multiplication region around the anode extends, resulting in a multiplication that is not any more homogeneous in the whole counter volume. Furthermore, the gain has to be increased to obtain sufficient multiplication at lower pressure, which leads to large statistical variation of the proportional amplification factor. Numerous efforts were made to achieve smaller simulated sites by the reduction of the cavity volume. Kliauga [Kli90] reports e.g. to have obtained acceptable spectra in simulated site diameters down to 5 nm in a mini cylindrical TEPC with a diameter of 0,5 mm. A new direction of development could be based on the application of gas electron multipliers (GEM) [Far04]. The basic concept of the GEM consists of a compact array of small apertures in metal-coated 50 μm thin Kapton foils [Sau97]. The GEM geometry allows for very high, stable proportional gains and a separation of the multiplication region from the readout electrodes in gaseous detectors.

# 4.3 Nanodosimeters

The intensive theoretical and experimental work of Grosswendt, Pszona, Colautti, Schulte, Garty and De Nardo et al. ( [Gro04], [Gro02a] [Gro02b], [Gar02], [Scl03], [Gar04] et al. [Nar02]) led to the development of a novel dosimetry technique, called nanodosimeter. The authors intend to simulate target volumes of 1,5-24 nm in diameter at unit density by measuring in millimetric target volumes, filled with low pressure gas. The central parameter of interest in this approach is the cluster size distribution. Models are proposed to relate the cluster size distributions directly to the biophysical effects of ionizing radiation ([Gar 04], [Scl03], see also chapter 2.6).
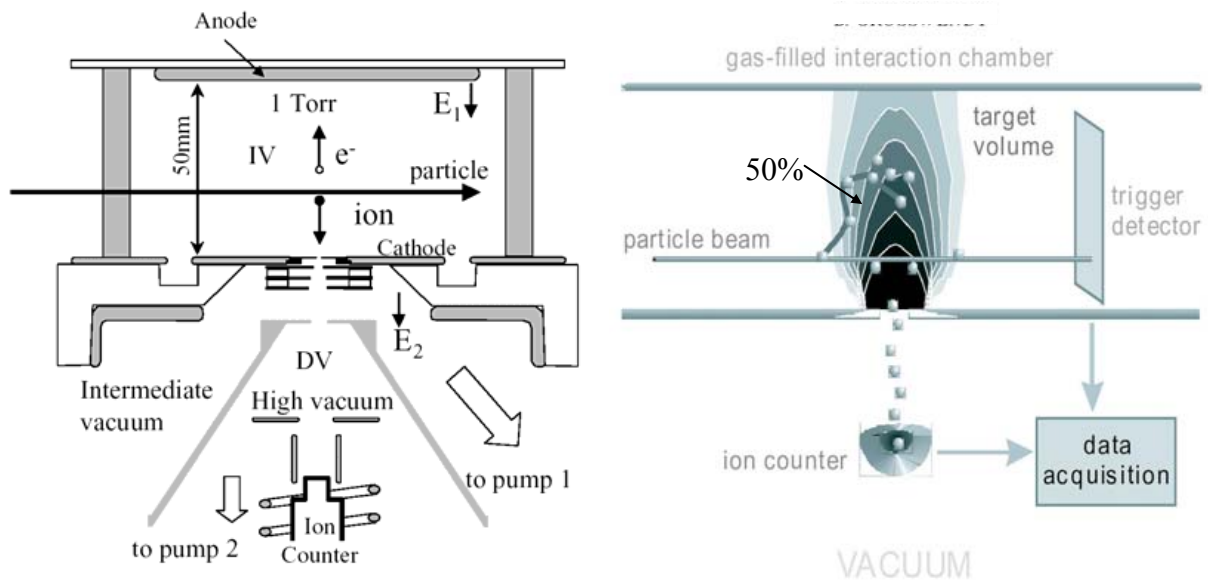


Figure 4.2: *Schematic arrangement (left) and conceptual scheme (right) of the ion-counting nanodosimeter ([Gar04]).*

The schematic arrangement and the conceptual scheme of the nanodosimeter, constructed at the Weizmann Institute of Science [Gar02], [Scl03], [Gar04], [Gro04] is shown in Figure 4.2. The ionization volume of the nanodosimeter is filled with a low-pressure propane gas. The projectile particle beam traverses this volume and is detected by a trigger detector. The electron-ion pairs, induced in the ionization volume by the beam are than separated by an electric field. The ions are extracted through the small aperture in the cathode into vacuum and detected the ion counter. The data acquisition system registers arrival time of the ions at the counter with respect to the trigger. This information can be used to determine the frequency of ionization cluster size.

The size and shape of the wall-less detection volume are determined by the extraction efficiency of ions through the applied aperture, and depends on gas density, aperture diameter and the electric fields above and below the aperture. In consequence, the sensitive volume is represented by a map of surfaces of equal ion-extraction efficiencies (see contours in the right image in Figure 4.2). The maps were determined by calculations based on the electric field geometry and on measured ion-transport parameters. The size of the sensitive volume, at unit density, is parameterized by the 50% contour of the ion-extraction efficiency, which corresponds to a cylinder with a diameter of 3,7 nm and a height of 90 nm in a typical measurement. Even smaller simulated sites are achievable by reducing the gas pressure or by reducing the acceptance volume by restricting the arrival time window of the ions reaching the counter.

There is an important fundamental difference between such an ion counting and electron counting system. Radiation-induced electrons have a wide range of kinetic energies (see chapter 3.2) while the ions, left behind, have low initial velocities. As a consequence, the track image obtained by an ion counting device will reflect the locations, where the ions are left behind, while an electron collecting track imaging system (such as OPAC) detects the electrons at the positions, where they reach thermal energies (let us abandon the diffusion here). However, the relevant energy transfer (resulting in e.g. DNA damage) was at the position, where the ionization occurred, which is essentially the place, where the ion remains. Thus, the electron based systems tend to shift the locations of measured ionizations from the track core to the δ-electron track ends resulting in e.g. a somewhat broader radial dose distribution than the biologically relevant one. The significance of this effect will be studied based on Monte Carlo simulations with TRAX in chapter 6.4.

A further advantage of an ion counting system is that the drifting ions undergo a significantly reduced diffusion, compared to electrons due to their large mass. This is the main reason, why the achievable spatial resolution is significantly higher, than by electron-collecting systems.

Nevertheless, the nanodosimeter has some drawbacks limiting the precision of the measurement. The sensitive volume is not defined unambiguously. The fact, that the calculated 50% contour of the ion-extraction efficiency represents the size of the sensitive volume, hides significant uncertainties regarding the simulated site size. The extraction of the ions through a membrane into the vacuum is also problematic. It was observed, that additional ions are created in the vacuum. However, counting in the vacuum makes it possible to use any filling gas; there is no demand on the gas to support high gain charge multiplication or scintillation (like in OPAC).

The nanometer at present cannot count reliably above an ion cluster size of about 20, hence the simulated site size has an upper limit. A further limitation of the device - at least in its actual assembly - that no cluster size can be measured away from the center line of the primary particle beam, for instance, radial dose distribution is not derivable.

The jet counter [Gro02a], [Psz02] is an alternative of the nanodosimeter, described above. The gas cavity is obtained by pulse expansion of a gas (nitrogen in [Gro02a]) into a walled interaction chamber. The simulated volume is a cylinder with equal height and diameter (0,15-1,3 nm at unit density). The system has a detection efficiency of about 40-50%.

The electron counting alternative of the ion counting nanodosimeters [Nar02b] essentially consists of an electron collector and a single-electron counter [Bre95]. Electrons are generated by ionizing interactions in a cylindrical sensitive volume, filled with propane gas. The electrons are than drifted into the drift column of the single-electron counter and arrive at the multistep avalanche chamber of the counter at different time intervals. Here each single electron generates an electron avalanche, which can be detected. The efficiency of the counter is about 25% at present. In contrary to the present ion-counting nanodosimeters, this counter allows for the measurement of cluster sizes at a broad range of distance from the track core.

## 4.4  Measurement of the radial dose distribution with high spatial resolution
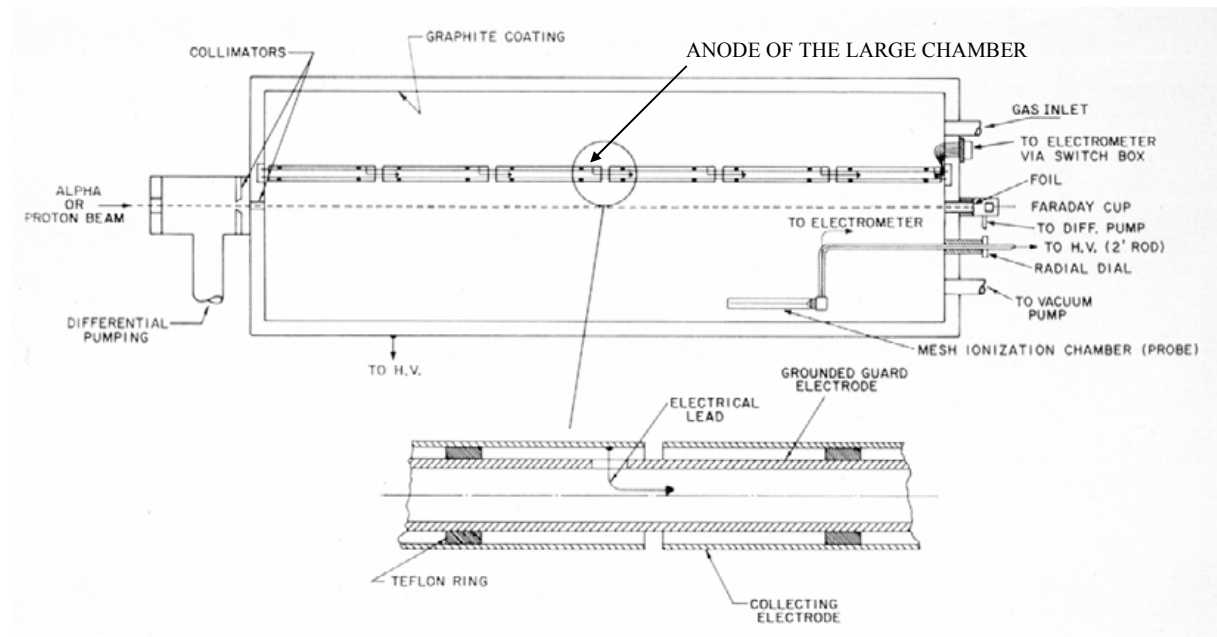


Figure 4.3: *Schematic diagram of the ionization chamber system. For details see text [Win76].*

The most comprehensive experimental studies of radial dose distribution down to nanometer distances from an ion track core were performed by Varma, Baum and Wingate et al. ([Bau74], [Var75], [Win76], [Var77], [Var80] and [Var90]). The experimental data are obtained by measurements with a small movable ionization chamber with a transparent mesh, located inside a large ionization chamber, filled with tissue equivalent gas (or hydrogen or nitrogen gas) (Figure 4.3). The beam of charged particles passes through the central axis of the large ionization chamber (90 cm long, 30 cm in diameter). The anode of the large chamber is placed slightly apart of its central axis, and is divided into six segments supported on a grounded tube (see the zoomed part in the image). This permits electron collection from any one of six cylindrical volume segments along the axis and provides a way to check on secondary electron equilibrium and wall effects.

To obtain the radial dose distribution, $d(r)$, at radius $r$, a small cylindrical ionization chamber (or probe) of almost transparent mesh wall was provided with a mechanism for moving it both radially and axially inside the large chamber. Dose is derived from the ionization current of the probe. The arrangement allows for the measurement of the radial dose at the same simulated distance in condensed matter at different radii in gas, if the gas pressure is changed correspondingly at the same time. Such checking measurements resulted in same dose values, as expected.

The authors ([Win76]) estimate overall experimental uncertainties in $d(r)$ values for radii greater than 5 nm to be +20% and for smaller radii, ±40% (protons and alpha particles at 1-3 MeV/u). However, comparisons with calculated data of Paretzke ([Par74]) show systematic discrepancies of more than 50% for protons at radii below 3 nm. And all experimental data fall lower than the theoretical values for radii greater than 10 or 20 nm by more than the estimated error. This difference is larger for alpha particles than for protons. In other regions (e.g. for alpha particles close to the track core) agreements turned out to be better. Heavier ions were also measured by the system. The agreement of the results was

mixed if compared to simulations. The lack of alternative experimental results makes it often impossible to justify, to what extent the discrepancies are to be attributed to the measurements and in what extent to the simulations.

## 4.5 Track imaging chambers

The experimental concept that shows the highest level of similarities to OPAC was developed in the seventies at Harwell, UK [Hod77]. To be more precise, it is not the experimental arrangement or the physical background of the measurement principle, but the structure of the results, which is very similar for both systems. Both the low-pressure cloud chamber at Harwell and OPAC deliver images of track structure of ionizing particles with a high spatial resolution. Both systems deliver primarily 2 dimensional projections of the track structures, but it is possible, with some restrictions, to reconstruct the full 3 dimensional information. It is therefore important to describe briefly the cloud chamber mentioning its advantages and drawbacks compared to OPAC, before starting the description of the experimental setup and measurement result of OPAC.

The cloud chamber is based on the Wilson cloud chamber from 1911. It contains a gas-vapor mixture which is suddenly cooled by a carefully controlled adiabatic expansion so that the partial pressure of the vapor after the expansion is above its saturated vapor pressure i.e. it is supersaturated. Unlike most chambers, the tissue equivalent or water vapor gas in the Harwell chamber is unsaturated before the expansion. Thus, the chamber is dry, enabling a reliable operation at 100 % condensation efficiency (i.e. two droplets for each single ionization) at a low background level. The pneumatic driven piston (see left picture in Figure 4.4) allows for a fast and reproducible gas expansion to a great extent (the expansion ratio varies between 1,16 and 1,76), which is necessary for the successful operation at low gas pressures (1-2 kPa).

Immediately after each expansion of the cloud chamber the chamber gas is irradiated with either α-particles or X-rays. The resulting positive and negative ions (the thermalized electrons are captured and form negative ions) serve as condensation centers for the supersaturated gas and optically detectable droplets are formed on each ion. Photographs are taken after each irradiation using two orthogonal cameras arranged to focus on a small volume in the middle of the chamber (see right picture in Figure 4.4). After recording the two-dimensional coordinates of ionization from the both photographs, the coordinates can be matched to obtain a three-dimensional track data. After a scaling of the relevant distances to water at standard density (for more details see chapter 4.1), the data is used to derive characteristic parameters of the observed α-particle, proton or low energy electron tracks. The 100% condensation efficiency and the very high spatial resolution allows for absolute measurements of macroscopic parameters, such as W values or stopping powers ([Bud81], [Sto93a]). The reported W values for low energy electrons or α-particles were within experimental uncertainties of existing data. The main purpose of the cloud chamber is, however, the determination of microdosimetric parameters, e.g. proximity functions, cluster size distributions or radial dose distributions of different radiation. These efforts [Bud83a], [Bud83b], [Sto93b] led to partly good, partly satisfactory results as these were compared to Monte Carlo simulations or as the sensitivity of results was checked.
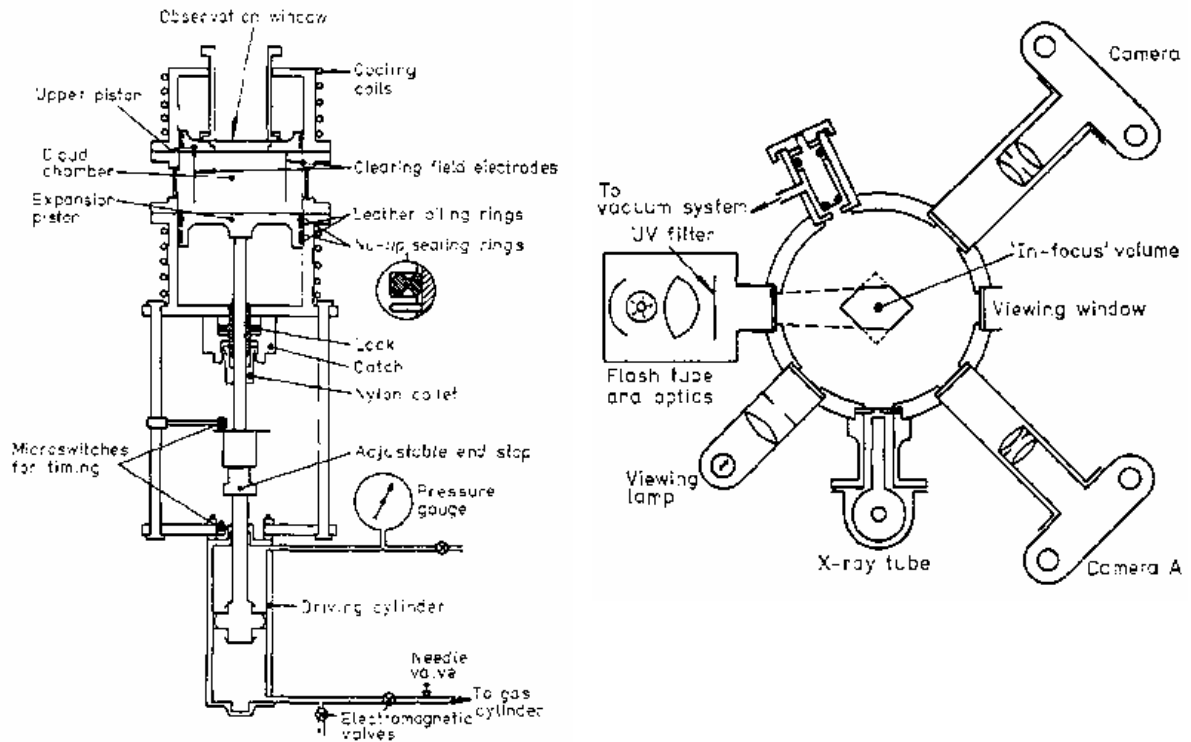
Figure 4.4: *Schematic layouts of the low-pressure cloud chamber [Hod77]. The side view (left picture) shows the expansion mechanics and the plan view shows the arrangement of the photographic system.*

The main advantage of the low-pressure cloud chamber, compared to OPAC, is its high spatial resolution of about 5 nm and its capability of imaging positive ions (for more on this issue see chapter 4.3). However, unfortunately, the positive ions can be imaged only together with the negative ions, and there is no way to distinguish them unambiguously. Statistical methods were developed to find out which droplets represent positive and which negative ions with higher probability [Bud83b]. This technique is based on the fact, that the negative ions suffer more from diffusion during the droplet growing process. The diffusion is the dominant factor that limits the spatial resolution of the chamber. Stonell et al. [Sto93b] determine the extent of diffusion in two ways. If it is determined directly from first principles, the value of the one-dimensional root-mean-square diffusion distance in water vapor scaled to 1 $g/cm^3$ density is for the positive ions is $\sigma_+ \approx 2,4 \pm 0,07$ nm and for negative ions $\sigma_- \approx 4,89 \pm 0,19$ nm. The other way is, to apply the "diffuse-to fit" concept. That means: searching for the most convenient diffusion parameters by means of folding the benchmarking Monte Carlo calculations with the parameters, to obtain the best fit to experimental data. The corresponding parameters, which are applied in [Sto93b] for the manipulation of the simulated results in order to compare them with the measured results, turned out to be significantly different ($\sigma_+ = 2$ nm and $\sigma_- = 5,8$ nm) making the justification of the comparisons questionable. Zaider and Minerbo ([Zai88a], [Zai88b]) propose unfolding methods to obtain non-diffused proximity functions from cloud chamber data. The main drawback of the application of these methods is that the amount of data needed for their successful implementation is well beyond that amount that would reasonably be obtained using the present form of the chamber. One of the biggest disadvantages of the low-pressure cloud chamber compared to OPAC is, namely, the much lower available frequency of taking track images.

*Low pressure cloud chamber Harwell*
*Track made at Harwell*
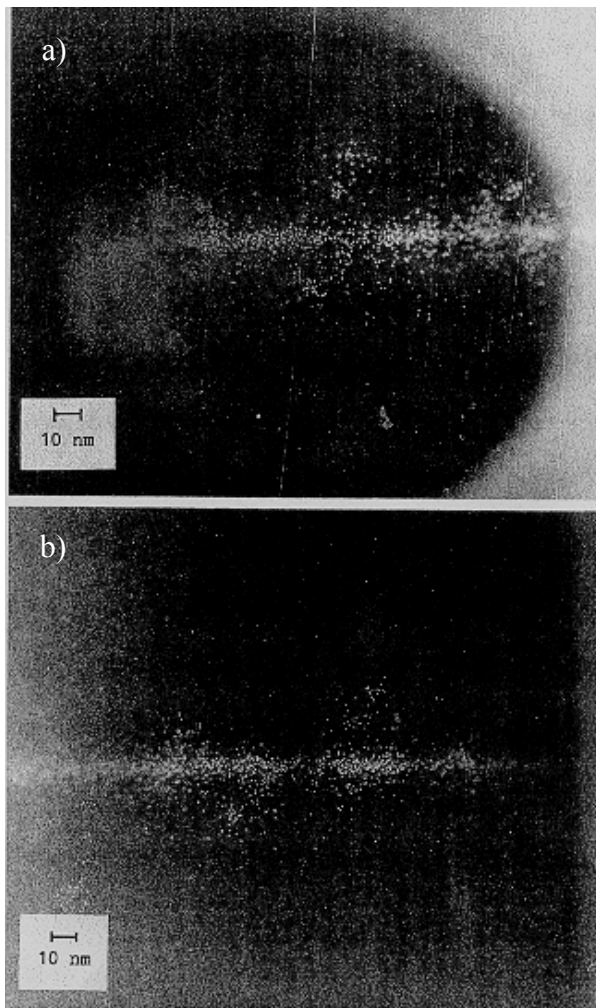
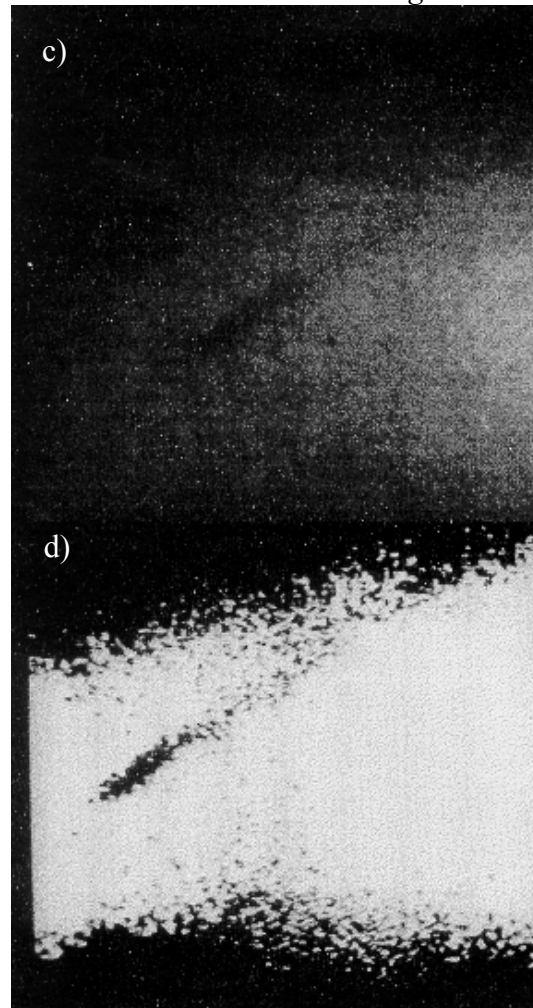*RF-stimulated gas scintillation chamber*
*Track made at Oak Ridge*

Figure 4.5 *a) and b) 5 MeV α-particles in pure water vapor, taken by the low-pressure cloud chamber at Harwell. The both images are a pair taken by the both cameras [Sto93a]. The scale gives the equivalent dimensions in water at 1 g/cm³. c) Photograph of an α-particle track, taken by the optical digital ionization chamber at Oak Ridge [Tur89]. d) Digitally enhanced image of the upper track.*

The track of a 5 MeV α-particle is imaged in Figure 4.5 a) and b) by the upper and lower camera (see Figure 4.4) respectively. The reconstruction of the three-dimensional track using this information turned out not to be feasible without generating an unknown fraction of fictitious droplets. The reason for it is fundamental, due to the misarrangement of the geometry (for details see [Sto93b]). For significant further progress to be made, a new low-pressure cloud chamber would have to be designed which allows the photography of droplets by cameras both orthogonal to each other and orthogonal to the direction of travel of the heavy ion tracks ([Sto93b]). It is also rare, to have the same part of a track in the region of focus of both cameras. For these reasons, some analysis was carried out using data obtained in two dimensions only. This approach, however, has the drawback, besides losing spatial information, that droplets seen in one photograph can mask each other increasing e.g. the measured W value or biasing the radial dose distribution. Resolving of droplets is especially at high LET problematic. In contrary to OPAC, the images of the low-pressure cloud chamber do not contain any intensity information i.e. at a certain position there is a droplet or there is no droplet. If there are two droplets behind each other only the front one can be imaged. A further image-biasing factor is because of gravity. Especially droplets formed on negative

ions, since they grow faster, can drift significantly downwards before the photo is taken ([Sto93a]).

The image of an α-particle track, Figure 4.5 c), was taken by the optical digital ionization chamber at Oak Ridge National Laboratory, USA. The electrons in the particle track are made to oscillate rapidly by the application of an external, short duration, high voltage, RF field. The resulting light emission is imaged by two digital cameras. The best achievable spatial resolution with the existing know-how presently available, is estimated to be 10 nm. For more information see [Tur89].

# 5 The optical avalanche chamber (OPAC)

The central idea of OPAC is based on achievements in the 1980s in the field of optically read out avalanche counters (see e.g. [Bre88], [Bre89] and related references therein). In contrary to conventional electronic read out the optical method focuses on the capture of the UV to visible light emissions, which accompanies the formation of charge avalanches in some gases. The successful implementation of this read out scheme was facilitated by the availability of gateable, image intensified CCD-cameras (IICCD) at moderate costs. Compared to electronic read out the optical method offers some advantages:

- It offers low cost, high resolution, genuine two-dimensional multihit read out capability.
- It is insensitive to electronic noise or RF-pickup signals in the detector environment.
- With proper choice of gases meshes can be used at low pressure instead of wires, which makes the chamber simple and rugged.
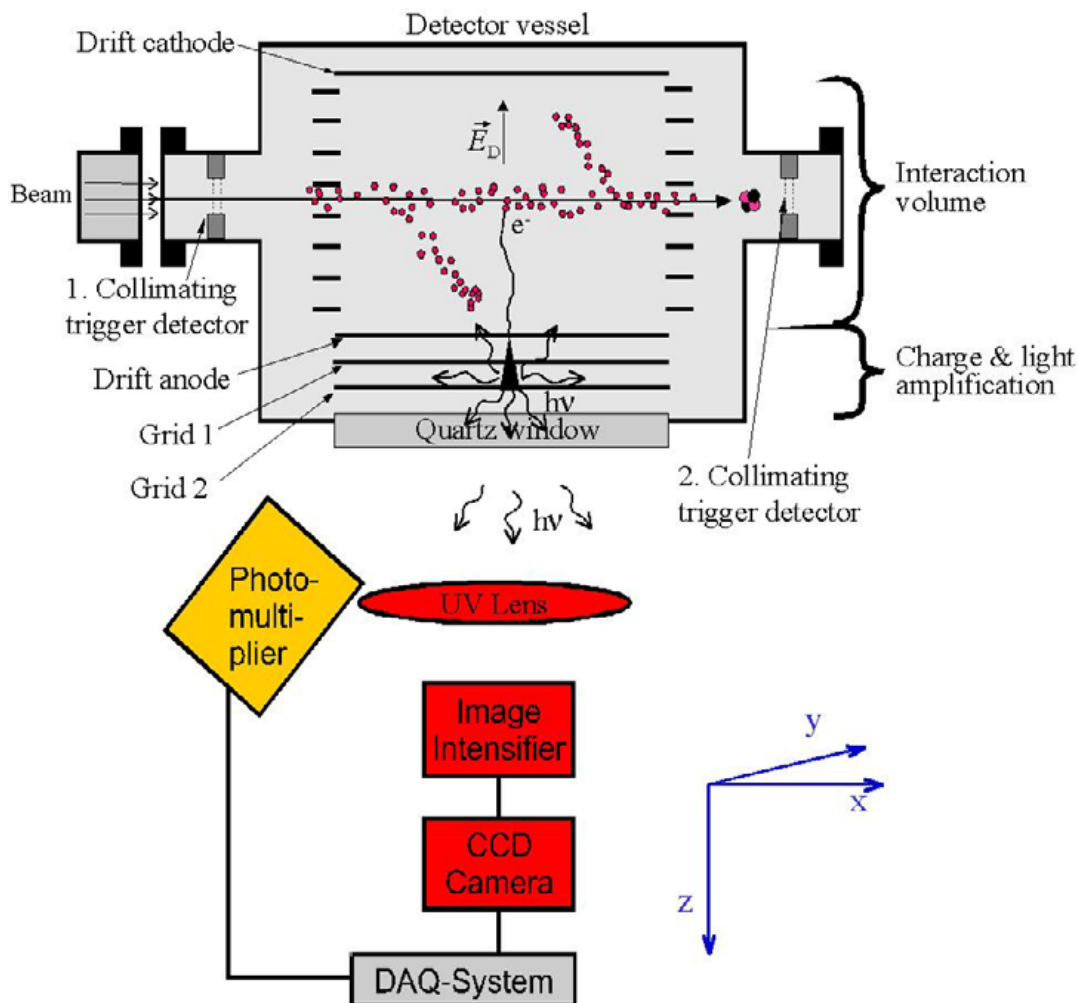
## 5.1 The detector



Figure 5.1: *Schematic view of the Optically read out PArticle track Chamber (OPAC). For details see text.*

53

The principle of OPAC is a time projection chamber (TPC) with a parallel-drift field ($\vec{E}_D$ see Figure 5.1). The chamber is filled with triethylamin (TEA, $(H_5C_2)_3N$) vapor. High gas quality is ensured by a continuous supply of fresh TEA vapor. (For more details on the gas supply and optional gas mixing technique see [Tit98]). The gas pressure in the framework of the presented measurement program was 4, 10 or 40 hPa. These values correspond to gas densities of 16,68; 41,7 and 166,8 $\mu g/cm^3$, respectively. Thus, a relevant distance in the gas between two well defined events of e.g. 1 mm corresponds to distances of about 16,7; 41,7 and 167 nm in liquid water according to equation (4.4) and comments in chapter 4.1. Charged particles (i.e. ions in the present work) cross the interaction volume in its center, orthogonal to the electric field. δ-electrons from the ion-TEA interaction get thermalized and cause further ionizations along their tracks during the thermalization process: the typical ionization pattern arises (see chapter 3).

The reduced electric field ($E/p$) of typically 8 Vcm$^{-1}$hPa$^{-1}$ is established by stainless steel wire meshes of 81% optical transmission between drift cathode (DC) and drift anode (DA) (see Figure 5.1). To ensure a homogeneous, parallel drift field a series of guard electrodes made of stainless steel rings is applied. The drift field gets the thermalized electrons to drift in "$z$" direction (see Figure 5.1). During this drift the electrons suffer from diffusion, hence the original $y,z$ coordinates of the electrons, which we want to measure, cannot be preserved exactly. This is the main factor that limits the spatial resolution of the system. The extent and importance of the diffusion to the ion track structure will be studied in chapter 6.

From the interaction volume the electrons enter an amplification zone. The detector has a two-step homogenous electric field amplification system, consisting of two grids (G1 and G2) arranged at a spacing of 3,2 mm. The grids are made of the same meshes as DA and DC. Electrons which drift into the amplification region are multiplied in a first proportional charge amplification stage between DA and the first grid ($G_1$). This stage is followed by a light amplification region, where the electric field, applied between $G_1$ and $G_2$ results in a proportional scintillation induced by electrons of the avalanche of the first amplification step. [Bre90]. The reduced electric fields, in the amplification stages were varied between 20 and 200 V/cm/hPa in the measurements according to the desired light yield and the energy deposited by the traversing ion (details in chapter 6.5.3).

The described optical time projection technique consisting of a parallel drift field and a double-step charge and light amplification structure has the advantage that light emission always occurs in the same layer. Therefore, only a small depth of field of the optical system is required and the maximum available optical aperture can be used to achieve a well-focused image. In addition, the scintillation light pulse is always proportional to the amount of electrons arriving at the amplification region in a certain time interval. As the drifting time of the electrons depends on the $z$-coordinate of their origin, a gateable (i.e. the time interval of sensitivity is adjustable with a high temporal resolution) image acquisition system can obtain spatial information about the charge distribution in "slices" from different $z$-intervals of the interaction volume. The uncertainty of the $z$-information is limited by the uncertainty of the drift time (diffusion in $z$) and the gate with (in nm). A rough information on the integral of the amount of charge as a function of $z$ can be derived by analyzing the time-dependent signal ratios of the photomultipliers (see Figure 5.1), which measure the light transient (see Figure 5.1, for details on this technique see page 40 in [Tit99]).

The selection of the filling gas, TEA, was motivated by the demand for a gas with high scintillation light yield in the visible or near UV range. TEA satisfies these criteria [Sau89]. It has large light yield in the described proportional mode in the near UV (peak emission at $\lambda = 280$ nm) which can comfortably be handled with regular quartz optics. In addition, the vapor pressure of TEA at normal temperature is sufficiently high (approximately 120 hPa at

300 K [Sau89]) allowing for low-pressure operation up to 60 hPa without need for heating the whole system (for more details on gas selection and flow control system see [Tit98]).

## 5.2   The optical readout system

The final result of the processes inside the chamber is, thus, the emission of scintillation light, which occurs between $G_1$ and $G_2$. The scintillation light pattern represents the two-dimensional projection of the spatial distribution of the ionization events, caused by the traversing ion in the interaction volume. Note, that this projection is not perfect, diffusion and other artefacts have to be taken into account for data analysis (details on data analysis in chapter 6). A UV lens focuses the scintillation light pattern onto the photocathode of an intensified CCD camera (IICCD). The resulting projected image of the track is then captured by a digitizer card and saved in a computer.

The type of the photocathode (UV enhanced S20 on quartz) has been selected with the purpose of converting the incoming UV photons into electrons with high efficiency (quantum efficiency: 21 % at 280 nm). In addition, the applied photocathode can be pulsed with very short (down to 1,7 ns) high-voltage pulses. As the amplification of photoelectrons takes place only if the high voltage is on, a controllable, variable and -if demanded- very short exposure time of the CCD is available. In the standard operation mode, the adjusted exposure time is about 1 µs in order to collect the light contribution of all drifting electrons but avoid the accumulation of multiple tracks and noise.

The "gate-on" time, i.e. when the gate pulse is sent to the photocathode, is defined by a coincidence signal of both trigger detectors (see Figure 5.1). The trigger detectors also act as beam collimators. The trigger detectors are installed in the input and in the output port of the chamber housing. Both of them have an aperture of 1 cm in diameter centered at the same distance from the DA and the DC. As a consequence, the readout system is activated only for that, which come from the accelerator and cross the interaction volume through its center.

The electrons from the photocathode are multiplied by a double-step multi-channel plate (MCP) and accelerated in a parallel electric field (see Figure 5.2). The accelerated electrons hit a phosphor screen which emits visible light with a decay time of 1 ms. The phosphor is coupled by a conical fibre-optical faceplate to the CCD (charge coupled device) of a standard slow-scan camera (EG&G, M4005). The CCD camera provides an image in a format of 512 x 512 pixels at a maximum rate of 15 $s^{-1}$. Finally, this image is captured and saved by the computer. For more information on the working principle of the specified devices see [Tit99].

S 20
Photocathode

2 x MCP

P43
Phosphor

Fibre optic

CCD

$h\nu$

$e^-$

$e^-$

$h\nu$

$\lambda_{peak} = 280$ nm

$\lambda_{peak} = 544$ nm
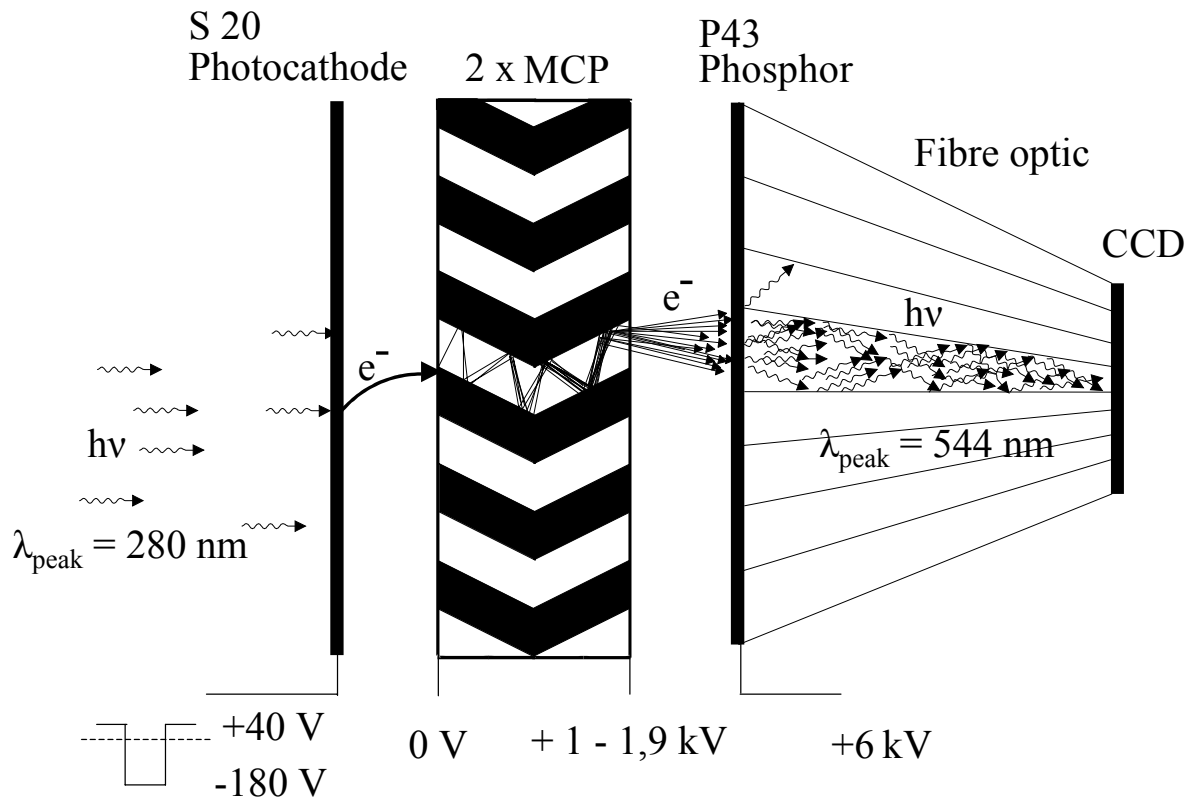
+40 V
-180 V

0 V       + 1 - 1,9 kV

+6 kV

Figure 5.2: *Schematic assembly of the image intensifier. The light intensification is accompanied by a wave length shift from the UV to the visible region.*

## 5.3  Operation of the chamber

Figure 5.3 a) shows a photo of the detector together with the optical readout system in its former status [Tit99]. The interaction volume and scintillation zone of OPAC are kept in the stainless steel housing (see "V" in Figure 5.3 a)). In the left, bottom part of the picture the chamber is extended to provide a possibility for pumping and TEA gas outflow. Also the capacitive pressure gauge ("G") for the control system, is seen at the pumping port. On the readout side of the detector six photomultipliers ("PM") are mounted. The UV lens and the IICCD are in the upper part of in Figure 5.3 a). The present system is similar to the original system of Titt [Tit99], but improved in some aspects to allow for a better optical resolution and lower background images (see details in the following chapters).

Figure 5.3 b) shows a photograph of the present, improved system mounted in front of the beam tube of Cave A at GSI, Darmstadt in august, 2003. The stainless steel housing of the detector can be seen in the upper part of the picture below the pressure sensors. At the top of the detector a turbo pump is connected. The optical readout system is shielded against external light by a blackened plastic tube. The CCD camera is in the lower part of Figure 5.3 b), behind the white fan, used to cool the CCD-camera to obtain a lower thermal noise level.
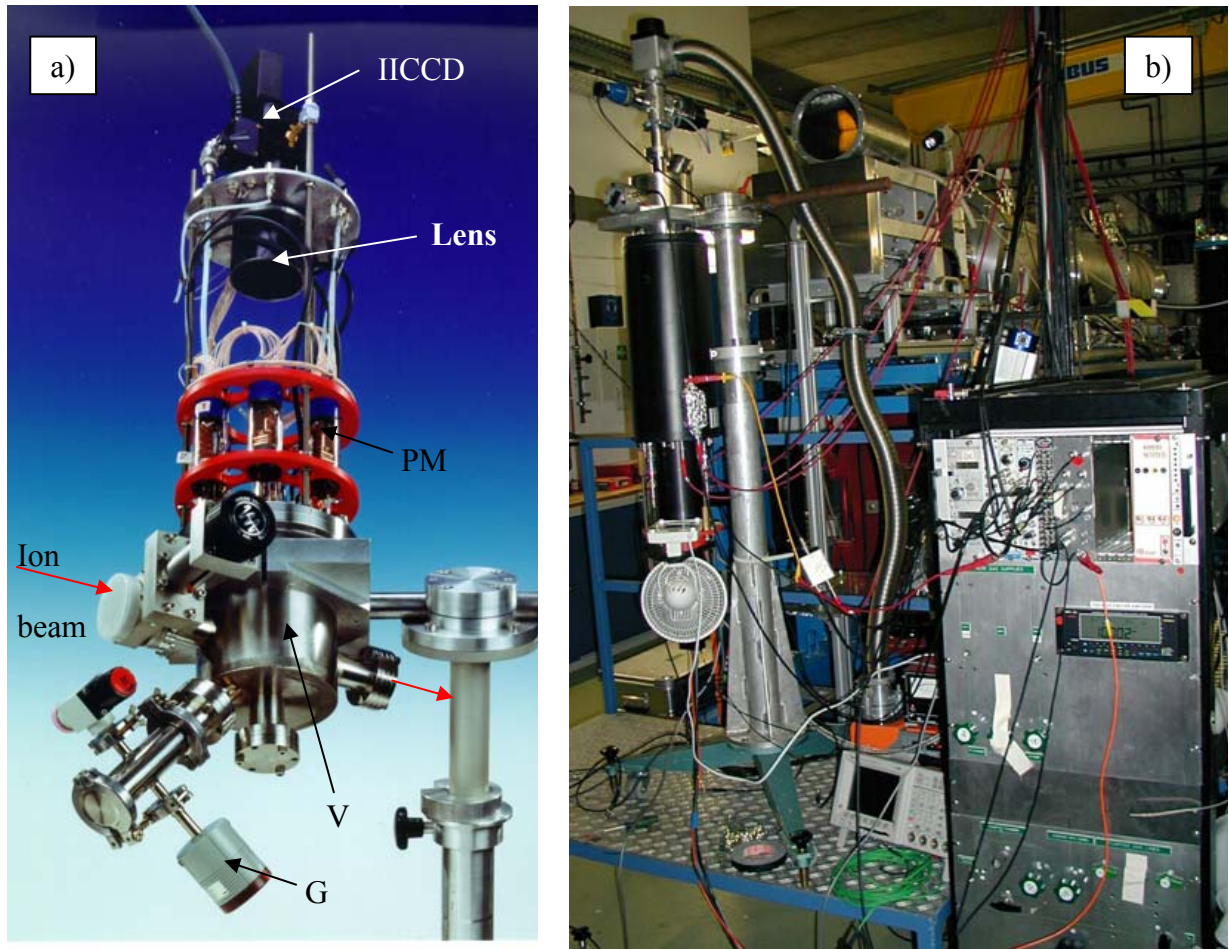
Figure 5.3: *a) OPAC in the laboratory without the light protecting tube, so that the photomultipliers and optical system are visible and b) OPAC in the radiation cave at GSI during the preparation of the measurements.*

The electronics, needed to supply, control and read out the detector and the imaging system is divided into two groups. One group is located near the detector, seen on the right side of the picture on top of the gas supply system. The second part is placed outside of the cave, inside the measurement hut. A PC, which controls the data acquisition, is placed near the experiment (not included by Figure 5.3 b)). This PC is connected to a laptop in the measurement hut. The laptop controls remotely the front end PC via the software, pcAnywhere.

## 5.4  System improvements

The previous status of the experimental system is reported by Titt et al. [Tit98] and in the PHD work of Titt [Titt99]. In the beginning of the present work the main focus was the further instrumental development of the measurement system and the upgrading of hardware and software units used for data acquisition and data analysis. To illustrate the progress obtained by these changes, Figure 5.4 a) and b) show a comparison between two α-particle tracks, imaged by the old and modified system, respectively. Below, a detailed description of the modifications, which are responsible for the obviously significant improvement is presented.
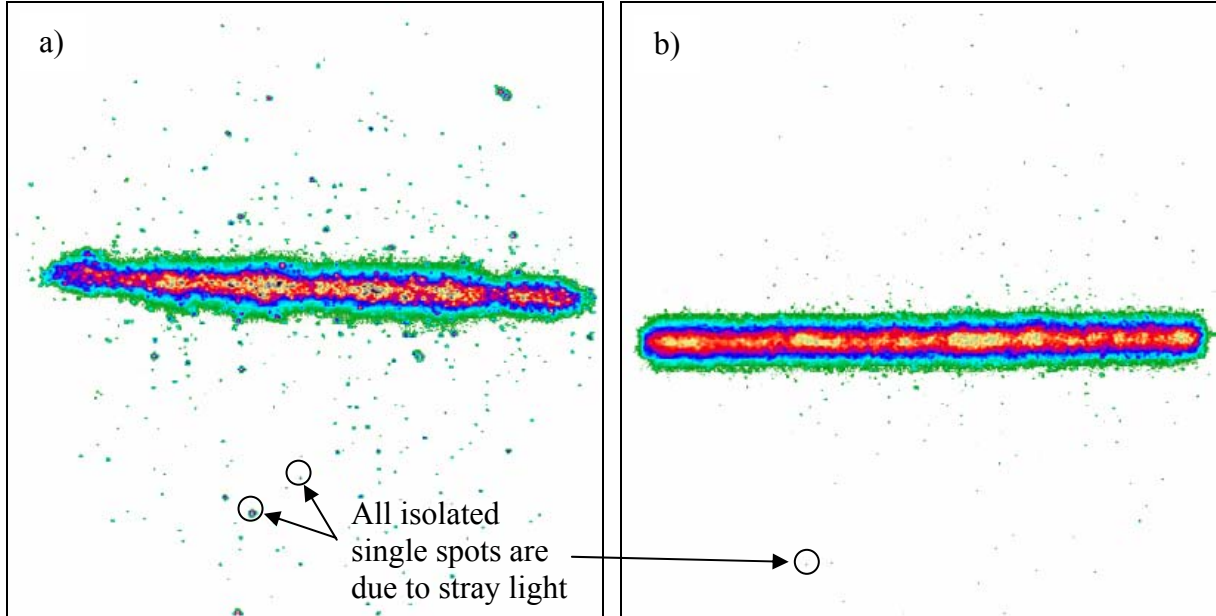
Figure 5.4: *Measured images of 3 MeV α-particle tracks with using the a) old and the b) improved OPAC system. The imaging quality was significantly improved due to the replacement of the UV lens and that of the image intensifier. The significant reduction of stray light (see the isolated spots in the images) is due to the covering of the internal detector parts with light absorber materials.*

## 5.4.1 Improved resolution with reduced diffusion

Figure 5.5 is a photo of the present assembly. As already mentioned in chapter 5.1, the dominant factor that limits the spatial resolution of OPAC is the diffusion during the electron drifting process. Electron drift in gases has a comprehensive theory (see e.g. [Feh83] or [Pei84]), the most important aspects for OPAC are summarized by Titt [Tit99]. Here, we summarize two relevant relations: The one-dimensional root-mean-square diffusion distance, $\sigma_{pr}$, is proportional with the square root of the drifting distance, $z_d$, and inversely proportional to the square root of the gas pressure at a given reduced electric field, $E/p$:

$$\sigma_{pr} \propto \sqrt{\frac{c_g}{E/p}} \sqrt{\frac{z_d}{p}} \tag{5.1}$$

Where $c_g$ is constant for a given gas and the index, pr, of $\sigma_{pr}$ refers to "projected radial", i.e. the radial broadening of the projected track is observed.

Guard electrodes
and interconnecting
resistors

Place for ion
penetration

Supply voltage
cables for grids

Spacer rods

Interaction
volume,
32 mm long

Charge & light
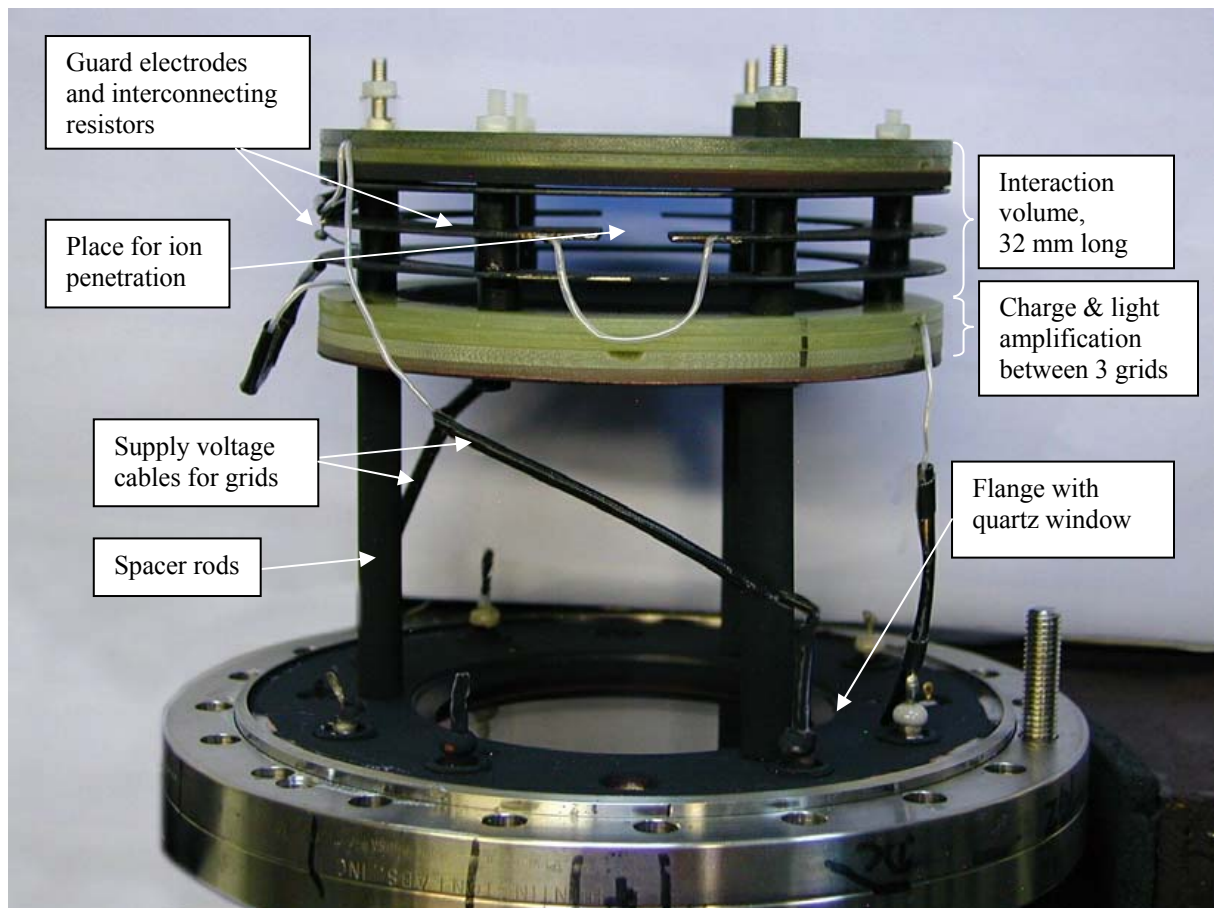amplification
between 3 grids

Flange with
quartz window

Figure 5.5: *Photo of the internal assembly of the modified detector chamber.*

A reduction of the drift length results in a reduced diffusion. For this reason, the width of the interaction volume was reduced from originally 10 cm to 32 mm, i.e. the drifting distance from $z_d' = 50$ mm to $z_d = 16$ mm, a reduction of diffusion by a factor of 1,77. The prize of the reduced length of the interaction volume is that fast δ-electrons with large ranges in *z*-direction cannot be imaged completely. However, the second advantage of the thinner chamber follows, actually, from this drawback. Later on, a mathematical method will be presented for the unfolding of the measured, projected dose distribution to derive the "real" radial dose distribution. Such an unfolding is straight-forward for an interaction volume with negligible thickness but more and more problematic, if each projected dose value contains the integral of radial dose values of an increasing range of radial distances.

The second modification inside the gas-filled detector volume was the reduction of internal optical reflections to reduce the stray light in the image (see Figure 5.4). A large amount of isolated spots is visible in Figure 5.4 a) central track region. There is no observable spatial correlation between these signals in contrary to tracks of δ-electrons made up of similar but spatially correlated spots. The energy of the α-particles was selected in that way, that the range of all δ-electrons must be well below 1 cm in TEA at the pressure of 10 hPa. Therefore, it can be excluded, that these events are caused by fast electrons of low LET.

First, it was suspected, that the signals could originate from ionization electrons caused by γ-rays. Also low energy photons were considered to transport energy away from the track core. Photons, γ-rays would ionize in the whole interaction volume, i.e. the resulting free electrons would produce light spots at different times according to the different drift lengths. However, we realized that isolated spots arose at the same time as the scintillation light, itself. After this was recognized, images of an LED light source were taken. The LED was

positioned in the center of the detector. For the same amount of light from LED and particle track, no significant difference in the amount of isolated spots was found.

The experiment proved, that the observed isolated spots are due to single photons scattered by reflective surfaces inside OPAC, which reach the photocathode of the IICCD outside the "regular" optical path, accidentally, i.e. stray light. The source of stray light is the scintillation light of the track, itself. This is concluded from the fact that the amount of scattered signals was found, within the measurement uncertainties, to be exactly proportional to the light yield of the track (or LED light source). Due to the strong radial drop of the dose distribution, stray light would largely distort the radial dose distribution, if it could not be eliminated. Therefore, to minimize this effect, all surfaces of all detector components, which are exposed to scintillation light of the track and might reflect photons, were coated with a light absorbing layer. The grids were blackened by electrodepositing of nickel. The internal surface of the detector's steel housing, the spacer rods, the cables, the guard electrodes and the lower surface of the carrier plastic rings of the grids were coated with a special black coating. (Nextel Velvet-Coating 811-21, manufactured and distributed by Mankiewicz). The system components outside the gas-filled volume, between the quartz window and the UV lens (e.g. photomultipliers, power supply cables) were also covered with the Nextel paint or with a black self-taping fleece textile, "Accor". The fleece was found to reflect less than 1 % of the incident light [Mir03].

## 5.4.2 Replacement of the UV lens

The originally applied Al mirror lens generated a strong pillow-like distortion of the image (see Figure 5.4 a)). The new UV-lens consists of five single lenses made of calcium fluoride and suprasil-quartz (manufactured by Berhard Halle Nachfl. GmbH, Berlin). The lenses are fixed in a 194 mm long blackened steel tube. The lens has a focal length of $f = 150$ mm and an $f/$ value of $f/2,5$. However, this latter value is significantly worse, than that of the old lens ($f/1,1$), but the efficiency of the system for imaging the thermalized electrons has to be limited anyway in order to achieve a non-distorted radial dose distribution (for details see chapter 6.5.3). Thus, there is no need for a better $f/$ value for the present measurements. On the other hand, the new lens ensures an excellent image quality: there is no observable distortion in the range of application (see Figure 5.4 b)), the chromatic aberration is negligible and the focus is optimized to be the sharpest in the wave-length region of 250-300 nm. In addition, the new lens has reduced the stray light problem significantly. The reason for this is the bad design and ageing of the old lens.

The black coating of the affected detector elements and the replacement of the UV lens, together, led to a reduction of stray light to 7,5% ± 1,5% of its previous level. This value was measured with an array LEDs and a mask with a thin slit, which simulates the central part of the particle track. This object was imaged with both lenses under the same circumstances as in the normal OPAC operation. The light yield of the image was compared to the light yield of the stray light for both lenses. The ratio of stray light was found to be 13 ± 2 times higher for the old system. The application of α-particles in normal OPAC operation mode instead of the LED light source led to the same result (compare Figure 5.4 a) and b)).

## 5.4.3 Optical adjustment and calibration of the new lens

Prior to the measurements of track structure, it is necessary to adjust the distances between object, lens and image intensifier properly. After adjusting the focus, the linear magnification

was determined. Several images of different objects were taken. The scaling ratio between object (in mm) and image of the IICCD (in pixels) was found to be:

$$M = 5{,}56 \pm 0{,}05 \text{ pixels/mm} \tag{5.2}$$

Pixels/mm is a useful unit for the scaling ratio in the case of OPAC. The result means, that a distance of 11 pixels, measured by the CCD camera corresponds to slightly less than 2 mm in the interaction region of OPAC. Taking into account the scaling ratio due to the pressure of the filling gas (see chapter 4.1), we can calculate the simulated distance in tissue corresponding to one pixel in the image at a given gas pressure:

$$M_{4\,hPa} = 10^6 \frac{\text{nm}}{\text{mm}} \frac{\rho_{\text{TEA-4hPa}} \Big/ 1 \frac{\text{g}}{\text{cm}^3}}{M} = 3\,\text{nm/pixels}$$

$$M_{10\,hPa} = 7{,}5\,\text{nm/pixels} \tag{5.3}$$

$$M_{40\,hPa} = 30\,\text{nm/pixels}$$

This result means, that a distance of 10 pixels of e.g. two $\delta$-electron end points from each other corresponds to 30 nm in tissue – i.e. at a simulated density of 1 g/cm$^3$.

## 5.4.4 Replacement of the image intensifier

The amount of light received by each pixel is measured with a dynamic range of 11 bit (2048 channels). Thus, the saved image is a function of two variables:

$$I = I(x,y) \qquad \begin{aligned} &x, y \in N(1,...,512) \\ &I(x,y) \in R(-30, 2048) \end{aligned} \tag{5.4}$$

After background and noise corrections, a pixel value may be slightly negative and it is not a whole number.

A part of an α-particle track, imaged with the new image intensifier, is shown in Figure 5.6 a). The data acquisition software enables the representation of the images as a surface plot of a mountain ridge. The track is built up of single peaks of different height but similar shape (see two examples in Figure 5.6 b)). Such a single peak is the response of the system made of the image intensifier, the CCD and the optical coupling between them to one photoelectron that was produced on the photocathode of the image intensifier (see Figure 5.2). The electron multiplication process inside the MCPs is of statistical character, this is the reason for the very different response heights. The second artefact with even more severe consequences to the analysis of the measurements is the broadening of the peaks. This effect will be studied in chapter 6.5 in detail.
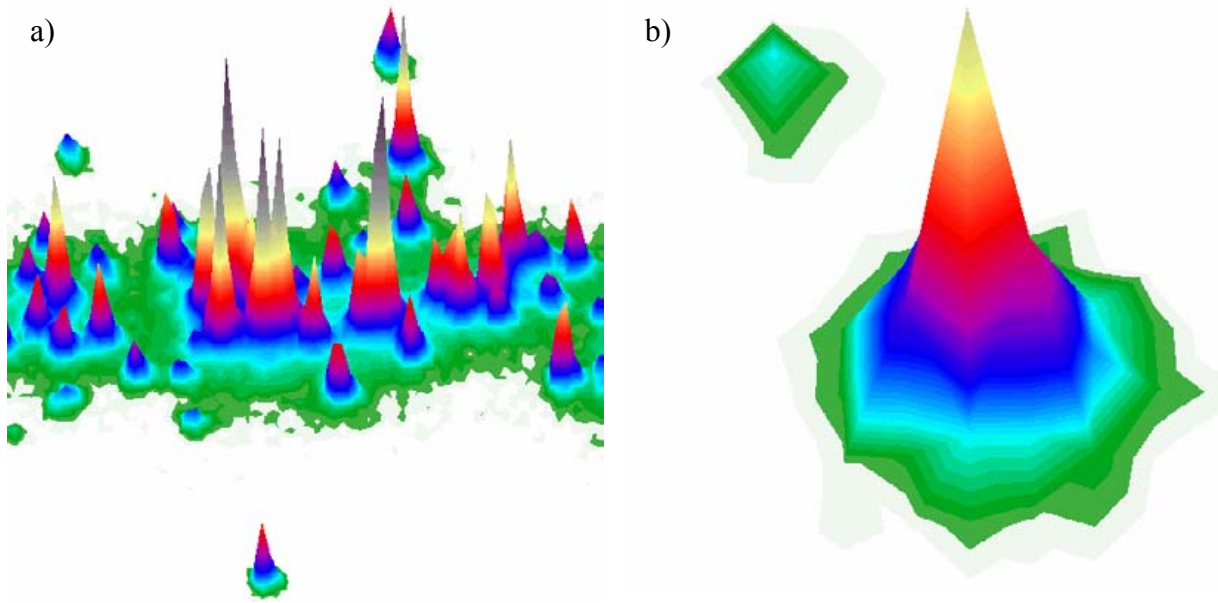
a)

b)

Figure 5.6: *a) A part of the track core of an α-particle and a few stray light peaks b) Two images of single photons, which have caused a photoelectron emission from the photocathode of the intensifier. Note the difference in height and volume.*

Let us introduce the terminology, single peak integral, $I_{sp}$, for the value of the double integral of the image values, $I(x,y)$, over a region of 5 x 6 pixels (the single peaks are typically broader in $x$ direction) around the center of a single peak:

$$I_{sp} = \sum_{5x6} I(x, y)$$

(5.5)

In Figure 5.4 a) (at the beginning of chapter 5.4), a very strong variation of single peak integrals of the stray light images is observable. This affects the precision of data analysis, because if the peak is not due to an arbitrary scattered photon, there is no way to determine the number of initial photoelectrons contributing to the peak. The probability density function of $I_{sp}$ was measured in order to quantify the effect and to search for its reason. The measurement was performed by taking images of single scattered background photons. The photocathode of the IICD was shielded by a semi-transparent textile to ensure that only about ten photoelectrons are emitted on the photocathode during the gating time of about 1 μs. As the few single peaks are distributed homogeneously on the CCD surface (512 x 512 pixels), the probability of a superposition of two or more single peaks can be neglected. All single peaks of about 1000 images were localized by the data analysis software and all $I_{sp}$ values were calculated. The spectrum of the $I_{sp}$ values was than derived and displayed in log-log plot (Figure 5.7). For direct visualization of the $I_{sp}$ contributions at different pulse-height regimes on the basis of the log-log distribution, the probability values were multiplied by the corresponding $I_{sp}$ values (for more details on the mathematics see page 20 in [Far04]).

Figure 5.7 shows the measured $I_{sp}$ spectra of the old and the new MCP. In standard operation mode, using a longer gating time of 1 μs, the probability density function of $I_{sp}$ shows an anomaly if the old intensifier is used (red symbols). Instead of falling sharply for higher peaks according to the expectable electron multiplication statistics of the MCP, a second peak can be observed. About 10% of all single peaks have an $I_{sp}$ exceeding the regular $I_{sp}$ values by about an order of magnitude. This behavior results in the large amount of anomalous intense stray light peaks in Figure 5.4 a). As the old image intensifier was already seven years old, we suspected, that evacuated region inside the MCP and between the MCP and the phosphor layer contained an increasing amount of residual gas originated from the solid surfaces. As the old image intensifier had only one single MCP (the new one has two, connected in a V-shape

(Chevron geometry), see Figure 5.2), the ionized atoms of this residual gas have a certain probability to be drifted back against the photocathode by the high voltage of the MCP. Such a feedback ion can ionize the material of the photocathode (even more than once), resulting in a secondary electron avalanche in the MCP.

This hypothesis was verified by measuring spectrum of $I_{sp}$ at different gating time adjustments. As visible in Figure 5.7, the ratio of anomalous high $I_{sp}$ to "normal" ones is much lower, if the gating time is reduced to 30 ns. At a gating time of 10 ns, the "second peak" almost disappears. This tendency confirms the anticipation of feedback ions. Namely, the ions have relatively high masses, therefore they need time to drift back to the photocathode. This time is of the order of 10 ns. At shorter gating time, the ions of the gas, produced by the primary avalanche of electrons, reach the PC after the PC-gate is turned off. Hence, ion induced electrons are not amplified anymore, therefore the afterpulse is suppressed.
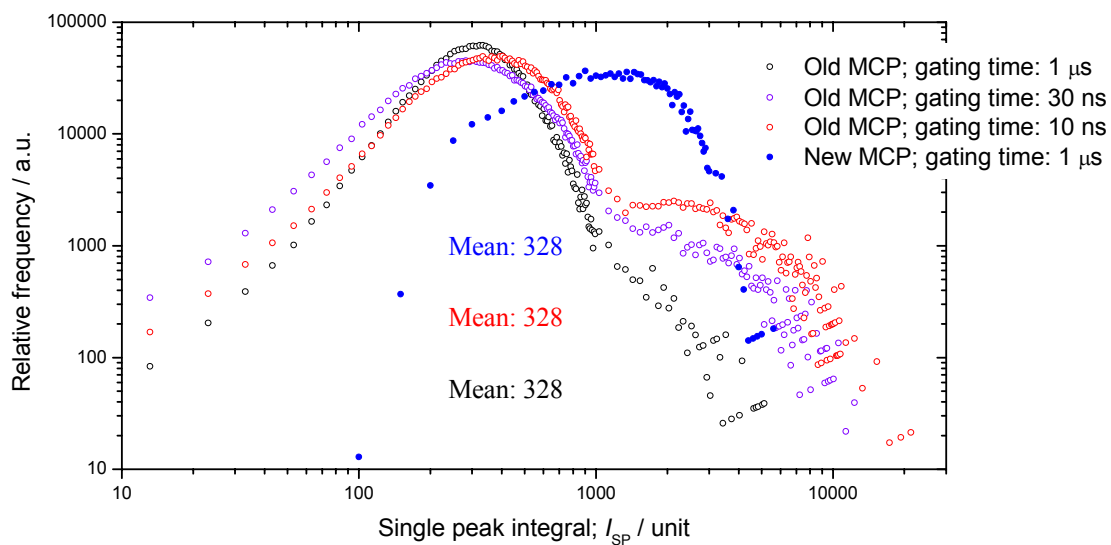


Figure 5.7: *Probability density function, f, of single peak integrals. The function is derived for both the old and the new image intensifier. A reduction in gating time results in a decline of the "second peak", which is present if using the old image intensifier.*

In contrary, the new image intensifier has two MCPs in Chevron geometry. Ions produced in the final avalanche have little chance to reach the PC. Thus, the high $I_{sp}$ contribution is effectively suppressed (see blue symbols in Figure 5.7). The absence of a "second peak" is even at a long gating time obvious. However, the main peak, itself, is somewhat broader, than it was, if measured with the old device. The broader main peak is due to the higher amount of electron multiplication steps in the double MCP of the new image intensifier. Nevertheless, the very sharp drop in the relative number of peaks with high or low integral values is a major advance if compared to the old device. Furthermore, the old MCP had to be operated at its maximum gain for the measurement of the peak statistics in Figure 5.7. In comparison, the intensifier with double MCP was operated at a very moderated gain, far away from its maximum gain capability. And in spite of this fact, the mean value of $I_{sp}$, $\overline{I_{sp}}$, amounts to 1080, while the same mean value of the single peak integrals, measured with the old device was 328, at a gating time of 10 ns and 508 at a gating time of 1 μs (mainly due to the "second peak"). Thus, the single photoelectron response of the new image intensifier is higher and much better defined in terms of its gain distribution. Furthermore, the photocathode of the new device is gateable down to 1,7 ns (as specified by the manufacturer) and has a quantum

efficiency of 21% for photons of 280 nm wave length. Similar values for the old device were 5 ns and 17%, respectively.

## 5.4.5 The new data acquisition system

The original data acquisition system was developed for operating systems (Windows 3.1). Therefore, the modernization of the data acquisition hard- and software was necessary. In its original version ([Tit98], [Tit99]), a frame grabber card was used to acquire and digitize the analogue signal of the CCD camera. With this technique the dynamical resolution obtained with an uncooled CCD camera was 8 bit (at best). The fast anode signals of the photomultipliers were digitized by a digital oscilloscope, and the data had to be transferred to the computer separately.

The old technique was replaced by a 12 bit, 100 MHz digitizer board (Spectrum Systementwicklung Microelectronic GMBH, MI. 3022 / SN 01439). The board is plugged into the PCI bus of the personal computer (AMD Athlon(tm) 2400+, 512 MByte RAM). It has two input channels and inputs for external trigger and external clock for external control of the sampling rate.

The flexibility of the described digitizer board enables the acquisition of the photomultiplier signal and the CCD image directly after each other. The photomultiplier signal arrives within 1 μs after the trigger. The delivered temporal function is sampled with a rate of 50 MHz. The CCD camera analog signal arrives about 5 ms after the PM signal and is sampled with 5 MHz for about 70 ms. The charge information of each pixel is sampled with the CCD's internal pixel clock fed to the digitizer board as external clock input. Appropriate electronics and software were developed, to allow for the necessary switch in the sampling rate between the photomultiplier data and the CCD camera readout.

The new software (OPtoMe - **OP**AC **to Me**) is developed for 32-bit operating systems, Windows 98 is installed on the PC that manages the data acquisition at present. The operating system has not yet restricted any function or the speed of data acquisition or data analysis so far. The software was developed in the Microsoft Visual C++ development environment. It offers the user a convenient platform to control the whole data acquisition process. Figure 5.8 shows the screen of the computer during the data acquisition process. The two-dimensional projection of the ion track (carbon ion at 200 MeV/u tracked at a gas pressure of 40 hPa in the imaged case) is visualized by OPtoMe. The color of a pixel represents the charge amount, which arrives the corresponding pixel of the CCD. The visualization is solved technically by using the software, Measurement Studio for Visual C++ (National Instruments[TM]). This software extends the Visual C++ environment by a set of class libraries providing a convenient tool for handling 3D graphs, etc.
OPtoMe is able to acquire and plots the temporal development of the scintillation light yield, delivered by the photomultipliers. In the example, shown in Figure 5.8, the maximum of the light yield was observed about 560 ns after the ion passed the chamber. This time delay corresponds to the drift time of the thermalized electrons.
Based on the measured two-dimensional light emission pattern, OPtoMe determines the direction of the track of the detected ion. The application of a standard linear regression method would not be satisfactory for this purpose because the stochastic occurring δ-electron tracks of inhomogeneous structure would have a large influence on the regression line. Instead, an algorithm was developed, which manages to exclude the δ-electron tracks from the consideration. As the trajectories of the projectiles are slightly different (the collimating trigger detectors have a diameter of 1 cm), the particle track has to be calculated for each ion individually. In the example of Figure 5.8, the two lines on both sides of the track show the fit

to the ion track. Its equation is also plotted during the data acquisition; In the upper right corner of Figure 5.8 the track parameters of the ion are shown: $y = ax + b$, $1000 \cdot a = 8$ and $b = 234$.

After determining the trajectory, OPtoMe plots the longitudinal (along the track) and the transversal (orthogonal to the track) dose distributions. In the example of Figure 5.8, the contribution of the both δ-electrons and especially their endpoints to the transversal distribution is clearly recognizable in the spectrum (see lower right spectrum in Figure 5.8). These results, obtained online during data acquisition are, however, just first approximations. Clearing the images from the remaining stray light and other artefacts (see details in chapter 6) is not feasible online, during the data acquisition, due to the higher time demand for the analysis and other reasons (see chapter 6). Due to the available low-cost, high-capacity hard disks, and because the process of storing the full images did not reduce significantly the track grabbing frequency, it was decided to store the full information for each track during the beam time. This philosophy has the advantage, that the full experimental information of the track is available for the further detailed analysis.

Beside of automatic data acquisition, file handling and data analysis features, OPtoMe provides a wide range of tasks (see buttons, output- and input boxes in Figure 5.8) in order to visualize and control data acquisition, -storage, and -reload measured data, and to modify different parameters and functions affecting the track visualization or data analysis.
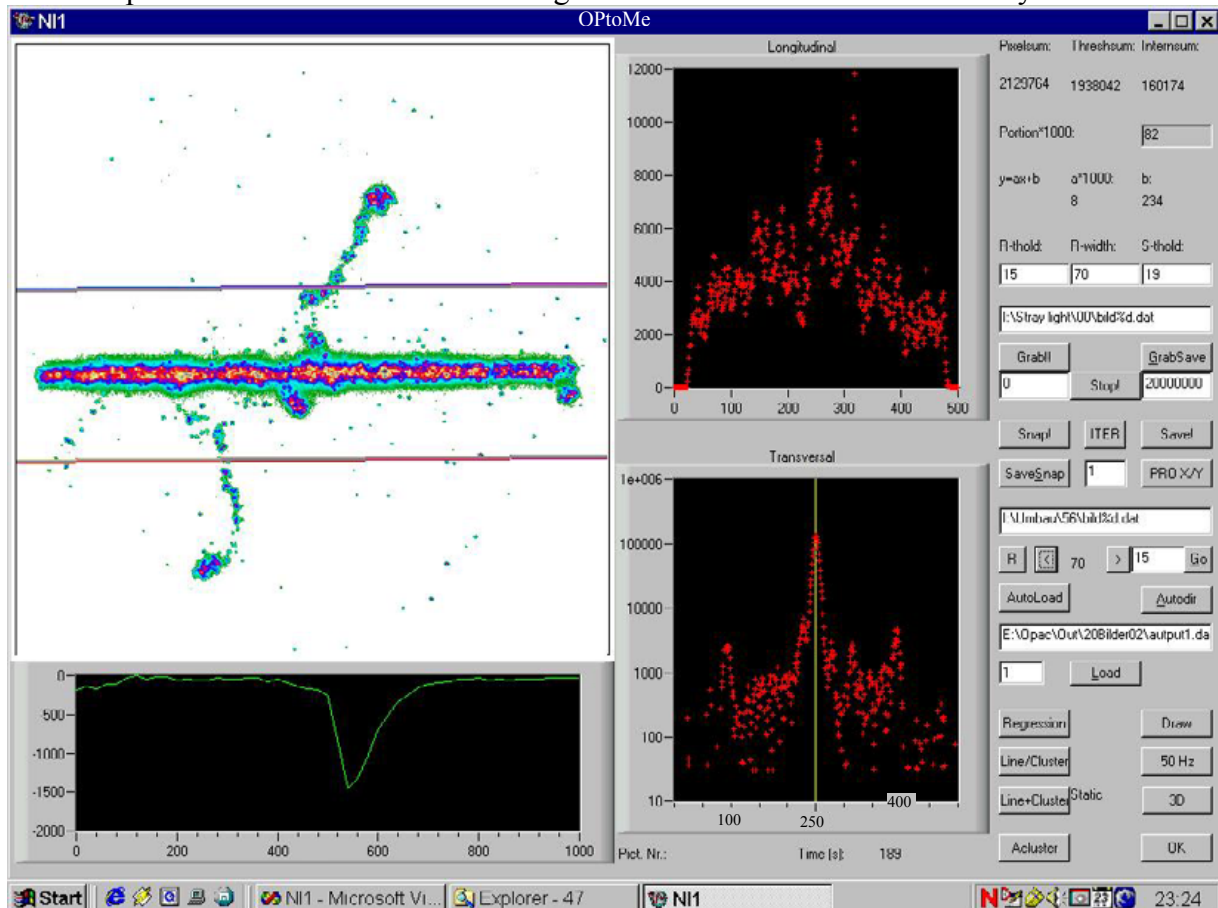


Figure 5.8: *Data acquisition with OPtoMe. The projected image of a $^{12}$C ion track is displayed in color-map coding. The longitudinal and transversal projections of the track are also plotted by OPtoMe. The temporal development of the light yield, detected by the photomultipliers, is plotted on the left downer part of the screen. Buttons, input- and output-boxes, in order to control the functions of the software, are placed on the right side.*

# 6 Experimental Techniques and Strategies of Data Analysis

The present work aims to compare measured (with OPAC) and simulated (with TRAX) radial dose distribution of different ions at various energies. It is also planned to use OPAC in the future for benchmarking other simulation codes or previous experimental data also regarding to other (e.g. stochastic) parameters of track structure within the resolution limitations of OPAC. The most important aspect with a general validity for any comparison is the fact, that both measurements and simulations merely model the physical process under investigation. Limitations and artefacts, present in the measurement or simulation method have to be taken into account when analyzing and interpreting the data. As mentioned in chapter 5.4.1, diffusion of the drifting electrons is the main limiting factor of the spatial resolution in the case of OPAC. As it will be shown chapter 6.3.3, diffusion results in a strong broadening of the radial dose distribution in the track core region, while not affecting significantly the radial dose distribution further away from the ion trajectory. There are principally two ways to ensure identical conditions for the simulated and the measured data, which is necessary for a correct comparison. The two possible approaches are the following:

1. The measured data have to be unfolded, so that the most probable locations of the thermalized $\delta$-electrons are found before diffusion took place. However, no unfolding process can regain information that was once lost through the uncertain direction and extent of diffusion. Thus, this approach has the drawback, that information on e.g. radial dose distribution from the unfolded measured data is affected by a large statistical error. In addition, if the diffusion parameters are not known exactly the systematic errors can get significant too.

2. The simulation of the particle transport has to be extended by the simulation of the response of the experimental system, which is in our case mainly diffusion in the interaction chamber. This approach has the disadvantage, that the quantities to be compared are only derivatives of the physical quantities of interest. Nevertheless, if the agreement between measured and simulated and folded data is reasonable, it can be assumed, that good agreement is also given between simulated raw data and a hypothetical measured data not suffering from diffusion. The condition of this assumption is that the diffusion in the chamber is well understood and simulated correctly. The advantage of this approach is that the folding process does not suffer from a strong increase in uncertainty due to the typically strong oscillations caused by the unfolding process. Thus, for benchmarking it is preferable to use this second approach.

Apart of diffusion also other properties of OPAC have to be taken into account for a correct comparison with simulated data by the application of one of the two approaches described above. Because of the described advantages and disadvantages of each approach the most appropriate one has to be selected for each experimental artifact under consideration. Generally, the first approach is preferred for artefacts which depend strongly on the specific measurement system and require a more complex explanation (such as stray light and single peak broadening). For artefacts where both approaches are feasible both methods will be compared. It is common to both approaches, that the comprehensive knowledge of the processes in the detector, e.g. the exact values of the diffusion parameters, is the prior condition of any meaningful comparison.

# 6.1 Simulation of ion tracks in OPAC

In order to allow for a comparison of measured and simulated data directly with the best available statistics, the TRAX code (see chapter 3.3) was applied in the most similar available setup as realized by OPAC. TRAX mostly uses water vapor cross sections obtained by semi-empirical methods. It was shown in chapter 4.1, that distances (e.g. mean free path) in TEA and in water vapor at the same density can be scaled identically, if the correspondent distances in liquid water at unit density are requested. Therefore, for the simulation of a specific measurement, made with a certain TEA pressure, simply the density of TEA has to be specified for TRAX in the input file. The gas density, the geometry of the interaction chamber, ion type and energy and its location of entering the chamber and its propagation direction are also specified to be identical with the OPAC experimental setup (see chapter 5.4.1) and the specific measurement conditions.

Figure 6.1 shows a carbon ion track at 100 MeV/u, simulated with TRAX in the OPAC geometry. The projected coordinates of the stopping locations of $\delta$-electrons are plotted (the cutoff energy was set to 13 eV in TRAX). The three images are the three projections of an arbitrary selected simulated ion track onto the *xz*, *yz* and *xy* planes, respectively. The dimensions of the three projections correspond to the dimensions of OPAC. The water vapor density, specified in the TRAX input file, is equivalent to TEA at 10 hPa pressure. No drift field, electron diffusion or imaging artefacts are included in this simulation. The *xz* projection provides a side view onto the track between the guard rings (Figure 5.5). In the *yz*-view the track is observed through the cut of the central guard ring, where the ions pass the sensitive volume. The *xy* projection corresponds to the projection viewed by the camera system of OPAC. The proportional scintillation gap has a visible area of circular shape with a diameter of 8,2 cm. The CCD camera images an area of quadratic shape with an edge length of 9 cm in the object plane. The *xy* projection shows the 8,2 cm long part of the simulated track inside the square with 9 cm edge length. In the example two high energetic $\delta$-electrons would leave the interaction chamber without being fully imaged. End points of $\delta$-electrons inside the simulated interaction volume of OPAC are also visible.

The volume, where the particle transport is simulated by TRAX extends actually beyond the dimension of the OPAC chamber. The ion transport, the $\delta$-electron production and transport is simulated also before and after this volume. The simulation in a larger volume is required, because $\delta$-electrons which are produced outside of central region of interest might penetrate and contribute to the total ionization in this volume. However, the consequences of this effect are not very significant. Therefore, a complete simulation of the OPAC chamber with all the details like the steel guard electrodes, spacers, etc. is not required. Instead, the diameter of the simulated volume of the gas-filled cylinder was extended to 11 cm – which is 0,5 cm beyond the physical volume of the chamber .
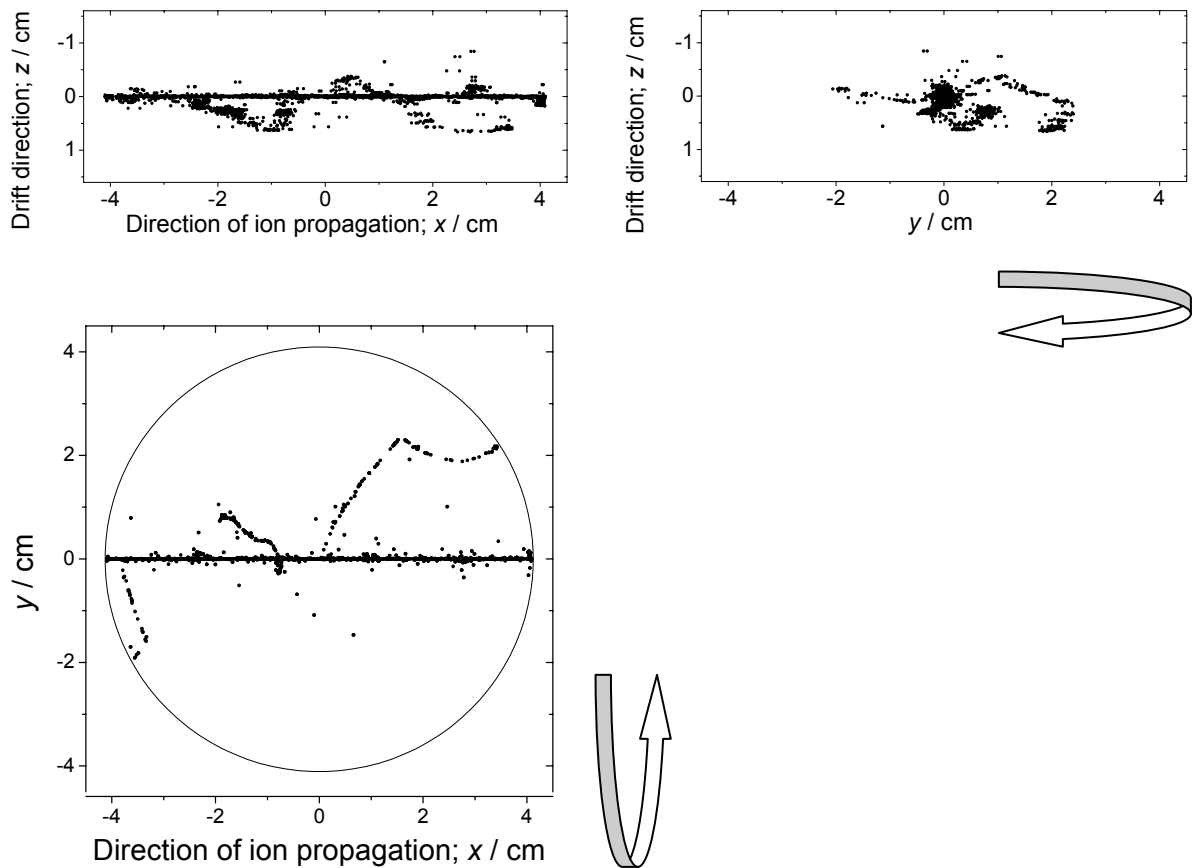
Figure 6.1: *A carbon ion track at 100 MeV/u simulated with TRAX in the OPAC geometry. The images are the three projections of an arbitrary selected ion track onto the xz, yz and xy planes, respectively. The water vapor density, specified in the TRAX input file, was the same, as that of TEA at 10 hPa pressure. The xy projection is the same one which is viewed by the CCD camera of OPAC. No diffusion or other experimental artefacts are included in this simulation.*

The presence of the homogeneous electric drift field in the interaction chamber may affect the trajectory of the fast δ-electrons emitted by the ion. TRAX simulations are performed without electric field during the traversal of the ion and the slow down of the electrons. The electron drift and diffusion simulation (see chapter 6.3) is then applied as add on to the ion track consisting of the spatial distribution of thermalized electrons produced by the energy transfers of ion and energetic electrons in an environment without electric field. In this chapter a rather phenomenological estimate will be given to the extent of the effect of an electric field present during ion and electron slow down. It will also be discussed, if the simplification is justified, that electron thermalization and drifting can be treated as two independent processes.

The inelastic mean free path of an electron at an energy of e.g. 1 keV is about 3 nm in polyethylene [Ash82]. It corresponds to a mean free path of about 0,1 mm in TEA gas at a pressure of 10 hPa. Even if its initial velocity has only a $z$-component (parallel to the drift field), the energy of the electron would decrease or increase only by 0,8 eV between 2 collisions (with a drift field strength of 80 V/cm). This value is only 2-3 % of the $W$-value ($W \approx 30$), i.e. many collisions must occur until enough additional electron energy is dissipated collected for one collision less - or more due to the electric field.

The impression, that the effect of the electric field on the electron stopping process is small can be further strengthened if the whole electron track is considered: Even if an energetic

δ-electron has its track against the field (in negative *z* direction), its energy can be reduced at most by 128 eV by the field as the track - drift cathode distance is 16 mm (Figure 5.5). If the range of the δ-electron is 16 mm, its initial energy amounts to about 4 keV [Ash82], i.e. the energy loss due to collisions is much larger that due to the field. Thus, the mean number of ionizations inside the sensitive volume (*V*) can be reduced (or increased) by the electric field by about 3% if the δ-electron endpoint is around the boundary of *V*. If the initial δ-electron energy is higher, the presence of the electric field results, merely, in a slight variation in the electron energy. The number of ionization events in *V* is affected only slightly by the slightly different LET-path function. Hence, we can conclude, that the relatively weak electric field in the interaction volume plays a minor role during the electron stopping process.

The effect is definitely negligible if taking into account, that the images are projections, where electron tracks that propagate into the opposite z-direction are added together. Thus, including the homogeneous electric field into the TRAX simulations or trying to unfold the measured images to eliminate its effect is not necessary.

Another important aspect to get a feeling for the typical characteristics of the particle transport inside *V* is the time scale of the various processes following an ion transit through the chamber. An ion with a specific energy of e.g. 100 MeV/u has a velocity of about 130 000 km/s, which can be treated as constant inside the chamber. The time required for the ion to pass *V* is less, than 0,8 ns. Even the slowest ions with an energy of 4,3 MeV/u which were measured with OPAC in this set of measurements needed less than 3 ns for the traversal. The transport and thermalization of the produced δ-electrons down to energies of about 10 eV (where no further ionization can take place) does not take more than 10 ns either.

Let us compare these typical stopping time values with the time, needed for the electron drift: The drift velocity of the electrons in the interaction volume, in TEA at 10 hPa at a reduced drift field strength of 8 V/cm/hPa was measured to be 5 μm/s [Tit98]. Thus, the total drift time at 10 hPa gas pressure is about 300 ns, which is much longer than the time needed for the transit of an ions and the thermalization of the ionization electrons. This consideration gives a further justification for the simplification, that the processes of electron thermalization and electron drift can be treated separately, in succession.

## 6.2 Calculation of the radial dose

OPAC images the *xy* projection of the particle tracks in the standard operation mode. There are, essentially, two possibilities to achieve dose distribution information along the third, *z*, coordinate. The first possibility is to pulse the photocathode of the IICCD with very short (10-20 ns) pulses following a variable delay time after the trigger signal. In this case, only electrons from a z-window with a drift time determined by the delay and width of the gate pulse contribute to the image. The gating was realized by a self-made computer programmable gate and delay electronics and a high-voltage gate pulser with a variable length in the range of 20 ns- 3μs) connected to the intensifier photo cathode. This feature of OPAC was not applied yet in a comprehensive measurement program, although it was tested with reasonable success. The method has several limitations:
1. In spite of collimating the ion beam by two trigger detectors before and behind the OPAC interaction chamber (Figure 5.1), the ions pass the chamber with a certain directional spread. A slight deviation in *z* of 5 mm results in a shift in the third coordinate of 200 nm in liquid water. This problem could partly be controlled by the photomultiplier signal, which delivers an independent information on the actual ion track position.

2.  The drift time of an electron is also influenced by longitudinal diffusion which adds an uncertainty to the arrival time of the order of a few 10 ns in the present OPAC geometry (for more information of this effect see [Tit99].
3.  The precision of the timing electronics is limited by the time base of the delay generator to about 10 ns.

Because of these problems an unfolding method was chosen to derive the real radial dose distribution, $d_r$, from the measured projected data. The measurements were performed in standard operation mode, i.e. the scintillation light of all drifting electrons from the entire interaction volume was collected by applying a sufficiently long gating pulse. The unfolding method can be explained best on a simulated example.
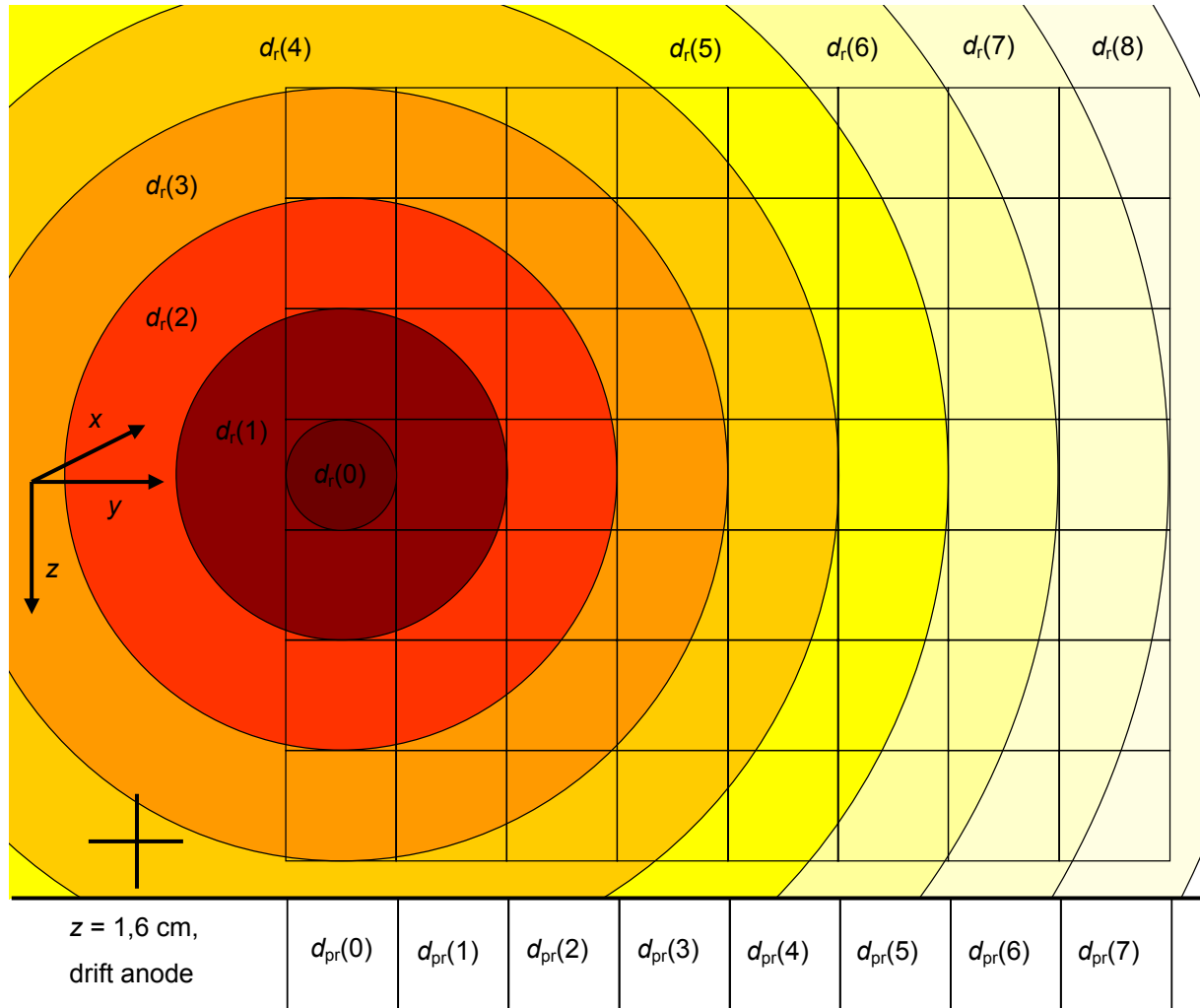


Figure 6.2: *The illustration shows the central region of the yz plane (around y = 0 and z = 0), where the track traverses the chamber. Darker colors correspond to higher local doses. The interaction chamber is divided into cubes with edge lengths corresponding to the edge length of a square corresponding to the size of one CCD pixel. The projected radial dose values, $d_{pr}(0)$, $d_{pr}(1)$, etc. can be constructed as a linear combination of the discretized radial dose values, $d_r(0)$, $d_r(1)$, etc...*

As $d_r(r)$ is a deterministic quantity it is reasonable to perform unfolding not to the single ion tracks, but to the average of many tracks. Furthermore, there is no need for an unfolding of the two dimensional images on a pixel-by-pixel basis, it is sufficient to unfold the "projected" radial dose distribution, $d_{pr}(y)$, a further deterministic quantity. $d_{pr}(y)$ is defined here as the average dose distribution of many tracks as a function of distance from the track core, after its

two-dimensional projection onto the imaging plane of OPAC. For a first demonstration, the effect of diffusion is not taken into account, hence, $d_{pr}(y)$ can be fully determined by to the $y$ coordinates of the electron stopping locations without considering their $x$ and $z$ coordinates. In the presented example 4000 carbon ion tracks were simulated in OPAC geometry and $d_{pr}(y)$ is derived from the projected tracks. $d_r(r)$ is calculated by unfolding of $d_{pr}(y)$ with the method described in this chapter.

Figure 6.2 illustrates the discretized $d_r(r)$ with the maximal average dose value at $(y,z) = (0,0)$. Darker colors symbolize higher dose values, after summing over many tracks and averaging over the areas of the rings which received hits. The rings have a radius of one pixel, corresponding to 7,5 nm in water at unit density under the simulation conditions (corresponding to 10 hPa TEA pressure). As diffusion is neglected, $d_{pr}(y = c)$ is a linear combination of $d_r(r = c)$, $d_r(c+1)$,.., $d_r(c+i)$,…, $d_r(c+ i_{cmax})$, where $c$ is a selected distance in pixels ($0 <= c <= 200$; $c = 0$ is used for an easier denotation, the average distance in the central cylinder is larger, than zero). A coefficient, $A_c^{c+i}$ of the $d_r(c + i)$ variable in the $(c+1)^{th}$ row accounts for the relative contribution of the area of $d_r(c + i)$ to $d_{pr}(c)$. In the example of Figure 6.2 this is the common area of the $(c + i)^{th}$ colored ring and the $(c +i+1)^{th}$ column (the index of the first column is 0).

OPAC delivers statistically useful information up to $y \approx 200$ pixels ($= 1,5$ µm $\rho = 1$ g/cm$^3$; 10 hPa). The $z$-range of the chamber corresponds to 2 x 89 pixels. Thus, the most distant $d_r$-ring with a contribution to $d_{pr}(y)$ is at $(c + i)_{max} = 200 + i_{200max} =$ round$\left(\sqrt{89,5^2 + 200,5^2}\right) = 220$. Thus, the solution of the unfolding problem is the solution of the following linear equation system consisting of 220 equations:

$$A_0^0 d_r(0) + A_0^1 d_r(1) + \ldots + A_0^{90} d_r(0 + i_{0\,max}) \qquad = d_{pr}(0)$$
$$A_1^1 d_r(1) + A_1^2 d_r(2) + \ldots + A_1^{1+i_{1\,max}} d_r(1 + i_{1\,max}) \qquad = d_{pr}(1)$$
$$\vdots \qquad\qquad \vdots$$
$$A_c^c d_r(c) + A_c^{c+1} d_r(c+1) + \ldots + A_c^{c+i_{c\,max}} d_r(c + i_{c\,max}) \qquad = d_{pr}(c)$$
$$\vdots \qquad\qquad \vdots$$
$$A_{200}^{200} d_r(200) + \ldots + A_{200}^{200+i_{200\,max}} d_r(200 + i_{200\,max}) \qquad = d_{pr}(200) \qquad\qquad (6.1)$$

$$d_r(201) - d_r(202) \qquad\qquad\qquad = 0$$
$$d_r(201) - d_r(203) \qquad\qquad\qquad = 0$$
$$\vdots \qquad\qquad \vdots$$
$$d_r(201) - d_r(220) \qquad\qquad\qquad = 0$$

where:

$$i_{0\,max} = \text{round}\left(\sqrt{89,5^2 + 0,5^2} - 0\right) = 90$$
$$i_{1\,max} = \text{round}\left(\sqrt{89,5^2 + 1,5^2} - 1\right) = 90$$
$$\vdots$$
$$\qquad\qquad\qquad\qquad\qquad\qquad\qquad\qquad\qquad (6.2)$$
$$i_{c\,max} = \text{round}\left(\sqrt{89,5^2 + (c+0,5)^2} - c\right)$$
$$\vdots$$
$$i_{200\,max} = \text{round}\left(\sqrt{89,5^2 + 200,5^2} - 200\right) = 20$$

$i_{cmax}$ is the number of rings contributing to the $(c+1)^{th}$ projected radial dose value. $A_c^{c+i}$ coefficients can be easily determined as a subtraction of two definite integrals. For example $A_0^0$ is the whole dark red area:

$$A_0^0 = 0,5^2 \pi = 0,785$$

or $A_2^3$ is the intersection area of the third ring (fourth color) and the third column:

$$A_2^3 = 2\left(\int_{1,5}^{2,5}\sqrt{3,5^2 - y^2}\,dy - \int_{1,5}^{2,5}\sqrt{2,5^2 - y^2}\,dy\right) = 2,905$$

The last nineteen equations indicate that the solution cannot be unambiguous as there are more "rings" than projected radial dose values. Thus, a prior assumption has to be applied to construct a correlation between the last twenty real radial dose values. However, due to the relatively flat interaction chamber (see Figure 5.5) and due to the typically quite flat radial dose distribution between 200 and 220 pixels distances, the practice shows, that the solution is hardly sensitive to slight variations of the prior assumption. In the example of Figure 6.2, the radial dose distribution was assumed to be simply constant between distances of 200 and 220 pixels. A variation of this assumption influences the resulting radial dose significantly only for about $r > 190$ pixels.

The linear equation system is solved by the software "Linear algebra 2" (www.numericalmathematics.com), after creating the coefficient matrix in an MS Excel table.
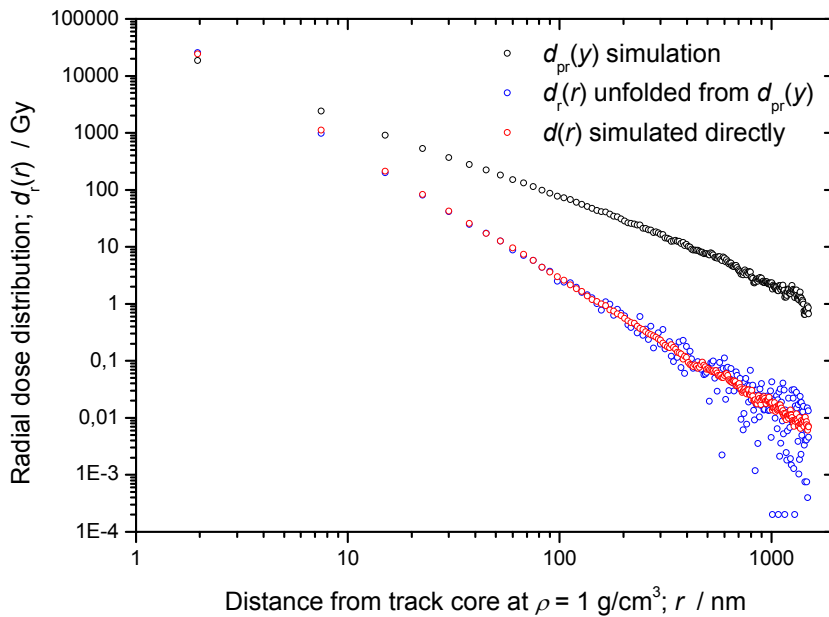


Figure 6.3: *Simulated projected radial dose distribution, $d_{pr}(y)$, in OPAC geometry and the radial dose distribution unfolded from $d_{pr}(y)$ compared to the directly simulated radial dose distribution. The unfolded $d_r(r)$ function suffers from large oscillations due to unfolding process. Four negative values are set (arbitrary) to $2\cdot10^{-4}$ in order to be able to plot them in log-log scale. The absolute dose specifications refer to the real radial dose functions and not to the projected radial dose distribution. $d_{pr}(y)$ is presented only as an illustration to show its different slope; the definition of local dose would not have a physical meaning in this case.*

To benchmark the accuracy and reliability of the unfolding method, a second set of simulated tracks was generated in a cylindrical geometry, where the tracks traverse the cylinder along its axis. The real radial dose, $d(r)$ is then determined directly without unfolding but discretized

into the same one-pixel-thick rings, as the unfolded $d_r(r)$. Figure 6.3 shows that the projected distribution, $d_{pr}(y)$, (black symbols) drops much weaker than the radial dose distribution. After the unfolding (blue symbols) $d_r(r)$ resembles nicely the same $1/r^2$ character (in agreement with the theory: chapter 2.7.3) as the directly simulated $d(r)$ (red symbols).

The main drawback of the projection-unfolding technique is obviously the occurrence of oscillations in the solution at large distances from the track core. The oscillations in $d_r(r)$ are much stronger than those in $d(r)$. Although, 4000 ion tracks were simulated for the derivation of $d_{pr}(y)$ and thus, $d_r(r)$ distributions, while only 1000 tracks for the calculation of $d(r)$. The original projected data have significant fluctuations at large $y$-values, because only a few $\delta$-electrons have such long tracks inside the narrow chamber. The relatively small fluctuations are necessarily amplified by any unfolding technique. Unfortunately, a typical measured $d_{pr}(r)$ function has larger initial fluctuations, than the simulated function, because less than 4000 ions are tracked with a single electron detecting efficiency below one. Therefore, a binning of data points is required for large radial distances prior to the application of the unfolding process. In order to preserve the data structure, a moving average filter is applied to the data set above an $y$-distance of 15 pixels instead of binning. Three data points were involved into the average building at $15 < y < 50$ pixels, five data points at $50 < y < 110$ pixels, and nine data points at $110 < y < 200$ pixels. The applied smoothing does not influence the character of the curves, the changes in integrals over e.g. 20 data points are negligible.

If the described smoothing is applied on $d_{pr}(y)$ before the unfolding process, an excellent agreement is observed between $d_r(r)$ and the directly simulated $d(r)$ (see Figure 6.4). As a consequence, the method of smoothing and unfolding, as described in this chapter, must also be applicable to the analysis of the experimental data and the derivation of the experimental radial dose distributions. The slight discrepancies between the red and blue curves for $r < 3$ pixels are due to the fact, that the discretization influences $d_{pr}(y)$ and $d_r(r)$ distributions in a slightly different way. This effect is negligible at larger distances from the track core due to the smaller gradients in $d_r(r)$. The slight discrepancies for larger $r$ values are of random nature, primarily due to the fact, that two independent sets of ion tracks were simulated for the determination of $d_{pr}(y)$ and $d(r)$ functions.
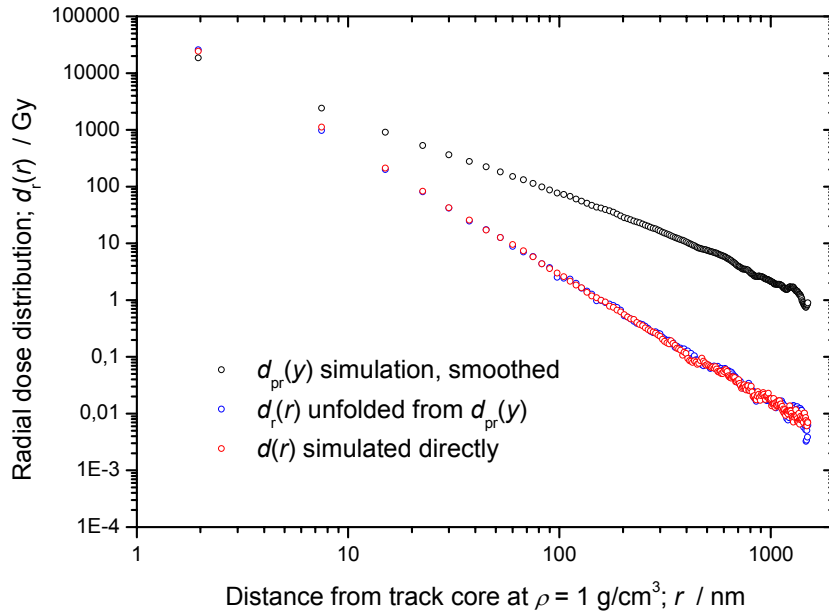
Figure 6.4: *The same comparison as shown in Figure 6.3, but the described smoothing process (see text) is applied to the projected radial dose distribution.*

# 6.3 Diffusion of the drifting electrons

## 6.3.1 Measurement of the diffusion

As denoted in the introduction of chapter 6, the precise knowledge of the extent of electron diffusion is essential for the comparison of simulated and measured tracks or track parameters. For the present application the best parameter to measure the influence of diffusion is the one-dimensional root-mean-square diffusion distance, $\sigma_{pr}$ (projected radial). According to equation (5.1), if its value is known for a given drift distance, $z_d$, and a given pressure, $p$, the extent of diffusion can be derived for any other $z_d$' and $p$', if the same reduced electric field is applied. $\sigma_{pr}$ for a drift length of 10 cm, a pressure of 10 hPa was measured by Titt et al. ([Tit98], [Tit99]) as a function of the reduced electric field. Because of the central importance of this parameter this measurement was repeated with the improved OPAC system.

The experimental setup was similar to the one used by Titt [Tit98]; the mesh as drift cathode in OPAC was replaced by an aluminum plate with a small aperture (0,1 mm in diameter). The cathode-anode distance was 42 mm. The aperture was hit by laser pulses (nitrogen laser, emission wavelength, $\lambda = 337$ nm, 3 ns pulse duration). Single photoelectrons produced by the laser in the Al wall of the aperture were transferred by the electric field through the drift zone into the charge and light amplification region. To assure single electron injection, the laser intensity was adjusted such that only one out of 10 laser pulses resulted in a free electron inside the drift region. The single-electron introduced scintillation locations were then recorded by the optical system (in these measurements only the new lens was available, the new image intensifier was not yet available. Only those images were used in the analysis, which contained well-defined single peaks as image of a single electron.

The measurement results are collected in Figure 6.5, where $\sigma_{pr}$ values are scaled for a chamber with a drift length of 10 cm filled with TEA gas at a pressure of 10 hPa. The new results for $\sigma_{pr}$ are significantly lower, than the results presented by Titt et al. [Tit98]. Especially the sharp increase in diffusion at very low field values could not be confirmed. The efforts to find a reason for these discrepancies did not lead to success. However, if the simulated data is folded with a diffusion using the older values, a strong overestimation of track broadening can be observed if compared to the recently measured data. Therefore, the results of the new measurements are accepted as valid for the improved OPAC.
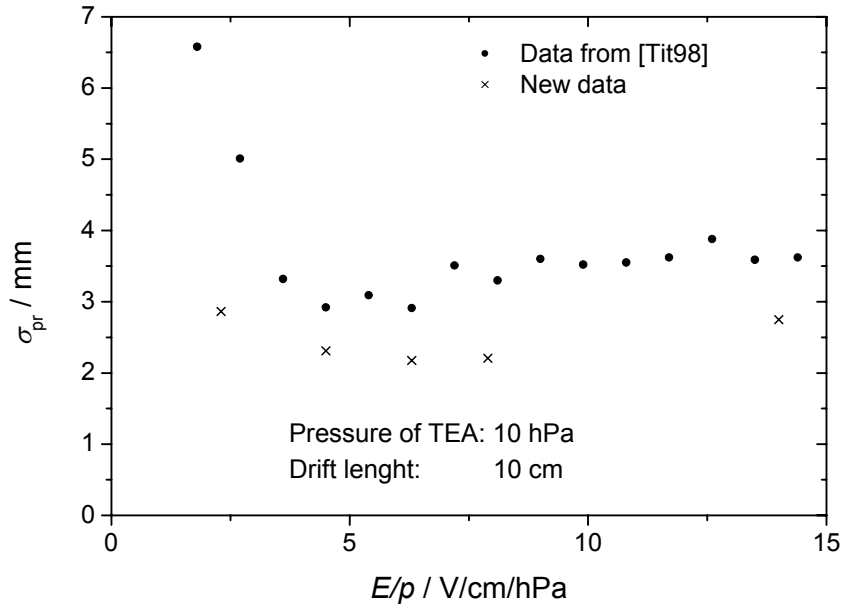


Figure 6.5: *One-dimensional root-mean-square diffusion distances as a function of the reduced electric field. The old data of Titt et al. Is compared to new measurements with the new system. All data are scaled for a drift length of 10 cm at a TEA pressure of 10 hPa.*

A major goal for the measurements of the ion tracks was the effort to reduce the effect of diffusion as much as possible. Therefore, the reduced electric field was chosen to be in the diffusion minimum of app. 5 V/cm/hPa (see Figure 6.5). At this reduced electric field, the value of the diffusion distance, if related to standard distance and pressure (10 cm and 10 hPa, respectively) is:

$$\sigma_{prs} = 2,2 \text{ mm} \tag{6.3}$$

The broadening of the radial dose distribution underlies the two-dimensional root-mean-square diffusion distance, $\sigma_{rs}$ "radial, standard" instead of the one-dimensional $\sigma_{prs}$ diffusion distance.

$$\sigma_{rs} = \sqrt{2} \cdot \sigma_{prs} = 3,11 \text{ mm} \tag{6.4}$$

The extent of the radial diffusion in the present chamber assembly (with a drifting distance of 1,6 cm) can be derived at any gas pressure according to the equations (5.1) and (6.4). The result can be expressed in pixels in the image (with equation (5.2)) or in simulated distance at a density of unity (5.3). E.g. at a gas pressure of 10 hPa the two-dimensional (radial) root-mean-square diffusion distance, $\sigma_{r\_10hPa}$, amounts to:

$$\sigma_{r\_10hPa} = \sigma_{rs}\sqrt{\frac{1,6cm}{10cm}} = 1,24mm \xrightarrow{\cdot 5,56pixels/mm} 6,89pixels\ (in\ the\ image)$$

$$\xrightarrow{\cdot 7,5nm/pixels} 52nm\ (at\ \rho = 1g/cm^3)$$

(6.5)

Similarly, at gas pressures of 4 and 40 hPa the radial diffusion distance amounts to:

$$\sigma_{r\_4hPa} = \sigma_{r\_10hPa}\sqrt{\frac{10cm}{4cm}} = 1,96mm \xrightarrow{\cdot 5,56pixels/mm} 10,9pixels \xrightarrow{\cdot 3nm/pixels} 33nm$$

(6.6)

$$\sigma_{r\_4hPa} = \sigma_{r\_10hPa}\sqrt{\frac{10cm}{40cm}} = 0,62mm \xrightarrow{\cdot 5,56pixels/mm} 3,45pixels \xrightarrow{\cdot 30nm/pixels} 103nm$$

## 6.3.2 Folding of the simulated tracks with the effect of electron diffusion

Folding of the simulated ion tracks with the effect of electron diffusion is carried out by a small Monte-Carlo routine, implemented into OPtoMe (which includes the code for the analysis of the simulated data). The polar form of the Box-Muller transformation provides two independent random numbers chosen from a normal distribution:

If $u_1$ and $u_2$ are uniform on (-1,1), $v_1$, $v_2$ and $r^2$ are constructed as follows:
$v_1 = 2u_1 - 1$
$v_2 = 2u_2 - 1$
$r^2 = v_1^2 + v_2^2$
New random numbers are generated, if $r^2 > 1$. If $r^2 < 1$, then

$$n_1 = v_1\sqrt{\frac{-2\ln r^2}{r^2}} \qquad and \qquad n_2 = v_2\sqrt{\frac{-2\ln r^2}{r^2}}$$

(6.7)

are independent numbers from a normal distribution. Thus, if the stopping coordinates of an electron are ($x_0$, $y_0$, $z_0$), the corresponding coordinates after drifting to the drift anode and diffusion ($z = 1,6$ cm) at a gas pressure of $p$, are the following:

$$x' = x_0 + \sigma_{prs}n_1\sqrt{\frac{1,6cm - z_0}{10cm}}\sqrt{\frac{10hPa}{p}}$$

$$y' = y_0 + \sigma_{prs}n_2\sqrt{\frac{1,6cm - z_0}{10cm}}\sqrt{\frac{10hPa}{p}}$$

(6.8)

$$z' = 1,6cm$$

Figure 6.6 shows an example for the effect of electron diffusion. In Figure 6.6 b) the electron coordinates are calculated according to (6.8) from the initial coordinates of Figure 6.6 a). The example shows the same simulated track as Figure 6.1 ($^{12}$C at 100 MeV/u, $p = 10$ hPa).
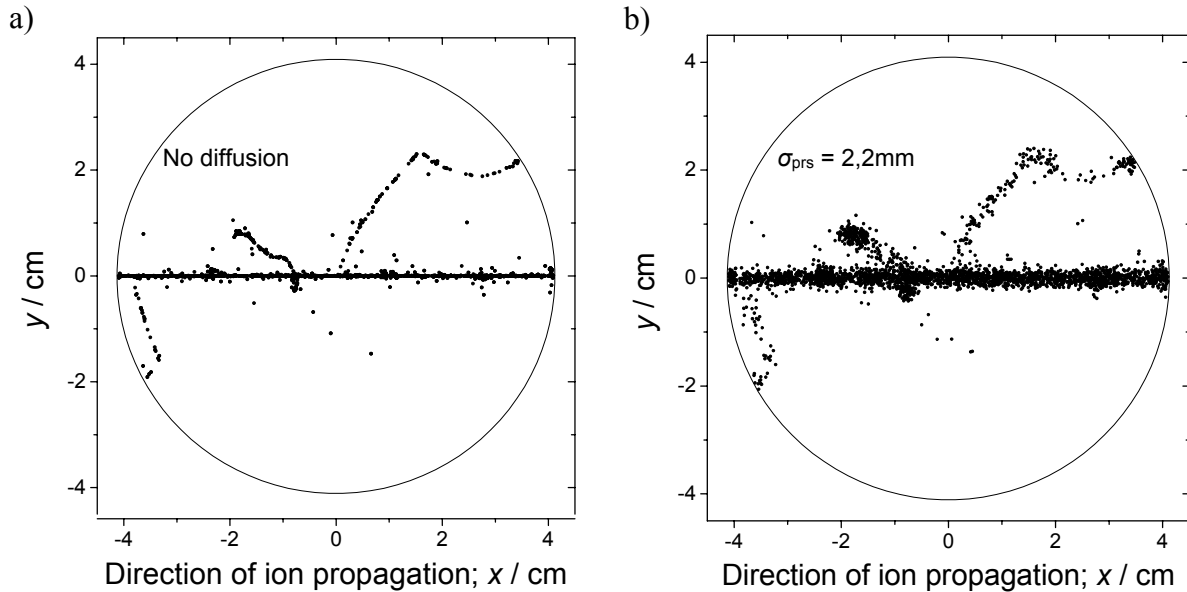
Figure 6.6: *The xy projection of an ion track a) without the effect of diffusion b) folded by the electron diffusion observed in OPAC. The example shows the same simulated track as Figure 6.1 ($^{12}C$ at 100 MeV/u, p = 10 hPa).*

## 6.3.3 Influence of diffusion on the radial dose distribution

The effect of electron diffusion in the chamber on one simulated ion track was shown in chapter 6.3.2. If $d_{pr}(y)$ is derived from a set of measured tracks, the resulting distribution is affected by diffusion as well. Let us introduce the "_d" flag in the subscript of a function, if the data is affected by diffusion: $d_{pr\_d}(y)$. The same unfolding method, as described in chapter 6.2 can be used on the broadened $d_{pr\_d}(y)$ distribution in order to derive the "diffused" but not projected radial dose distribution, $d_{r\_d}(r)$. It has to be noted at this point, that this latter quantity is rather artificial. The phenomenon of diffusion is merely a side effect of the projection, thus no diffusion would occur, if the projection was not necessary for the imaging. Nevertheless, it is useful to proceed in this way, because this "hypothetical" diffused radial dose distribution is a good compromise to compare measured and simulated data with each other (see comments on this issue in the introduction of chapter 6).

Figure 6.7 illustrates, that the $d_{r\_d}(r)$ distribution can be regarded as a radial dose distribution of Gauss-broadened ion tracks, whereas the same $\sigma_{pr\_1,6cm}$ is applied for all three coordinates of all $\delta$-electron stopping locations. As if the whole track was drifted uniformly by 1,6 cm and the electrons suffered from the same diffusion parallel to the electric field as orthogonal to it. $d_{\_d}(r)$ is the diffused radial dose distribution determined after this uniform broadening without the projection step. In Figure 6.7 the $d_{r\_d}(r)$ distribution is simulated and subjected to the same unfolding procedure, which will be applied also to the measured data:
1. 6000 tracks are simulated, whereas the boundary conditions obey the OPAC geometry (see chapter 6.1)
2. The thermalized electrons are diffused as described in chapter 6.3.2. Thus, in contrary to $d_{\_d}(r)$, the drift distance of the electrons varies according to their original z-coordinate.
3. The average projected radial dose distribution, $d_{pr\_d}(y)$, is derived.
4. The diffused radial dose distribution, $d_{r\_d}(r)$, is determined with the unfolding technique, described in chapter 6.2.

The principal difference between the plotted $d_{r\_d}(r)$ and $d_{\_d}(r)$ distributions is the varied and uniform drifting distance, respectively. There is a further difference in their origin: no projection and unfolding were applied for $d_{\_d}(r)$, it was derived directly with axial symmetric (with $x$ as an axis) boundary conditions. Despite these differences, there is no significant deviation between the two curves (smoothing was applied on $d_{pr\_d}(y)$ before unfolding). Thus, the application of the (6.1)-(6.2) unfolding technique can be justified for the measured data including diffusion as well.
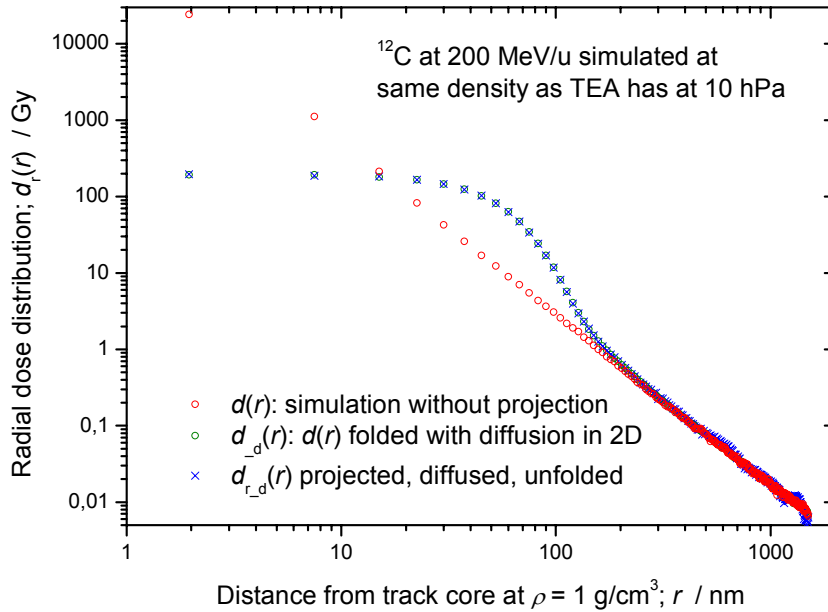


Figure 6.7: *Effect of diffusion on the radial dose distribution. The data drawn in blue crosses were generated under experimental conditions present in OPAC (including diffusion). After radial unfolding they are in good agreement with the data denoted in green circles, which were generated in axial symmetric geometry (with its axis along the ion trajectories).*

Figure 6.7 also demonstrates the effect of diffusion on the radial dose distribution. The $1/r^2$ characteristics of $d_r(r)$ is not influenced by the diffusion significantly above a $r$-distance of about 150 nm from the track core. According to equation (6.6), the value of 150 nm corresponds to about $3 \cdot \sigma_{r\_10hPa}$ at the gas pressure of 10 hPa. At an $r_0$ below about 100 nm ($\approx 2 \cdot \sigma_{r\_10hPa}$) the radial dose distribution is clearly dominated by electrons, which are drifted to the region of $r_0$ from the close neighborhood of the track core (i.e. noise), while the ratio of electrons which were really stopped in the region of $r_0$ (i.e. signal) is very small. The smaller we select $r_0$, the lower the signal to noise ratio. The low signal to noise ratio for low $r$ is, basically, due to the very steep drop in the $d_r(r)$ distribution. As a consequence, the measurement results deliver valuable data for the searched $d(r)$ distribution only above a radial distance of $3 \cdot \sigma_r$. According to the equations (6.6) and (6.6), the lowest $\sigma_r$ is expected at the gas pressure of 4 hPa and its value is $\cdot \sigma_{r\_4hPa} = 33$ nm (scaled to $\rho = 1$ g/cm$^3$) - i.e. the lower limit of $r$, where the measured $d(r)$ values are not significantly affected by the effect of diffusion, is about 100 nm. Nevertheless, in chapter 7 we show the comparison of the measured and simulated results in the whole measured region of $r$, down to $r \approx 3$ nm. For $r < 100$ nm, the comparison is based on simulations that include the effect of diffusion ($d_{\_d}(r)$ or $d_{r\_d}(r)$). However, the generally observed good agreement indicates that the main physical processes behind the ion and electron transport and the electron diffusion cannot be strongly misunderstood, due to the low signal to noise ratio the data is weak to claim that the

simulations are in agreement with the measurements down to 3 nm. In chapter 9 we show a few possible further improvements on OPAC to reduce this problem concerning the diffusion of the drifting electrons.

## 6.4  Transport of electrons instead of positive ions

Relating to the Harwell cloud chamber (see chapter 4.5) it was already mentioned, that the detection of the positive ions from the ionization process would be of great advantage if we compare it to the imaging of the diffused electrons. In addition to the negligible effect of diffusion of the heavy positive ions, the location of the positive ions corresponds to the true locations of ionization events. With TRAX it is possible to simulate the distribution of the electrons and the ions in the particle track and to compare both distributions..
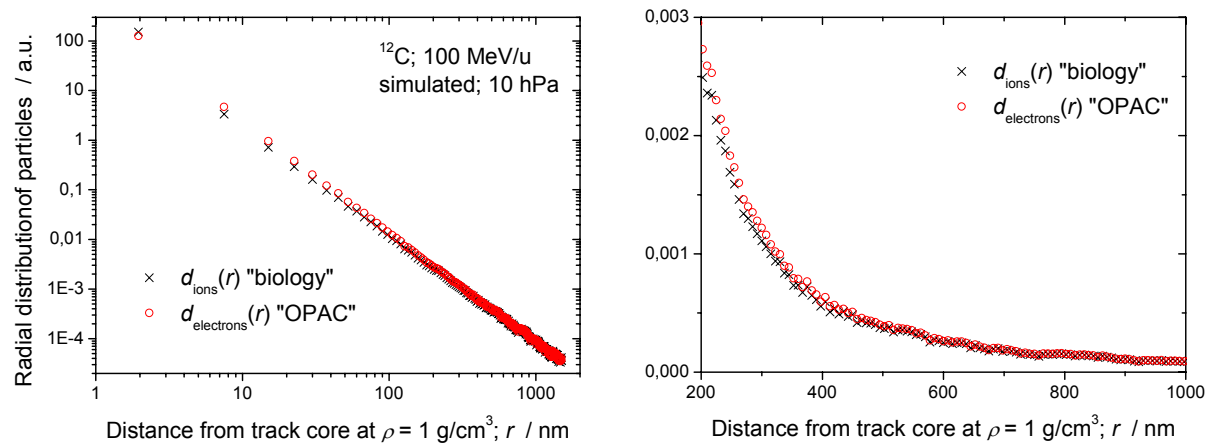


Figure 6.8: *Radial distribution of the position of the ionization events (ion distribution) and that of the locations of the thermalized electrons. The left diagram provides a comparison on a log-log scale. The right diagram shows the same comparison on a lin-lin scale above 200 nm distance from the track core.*

Figure 6.8 shows the comparison between the two simulated data sets on two different scales. As expected, the radial distribution based on the locations of electrons is slightly broader than that based on ions. The relative discrepancies amount to 20-30% below a simulated distance from the track core of about 80-100 nm. The discrepancies drop significantly below 10% above a simulated distance of 350 nm and below 5% above 700 nm. For our comparison with the experimental data the simulation was made with the stopping locations of the electrons. The comparison above implies that both, the presented OPAC and TRAX data, suffer from a systematic error which depends on the distance from the track core. Due to the different magnification at different pressure the measurements and simulations at 4 hPa gas pressure are more affected by this effect then the data obtained at higher (e.g. 40 hPa) TEA pressure.

## 6.5  Handling of peak broadening

### 6.5.1 Treatment of the halo in the IICCD response function

So far in this chapter it was assumed, that the projected, diffused $x$ and $y$ coordinates of the thermalized $\delta$-electrons can be determined unambiguously. However, as already indicated in

chapter 5.4.1 and 5.4.2, not only the gas-filled chamber but also the IICCD imaging system has artefacts influencing significantly e.g. the radial dose distribution. It was shown in chapter 5.4.2, that the new image intensifier has a much larger and better defined pulse-height distribution for single photoelectrons (see Figure 5.2 and Figure 5.7). But also the single electron peaks of the new image intensifier suffer from a geometrical broadening. While in the center region of the peak the intensity, $I(x,y)$, drops sharply (see Figure 5.6 b)), but they have very broad tails that surmounts the background clearly; on an average even at a distance of 20-30 pixels away from the center of the peak.
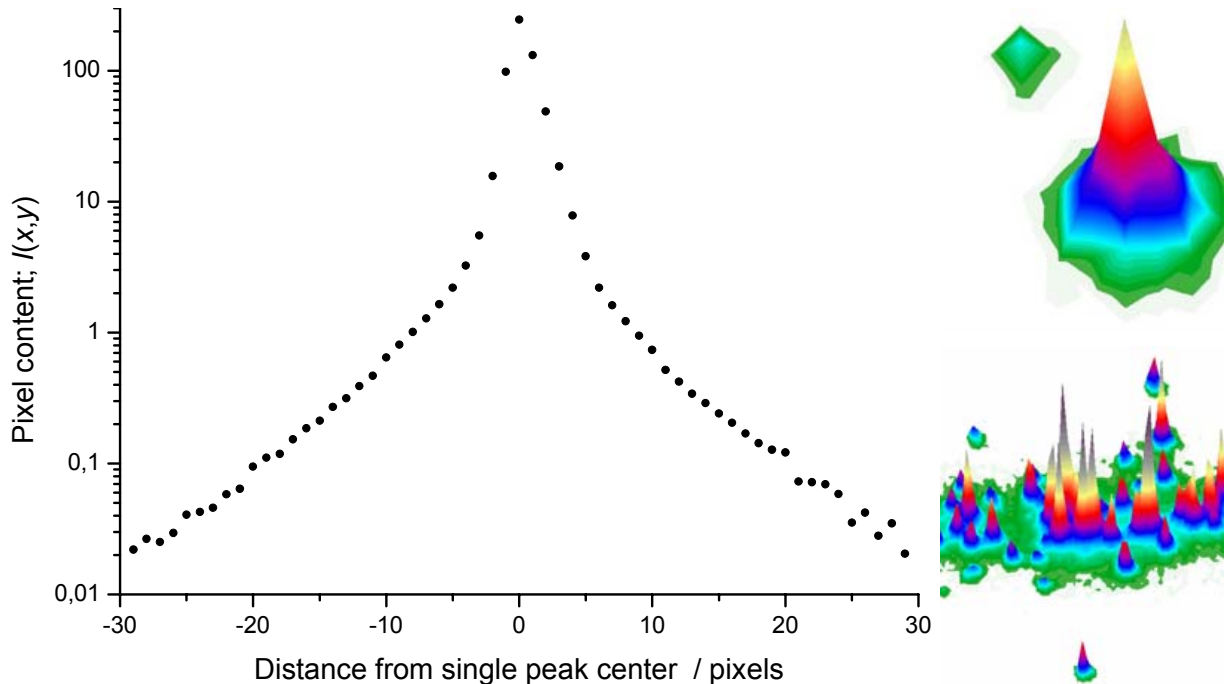


Figure 6.9: *Average shape and height of single photoelectron peaks along their central section. As an illustration, two arbitrary selected single peaks (with very different heights) are shown in the right upper corner. The segment of an ion track in the right lower corner illustrates, that an increased (green) halo surrounds the track due to the superposition of many individual, low intensity but far ranging single peak halos.*

Figure 6.9 shows the average shape and height of the single peaks at the typical high voltage level applied to the MCP. Data of nearly 15000 single peaks was taken into account for the derivation of this plot. The calculation was carried out with the full 2-dimensional data set. The plot shows the shape along a central section (i.e. it is not a projection of a full, axial symmetric peak to an axis). According to Figure 6.9 the height of the peak drops below 10% of its maximum value within distance of 1-2 pixels and below 1% within 4-5 pixels. This effect would be negligible compared to the broadening due to the electron diffusion, if the pixels further away were not affected. But the gradient of the decay decreases and even at a radial distance of 30 pixels from the center of a single peak a measurable contribution can be observed. At the first glance, the small contribution in the halo of less than 0,1% of the peak value at a radial distance of 15 pixels seems to be negligible. In reality, however, it turns out that this is not the case:

1. The overall contribution at a distance of e.g. $r = 15$ pixels is increased largely by the multiplication with the surface of the contributing area (which is proportional with $r^2$).
2. The high ionization density along the ion trajectory results in a high spatial density of single peaks, and the pile-up of the halo of many singe peaks eventually results into an extended halo on both sides of the tracks. This emerges as a green surrounding, if using the typical color plate of the data acquisition software (see track segment in the

right lower corner of Figure 6.9). The result can be interpreted as an increased local IICCD background in the regions, where the ionization density is high. As a consequence, the shape of the radial dose distribution would be distorted, if this effect would not be taken into account accurately.

Theoretically, the distorting effect does not arise necessarily. Namely, the same tails are also present around individual single peaks that are typical observed further away from the ion track core. If the data acquisition system is able to measure the very low background around each individual peak to the same extent as it measures the "green" background of many superposed single peaks around and inside the track core, than no bias would occur. The reason that inhibits this approach is the fact, that due to pixel statistics and CCD noise a threshold is required to accept a pixel value as valid.. At a given, large distance from the track core there is only one pixel out of many hundred or thousand, that contains real information. But if the content of each pixel would be summed up at that distance, the sum of the many low noise contributions would overlap -or at least get comparable- with the real content of the single pixel. Like diffusion, the effect of the overlapping halos of a multitude of single peaks causes a broadening of the track. Though the halo is less in magnitude than diffusion it is more difficult to treat mathematically, because it does not follow a Gaussian distribution which is easier to treat in appropriate unfolding codes.

## 6.5.2 Application of a simple threshold method

The problem of CCD camera noise can be eliminated and that of the track broadening by the above described halo can be reduced by the application of a threshold. However, applying a threshold involves a distorting effect which is illustrated in Figure 6.10. The red peak represents a single peak isolated from its neighborhood. If e.g. a threshold of 30 is applied, the pixel values of the ten central pixels of an average peak contribute to the result. (Not nine but ten (3 x 3 + 1) because the peaks are slightly asymmetric; Figure 6.10 plots the asymmetric cross section of the peak with four pixels above the threshold.) In the case of overlapping peaks, the halos around each peak pile up and rise eventually above the threshold level. Therefore, in the central region of the image, where the ionization density is high, the overlapping halos add up and contribute significantly to the result even after applying a threshold. The most severe consequence of this effect is, that it affects the central part of the track stronger than the regions further away from the track with rather sparsely ionization and thus isolated single peaks.
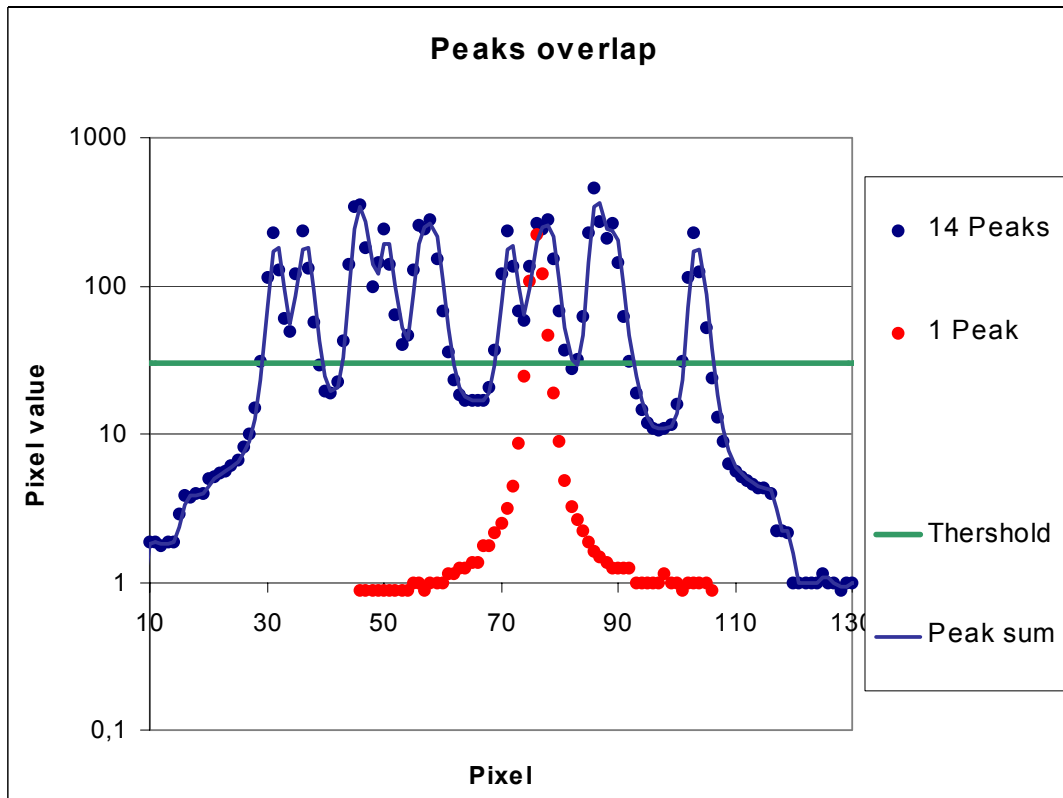
Figure 6.10: *Illustration of overlapping peak tails and the problem with applying a simple threshold. The red peak is assumed to be isolated. Only the highest part of the peak delivers a contribution to the radial dose distribution. In contrary, the tails of the overlapping peaks are partly lifted above the threshold level resulting in an unproportional contribution.*

## 6.5.3 Experimental requirements for application of unfolding methods

The new image intensifier can be operated in a wide gain range, $A_{MCP}$. Simultaneously, the magnitude of charge and light amplification, $A_{c\&l}$, between DA and $G_2$ (see Figure 5.1) of OPAC can be varied by adjusting the voltages to the grids $G_1$ and $G_2$ ($U_{G_1}$ and $U_{G_2}$). The light yield and thus the number of single peaks, generated in the IICCD can be adjusted for a given experiment via varying $A_{c\&l}$ (Note, that there are numerous fixed system-dependent parameters, e.g. solid angle or quantum efficiency of the photocathode, which influence the number of the formed single peaks as well.) The maximum of $A_{c\&l}$ is determined by the condition of stable detector operation at a given gas pressure and particle LET. If the intensifier gain, $A_{MCP}$ is large enough, practically all single peaks get sufficiently amplified to be reliably detected by the CCD camera as a signal above its noise level. If this condition is fulfilled, $A_{MCP}$ does not influence the yield of single peaks further. $A_{MCP}$ than affects merely the height and integral of peaks.
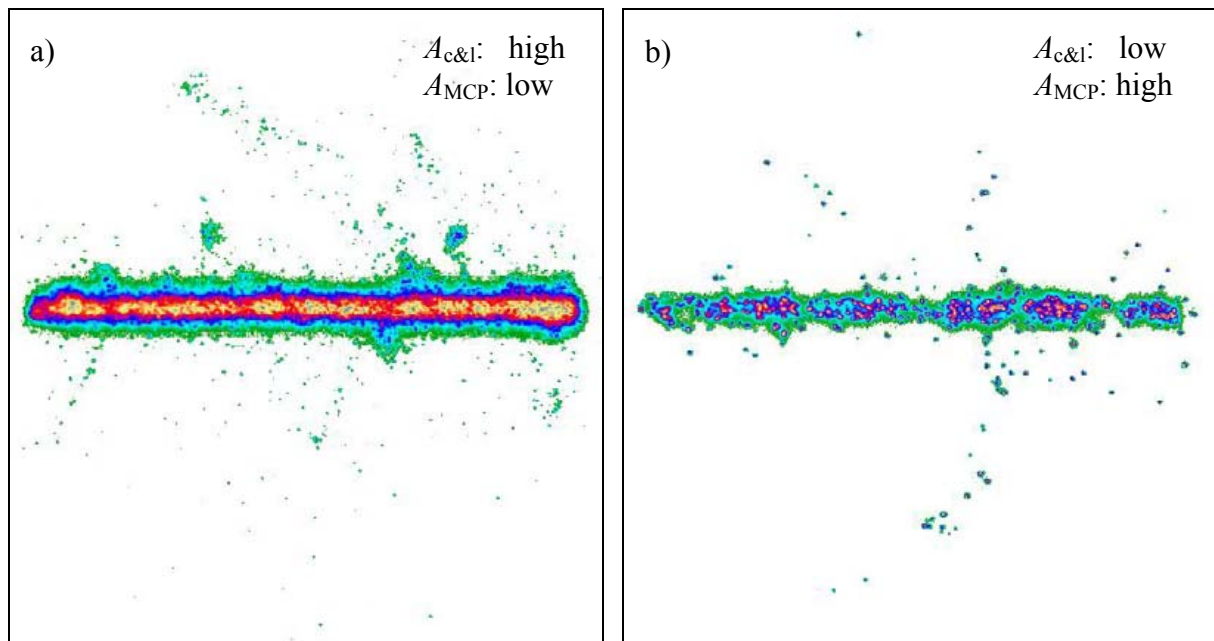
Figure 6.11: *Measured tracks of $^{12}C$ ions at 15 MeV/u energy at p = 10 hPa. a) Measured with grid voltages just below their maximum stable level and at low MCP gain, b) at higher $A_{MCP}$ (still far from its maximum) and lower $A_{c\&l}$. The green background as a superposition of single peak tails (or halos) is observable in both cases. Both images contain some single peaks occurring occasionally due to stray light.*

A principal condition of any quantitative analysis of the images is that the exposure of the CCD is within its linear range, i.e. even the largest local light exposure of the CCD does not lead to saturation of CCD Pixels. Therefore a proper combination of the OPAC light gain, $A_{c\&l}$ and the intensifier gain, $A_{MCP}$ is needed. Figure 6.11 shows the image of a carbon ion track of the same energy at two different amplification combinations of $A_{MCP}$ and $A_{c\&l}$. The left image was taken with the aim of achieving a very high single electron detection efficiency. Therefore, $A_{c\&l}$ was at the maximum, of the stable operation limit of OPAC. In this image various $\delta$-electron tracks are observable, partly they are stopped inside the interaction volume (visible by the intense "blob" at the end of their trajectory, while others, which leave the chamber, are only visible by their faint track of secondary ionization electrons. Due to the high single peak density in the ion track core, $A_{MCP}$ had to be reduced to a relative low value applied in order to avoid saturation effect.

Figure 6.11 b) is obtained under exactly reverse conditions: low $A_{c\&l}$ but high $A_{MCP}$. With this parameter setting, only a small fraction of the ionization electrons "succeed" to produce a single photoelectron on the photocathode of the intensifier; but due to the high intensifier gain this photoelectron is then detected as significant peak above noise by the CCD camera. In this mode only a sparse sample of the ionization electrons is detected, but, provided the gas gain is uniform and independent from the local ionization density, the sampling ratio is also uniform in the imaging plane and the relative local ionization density is preserved also in this sampled electron distribution.

The advantage of this operation mode is that the single peaks and compound peaks (i.e. superposition of two and more single peaks) can be distinguished from the "green background" even in the region of the central track core. In the left image the very small single peaks disappear in the background of the superposed halos of the densely packed peaks. On the other hand, in the areas farther away from the track core the already small event statistics in Figure 6.11 a) is further reduced in the sampling mode of Figure 6.11 b) due to the much fainter $\delta$-electron tracks.

For the analysis of the radial ionization density of ions we have decided to choose the electron sampling mode (low $A_{c\&l}$ but high $A_{MCP}$) because there was no way seen to assure a non-distorted data analysis in the high gain mode of OPAC. We have chosen this mode despite the disadvantage of the low event statistics farther away from the track core, which is compensated by increasing the number of measured ion tracks.

For the analysis it is required to have precise knowledge of the single electron peak structure. It is evident, that this information (which is illustrated in Figure 5.7, Figure 6.9 and Figure 6.10) has to be derived at the same MCP settings which were used for the acquisition of the ion tracks in the experiments.

## 6.5.4 Test of an iterative unfolding algorithm (SAND-II)

In chapter 6.5.2 it was shown that a simple threshold method does not offer satisfactory results. A more sophisticated method had to be found to handle the problem related to the broad peaks. The first attempt was made by applying the SAND-II unfolding algorithm (see [Mat97] and [Reg02]) to the CCD images. SAND-II is an iterative unfolding algorithm which tends to sharpen the peaks. Implementing SAND II to the OPAC data and running 20-40 iteration steps, the peaks became significantly narrower and large parts of the halo disappear. However, it was observed that the unfolding process does not preserve the peak integrals and even changes the relative intensities of the peaks: while the height and peak integral of isolated single peaks were reduced relatively to the total pixel integral, the height and peak integral of overlapping huge peaks consisting of many single peaks were increased. By itself, this artifact would not be a killer argument for the application of the SAND-II algorithm. If the code would be able to separate all single electron peaks and enable a peak counting algorithm to analyze ionization density distribution we would not be affected by the distortions of the peak integrals. The capability of SAND II to separate and enable counting of two close peaks as function of their distance was tested by simulation. It was found that a separation was only achieved for peaks with larger distances between their centers. For simulated peaks which were placed at a distance of two pixels or less, the algorithm merged the two peaks in most cases into one peak. Furthermore, noise in the original image resulted in the generation and amplification of additional, "artificial" peaks.

## 6.5.5 The OPAC-specific iterative unfolding code

The experience with the SAND-II algorithm has shown that it is not easy to find a general code or algorithm that delivers a result which does not distort the shape of $d(r)$ and has a precision needed for biophysical applications. The reason for this could be the complex data structure (e.g. interaction between thermal CCD noise and halo around single peaks). Of course it cannot be stated, that such a generally used and accepted algorithm does not exist. Nevertheless, due to the very sophisticated knowledge about the CCD camera response function (i.e. shape single peaks) and the well defined requirements we preferred to develop our own algorithm which is optimized for the very special data structure and requirements of our application. In this chapter we present the strategy used by this code to clean the images of artefacts and obtain the desired $d(r)$ functions:

In the first step the algorithm searches for the peaks in an image. The code searches for local maxima above a certain threshold. It was found, that a threshold level of ca 2% of full range is satisfactory, because at the high intensifier gain used in the sampling mode (see chapter 6.5.3) practically all single peaks have higher amplitudes, while the noise level of the CCD was significantly below this level. This threshold is only used for the peak searching process and

will not affect the results of the further unfolding process in the negative way as described in chapter 6.5.2. After the peaks are found, their whole neighborhood will be treated in the further unfolding process including the pixels below the threshold level.
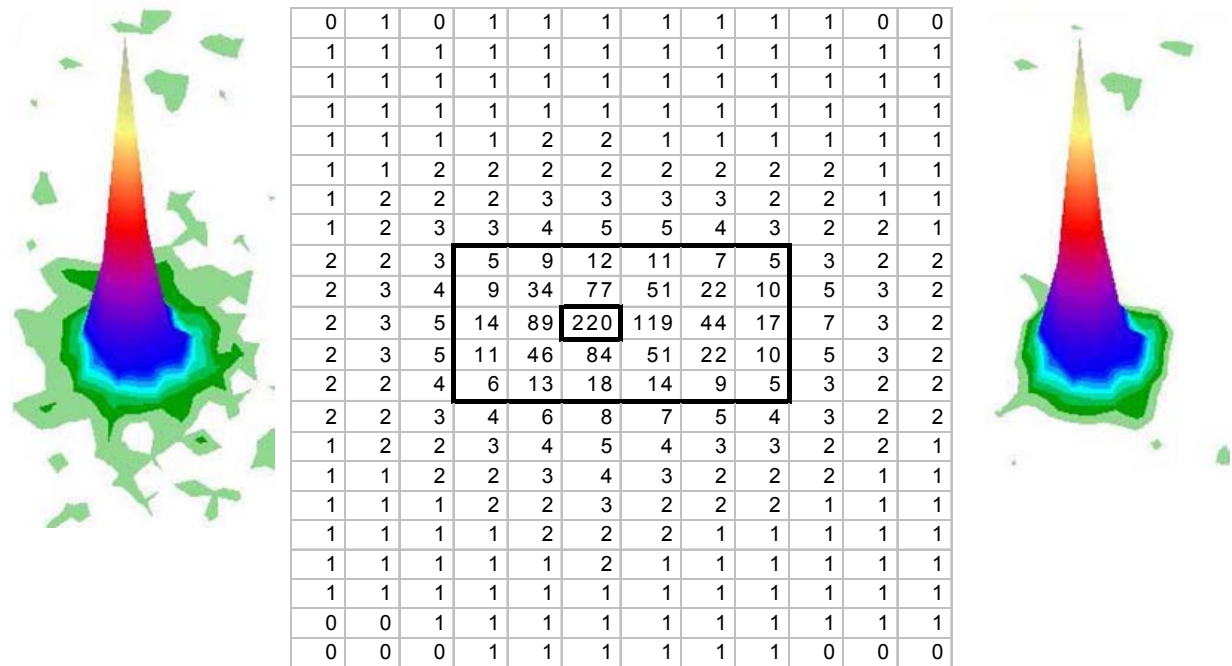
| | | | | | | | | | | | |
|---|---|---|---|---|---|---|---|---|---|---|---|
| 0 | 1 | 0 | 1 | 1 | 1 | 1 | 1 | 1 | 1 | 0 | 0 |
| 1 | 1 | 1 | 1 | 1 | 1 | 1 | 1 | 1 | 1 | 1 | 1 |
| 1 | 1 | 1 | 1 | 1 | 1 | 1 | 1 | 1 | 1 | 1 | 1 |
| 1 | 1 | 1 | 1 | 1 | 1 | 1 | 1 | 1 | 1 | 1 | 1 |
| 1 | 1 | 1 | 1 | 2 | 2 | 1 | 1 | 1 | 1 | 1 | 1 |
| 1 | 1 | 2 | 2 | 2 | 2 | 2 | 2 | 2 | 2 | 1 | 1 |
| 1 | 2 | 2 | 2 | 3 | 3 | 3 | 3 | 2 | 2 | 1 | 1 |
| 1 | 2 | 3 | 3 | 4 | 5 | 5 | 4 | 3 | 2 | 2 | 1 |
| 2 | 2 | 3 | 5 | 9 | 12 | 11 | 7 | 5 | 3 | 2 | 2 |
| 2 | 3 | 4 | 9 | 34 | 77 | 51 | 22 | 10 | 5 | 3 | 2 |
| 2 | 3 | 5 | 14 | 89 | 220 | 119 | 44 | 17 | 7 | 3 | 2 |
| 2 | 3 | 5 | 11 | 46 | 84 | 51 | 22 | 10 | 5 | 3 | 2 |
| 2 | 2 | 4 | 6 | 13 | 18 | 14 | 9 | 5 | 3 | 2 | 2 |
| 2 | 2 | 3 | 4 | 6 | 8 | 7 | 5 | 4 | 3 | 2 | 2 |
| 1 | 2 | 2 | 3 | 4 | 5 | 4 | 3 | 3 | 2 | 2 | 1 |
| 1 | 1 | 2 | 2 | 3 | 4 | 3 | 2 | 2 | 2 | 1 | 1 |
| 1 | 1 | 1 | 2 | 2 | 3 | 2 | 2 | 2 | 1 | 1 | 1 |
| 1 | 1 | 1 | 1 | 2 | 2 | 2 | 1 | 1 | 1 | 1 | 1 |
| 1 | 1 | 1 | 1 | 1 | 2 | 1 | 1 | 1 | 1 | 1 | 1 |
| 1 | 1 | 1 | 1 | 1 | 1 | 1 | 1 | 1 | 1 | 1 | 1 |
| 0 | 0 | 1 | 1 | 1 | 1 | 1 | 1 | 1 | 1 | 1 | 1 |
| 0 | 0 | 0 | 1 | 1 | 1 | 1 | 1 | 1 | 0 | 0 | 0 |

Figure 6.12: *The matrix shows the pixel values of an average single peak. The halo around an arbitrary selected single peak (left image) is reduced by the Process described in the text. As a result, the broad tail disappears (right image). Only some CCD camera noise remains.*

The algorithm finds both the isolated single peaks and the compound peaks, i.e. local maxima of regions, where the superposition of many single peaks produce an area of a peak cluster. Let us focus first on an arbitrary isolated single peak. The algorithm proceeds in the following steps:

1. The single peak integral, $I_{sp}$, is determined according to (5.5); all pixel values are summed around the peak center in a region of 5 x 6 pixels (inside the square in Figure 6.12). The reason for the slightly asymmetry in the peak shape could not be found. Let us name the region of the 5 x 6 pixels around the peak $Q_1$.

2. The ratio, $r_1 = I_{sp} / \overline{I_{sp}}$, of this integral and that of the average peak (standard peak) is calculated. The standard peak integral, $\overline{I_{sp}}$, was determined using the same $Q_1$ area surrounding each single peak contributing to the average peak.

3. The contribution of the halo outside this inner peak region $Q_1$, is accounted for by defining a larger square of 25 x 25 pixels, $Q_2$, around the peak area. All pixel values in the region $Q_2$ but outside $Q_1$ are reduced by a value which corresponds to the halo of the peak. The halo and its corresponding pixel values around a peak with the integral $I_{sp}$ are calculated by assuming a constant scaling factor of peak integral and halo, $r_1$, i.e. the hypothetical halo around the peak is defined by the halo of the standard peak multiplied by the scaling factor, $r_1$.

4. As the shape of the peaks after normalization is essentially independent of their peak integrals, this procedure eliminates efficiently the peak halo outside of $Q_1$ for a peak of any height. The left image of Figure 6.12 shows the raw data of a peak. Compare it with the right image of the same peak after the background subtraction. The procedure does not affect the pixel values inside the central peak area, $Q_1$.

The application of the method, described above for isolated single peaks, is not so straight forward applicable in regions with high ionization density. Figure 6.13 a) shows a segment of an ion track along its track core. Due to the high ionization density, many single peaks of various heights overlap in a complex way building numerous compound peaks, which are overlapping either. The largest compound peak in this image most probably consists of two or more single peaks, because of its very atypical shape and extraordinary high peak integral. However, as the formation has only one, common local maximum and its peak integral is elevated by the neighboring compound peaks, a more sophisticated algorithm is needed to derive the most probable number of single peaks hidden below the complicated contour.

The question is, if there is a way to handle the compound peaks in the direct neighborhood of other compound peaks in order to get rid of the overlapping halos. The contribution of the halo has to be subtracted from the whole neighborhood: from the regions, where no single peaks but only piled up (or superposed) halos are present, and from the neighbor peaks as well. The central simplification of the presented algorithm assumes that any compound peak can be treated as a large single peak with the same geometrical structure. In particular this implies, that the ratio of the volume of the central peak and the volume of the halo is the same for a standard single peak and a compound peak. Note, that the term "single peak" is used for the response function of the IICCD system to one photoelectron. This should not be confused with the "isolated peak". In the present case, the single peak is not isolated from the surrounding peaks, i.e. it is affected by their tails.

In the core region of the track the peaks are typically closer to each other than four pixels. In this case, the $Q_1$ neighborhoods of the peaks have to be restricted in space. Each pixel between the peaks is handled individually and related to that peak, towards which the gradient is the highest. The pixels that are related to a selected peak compose the $Q_1$ surrounding of this peak. The resulting $Q_1$ neighborhoods may contain much less than the 30 pixels of the standard area Q1, therefore the calculation of the compound peak integrals, $I_{cp}$, and $\overline{I_{sp}}$ has to be also restricted to the corresponding regions. After assigning the pixels to the peaks corresponding steps as in the case of isolated peaks are performed for each compound peak:

1. $I_{cp}$, is determined according to (5.5) taking into account, that $Q_1$ region of interest can differ from the standard 5 x 6 square.
2. The ratio, $r_I = I_{cp} / \overline{I_{sp}}$, of this integral and that of the average peak is calculated, where $\overline{I_{sp}}$ is determined over the correspondingly restricted $Q_1$. $r_I$ is the expected number of single peaks hitting the pixels of $Q_1$.
3. *For the pixels which are in the relative complement set of pixels of $Q_2$ (25 x 25 pixels) in $Q_1$ the pixel values are reduced by the corresponding pixel values of the halo of the peak (which is the product of halo of average peak times $r_I$).*
4. The same procedure is carried out for all peaks. Thus, the peak integral of a given peak is reduced so many times by the contribution of the halo of surrounding peaks, as surrounding peaks have $Q_2$-areas overlapping with the Q1-area of the selected peak.

Figure 6.13 b) shows the result of this procedure. The overlapping tails disappear and the reduction in peak height can be observed as well. A further expected effect: the peak in the center, marked with $P_1$, was originally somewhat higher than the isolated peak in the right upper corner, $P_2$. After the subtraction $P_2$ is clearly higher. Due to the many high peaks in the direct neighborhood of $P_1$, P1 is strongly reduced because all the contributions of the halos of the neighboring peaks to the pixels of P1 are subtracted.
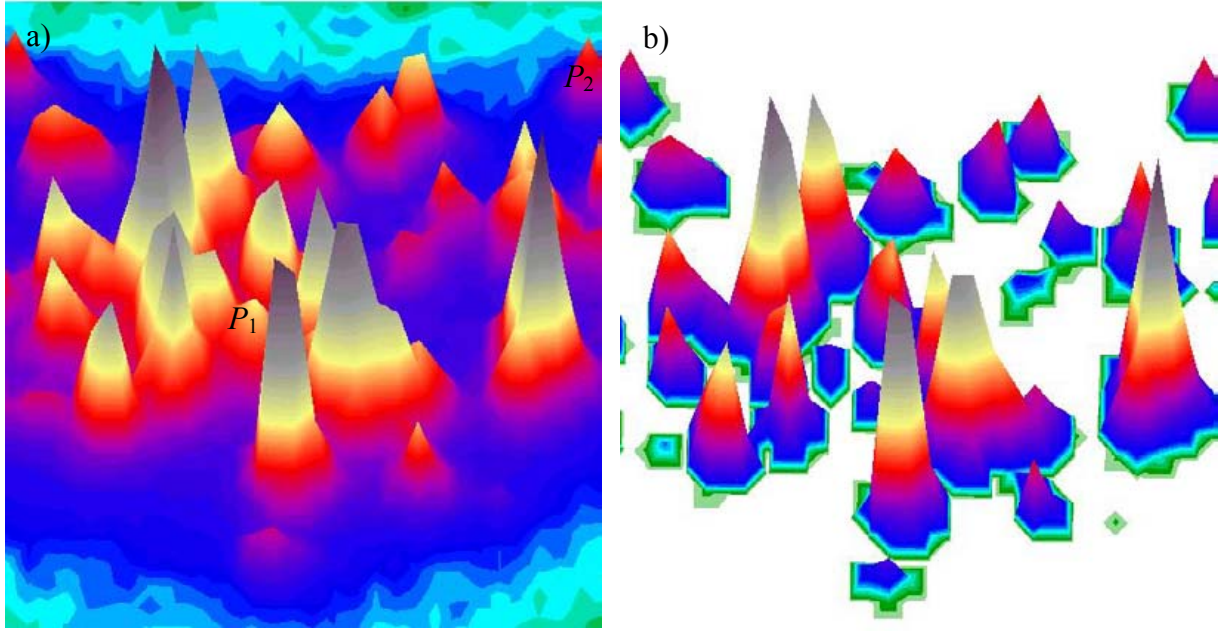
Figure 6.13: *a) A segment of a carbon ion track core (100 MeV/u, 10 hPa). b) the same segment from the same observation angle after a single iteration step of peak halo subtraction.*

However, Figure 6.13 b) is not yet the final solution as it still contains a contradiction. The peak integrals of the compound peaks were calculated with the data of the original image, therefore the resulting $I_{cp}$ contain also contributions of the halo from the surrounding peaks. Hence, the calculated $I_{cp}$ values overestimated the corresponding peak integrals so far. In addition to the single peaks with their centers inside $Q_1$, halo contributions of numerous peaks centered outside of $Q_1$ were also taken into account. As a consequence, also the subtracted tail contributions in the neighborhood of the peak were overestimated. Therefore, in a second step, the $I_{cp\_2}$ value of each peak is determined on the basis of the reduced peaks of Figure 6.13 b) and the subtraction of the halos from Figure 6.13 a) is performed according to the new $r_{1\_2} = I_{cp\_2} / \overline{I_{sp}}$ ratios. With this correction a better approximation of the correction is achieved. However, this second iteration suffers from the same type of errors than the 1$^{st}$ one, though to a lower extent - and the halo contributions are underestimated rather than overestimated. Therefore further, similar iteration steps have to be added..

The second major assumption for the application of the algorithm is, that $I_{cp\_i}$, the compound peak integral converges after $i$ steps to the "ideal peak integral" that would be measured if the peaks had no halos, if $i$ converges to infinity. Thus, the first four steps which are similar for both cases (isolated peak and compound peak) must be complemented by the following procedures if a compound peak is needed to be handled:

5. Based on its reduced pixel values, the peak integral of the compound peak, $I_{cp\_2}$ has to be determined again.

6. $r_{1\_2} = I_{cp\_2} / \overline{I_{sp}}$ has to be determined for the same $Q_1$ as $r_1$ in the second step.

7. The halo subtraction based on the shape of the average peak and scaled by $r_{1\_2}$ is carried out on the initial image again.

8. The same procedure is repeated for each peak, the resulting image is the second iteration step (see Figure 6.14 a)) which is used, to determine the new compound peak integral values, $I_{cp\_3}$.

9. The same procedure is continued in a third iteration step, and so on. The approximated values found for the halo in each of these iteration steps is always applied onto the initial image.

10. $I_{cp\_i}$ converges in that way (if $i$ converges to infinity), that its value remains below the expectable halo-free peak integral value after odd iteration steps, while it overestimates the peak integral value after even steps. Therefore, the best estimate can be achieved, if after $n$ (about 10 to 50) iterations the average, $I_{cp\_\infty} = \dfrac{I_{cp\_n} + I_{cp\_n+1}}{2}$ is taken.

11. The final halo elimination is than carried out by these $I_{cp\_\infty}$ values.

Figure 6.14 a) shows the same track segment as Figure 6.13 after two iteration steps and Figure 6.14 b) after applying the entire iterative unfolding process. The same observations are valid for the result of the iteration process, as already discussed for the first iteration step just to a smaller extent. Only the peak height reduction, compared to the original data, is smaller than after the first step.
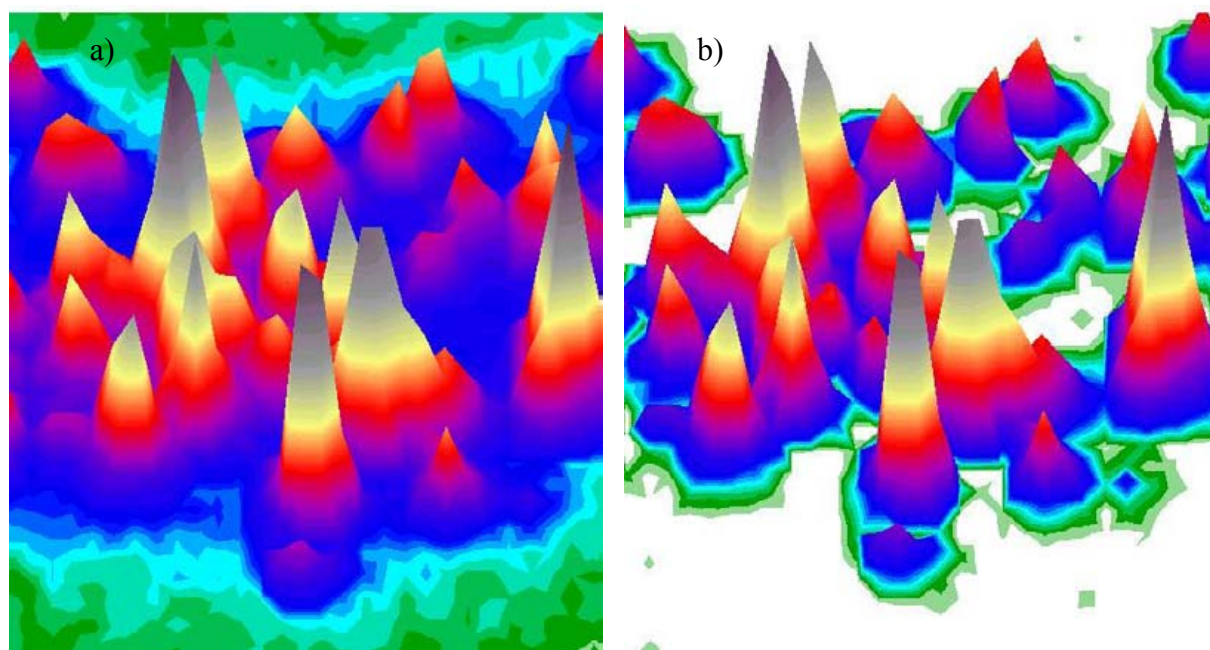


Figure 6.14: *The same ion track segment as shown in Figure 6.13 but a) after two iteration steps and b) the final result of the unfolding process (average of the 50th and 51th steps).*

The behavior of the peak iteration method is illustrated well by Figure 6.15, where the $I_{cp\_i}$ values of several arbitrary selected compound peaks are plotted as a function of $i$. The initial peak integral value is the highest in each case followed by an attenuating oscillation. A fast convergation is observable in each case. The initial peak integral, $I_{cp\_1}$, values are largely different in the selected cases, as well as the magnitude of the first oscillation steps. E.g. in the case of the blue curve $I_{cp\_1}$ is hardly different from the corresponding $I_{cp\_i}$ values after $i-1$ iteration steps (for any value of $i$). Such behaviour is typical for peaks which are almost isolated. On the other hand, the integrals of peaks which are affected by many overlapping halos of surrounding peaks can oscillate strongly in the first iteration steps (see e.g. red curve). In the case of the lowest curve the result of the unfolding process is $I_{cp\_\infty} \approx 0$. Thus, the curve belongs to an artificial peak which arises merely due to the overlapping halos of the neighbouring peaks, rather than reflects the location of a real photoelectron. (The "green background" can build small local maxima due to the superposing stochastical thermal and electronic noise of the CCD-camera.)
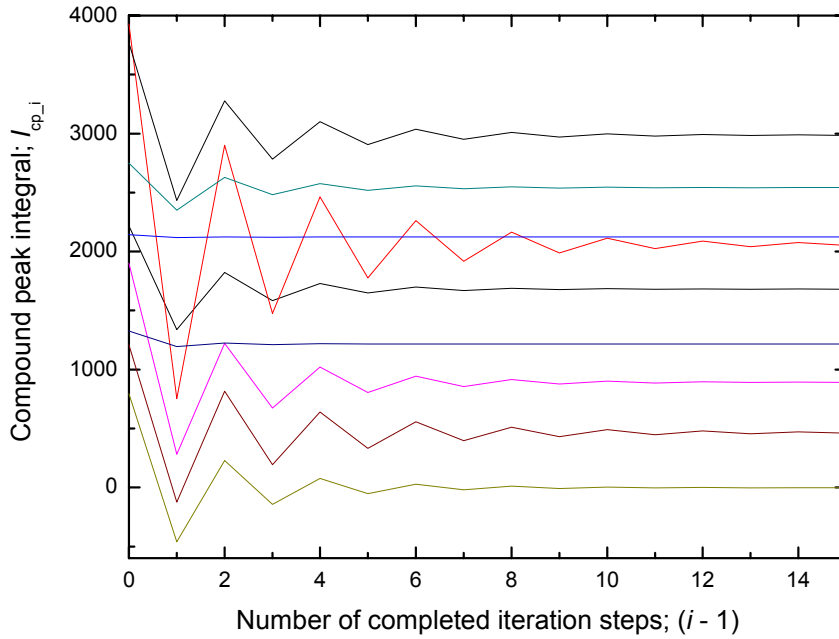
Figure 6.15: *Development of the peak integrals of several arbitrary selected compound peaks during the iteration process. The initial peak integral value is the highest in each case followed by an attenuating oscillation. A fast convergation is observable in each case.*

The separated description of the development of an isolated single peak and an overlapping compound peak with the progress of the iteration procedure was merely chosen to illustrate the effects of each iteration step on two relevant structures in a typical track image. In the practical application there is no need to distinguish between isolated single peaks and compound peaks. The whole algorithm is constructed in a way to handle all structures of an image at the same time correctly. It is easy to see that the iteration process does not affect the isolated single peaks at all. Such peaks preserve their initial peak integral over $Q_1$ which is 5 x 6 pixels large in this case. At the same time, the compound peaks are reduced to the desired extent by the iteration process. In summary, the method proves to be a very effective tool to separate the compound peaks of a measured electron track structure (see Figure 6.16 b which shows the effect of the method on the entire ion track).

The output of the unfolding algorithm provides not only the corrected images like Figure 6.16 b), but also the integral of each peak (the integral is the sum of the content of all pixels in the corresponding $Q_1$ region of interest). Thus, if $Q_1$ is restricted by the presence of neighboring peaks, the peak integral has to be divided by a similarly restricted $\overline{I}_{sp}$ to obtain the estimated number of single electrons, $<n_{sp}>$, that hit the IICCD inside $Q_1$.

Finally, $<n_{sp}>$ is associated with the coordinates of the local maximum in $Q_1$. As a consequence, the final result used for the quantitative analysis is fully independent from the IICCD single electron response function. However, the result cannot provide the exact coordinates of the single photoelectrons, produced in the photocathode of the image intensifier. All detected peaks, even isolated "single" photoelectron peaks, are described, additionally to their position coordinates by their most probable content of single electrons. This value is not necessarily integer but can be e.g. $<n_{sp}> = 0{,}3$ or $2{,}3$. I.e. even if it is obvious, that a measured peaks due to a single photoelectron, it is associated with a non-integer number of "photoelectrons" which is the ratio of the measured peak integral and the integral of an average single photo electron peak. It is obvious that only the statistical average

of the $<n_{sp}>$ values for a multitude of non-overlapping isolated single peaks will result to 1. As there is a sufficient amount of images available, the projected radial dose distribution, derived from this distribution of "photoelectrons with an average IICCD response", returns the correct distribution of real photoelectrons.
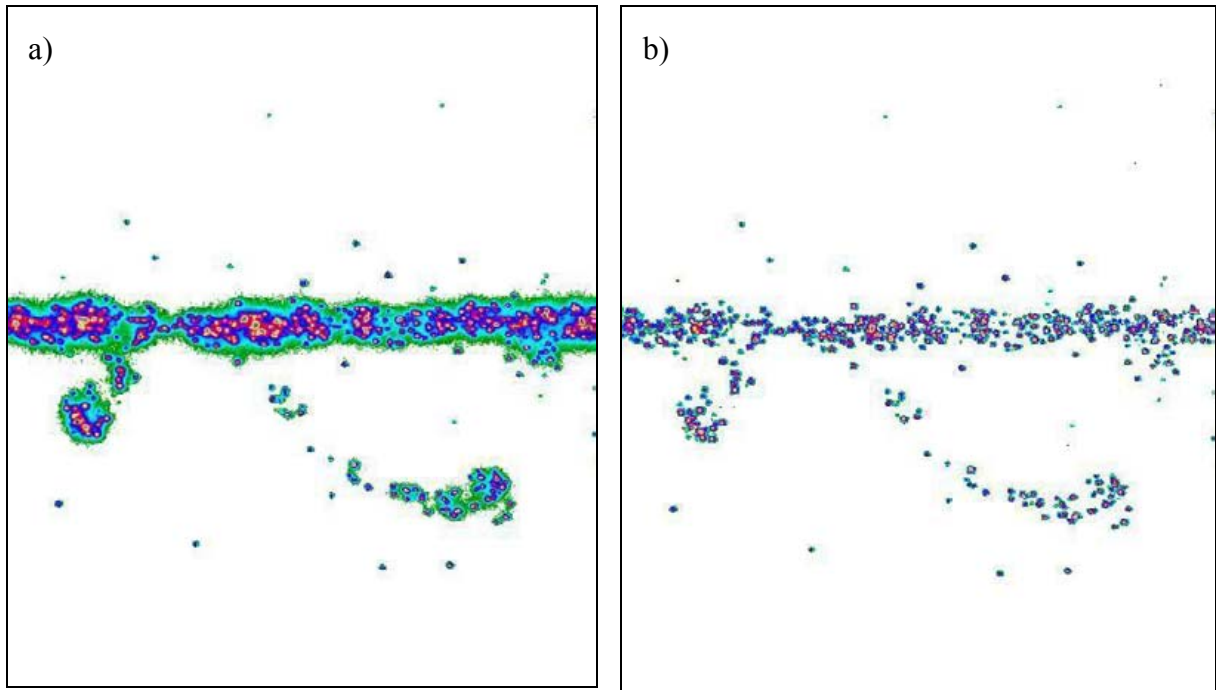


Figure 6.16: *a) Measured track of $^{12}C$ ion at 100 MeV/u at a gas pressure of p = 10 hPa. The plotted segment has a width of 300 pixels corresponding to 2,2 μm at ρ = 1 g/cm³. b) The same track segment after the unfolding process (the average of the $50^{th}$ and $51^{th}$ iteration steps). The algorithm clears the track from the background separating overlapping peaks.*

## 6.5.6 Reliability of the peak-unfolding algorithm and uncertainty analysis

The iterative peak-unfolding algorithm, described in the last chapter, requires some experimental observations and is based on a few assumptions and simplifications:

1. The useful content of a track image can be described as superposition of "single peaks". The superposition obeys linear additivity in the two measured dimensions, pixel by pixel. (The superposition of two or more peaks results in a "compound peak".) This assumption can be accepted if the operation limits of the experimental system are properly accounted for - namely the limits of image intensifier and CCD camera. The only condition is that neither the MCP amplification nor the charge in any pixel of the CCD camera is saturated.

2. If normalized to an average "peak integral", the relative shape of the single peaks — including their halo — is independent of the peak integral. This second assumption is based on experimental observations with the new image intensifier and was confirmed by systematic analysis

3. If a compound peak is made up of two or more single peaks hitting the same $Q_1$ region of the IICCD surface, the shape of the compound peak might be significantly deformed. The assumption is: in spite of this deformation the expected shape and contribution of the halo from the compound peak in the pixels outside the central peak area ($Q_1$) does not differ significantly from the halo of a single photoelectron peak of same peak integral and same center. A superposition of several single peaks produces a single and common local maximum, (i.e. one common compound peak and one common $Q_1$) if the centers are very

close to each other (within 1-2 pixels) or if one peak is very dominating in height. Therefore, in the larger distance outside Q1 the deformation of the overlapping halos remains small. Nevertheless, if the peak densities are too high, this point can limit the success of the algorithm. This and the unambiguous peak recognition even in regions with many overlapping halos (visible as large areas of "green background" in the images) are the main reasons for choosing measurement condition with relative low gas and light amplification ($A_{c\&l}$ ) but relative high optical amplification of the intensifier ($A_{MCP}$ )(see chapter 6.5.3).

4. The effect of the peak halo is negligible outside the larger neighborhood ($Q_2$) of the peaks. The effect of the halos outside of $Q_2$ (25 x 25 pixels) is not yet zero, as shown in Figure 6.9. However, the pixel content drops to very low — hardly measurable — values there.

5. The structure of a compound peak is not relevant inside its central region, $Q_1$, - at least for our present application. At the end of the unfolding process, the calculated number of electrons inside $Q_1$ is associated with the position of the local maximum in $Q_1$. The spatial uncertainty due to electron diffusion has a $\sigma_{pr} = 2,45$ pixels even at 40 hPa pressure. Therefore, the exact signal distribution inside $Q_1$ and the fact, that some pixels which were ordered to one of the neighboring peaks, while having contributions from all of them, do not have a resolution-limiting effect on data analysis. In fact, the effect is assumed not to affect the spatial resolution by more than one pixel, if radial dose distribution is derived. Compared to the two-dimensional diffusion distance of $\sigma_{r\_40} = \sqrt{2}2,45 \text{pixels} = 3,46$ pixels at $p = 40$ hPa and $\sigma_{r\_4} = \sqrt{10}\sigma_{r\_40} = 10,94$ pixels at $p = 4$ hPa this is considered negligible.

6. Associating a single or a compound peak with a calculative number of average peaks at the locations of its local maximum, and thus, substituting it with a real number, $<n_{sp}>$ does not lead to a bias or high uncertainties - at least if many track images are available. The assumption is justified due to the high number of track images. Even at a distance from the track core of 200 pixels we have typically several thousands of peaks contributing to the radial dose. Due to this and because of the better definition of the single electron peak by the new image intensifier (see Figure 5.7), only a very slight contribution to the random uncertainty of the radial dose shape at large distances is expected.

Instead of examining each single assumption in detail, it was chosen to compare the original measurement data with the unfolded data after folding them again with the experimental response function. This procedure is expected to be very sensitive to errors and uncertainties due to unjustified assumptions because the refolding of an incorrect unfolded image is not expected to result in the original image again (provided we can rely on the correctness of the folding procedure). The practical procedure is rather simple. Let us assume, that a peak at position $x_i$ and $y_i$ is calculated to have a magnitude of $<n_{sp}>_i$ average single peaks. The code simulates the corresponding "hypothetical peak" around ($x_i,y_i$). I.e. the pixel values inside the $Q_2$ surrounding of ($x_i,y_i$) are determined by multiplying the corresponding pixel values of an average peak by $<n_{sp}>_i$. The same procedure is carried out for each peak. Where halos of several peaks overlap, the pixel value is the sum of all the halos around the contributing peaks.

Figure 6.17 a) shows the same carbon ion track segment as Figure 6.16 a. Figure 6.17 b) is the same track segment after unfolding (this stage can be seen in Figure 6.16 b)) and folding: the full IICCD response was reconstructed by using only $<n_{sp}>_i$ and ($x_i,y_i$) results from the unfolding procedure. The high similarity of both images is a convincing argument of the high efficiency of the algorithm and the well understood behavior of the IICCD response function.
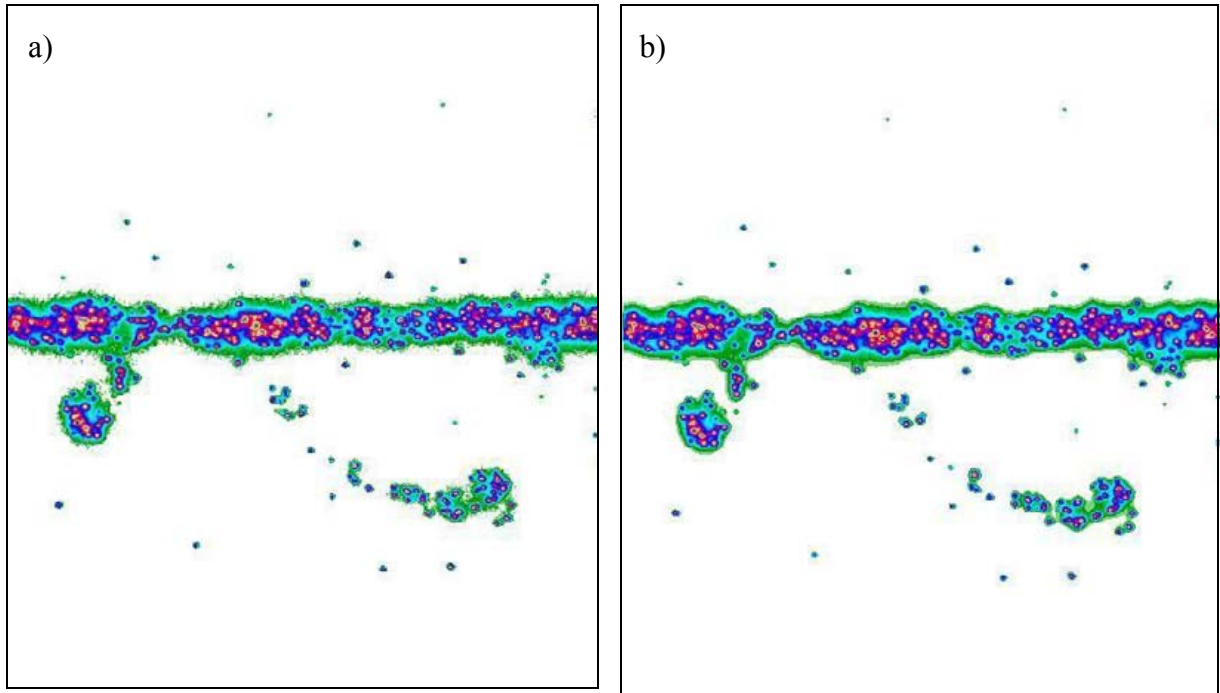
Figure 6.17: *a) The same track as in Figure 6.16 and b) shows the track after unfolding and subsequent folding of the image with experimental single electron response function. Obviously, the originally measured a) is nicely reproduced in b), which is a convincing proof for the validity of the method.*

However, the differences between the both images can be revealed if a short track segment is further magnified. We show such an example and further explanations to the method in Appendix .

In addition to the qualitative check of the unfolding process ─ as presented above ─ a more quantitative evaluation is presented here and illustrated in Figure 6.18. The same diagram is plotted with four different scalings. In order to assure a better comparison, the presented distributions are not transformed into real radial dose distributions, as described in chapter 6.2 but the projected values are plotted directly after normalization. Over 2000 images of $^{12}$C trajectories ($E = 100$ MeV/u; $p_{gas}$ =10 hPa) served as input for the determination of the plotted distributions.

The projected radial dose distribution of the red curve in Figure 6.18 is achieved after the application of a threshold for the pixel values (see chapter 6.5.2). Only that pixel values were taken into account for the determination of the curve, which exceeded a value of 36 (this value was chosen because CCD noise is below but most of the maxima of the peaks are above that value).

The distribution illustrated by the black symbols of Figure 6.18 was achieved after the unfolding process (see chapter 6.5.5) was performed on the same data that was used for the derivation of the red curve. After each image is unfolded, the projected radial dose distribution is determined only on the basis of $<n_{sp}>_i$ and $(x_i,y_i)$ information of the peaks (black symbols). Each of the about 2000 images contains about 700 detected electrons, thus: $i \approx 1 \ldots 1400000$. As no pixel values, but expectation values for the amount of single electron peaks were summed up in this case, the corresponding projected radial dose values cannot be compared to the case where pixel values were summed directly (i.e. red curve). Figure 6.18 shows a comparison after normalizing the curves to the same hit amount.

After the role of overlapping peak halos is eliminated by the iterative unfolding process, the height of peaks in the track core region is reduced. However, this reduction and the elimination of the low level background (see green areas in e.g. Figure 6.17 a)) is not observed directly in the diagram (compared the red curve with the black symbols Figure 6.18) due to the normalization. It is rather the relative increase of the projected radial dose values at large distances from the track core that reflects the successful peak tail subtraction of the iterative unfolding method. In agreement with the predictions of chapter 6.5.2, the simple threshold application results in an underestimation of dose at large radial distances.
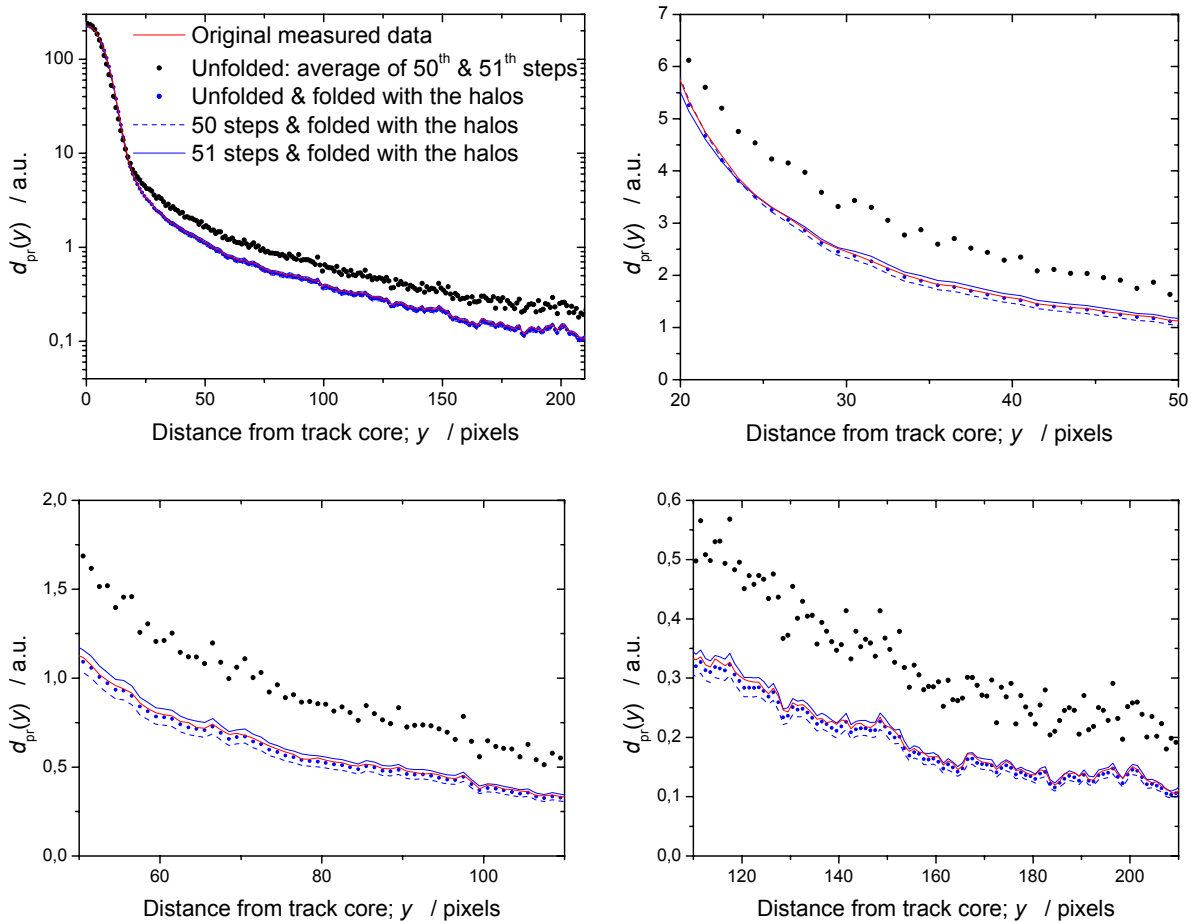


Figure 6.18: *Projected radial dose distributions determined directly (red line) and after the application of the iterative peak unfolding algorithm (black symbols). The blue symbols represent the corresponding distribution after refolding the unfolded peaks with the tail contributions. The good agreement between the red line and blue symbols indicates that the iterative unfolding process works correctly. Different regions of the identical distribution are plotted with different scalings in the three diagrams to enhance the visibility of deviations of both curves.*

After reconstructing the peaks halos, as described above, the corresponding projected radial dose distribution is plotted in Figure 6.18 by blue symbols. The pixel values according to $<n_{sp}>_i$ and $(x_i, y_i)$ data and the average peak shape (i.e. response function for $<n_{sp}>_i = 1$) were determined only for those pixels which contain data above the threshold of $36$ — i.e. the data which were used to calculate the red curve. The excellent agreement between the red curve and the unfolded and refolded graph of blue symbols is obvious. To enhance the visibility of this agreement even more, the three other graphs in Figure 6.18 show linear representations of parts of the first diagram: The discrepancies between the both distributions remain below 3 % in the whole range of interest. However, the blue symbols are systematically lower than the

red data line for radial distances $y > 20$ pixels. Thus, the tail contributions were probably not perfectly eliminated by the iteration process in the track core region. Nevertheless, the nearly perfect agreement is a strong indicator for the reliability of the iteration algorithm and more generally, for the good understanding of the effect of the overlapping peak halos.

In order to examine further the characteristics of the iteration process, the reconstruction of peak halos was performed not only on the averaged results of the $50^{th}$ and $51^{th}$ iteration steps of the unfolding process (black symbols), but also on the corresponding unfolded peak distributions after 50 and 51 steps, separately (not shown in Figure 6.18). After refolding the both set of unfolded images with the expected tail contribution the resulting distributions are plotted with dashed and compact blue lines. It is well observable, that the original distribution (red line) remains inside the "tube", defined by the both blue lines in the whole range of interest. As expected, the extent of tail correction is underestimated for even numbers and overestimated for odd numbers. The discrepancies amount to about 10 % between the refolded distributions after 50 and 51 unfolding steps. The experience has shown, that no significant further convergence to the average is expectable, if the iteration process is continued. If the average of two successive steps is built, the solution turned out to be quite stable after not more than 10 iteration steps. Similarly, if the algorithm is continued for more than about 50 steps no instability or oscillation effects arise. Thus, about 50 iteration steps were a compromise that already delivers very stable results but does not cost a significant increase in computation time. (The whole image loading, track searching, unfolding and analyzing process takes about 1,5 s per image performed with a PC of 2 GHZ processor speed).

As a summary, it can be stated, that the uncertainties due to the simplifications and assumptions, described at the beginning of the chapter, affect the radial dose distribution merely in a very limited manner. If higher precision especially in the track core region is desired, the peak searching algorithm and particularly the algorithm, that orders the single pixels to one of the neighboring peak, could be further improved. On the other hand, the main strength of the method is the dynamical, pixel to pixel treatment of each single image. Only those pixel values are taken into account, which are in a $Q_1$ region of a single or compound peak. Other pixels, irrespective the fact if their values are below or above the threshold, are not considered at all; if the peak density is high, then the halo contributions can raise the pixel values much higher than the threshold value of 36, even above 100. But if no local maximum can be identified in that neighborhood, such regions (see green areas e.g. in Figure 6.17 a)) are often outside of the $Q_1$ surrounding of any peak and not considered by the analysis at all. A further validation of the algorithm was performed by the examination of such regions around the track core. It was found, that due to the fact, that such "green" pixels are in $Q_2$ of many peaks, their values are reliably reduced to around zero by the iterative unfolding algorithm. And this is achieved irrespective of their original pixel values; i.e. any pixel with an original value of 15, 40 or 100 is reduced to about $0 \pm 10$ after applying the algorithm, if it was outside of all $Q_1$ regions; i.e. the process finds for each pixel individually to which extent it was affected by overlapping peak tails.

A further benefit of the described checks (e.g. Figure 6.18) of the unfolding method is the possibility to estimate the measurement uncertainties due to the application of the iterative algorithm. As shown above, the discrepancies of the unfolded─folded $d_{pr}(y)$ values from the measured raw data are below 3 %. Therefore, it is justified to presume, that that component of the overall measurement uncertainty of the radial dose which can be attributed to the effect of the peak halos, is not higher than 3 % after the iteration unfolding method was applied.

The estimated measurement uncertainties of 3 % are valid for the example of Figure 6.18 where 700 average peaks per image were present and the gas pressure was $p_{gas} = 10$ hPa. In

general, it can be said, that the uncertainties increase if the gas pressure increases or the number of peaks per image increases. For higher gas pressure and larger number of peaks per image the peak density increases, hence the compound peaks get more complex and overlapping plays a more important role. Furthermore, the probability not to detect smaller peaks by the algorithm in the higher background ("green" regions) increases. Examinations showed, however, that 5 % uncertainty is a good upper estimate for the case of $p = 40$ hPa either, if less than 800 average peaks are present.

In the track core regions the role of electron diffusion is the dominant contribution to uncertainty and causes a systematic deviation from the original electron distribution. Nevertheless, due to the shape of compound peaks and the ordering of pixels to one of the surrounding peaks, it can be estimated, that the determined location of each peak has a standard deviation of about 0,5-1 pixel — slightly higher for higher pressure. In addition, it was pointed out before, that in spite of collimating the beam by means of the two trigger detectors, the trajectories of single ions passing the chamber have a certain degree of freedom and have to be found individually per software. Let us suppose, that a peak is characterized after unfolding by the parameters, $<n_{sp}>_i$ and $(x_i, y_i)$. Due to a slightly tilted trajectory of the track, the $y_i$-coordinate of the peak is not identical with its real $y$ – coordinate: projected radial distance from the track core. Hence, to the uncertainty of $y_i$ a further component is superposed as the trajectory finding algorithm, which has to exclude the longer $\delta$-electron tracks, cannot be perfect, either. The uncertainty contribution of $y$ due to the trajectory fitting procedure is also estimated to be in the order of 0,5-1 pixel.

In order to account for the artefacts that are independent from electron diffusion but result in a further broadening of the track, a pressure independent broadening factor, $\sigma_d$, is introduced. Both the uncertainty of $y_i$ and that of $y$ for a given $y_i$ are components of $\sigma_d$. Both components are practically independent from the gas pressure if expressed in pixels (in contrary to $\sigma_{pr}$ which is smaller for higher pressure, if expressed in pixels). Another contribution to $\sigma_d$ is due to the optical distortion and broadening due to misalignment and resolution of the optical system. The extent of the broadening due to optics was estimated to be not more than 0,5 pixel. For the value of $\sigma_d$, these rough estimates of the contributing factors lead to a pressure independent systematic broadening of $\sigma_d \approx \sqrt{0{,}75^2 + 0{,}75^2 + 0{,}5^2} \approx 1{,}2$ pixels.

$\sigma_d$, the cumulated pressure independent position broadening factor is a one-dimensional root-mean-square broadening distance, similarly to $\sigma_{pr}$ (introduced in chapter 6.3). Therefore, the overall one-dimensional root mean square error, $\sigma$, can be built of the two uncertainty contributions. Hence, the second equation of (6.8) should be modified as follows:

$$y' = y_0 + \sigma = y_0 + \sqrt{\sigma_{pr}^2 + \sigma_d^2} = y_0 + \sqrt{\left(\sigma_{prs}\sqrt{\frac{1{,}6\text{cm} - z_0}{10\text{cm}}}\sqrt{\frac{10\text{hPa}}{p}}\right)^2 + \sigma_d^2} \qquad (6.9)$$

where $\sigma_{prs}$, $y_0$ and $y'$ are now measured in pixels. In the case of $p = 10$ hPa, the first component below the square root has a value of 4,9 pixels (converted from the value of 2,2 mm according to equation (6.3) thus, the diffusion is more than four times as important, as the broadening due to the pressure-independent factors. Because of the root mean square uncertainty combination, the diffusion distance is "increased" by only $\left(\sqrt{4{,}9^2 + 1{,}2^2} - 4{,}9\right)/4{,}9\text{x}100 \approx 3$ % due to $\sigma_d$. This increase amounts to about 11 % for $p = 40$ hPa and 1,5 % for $p = 4$ hPa. Thus, the additional detecting broadening plays a real significant role only at the highest applied gas pressure and within a distance from the track core which is less than about 2-3·$\sigma$ (see discussion for Figure 6.7). Its relative negligible role is the reason, why a more precise determination of $\sigma_d$ was not performed in the framework of the present work.

## 6.6  Stray light subtraction

After the iterative unfolding procedure of an image the coordinates and expectation values of the number of photoelectrons, produced in the photocathode of the IICCD, are given (($x_i$,$y_i$) and $<n_{sp}>_i$). There is, however, a further artefact to be taken into account: not all photons, hitting the photocathode, arrive from the focus of the optical readout system, i.e. the plane between the grids $G_1$ and $G_2$, where the secondary scintillation process occurs. The scintillation light is emitted in all directions and some of the photons are reflected by surfaces in the chamber. Also these photons may reach the photocathode "accidentally" and produce single electron peaks that obey the same statistical rules as any other isolated single electron peak. As described in chapter 5.4.2, the replacement of the UV-lens and image intensifier and the painting of reflecting surfaces with a highly absorbing coating resulted in a reduction of this stray light by one order of magnitude. However, far away from the central track core, where ionization by $\delta$-electrons is faint, the stray light contribution is still not negligible; while the projected radial dose of heavy ions typically falls from the track core to regions of high $y$ by three orders of magnitude, the stray light peaks are distributed much more homogenously. Hence, their role increases with increasing $y$ strongly.

Figure 6.19 a) shows the image of a carbon ion track after the overlapping halos of the peaks were eliminated by the described iterative unfolding procedure. The track includes two high energetic $\delta$-electron tracks which are sparsely ionizing compared to the central region of the ion track. The other isolated peaks in the image, which are too far from the track core and from the $\delta$-electron tracks to get there e.g. by diffusion, are probably due to the scattered photons described above. However, it is not possible to justify from peak to peak unambiguously, if it is due to a scattered or a "regular" photon. Stray light can be present everywhere in the image, also inside the track core and each peak in the two $\delta$-electron tracks can be due to scattered light as well. E.g. the peak, marked with the red circle can occur either due to a "diffused" ionization electron produced by a $\delta$-electron, or it could be caused by a scattered photon from somewhere in the chamber.

Furthermore, depending on gas pressure, gain and LET of the primary ion, it is also possible, that the tracks of high energetic $\delta$-electrons cannot be distinguished from stray light at all. Figure 6.19 b) is a typical image of a Xenon track. The LET of $^{132}$Xe is by two orders of magnitude higher than that of the $^{12}$C ion at the given energies. The operation condition (i.e. $A_{c\&l}$ and $A_{MCP}$ — details in chapter 6.5.3) for $^{132}$Xe had to be adjusted in that way to assure a single peak density that is not too high for the unfolding process (see chapter 6.5.5). The measured single peak density for $^{132}$Xe is adjusted to be similar as for $^{12}$C. As a result, the voltages of $G_1$ and $G_2$ have to be reduced to such an extent that the detection efficiency of single thermalized electrons is about two orders of magnitude lower, than the corresponding single electron detection efficiency in the $^{12}$C measurements. Therefore, the track of the $^{132}$Xe ion but also that of the resulting delta electrons are sampled only with a rate of about 1 out of 1000 electrons. Under such circumstances, the measured ionization density in the track of $\delta$-electrons is not high enough to create a continuous track which can be distinguished from other $\delta$-electron tracks or from stray light. Not even the relatively densely ionizing end points of the electron tracks are identifiable in the measurements with very heavy ions. It is rather typical that each end point is represented in the image by 0, 1 or a few single peaks sampled from the end point by chance. It is also probable, that high energetic $\delta$-electrons which cannot be stopped in the chamber leave it without producing a single signal in the image intensifier. The upper $\delta$-electron track seen in Figure 6.19 a), for instance, is made up by about 30 single electron peaks. In the case of $^{132}$Xe (see Figure 6.19 b)) the single electron detecting efficiency is about 100 times lower. Therefore, about three such $\delta$-electrons are needed, on average, to see at least 1 single electron peak! In the latter case, the information from a

continuous track structure is lost – instead only an irregular distribution of spots is seen similar to what is observed for pure stray light. This effect, however, does not lead to a distortion in the measured radial dose distribution as long as the detection efficiency of ionization electrons is constant across the detector area and independent of the ionization density. Nevertheless, there is no way to judge in a case like the Xe image in Figure 6.19, if a certain peak is due to a regular electron from the track of a δ-electron track or a scattered photon. Thus, in order to eliminate the stray light contribution from the radial dose distribution, a statistical method is needed, rather than a peak-to-peak consideration.
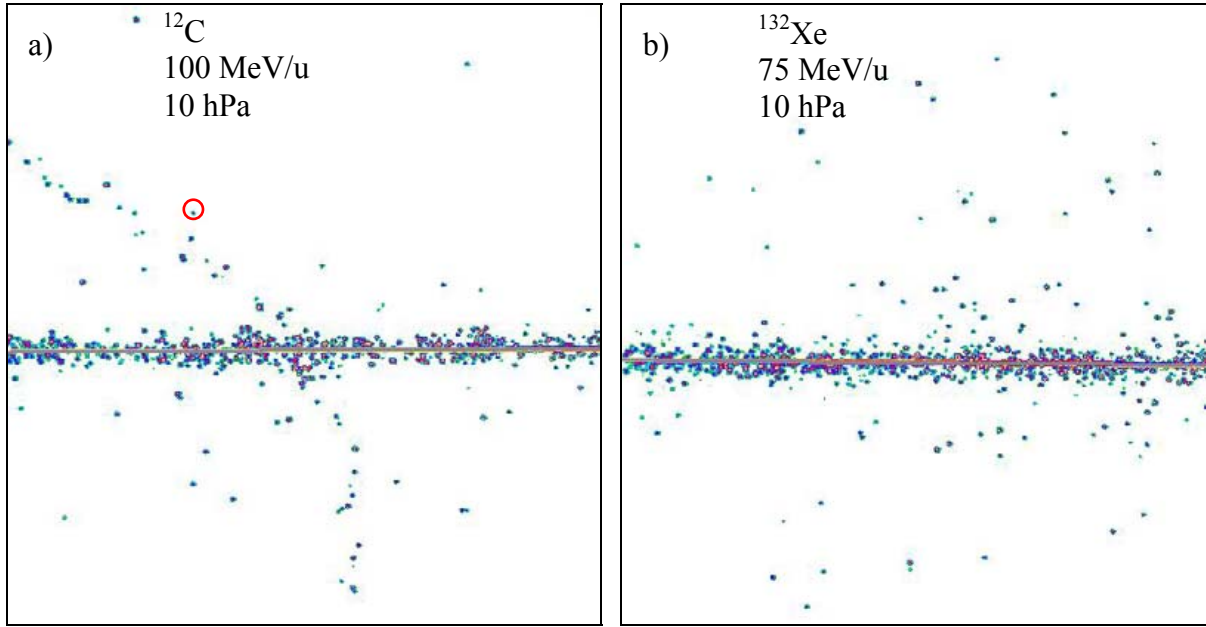


Figure 6.19: *Comparison of $^{12}C$ and $^{132}Xe$ tracks (after the iterative unfolding procedure). The ion trajectories have been found by the automatic algorithm and are plotted as gray lines. No coherent δ-electron tracks are observable in the image of the Xe track. However, most of the isolated peaks are samples from δ-electron tracks, and only a few of them are due to stray light.*

In order to subtract the stray light contribution from e.g. the projected radial dose distribution, a reference data set is needed for the stray light contribution as a function of $y$ for a given total amount of light. With this single data set it is possible to derive the expectable stray light distribution under all experimental circumstances based on the assumption, that the mean amount of stray light (both in the whole image and e.g. at a given $y$ distance) is proportional to the integral amount of primary light.

The straight forward way to create this data is to measure the light distribution as a function of $y$ around a thin, line-formed light source. The presence of stray light is observed for any kind of light source between the amplification grids $G_1$ and $G_2$. However, the application of e.g. a chain of LEDs, as a light source, does not lead to a reliable result, as the wave length distribution of LEDs is different from that of the scintillation light in TEA. Light reflecting properties of different surfaces can depend largely on wave length.

Another method, tried in this work, was the use of a thin wire with a diameter of 200 μm, stretched parallel to and in between $G_1$ and $G_2$. The wire is biased with positive high voltage relative to the neighboring grids so charge amplification and scintillation occurs around the wire close to its surface. The detector chamber was operated under standard operation conditions with TEA filling. Free electrons were produced by α-particles, passing the interaction volume as in standard operation mode. This method, however, did not lead to success, because a major part of the scintillation light was produced behind the wire.

Therefore, in the center of the image only the thin shadow of the wire was visible surrounded by bright light on its both sides, but the even brighter central part was shadowed by the wire itself. On the other hand, the shadowed light is still present in the chamber, delivering its contribution to the stray light. Although the experiment did not allow for the quantitative estimate of stray light, the fact that the shadow of the thin wire was visible indicates the good optical resolution of the system and the correct optical focusing.

The above experiences have shown, that modeling the exact, quantitative contribution of stray light is problematic. Therefore, it was chosen, to measure it under circumstances that are as similar to the real measurement conditions as possible. A comprehensive description of the method, the results and the uncertainty discussion of the stray light correction procedure can be found in Appendix 10.2

# 7 Results and discussion

The most important aspects of data analysis were discussed in the previous chapter. After applying the peak unfolding algorithm and the stray light reduction techniques to eliminate various imaging artefacts, a wide spectrum of microdosimetric and track structure quantities can be derived from the measured ion tracks. The present work is focused onto the experimental determination of the radial dose distribution around fast heavy ion tracks in order to benchmark corresponding simulation results. Excellent agreement will be shown between the distributions derived from OPAC and TRAX data for carbon ions if the simulated images are folded with the diffusion. The agreement is worse for heavier ions for which the BEA model, applied by TRAX (chapter 3.3.4.2), has some deficiencies.

The data presented in this work are from the beam time campaigns at GSI, Darmstadt from summer and autumn, 2003. The improved measurement system was applied. OPAC was installed in the "Cave A" of the SIS experimental facility as described in chapter 5.3.

All quantitative results of our measurements refer to a given ion energy. Thus, it is very important to ensure a well-defined energy for the ions that pass through the chamber. Under this aspect it has to be taken into account that the ions have to pass several layers of materials before entering the interaction volume of OPAC. The thickness of air between the exit of the beam tube and the entrance port of OPAC was 1,1 m. Furthermore, an ionization chamber was installed in this region to measure the shape and intensity of the beam. The ionization chamber has 2 walls made of kapton foil with a thickness of 20 μm. The beam entrance window of OPAC is made of stainless steel with a thickness of 100 μm. Behind the entrance window the ions propagate in TEA at the adjusted pressure. The overall ion-stopping effect of the described layers corresponds to that of a water layer with a thickness of $3,7 \pm 0,3$ mm for 50 MEV/u carbon ions. This value was determined with the particle transport software, SRIM 2003, which derives stopping power and range data for any ion type in any matter as a function of the projectile energy. The comparison of ranges in air, steel and kapton with that of water leads to the result above. The value of 3,7 mm varies slightly depending on the projectile ion and its energy.

The energy degradation of an ion passing a water layer with the given thickness is negligible for light and fast ions. The 400 MeV/u carbon ions are slowed down to about 398 MeV/u, while 100 MeV/u carbon ions to about 92 MeV/u and 35 MeV/u carbon ions get stopped after passing through a water column of 3,7 mm length. Heavier ions with higher LET and shorter range values at the same specific energy are affected more. E.g. 125 MeV/u $^{238}$U ions are slowed down to 50 MeV/u. The energy degradation was calculated from the ion range tables in [Krm04].

The first part of the measurement program consisted of the imaging of carbon ion tracks at various energies. Heavier ions were measured in the second part. The selection of the ion types and energies was motivated by the effort to compare radial dose distributions of ions with very different $Z$, atomic numbers but having similar LET values in matter (see chapter 2.7.1). The measurement program was performed with the following adjustments:
- $^{12}$C ion tracks were imaged at $E = 400$, 195 and 92 MeV/u (the energy reduction by the materials between the beam tube and OPAC is included).
- Ion energies below 100 MeV/u cannot be provided by the synchrotron (SIS) directly. A water column was installed in front of OPAC in order to adjust also lower energies than 100 MeV/u down to Bragg-peak energies. The thickness of the water column can be remotely adjusted.
- $^{40}$Ar ion tracks were imaged at $E = 1600$, 600, 240 and 75 MeV/u.

- $^{84}$Kr ions at $E = 1400$, 650, 150 and 20 MeV/u. The latter energy was obtained by reducing the energy of the 150 MeV/u ions with an aluminum plate (thickness: 5,5 mm).
- $^{132}$Xe ions at $E = 850$ MeV/u.
- $^{238}$U ions at $E = 1000$, 500, 190 and 50 MeV/u.
- Measurements were performed at $p = 4$, 10 and 40 hPa for each ion type and energy adjustment.
- Measurements were performed at low and high gas amplification: a) sampling mode which is low gas amplification ($A_{c\&l}$)and high optical gain ($A_{MCP}$) to achieve good results from the peak unfolding algorithm and b) high $A_{c\&l}$ and low optical gain ($A_{MCP}$) for optimal single electron detecting efficiency (for details see chapter 6.5.3). In this work we were unable to obtain reliable quantitative results - free from systematic errors- from the type b) data, therefore only the data obtained in sampling mode a) were analyzed.
- 500 to 2000 images were taken in each case, described above, in order to achieve sufficient statistics for the quantitative data analysis.

## 7.1 Qualitative results, ion tracks
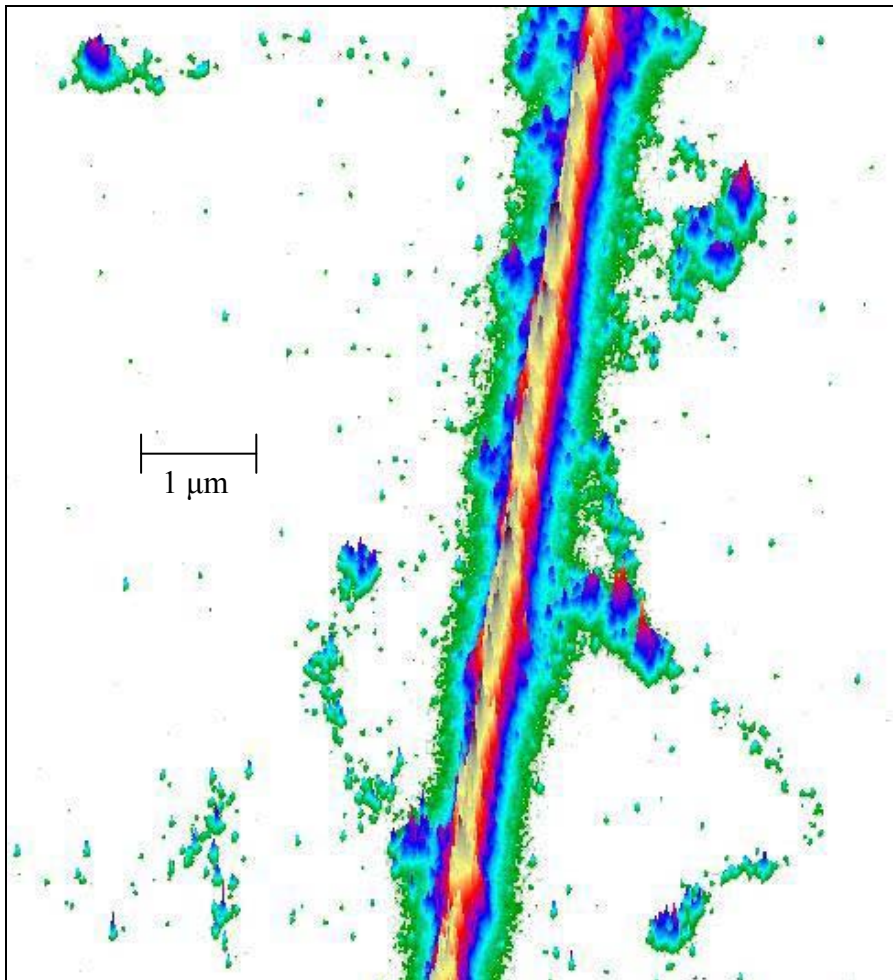


Figure 7.1: *Three-dimensional visualization of the track of a carbon ion (35 MeV/u; $p = 40$ hPa). The length scale of 1 μm refers to liquid water at $\rho = 1$ g/cm$^3$.*

Figure 7.1 shows a track of a $^{12}$C ion at $E = 35$ MeV/u, measured at a gas pressure of $p = 40$ hPa. Since we do not aim here for a quantitative analysis this image is selected from the batch of tracks imaged at large gas amplification (high $A_{c\&l}$). Therefore it contains both, a

lot of stray light and overlapping peak halos ("green" background) due to the high sampling frequency of ionization electrons (see chapter 6.5.3).

The data acquisition software has the capability of imaging a track with a height-coding of pixel contents and an observation from any desired angle. Such images are excellent for demonstrative purposes e.g. in classes, where radiation action in matter or its biological effect is taught. The central track region is the diffused representation of the copious amount of very low-energy $\delta$-electrons with ranges below about 100 nm. The end points of faster $\delta$-electron tracks are visible as "blobs" in dark blue color. Some of the end points are very close to the track core, while others belong to longer $\delta$-electron tracks with ranges of several μm. Based on the energy-range tables of [ICR96], such electrons have initial energies of 10-20 keV.

Figure 7.2 shows a collection of $^{12}$C tracks imaged at 40 hPa gas pressure, i.e. the image size of 450 pixels corresponds to 13,5 μm in liquid water ($\rho = 1$ g/cm$^3$). The images were obtained at low optical gain and high gas amplification gains in the chamber. The images in the three rows were tracks of carbon ions at three different energies. It has to be noted, that the representation of the ionization density by the color tables between the three images are not comparable because in the high gas gain mode of the chamber the gas gains were selected for each ion energy (i.e. LET) individually in order to achieve an optimal single electron detection efficiency with sufficiently high operation stability of the detector. The lower the LET is, the higher gas amplification is achievable. This is the reason, why the intensity of $\delta$-electron tracks or that of their end points is higher, if the carbon ion energy is higher.

Figure 7.2 a) and b) are two typical tracks selected out about 1500 tracks, imaged under the same circumstances (same gain, ion energy, gas pressure, etc.). The relative low LET of 16 keV/μm at $E = 200$ MeV/u [Krm04] enables a high $A_{c\&l}$ adjustment and thus a detailed visualization of $\delta$-electron tracks. Figure 7.2 b) contains the line, fitted by the automatic trajectory finding algorithm. Obviously, the line fits the central track core very well irrespective of the $\delta$-electron tracks.

In Figure 7.2 a) and b) a few end points of $\delta$-electron tracks are observable well separated from the track core. The light yield (i.e. ionization density) of the end points is comparable with the light yield in the track core itself (both are typically colored in red or yellow). This observation is in agreement with the theory: According to [Ash82], the stopping power of electrons in polyethylene is between 100 and 200 MeV·cm$^2$/g for electron energies between 30 and 1000 eV (the stopping power is lower for electron energies outside of this energy window). If a simple scaling with the ratio of densities is applied (see chapter 4.1), the stopping power is between 10 and 20 keV/μm for end point-electrons at $\rho = 1$ g/cm$^3$: indeed the same order of magnitude, as the stopping power of the primary ion itself.
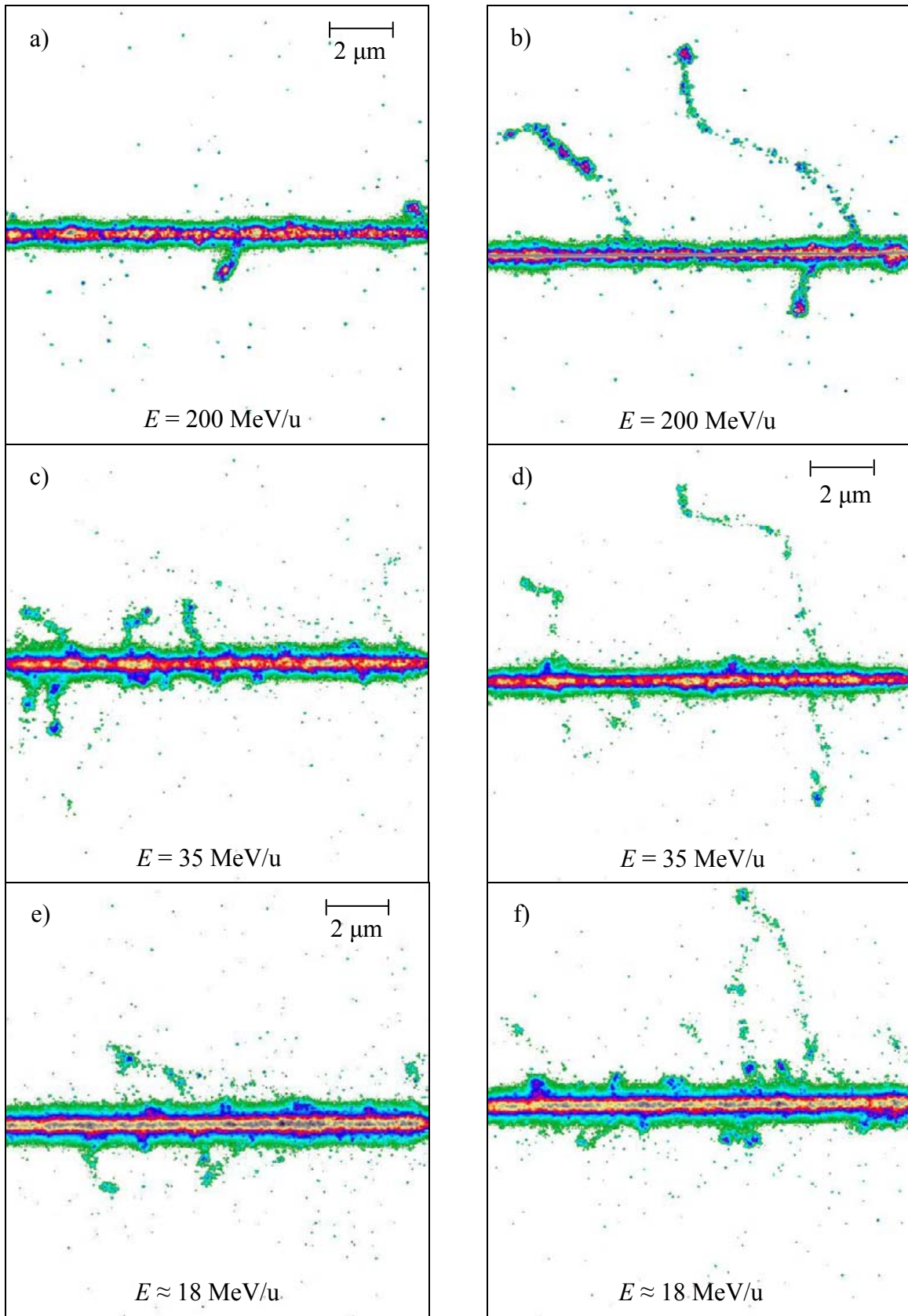
Figure 7.2: *Images of $^{12}C$ ion tracks at p = 40 hPa. The color representation of the light yield of ion images at different energy cannot be directly compared due to the difference in the gain parameter settings (see text).*

Figure 7.2 c) and d) are two examples from a measurement, where the length of the water column was chosen to be 268 mm in order to degrade the energy of $^{12}$C ions from originally 400 MeV/u down to 35 MeV/u (LET = 59 keV/μm). Due to the higher LET the gas gain and the optical gain are reduced compared to the images at higher energy in a) and b). The ionization density of one single energetic $\delta$-electron is significantly lower in this case, than that of the track core (which is due to superposition of many low-energy $\delta$-electrons). On the other hand, the spatial frequency of energetic $\delta$-electrons, with tracks separable from the track core, is higher than in the case a) - b). According to equation (3.4) and [ICR96], the maximal range of $\delta$-electrons is about 70 μm for $\delta$-electrons from 35 MeV/u carbon ions, i.e. an order of magnitude higher, than the maximal observable range in the chamber at the given pressure. There are some relative sparsely ionizing energetic $\delta$-electron tracks leaving the interaction volume of the chamber without getting stopped. At least three such tracks are visible in Figure 7.2 c).

To an even larger extend, similar observations can be made for the images in the last row. The spatial frequency of energetic $\delta$-electrons is increased further, while fewer have high energies and can leave the chamber. Note, that all images presented here are planar projections and the $z$-coordinates (in drift direction) of the electron location cannot be depicted. As a consequence, the track core itself includes the information of all $\delta$-electrons where the extension into the $y$-direction (perpendicular to the track and to the drift direction) component is negligible. Furthermore, the lengths of the energetic $\delta$-electron tracks are longer in reality than in the images due to the additional $z$-coordinate not visible in the projected images. The method, described in chapter 6.2, corrects for this artifact in order to achieve the real radial dose distribution without the effect of projection.

Similar to Figure 7.2, Figure 7.3 shows examples for tracks of $^{12}$C ions at three different energies, but measured at a pressure of $p = 10$ hPa instead of 40 hPa. The 4-times lower pressure increases the distances between interactions by four times- while the diffusion width doubles. Enhanced distances between energetic $\delta$-electrons result in the fact that the majority of images of 400 MeV/u $^{12}$C ions are like Figure 7.3 a) in a sense that the $\delta$-electrons, fitting into the imaged region, have low energies and their tracks are within the diffused track core. I.e. tracks like the one in Figure 7.3 b) with two longer (from track core distinguishable) $\delta$-electron tracks are relatively rare. The endpoint of the longer $\delta$-electron track has an ionization density of the same magnitude than the spots in the track core. The second more energetic $\delta$-electron in this image has part of its track (or its end point) behind or in front of (in $z$) the track core resulting in a locally increased ionization density ("black" region in the image).
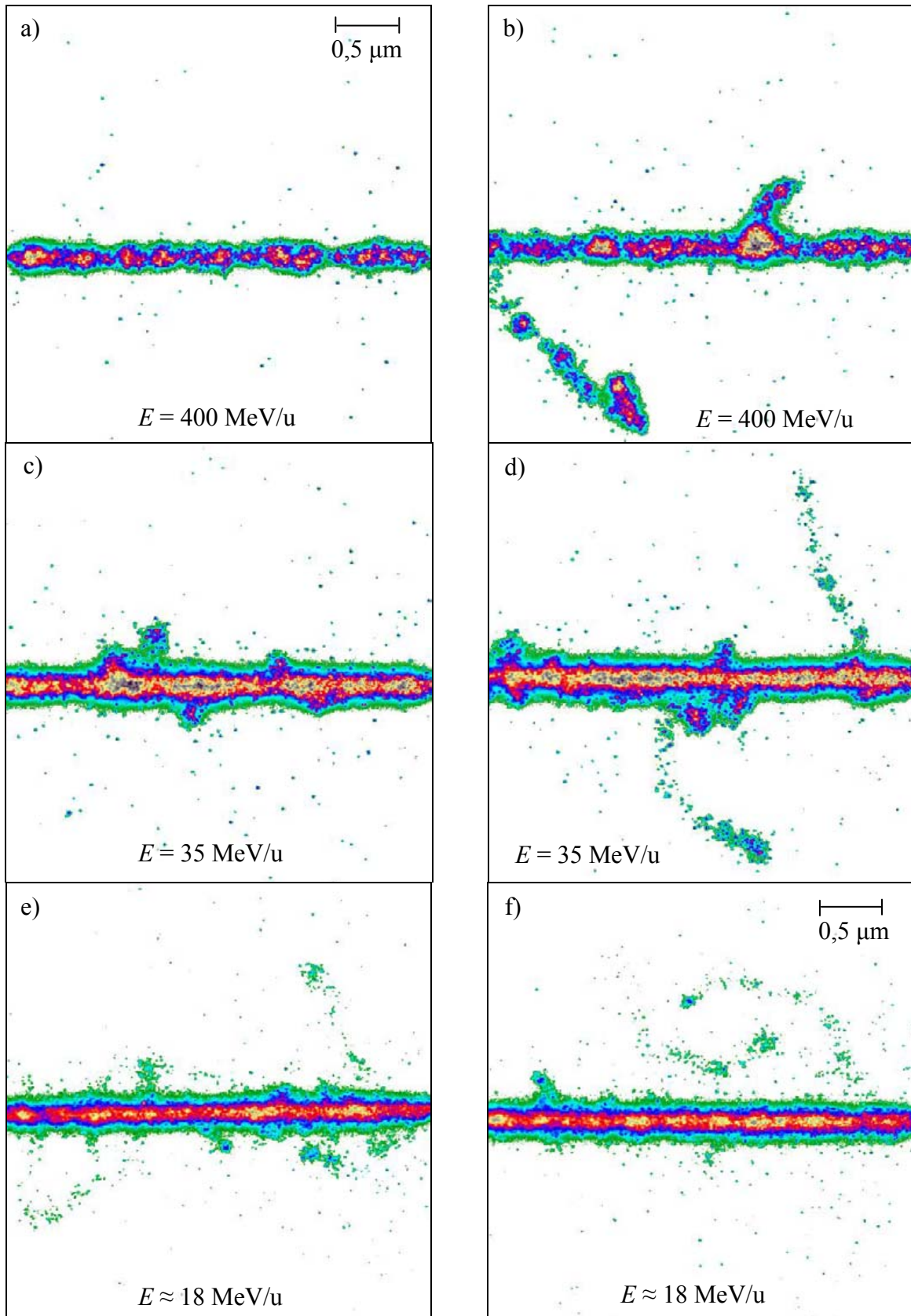
Figure 7.3: *Images of $^{12}C$ ion tracks at p = 10 hPa.*

$^{12}$C ion tracks imaged at $p = 4$ hPa, the lowest applied gas pressure in Figure 7.4. The ionization events in the region of the track core occur in clusters. This characteristic property of fast ion transport in matter is very well observable in Figure 7.4 a) and b). Such clusters

104

arise around δ-electrons with initial energies of several hundreds of eV and thus ranges of few tens of nm. Such ranges are in the order of magnitude of diffusion distances in OPAC at $p = 4$ hPa. Furthermore, most of the δ-electrons are emitted in forward direction under small angles. Although low energy electrons have short free paths and the scattering angle varies strongly, the length of the endpoint "blobs" (in the initial electron propagation direction) is typically greater than their width (perpendicular to the initial propagation direction). Due to this effect and due to the planar projection many δ-electrons with somewhat higher initial energy and a range of e.g. 100-200 nm appear in the images as clusters in the track core (see left side of Figure 7.4 b)).
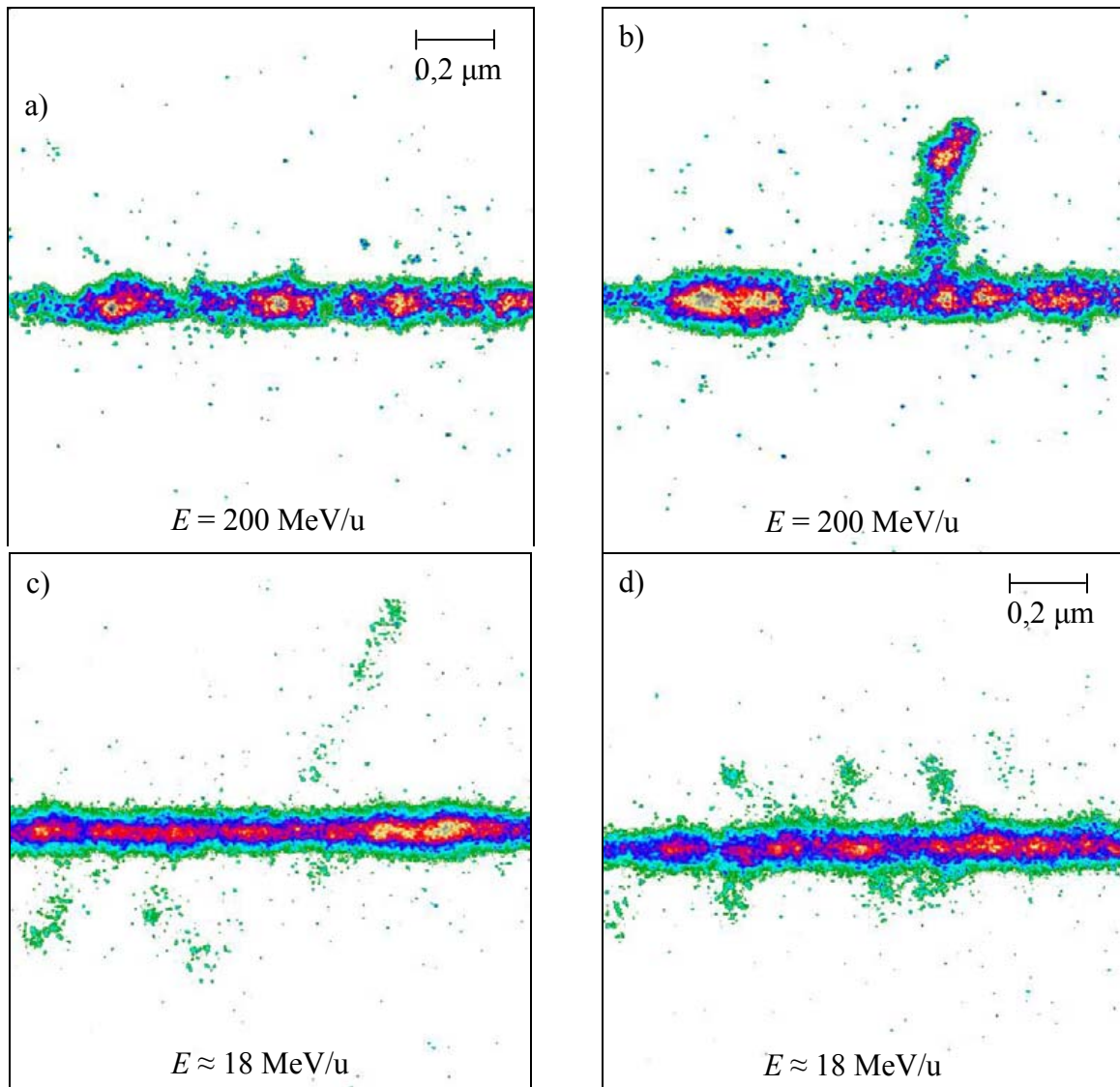


Figure 7.4: *Images of $^{12}C$ ion tracks at $p = 4$ hPa. $A_{c\&l}$ and $A_{MCP}$ gains are reduced at the lower ion energy.*

The ionization density along the track core is more homogenous in Figure 7.4 c) and d) due to the higher spatial frequency of ionization events and the lower average δ-electron energy at lower ion energy. Numerous δ-electrons are visible in Figure 7.4 d) which have an *y*-component of range of about 200 nm. Such δ-electrons are not distinguishable from the track core in Figure 7.2 due to the worse spatial resolution.

The images of Figure 7.2, Figure 7.3, and Figure 7.4 illustrate nicely the processes that take place if fast, heavy ions propagate though matter. Nevertheless, no reliable peak unfolding was possible due to the large number or overlapping electron peaks in the track core when

operating the detector at large gas amplification. This is the reason why the quantitative measurements were made in sampling mode, i.e. low gas amplification and high optical gain. A further complication of data analysis arises due to the application of the water column to produce the low energy ions from initially very high energies. The example of Figure 7.5 illustrates what happens when transporting and slowing down C-ions in matter from initially 400 MeV/u down to Bragg peak energies. This is quite similar to what happens in ion therapy where the radiation has to penetrate a certain layer of tissue before reaching the tumor where the ion has to reach Bragg peak energies and finally comes to rest. The six images are of very different character, but all of them were taken under the very same circumstances: 400 MeV/u $^{12}C$ ions were slowed down by the water column with a thickness of 273 mm. Like before high gas gain and low optical gain were selected for the measurement.

Due to the statistical characteristics of the ion stopping process the range of each ion differs slightly from the others (range straggling). In our experiment this translates, that at a fixed length of the water column, each single $^{12}C$ ion has a slightly different energy when passing the sensitive volume of OPAC (energy straggling). The length of the water column was calculated to slow down the 400 MeV/u $^{12}C$ ions to Bragg-peak energy when passing the detector (the additional water-equivalent thickness of 3,5 mm of the structure materials in front of the detector has to be taken into account). Due to energy straggling, the energies of the imaged carbon ions scatter to a large extend. Figure 7.5 d) shows a carbon ion being stopped inside the interaction volume of the chamber (real Bragg peak). Due to [Krm04], a $^{12}C$ ion has a remaining range of 5,1 μm, if it has an energy of 0,3 MeV/u, where the LET peaks. The comparison of the plotted unit corresponding to 2 μm in water and the range behind the estimated Bragg peak location, signed with the arrow, leads to a similar result. More precise determination of this parameter from the measurement results was not performed, because the measurement conditions were not optimal for this purpose. For example numerous pixel values are saturated close to the Bragg peak, i.e. the selected optical gain was too high. Only the first trigger detector on the incoming side of OPAC was operated for these measurements, otherwise the detector would not see an ion which is stopped inside the chamber, loosing its energy inside the interaction volume.

The amount of energy which the carbon ions of Figure 7.5 a), b) and c) deposit in the chamber can be derived from amount of light, which is the sum of the pixel values in the images. Let us term this quantity image integral, $I_I$. The image integral is proportional with the LET of the imaged particle, if the following conditions are fulfilled:
1. Measurements were made at the same gas amplification and optical gain.
2. The pixel values are not saturated.
3. Thermal and electronic noise of the IICCD system is corrected for or negligible.
4. All $\delta$-electrons are fully stopped inside the interaction volume. Otherwise, the image integral has to be corrected with a factor relating to the estimated ratio of energy $\delta$-electrons carry away, out of the chamber.
5. The particle should not be stopped inside the chamber and its LET should be approximately constant in the interaction volume. Otherwise, e.g. close to the Bragg peak, only a segment in $x$ can be treated and the result has to be normalized to the reduced volume.

As the measurement conditions were constant while imaging the tracks of Figure 7.5, the first condition is fulfilled. Compared to the very high light yields of the images a), b) and c) the noise of the IICCD system is negligible (in contrary to the case, described in chapter 6.5.2, where very low signal values at high radial distances are influenced by the IICCD noise significantly). Due to the low ion energies, the range of the $\delta$-electrons is low, thus the energy dissipated outside the interaction volume is negligible. However, it is not zero in the case of

Figure 7.5 a). The pixel values in the images a), b), and c) are not saturated (black color means pixel values above 700, while the saturation level is 2047).
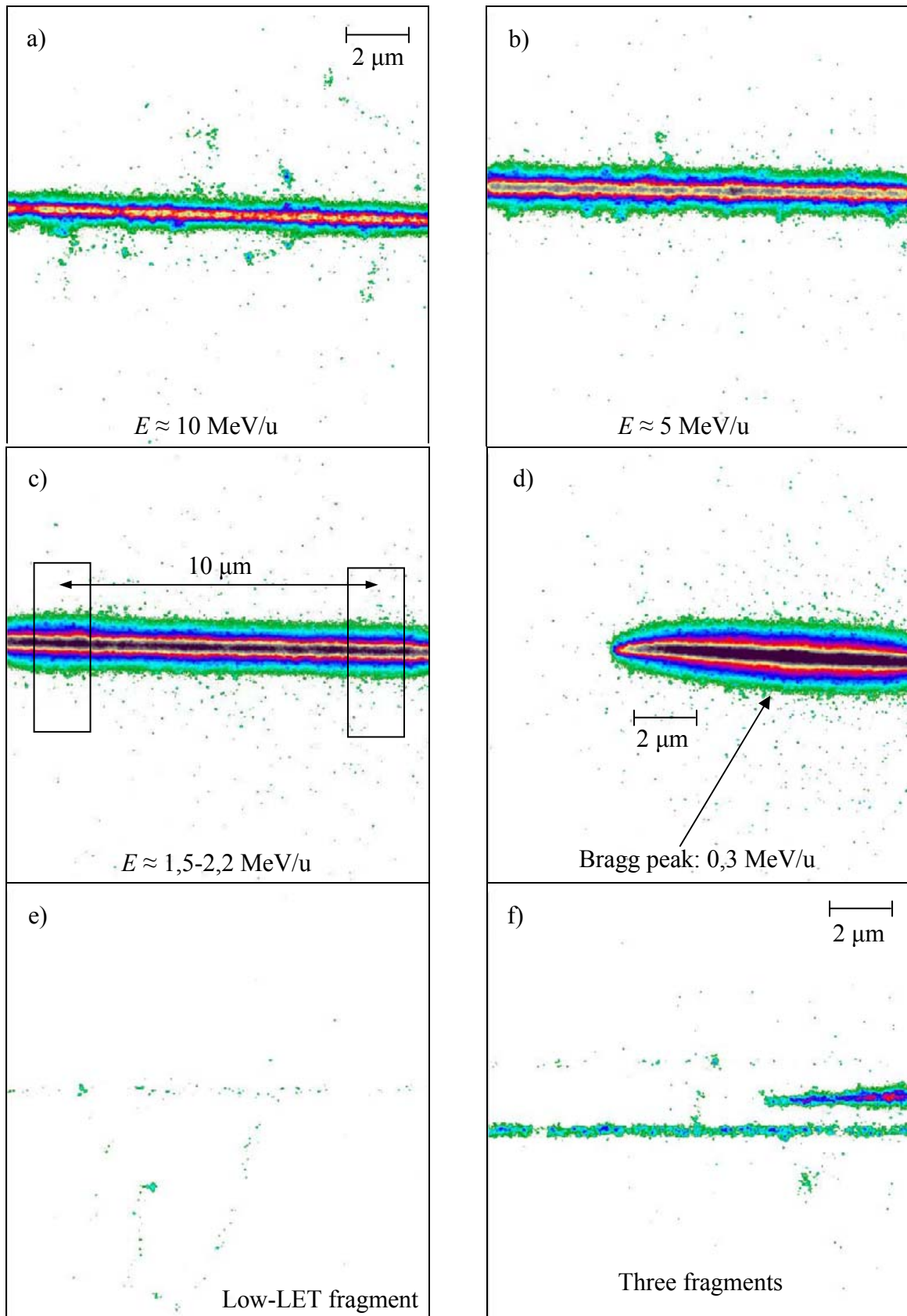


Figure 7.5: *Images of ion tracks behind a water column. $^{12}$C ion energy before traversing the column: $E_i = 400$ MeV/u; $p = 40$ hPa. The ions propagate from the right to the left.*

Unfortunately, the selected optical gain turns out to be too high in Figure 7.5, as there are numerous saturated pixels in the Bragg peak region in d). This inhibits the exact determination of the image integral at the Bragg peak which would otherwise be used as a reference at the maximum of the LET value of this ion. Figure 7.5 c) does not contain saturated pixels (already pixels with values of 30 % of the saturation level are black-colored). The LET of the track segment in Figure 7.5 c) is estimated to be about 500 keV/µm on the right- and 600 keV/µm on the left side of the image. These estimates are based on the comparison of the pixel integrals in the boxes in the left- and right side of Figure 7.5 c). It was found to be 20 % higher in the left side. According to the tables in [Krm04] the LET of the carbon ion must be 500 keV/µ to get increased by 20 % after a propagation of 10 µm in water (which is the water-equivalent distance between the both boxes). Due to the shape of the LET($E$) curve (see Figure 2.2 a)) there is an unambiguous correlation between the energy loss in 10 µm and the LET and thus the energy of a given ion (provided that the track has not yet reached its Bragg peak, i.e. the maximum of the curve). Taking into account the uncertainties of the pixel integrals in the boxes, a conservative estimate for the uncertainties of the values of 500 keV/µ and 600 keV/µm of 20 % follows.

According to the corresponding local pixel integrals and to the LET($E$) table in [Krm04] the energy of the ion in Figure 7.5 c) drops from (2,2 ± 0,7) MeV/u to (1,5 ± 0,4) MeV/u. As Figure 7.5 c) does not contain saturated pixels, the LET of the $^{12}$C ions, shown in Figure 7.5 a) and b), can be determined from the ratio of the corresponding image integral to the pixel integral (normalized to the amount of pixels) in one of the boxes in Figure 7.5 c). The achieved values are 160 keV/µm (± 20%) and 290 keV/µm (± 20%), respectively. The corresponding ion energies are (5 ± 1,5) MeV/u and (10 ± 3) MeV/u.

The energy straggling does not only cause a large variation in the energy loss of the traversing ions but also influences the microscopic properties of the track structure. Only stray light but no $\delta$-electron tracks can be distinguished from the track core in Figure 7.5 c) and d). This observation is explained by the fact, that the highest possible $\delta$-electron energy is about 4 keV due to the impact of a 2 MeV/u-ion. On the other hand, the track of Figure 7.5 b) shows many small irregularities in the direct neighborhood of the track core indicating the presence of $\delta$-electrons with ranges having $y$-components of several hundreds of nm, which extend well beyond the range of the central track core. Two end points of $\delta$-electron tracks are observable at a distance of about 1,5 µm from the track core. The track of Figure 7.5 a) is much more extended in $y$ (i.e. in $r$ as well). $\delta$-electrons due to the impact of a 10 MeV/u ion can have an initial energy of up to about 20 keV and a range of up to 10 µm.

The last two images of Figure 7.5 do not show tracks of carbon ions, but tracks of carbon fragments. As described in chapter 3.1, many of the carbon ions undergo nuclear reactions and are fragmentized while propagating through the matter (i.e. the water column). The lighter fragments have smaller LET values and thus a larger range at the same initial velocity as the original carbon ion. Therefore, various fragments of different masses and energies are present behind the Bragg peak region of the carbon ions. Figure 7.5 e) shows a low-LET fragment of $^{12}$C (probably proton) with a spectacular $\delta$-electron track together with its end point. Figure 7.5 f) is one of the few images, where three fragments of the same ion could be tracked in one image. The heaviest fragment has its Bragg peak in the interaction volume of OPAC, while the two other fragments, with strongly different LETs, traverse the chamber..
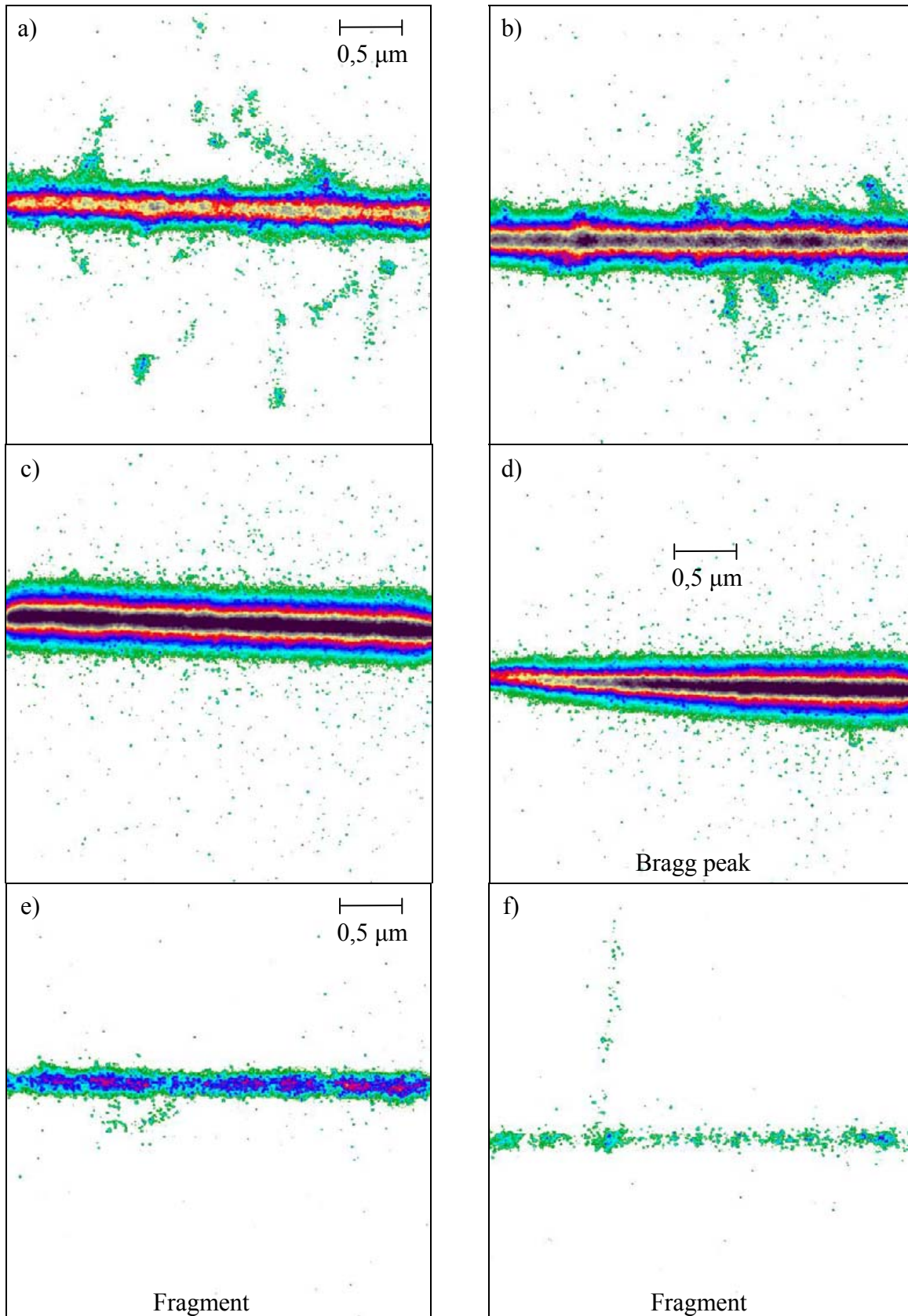
Figure 7.6: *Images of ion tracks ($^{12}C$ and its fragments) behind a water column; $E_1$ = 400 MeV/u; p = 10 hPa.*

Figure 7.6 shows tracks imaged behind the same water column as the tracks of Figure 7.5 but at $p$ = 10 hPa. The achievable light and charge amplification gain in the chamber is different

for different gas pressures and so far no efforts were made to determine the exact gain values. The optical gain was unfortunately selected too large because both the images c) and d) have regions with saturated pixel values. (The reason for the unfortunate choice of the optical gain was that due to the large energy straggling and fragmentation for this setting of the length of the water column a compromise had to be found between over- and underexposure of the various tracks - in fact the majority of the images were far from saturation.) We refrain from specifying estimated energy values for the carbon ions of the images a), b) and c).

Another set of measurements comprised imaging tracks of very heavy fast ions (Ar – U). The qualitative results of these measurements are less meaningful. With increasing Z of the ions the LET of the measured ion increases. To operate OPAC at stable conditions (i.e. small spark rate) the gas amplification had to be reduced accordingly. Figure 7.7 shows tracks of heavy and very fast ions. While the $\delta$-electron tracks around the argon ion are still well recognizable, they still can be anticipated in the case of krypton, but the low gain and thus the sparse sampling of ionization electrons inhibits a reconstruction of the copious $\delta$-electron tracks around the uranium track. If the heavy ions are slower, ionization densities are even higher and the gain in the chamber lower, thus the fain signal of the $\delta$-electrons vanishes even more. This effect does not affect significantly the quality of the quantitative results, as the gain reduction is same for the track core and for the halo around it and the methods of stray light subtraction (chapter 6.6) and peak halo elimination (chapter 6.5.5) can handle both cases without distortion.

The second major aim of the present work was to compare the track structure of different ions having similar LET. E.g. carbon ion at $E = 35$ MeV/u has an LET $= 59$ keV/$\mu$m and argon at 1600 MeV/u has an LET $= 67$ keV/$\mu$m. Hence, Figure 7.2 c), d) and Figure 7.7 a), b) are comparable in this sense. However, based on two single track segments it is of course not possible to quote significant and representative discrepancies between the track structures of the both ions. The most important difference of these 2 ion tracks might be observable at distances from the track core not any more accessible by OPAC: the largest range of the most energetic $\delta$-electrons in water is about 70 $\mu$m in the case of the 35 MeV/u ^{12}C and 1,5 cm! in the case of the 1600 MeV/u [40]Ar. However, the radial dose distribution around heavy ions at such high radial distances from the track core is not any more of great interest from the biophysical point of view.

Figure 7.8 shows [40]Ar and [84]Kr tracks at $p = 10$ hPa. Similar observations can be made as in the case of Figure 7.7.
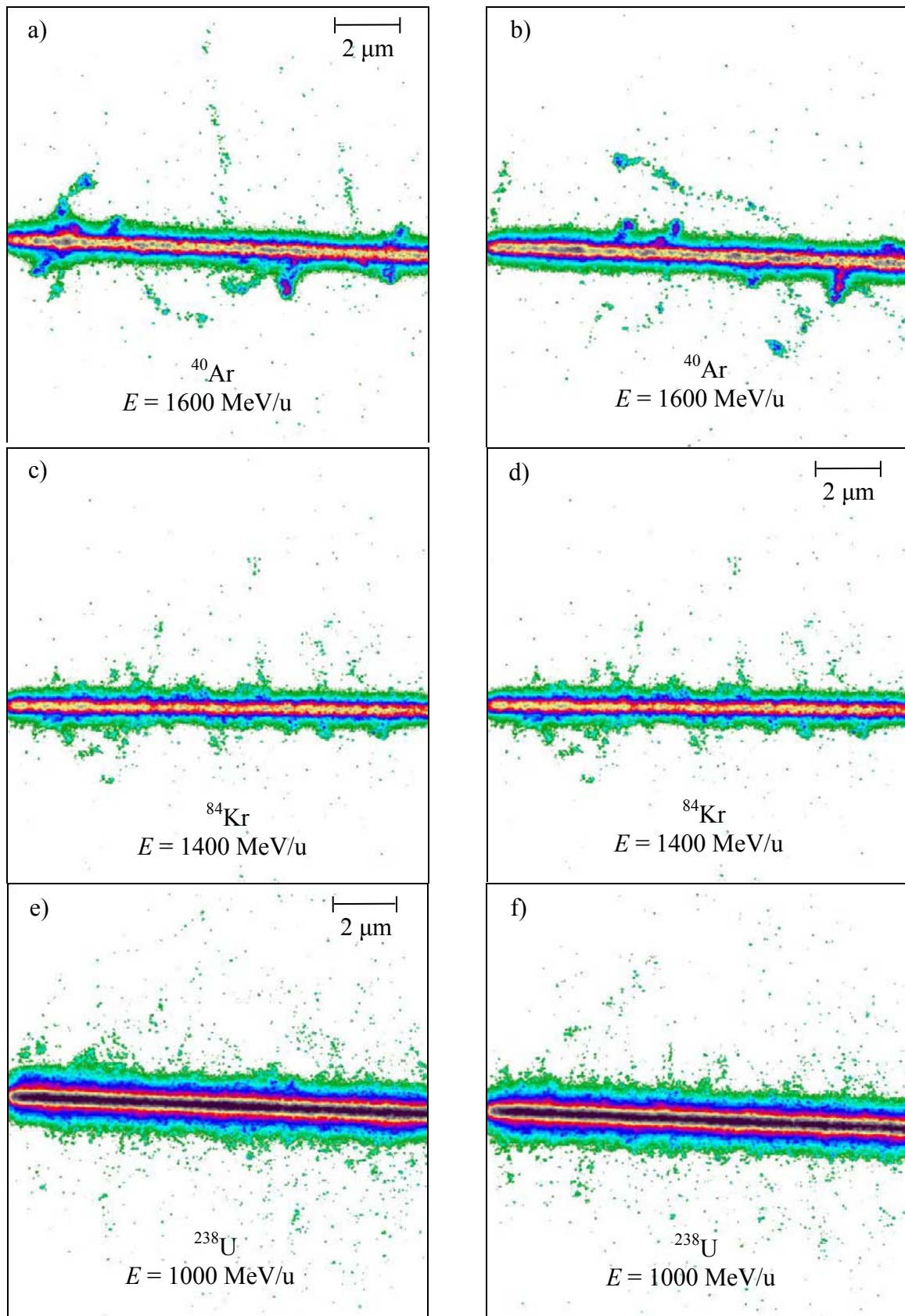
Figure 7.7: *Tracks of very fast heavy ions, imaged at p = 40 hPa. The gas amplification gain and the optical gain were selected for each ion individually, thus the integral light yields are not proportional with the deposited energies (or restricted LETs).*
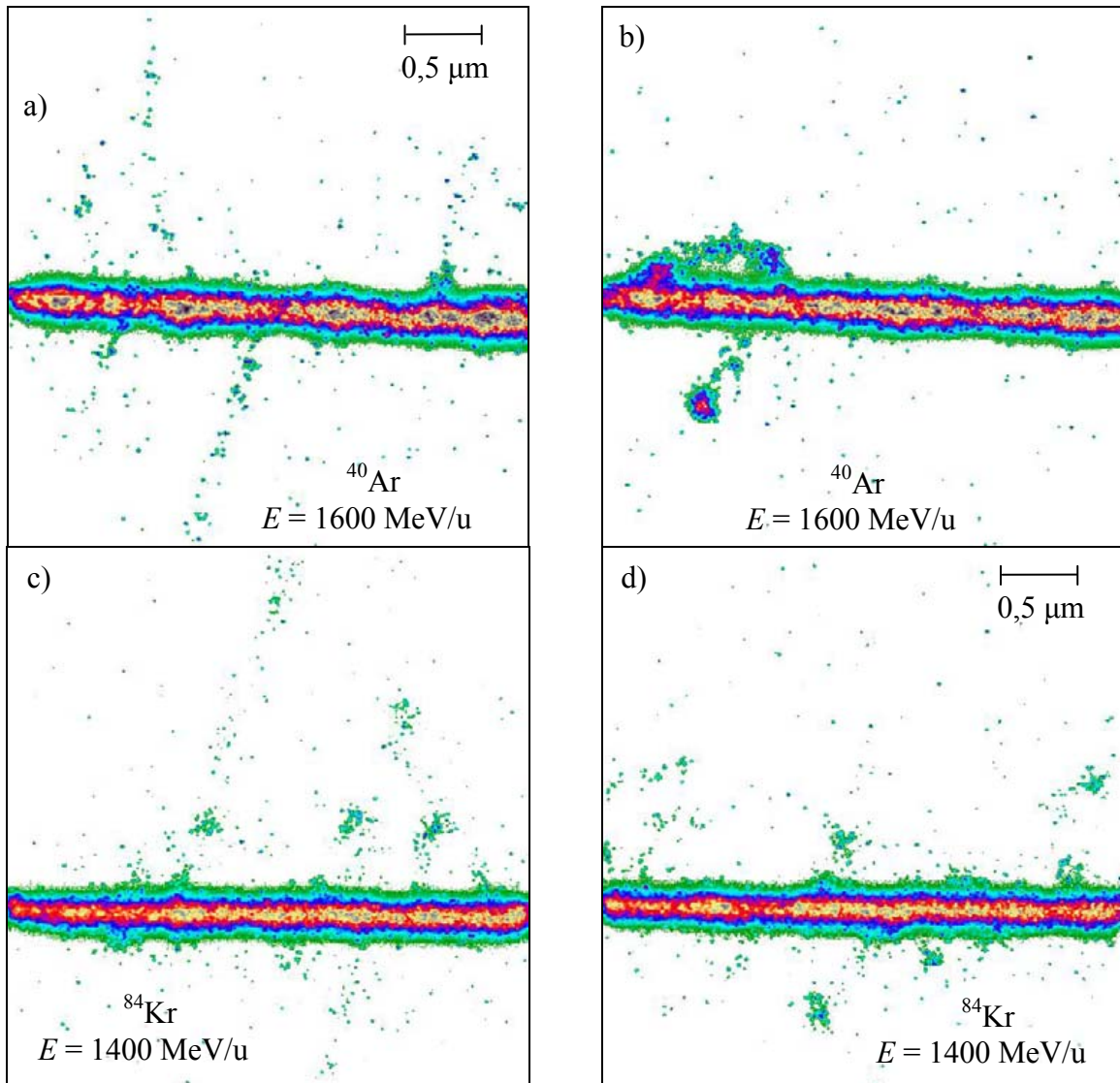
Figure 7.8: *Tracks of very fast heavy ions, imaged at p = 10 hPa.*

# 7.2  Quantitative results

## 7.2.1 Comparison of measured and simulated results

As described in chapter 6 in detail, the main condition to be fulfilled for benchmarking the simulated data with the measurement data is that simulations and measurements consider the same conditions and include the same artifacts (e.g. chamber response). Figure 7.9 shows the comparison of measured and simulated distributions. To assure comparable conditions the following data analysis was performed on the measured raw data:

1. Each image is cleared from the major part of thermal and electronic noise of the CCD camera.

2. If water column was applied, only those images are taken into account for further analysis, which have an image integral, $I_I$, (see chapter 7.1) inside a "window". Images with too low light yields correspond to tracks of fragments. On the other hand, there are a few images with extraordinary high light yields due to energy straggling or scattering in solid matter.

This image selection can be a source of relatively high errors. (For more details see chapter 7.2.2.)

3. A straight line is fitted to the ion trajectory of each measured image. The fitting algorithm does not take into account the $\delta$-electron tracks, which are separable from the track core. The results of this step are two parameters: $a$ and $b$ which describe slope and position of the line in the two dimensional frame of the CCD image.

4. The iterative peak unfolding process is applied on each image in order to subtract the peak halos (see chapter 6.5.5). The results of this procedure are position coordinates $(x_i, y_i)$ and expectations values $<n_{sp}>_i$ for the average number of electrons of the $i^{th}$ peak.

5. The light yield distribution as a function of the projected radial distance $(y)$ from the central track is calculated by summing of all $<n_{sp}>_i$ values as a function of the distance of $(x_i, y_i)$ peak location from the line, described by the parameters $a$ and $b$. All peaks of all images belonging to one ion and parameter set are summed up into one distribution.

6. The light yield distribution function is corrected for stray light contribution by subtracting the stray light distribution function according to chapter 6.6.

7. The resulting projected radial dose distribution function is than plotted as a function of $y$, where $y$ is given in nm. The conversion from the directly measured pixels to the water equivalent in nm is given by the optical transfer function of the system and the gas pressure (see chapter 4.1).

To compare the measured and analyzed data with the results of TRAX the simulation was made regarding the following conditions:

1. The environment for the Monte Carlo simulation is defined according to the OPAC-circumstances: same geometry and water vapor density are assured for the simulations as given in the measurements (see chapter 6.1). However, the simulation of the stainless steel meshes and potential rings and the electric fields inbetween (see Figure 5.5) is not included. 100 to 10000 primary ions are simulated depending on the LET to achieve a good statistics within a reasonable computation time.

2. The diffusion of the thermalized ionization electrons is simulated as described in chapter 6.3.2. A constant Gaussian broadening from the optical resolution function, independent on drift length and pressure, is added to the electron diffusion broadening (see chapter 6.5.6). This modification is negligible if $p < 15$ hPa.

3. The projected radial dose distribution function is determined by counting each diffused-thermalized electron of each simulated track as a function of the distance of the given electron from the track core.

Figure 7.9 contains the measured and simulated distributions of the projected radial dose of carbon ions at five different ion energies. All functions are normalized to the total sum of electrons present in the interaction volume. I.e. the ionization electrons were summed up just inside the interaction volume of OPAC, neglecting the contribution by energetic $\delta$-electrons which leave the chamber volume. The defect on lost deposited energy by the escaping electrons is, of course, larger for faster ions (e.g. with an energy of e.g. $E = 92$ MeV/u) than for slower ones - e.g. at 7,3 MeV/u all delta electrons are stopped in the chamber.

Thus, Figure 7.9 just serves as a tool for comparison of one common artificial parameter of the measured and simulated tracks at five ion energies. This is the reason why the values are given in arbitrary units. For data with more physical and biophysical relevance, see the next chapters.
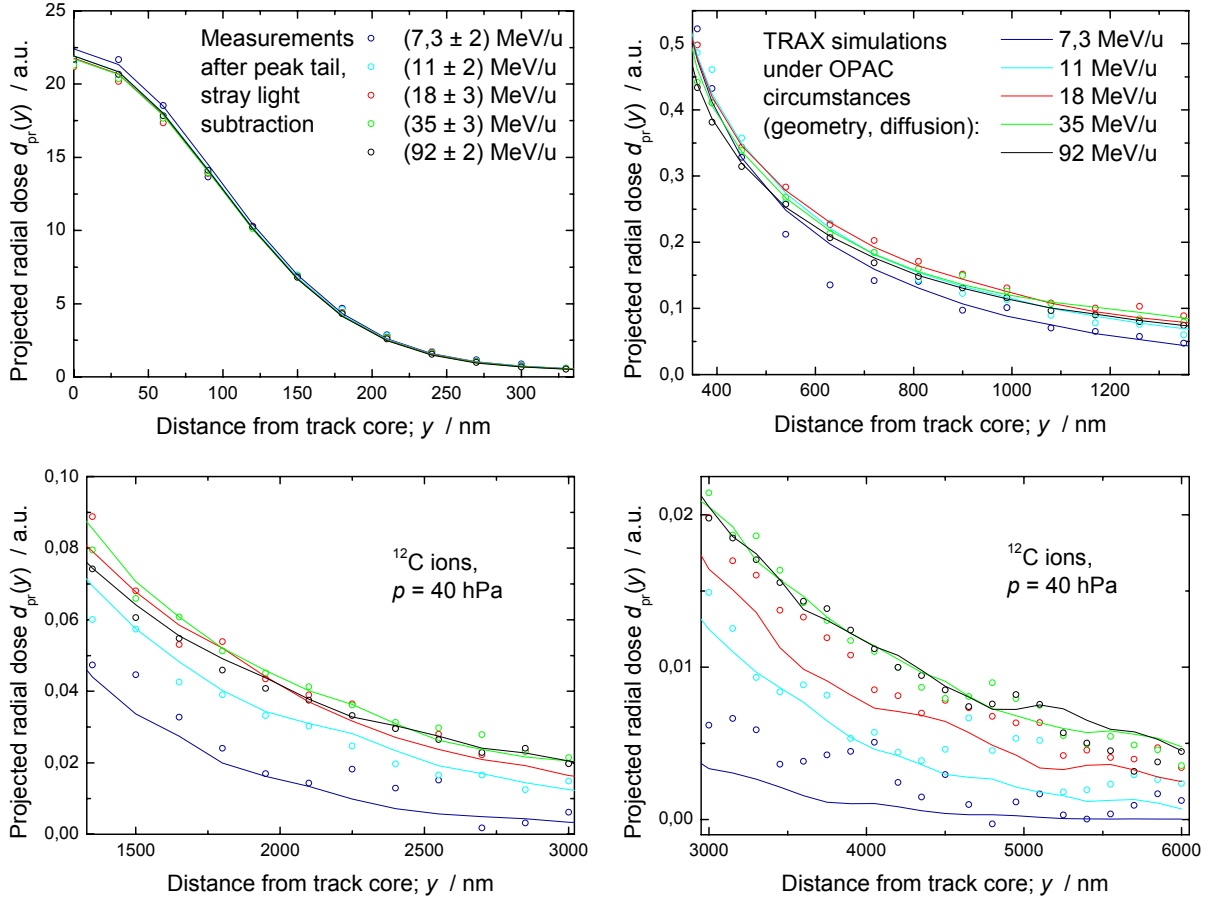
Figure 7.9: *Comparison of measured and simulated projected radial dose distributions (p = 40 hPa). The four diagrams display the same functions in four ranges of y. All distributions are normalized to a common yield of electrons in the interaction volume of the chamber.*

One pixel in the image corresponds to 30 nm at $p = 40$ hPa. The derived projected radial dose data is not plotted pixel by pixel in the whole range of Figure 7.9. The presence of all function values would obscure the diagram and make the comparison of simulated data (lines) and the measured distribution (symbols) difficult. Furthermore, the statistical uncertainties of the radial dose values at high $y$ if each single pixel resolved are too high and that spatial precision is not even desired. Therefore, a binning of neighboring function values was applied for $y > 600$ nm. Three values were binned in the region of 600 nm $< y <$ 1300 nm and five values if $y > 1300$ nm.

The discussion of the results starts with the fourth diagram in Figure 7.9 which represents the data at large radial distances. The measured distributions at the lower ion energies at large radial distances have large statistical fluctuations. It can be explained by the large energy straggling when using a water column to reduce the initial ion energy of 400 MeV/u to energies close to the Bragg peak. E.g. a water column thickness of $t_w = 273$ mm is needed in order to reduce the initially high ion energy of $E_1 = 400$ MeV/u to $E_1 = 7,3$ MeV/u. (The same length of the water column which is used for imaging of the tracks in Figure 7.5)

The large energy straggling and fragmentation requires a selection of images belonging to a defined ion-energy out of the whole set of measurements with its wide energy distribution. Only those images are chosen for the analysis, for which the image integral, $I_I$ is inside a certain window:

$$I_{Imin} < I_I < I_{Imax} \tag{7.1}$$

The mean image integral of all images, $\overline{I_{\mathrm{I}}}$, fulfilling the criteria (7.1) is than calculated. The mean LET of the considered tracks can be estimated based on the $\overline{I_{\mathrm{I}}}$ value in the same way as explained in respect to Figure 7.5 in chapter 7.1. The expectable energy of the considered ions is than estimated according to [Krm04] LET-ion energy table.

The application of the criteria (7.1) has two consequences:

1. The images that have $I_{\mathrm{I}} < I_{\mathrm{Imin}}$ or $I_{\mathrm{I}} > I_{\mathrm{Imax}}$ do not contribute, which results in a reduction of the number of "valuable" tracks. E.g. in the case of $E_1 = 7,3$ MeV/u only 45 images out of 486 recorded images could be used for the derivation of the $d_{\mathrm{pr}}(y)$ function.

2. It is impossible to define $I_{\mathrm{Imin}}$ and $I_{\mathrm{Imax}}$ in a way that assures a precise selection in the ion energy. Even if no water column is applied, there is a difference in the $I_{\mathrm{I}}$ values of single ions of up to a factor of two (up to a factor of three at $p = 4$ hPa). This is due to the statistics of the energy transport and detecting processes. Therefore, $I_{\mathrm{Imax}}$ was selected to be:

$$I_{\mathrm{Imax}} = 3 \cdot I_{\mathrm{Imin}} \tag{7.2}$$

Due to the energy straggling and due to the statistical variation of the correlation between $I_{\mathrm{I}}$ and E the energy corresponding to a certain $I_{\mathrm{I}}$ - window can only be given with a certain uncertainty. In Figure 7.9 the ion energies corresponding to the measured distributions are given with uncertainties. E.g. $E_1 = (7,3 \pm 2)$ MeV/u has to be interpreted in that way, that at least 68,3% of the considered ions had an energy in the interval of [5,3 ; 9,3] MeV/u. This is a conservative estimate.

Now, if taken into account that only 45 images were considered which are also distributed over a relatively large energy range, the statistical fluctuations of the radial ionization distribution for slow ions (dark blue symbols in the fourth diagram of Figure 7.9) is not surprising. The corresponding simulated function has only very small values at the large radial distances plotted in the last diagram and drop practically to zero for $y > 5000$ nm. The values of the measured distribution are significantly higher. These discrepancies are supposed to have two reasons:

Firstly the rather large energy window due to the before mentioned effect of energy straggling: Due to the energy selection process part of the ions have energies above 7,3 MeV/u. They produce energetic $\delta$-electrons which transport dose in the regions which otherwise would not be in the range of the fastest electrons of the nominal energy value of 7,3 MeV, which is used in the simulation. Furthermore, it is also possible, that the estimate of the mean energy of 7,3 MeV/u is not exact, due to the stochastic nature of the $E(I_{\mathrm{I}})$ correlation (the interval of $\pm 2$ MeV/u includes this uncertainty). Secondly, the uncertainty of the TRAX simulation results is also not negligible at large radial distances, i.e. around the cutoff distance of the radial dose. This is due to the many interactions, the fastest $\delta$-electrons have to undergo before getting thermalized through which uncertainties related to each interaction are accumulated.

It would have been easy to perform much more precise measurements with OPAC in order to specify radial dose distribution at low energy in this critical $y$-region. $^{12}$C ions of much lower energy can be provided e.g. by UNILAC at GSI. OPAC could be directly connected to the accelerator via a thin vacuum window with only a thin energy degrading foil to obtain the required energy of about 11 MeV/u even by direct adjustment by the accelerator. For the cases of $E_2 = 11$ MeV/u and $E_3 = 18$ MeV/u in Figure 7.9, the role of energy straggling is less pronounced. The thicknesses of the applied water columns are 271,7 mm and 270,5 mm, respectively. A carbon ion at $E_2 = 11$ MeV/u has a remaining range of about 0,5 mm in water and that of $E_3 = 18$ MeV/u has a range of about 1,2 mm [Krm04]. These values exceed the extent of range straggling, hence the scattering of the image integral values of individual

images is less strong. The ion energy values were determined according to the overall water-equivalent thicknesses of the material in front of OPAC. These calculations were evaluated by comparison of the $\overline{I_\mathrm{I}}$ values at e.g. $E_2 = 11$ MeV/u with $\overline{I_\mathrm{I}}$ values of measurements with exactly known LET (e.g. at $E_5 = 92$ MeV/u). For this the operation parameters of the chamber (gas amplification and optical gain) and the "lost" energy due to long range $\delta$-electrons have to be carefully considered. The estimated uncertainties of $E_2$ and $E_3$ are given in Figure 7.9.

The agreement of the measured and simulated distributions at the energies of 11 and 18 MeV is much better than that at 7,3 MeV. The reason for this is that the statistics is much better because at higher energies more images fulfill the criterion of (7.1) and the energy determination is more precise, e.g. the energy window ((7.2) can be defined narrower. Furthermore, the qualitative difference between the shapes of the $d_\mathrm{pr}(y)$ distributions for slightly different ion energies is less pronounced at higher ion energies.

Almost perfect agreement is observable between measurements and simulations at the highest energies in Figure 7.9 ($E_4 = 35$ MeV/u and $E_5 = 92$ MeV). The ion energy of 92 MeV/u was directly produced by the accelerator (originally 100 MeV; slightly degraded in the foils and gases in front of OPAC). Ions of 35 MeV/u were produced with the water column from initially 400 MeV/u. The required length of the water column for this energy reduction is $t_\mathrm{w} = 267,5$ mm. The energy straggling does not play a very important role in these cases. Furthermore, more than 1300 images were available for the analysis in both cases.

As discussed before, the OPAC-specific geometry and response function do not allow the drawing of physical conclusions directly (i.e. before applying the radial unfolding method, see chapter 6.2). However, it is possible to examine, if the shape of the $d_\mathrm{pr}(y)$ distributions follow similar tendencies for the measured curves as for the simulated ones. In this sense, it is useful to compare the relative shapes of $d_\mathrm{pr}(y)$ distributions at different energies.

In spite of the high uncertainties in ion energies and the insufficient amount of available images, it is true for both the measured and the simulated distributions, that in the $y$-region of the last diagram ($y > 3000$ nm) the values for the 7,3 MeV/u ions are significantly lower, than the corresponding $d_\mathrm{pr}(y)$ values for ions at higher energies. The second lowest values belong to ions of 11 MeV/u and the third lowest values to ions of 18 MeV/u energy.

The simulated data predict that the shape of the $d_\mathrm{pr}(y)$ distribution for $3$ μm $< y < 6$ μm (see last diagram in Figure 7.9) is practically the same for the ions with an energy of 35 and 92 MeV/u. This is confirmed by the experimental results. The experimental data in this region do not differ significantly at $E = 200$ and 400 MeV/u either - in line with the predictions of the simulations. (These distributions are not plotted in Figure 7.9 in order to avoid confusion.)

The third diagram in Figure 7.9 presents the projected radial distance region from $1,3$ μm $< y < 3$ μm. The $d_\mathrm{pr}(y)$ distribution for 7,3 MeV/u is still the lower than the ones at higher energies. The agreement between simulation and measurement improves compared to the larger radial distances due to the better ionization statistics in this range. While the functions for 11 MeV/u also remain below the high-energy reference (92 MeV/u, black curve and symbols in Figure 7.9) in the whole region, the functions corresponding to the moderate energies tend to be the highest for $y < 2$ μm. This tendency is visible on both data sets, (i.e. simulations and measurements).

The second diagram in Figure 7.9 ($350$ nm $< y < 1300$ nm) shows excellent agreements between the predictions of TRAX and measured distributions of OPAC. The only exception is the strong statistical errors of the data points for 7,3 MeV/u. For $y > 1$ μm the values for medium energies (18 and 35 MeV/u) are the highest (both in the cases of the measurements and simulations). The 11 MeV/u curve exceeds the 92 MeV/u curve at $y < 1$ μm and it

exceeds the 35 MeV/u curve at $y < 700$ nm. Very similar relations are valid in the case of the corresponding measured data, too. And finally, the 7,3 MeV/u curve and symbols (again together) exceed the black at $y < 500$ nm.

The shape of the first diagram in Figure 7.9 is determined by the diffusion. Due to normalization by the total hit amount and the dominating role of diffusion at low radial distances, no significant differences in the curve shapes are observed. The folding of the simulated electron distribution with the diffusion of the electrons in the gas and the optical broadening reproduces the measured data very well.

It can be concluded, that for carbon ion energies, where the water column was not used ($E_5 = 92$ MeV/u) or did not affect significantly the energy definition of the tracked ions ($E_4 = 35$, $E_3 = 18$ and $E_2 = 11$ MeV/u) surprisingly good agreement was found between the shape of the measured and simulated $d_{pr}(y)$ distributions. E.g. at $E_5 = 92$ MeV/u the relative difference between the measured and simulated $d_{pr}(y)$ values is less than 5% for any $y$ if $y < 4,5$ μm. And only the relatively small number of both measured and simulated tracks and the low ionization density at large radial distances causes larger statistical discrepancies for higher $y$ values. The somewhat inferior agreement at lower ion energies can mainly be attributed to the inconvenient method, used to produce the low ion energies. Further studies and discussion of the reasons for the slight discrepancies and for the uncertainty analysis of the measured $d_{pr}(y)$ distributions can be found in chapter 7.2.2.

Figure 7.10 presents the same plots as Figure 7.9, but for a pressure of $p = 10$ hPa (instead of 40 hPa) in the OPAC chamber. The lowest carbon ion energy was 4,4 MeV/u in this case. The number of images for the lowest energy was larger than in the examples in Figure 7.9 (330 instead of 45). This is the reason of the quite good agreement with the simulated curve. However, at smaller radial distances (120 nm $< y < 700$ nm) the agreement between the measured and simulated distributions is worse. The same holds for the case of the two highest ion energies plotted in Figure 7.10. The simulated $d_{pr}(y)$ values are higher by up to 20% than the corresponding measured values. For $y < 120$ nm, the effect of diffusion determines the behavior of the curves and masks the small differences in the curve shape. For the medium ion energies (12 and 18 MeV/u) the agreement between the simulated and measured distributions is better compared to the high energy cases. Discrepancies of up to 10% appear only below $y = 300$ nm in these cases.
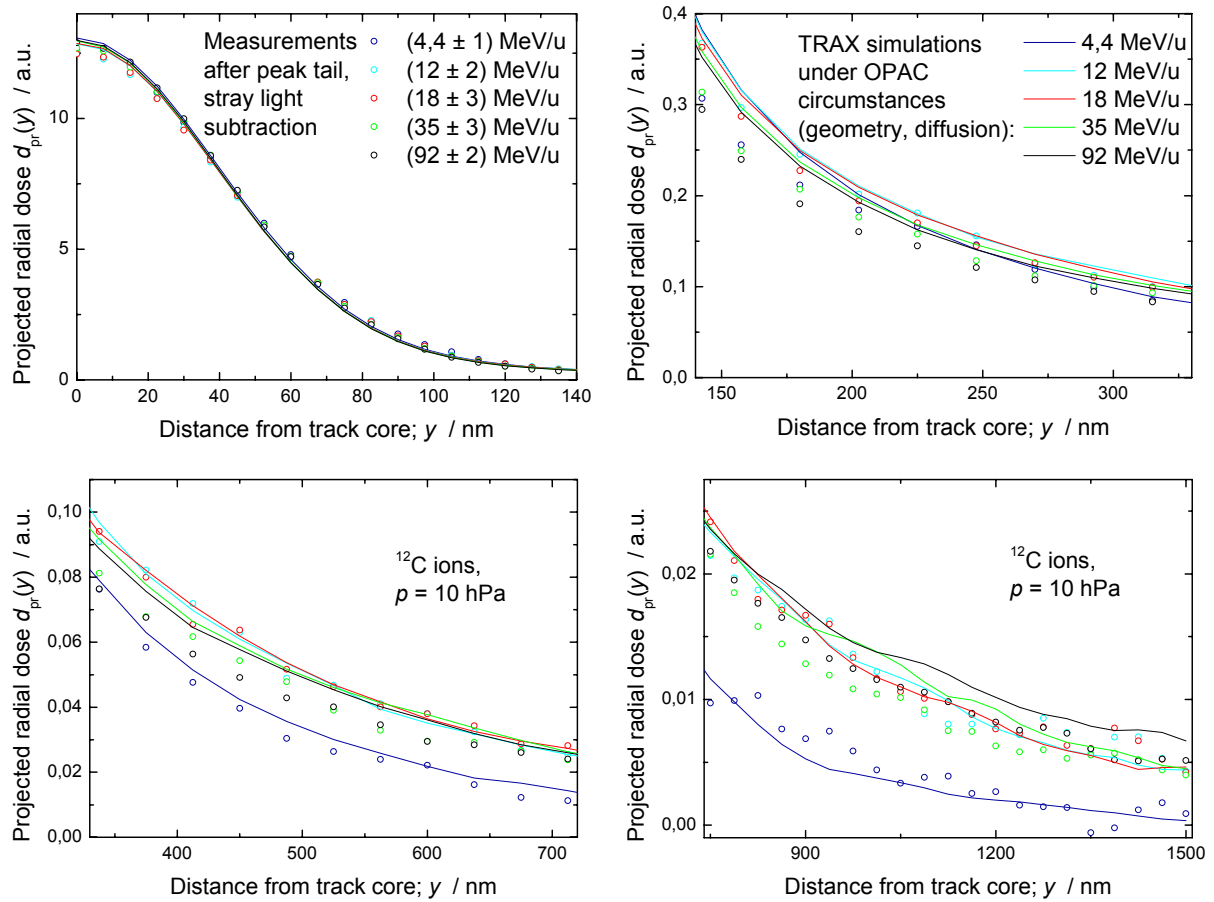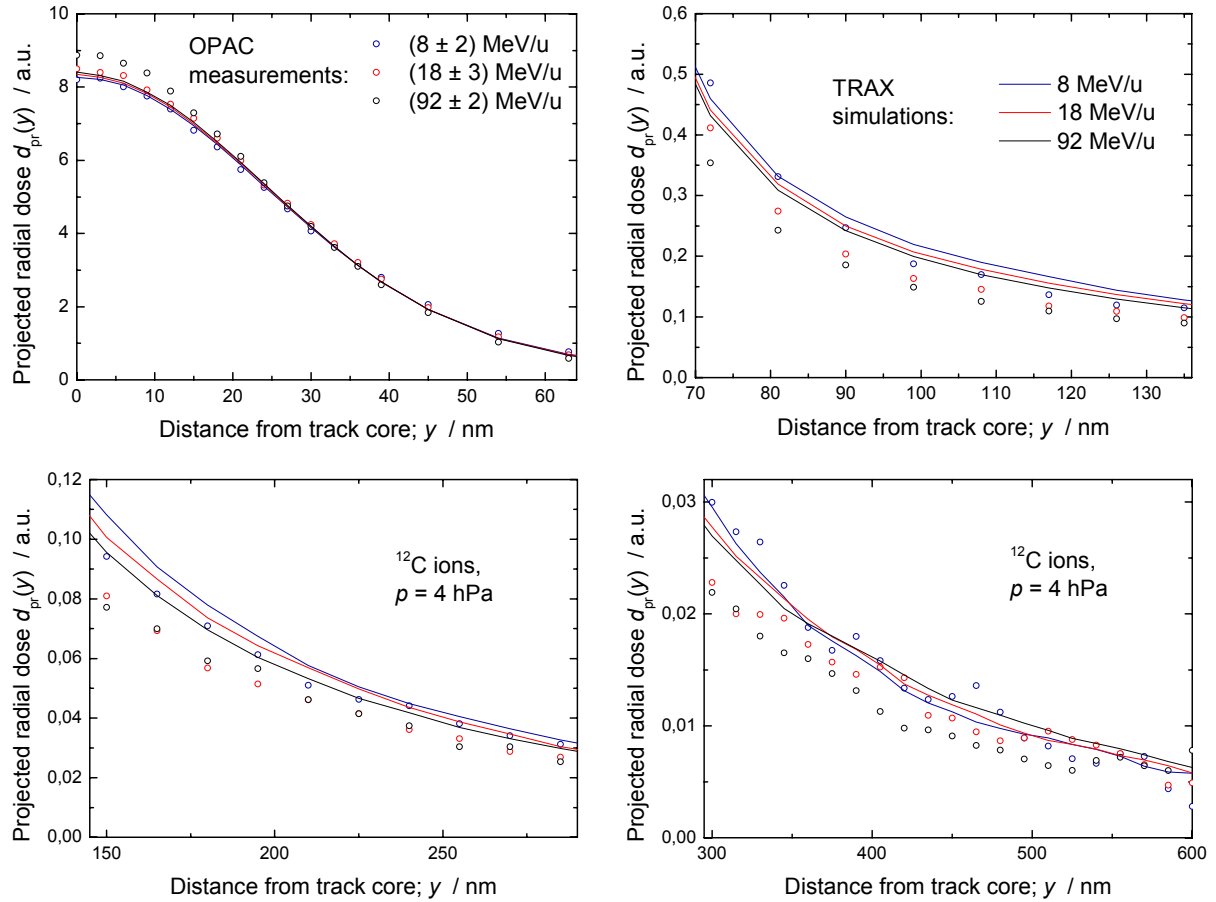
Figure 7.10: *Comparison of measured and simulated projected radial dose distributions (p = 10 hPa). The four diagrams display the same functions in four ranges of y. Like in Figure 7.9, all distributions are normalized to a common yield of electrons in the interaction volume of the chamber.*

It should be noted, that the direct comparison between Figure 7.9 and Figure 7.10 is not straightforward due to artefacts caused by the projection. E.g. the value of $d_{pr}(y)$ at $y = 1200$ nm arises as a projection of ionization electrons from a radial distance of 1200 nm $< r <$ 1380 nm from the track core at $p = 10$ hPa (see chapter 6.2). At $p = 40$ hPa, $y = 1200$ nm corresponds to 40 pixels. In this case, $d_{pr}(1200$ nm$)$ is a projection of electrons from a radial distance range of 1200 nm $< r <$ 2950 nm. I.e. the two distributions at identical $y$ value average over different radial distance ranges. For low projected radial distances, $y$, the comparison is further complicated by the diffusion of drifting electrons. While the distances between interactions of interest vary proportional with the pressure, the extent of diffusion varies proportional with the square root of the pressure. I.e. at the lower pressure of 10 mbar in Figure 7.10 the distribution at $y = 150$ nm ($\approx 3 \cdot \sigma$) is not affected significantly by diffusion while in the case of $p = 40$ hPa (Figure 7.9), $y = 150$ nm corresponds to only about $1,5 \cdot \sigma$, thus the diffusion largely determines the shape of $d_{pr}(y)$ (see chapters 6.3.3 and 6.6).

Figure 7.11: *Comparison of measured and simulated projected radial dose distributions (p = 10 hPa). The four diagrams display the same functions in four ranges of y. Like in Figure 7.9, all distributions are normalized to a common yield of electrons in the interaction volume of the chamber*

Figure 7.11 was derived in the same way, as Figure 7.9 and Figure 7.10 for the case of $p = 4$ hPa. As shown in chapter 6.5.6, track broadening due to the optical system is negligible at this low pressure; therefore, the observed broadening is only determined by the diffusion of the drifting electrons in the gas. The measurements at 4 hPa enable the best spatial resolution, achieved with OPAC so far. Diffusion determines the shape of $d_{pr}(y)$ distribution up to about $y = 60$ nm and its effect is visible in the $d_{pr}(y)$ up to about $y = 100$ nm ($\approx 3 \cdot \sigma$). For larger radial distances a spatial resolution of about 10-15 nm is achievable. Similar to the case of $p = 10$ hPa, the simulated $d_{pr}(y)$ distribution has always higher values than the measured distribution. The best agreement can be found for the lower ion energies at $y > 250$-300 nm.

## 7.2.2 Uncertainty analysis of the measured and simulated distributions

A common reason for the slight discrepancies between the measured and simulated distributions could not be identified so far. Both, the measured and the simulated data, are affected by various uncertainties. The main sources of possible errors of the data acquisition and data analysis process are the following:

1. The spatial distribution of charge amplification and light scintillation in the gas filled chamber of OPAC is not perfectly homogeneous. The inhomogenity of the gain is also not stationary over time due to aging of the amplification grids during the operation of the

chamber. It is also more pronounced at lower pressures and higher gain. The precise study of this artefact was not yet performed, because a very homogenous source of thermalized electrons, coming from the interaction volume of the chamber, would be needed for the quantitative comparison. An upper estimate of error due to this effect is 5%.

2. Also the IICCD system (see Figure 5.2) has a slightly inhomogeneous spatial response. This has a number of reasons like spatial variation of the quantum efficiency of the photocathode or gain inhomogenity of the MCP stack etc. An upper estimate of uncertainties in the measured $d_{pr}(y)$ values due to this effects is 5%.

3. The relative uncertainty due to the peak halo subtracting algorithm was estimated to be less than 5% in the whole radial distance region measured in these experiments (see chapter 6.5.6).

4. The estimated relative uncertainty induced by stray light and the associated subtraction process is given in Appendix 10.2.

5. The application of the water column as energy degrader is responsible for further uncertainties in the case of the low ion energies (see details about the phenomenon in chapter 7.2.1). The extent of relative uncertainty due to the uncertain energy definition has to be estimated for each measurement individually. The estimate is given by performing the simulation of the $d_{pr}(y)$ distribution for the lower and the upper limit of the estimated energy window. E.g. in the case of the 7,3 MeV/u $^{12}$C ions, where the uncertainty of the energy is given as ± 2 MeV/u, the $d_{pr}(y)$ distribution is simulated for 5,3 and 9,3 MeV/u as well. The searched uncertainty – as a function of the projected radial distance – is determined according to the discrepancies in the $d_{pr}(y)$ values for the different energies. In the case of 7,3 MeV/u $^{12}$C ions, the relative uncertainty reaches 40 % for $y = 200$ pixels.

6. There are also various sources of events accompanying the traversal of an ion which may obscure the measurement results: The effect of energy straggling and fragmentation when using the water column was already discussed in chapter 7.2.1. But also without the water column in front of OPAC there is always a fraction of lighter ions from fragmentationation of the original ion in the entrance window of OPAC or other material in front of the device. Fragments have lower LET and thus lower $I_I$ (image integral) values, than the ions of the original species. It may also happen that an ion passes the interaction volume after scattering in the chamber wall of OPAC or in other solid material. In this interaction the ion may loose significant energy and in consequence has higher LET and deposits much larger energy in the chamber. In some cases, the traversal of an ion causes the trigger detector to spark. In this latter case, additional light from the discharge obscures the image. A further possible problem was the occasional presence of two $^{12}$C ions in the image at the same time. In order to reject such artefacts a window for $I_I$ was applied to the images to select only valid ones for the further analysis. In the data sets, measured without the use of the water column, only about 5% of the images were rejected by this filter. Nevertheless, it is possible, that some of the images were rejected by mistake (i.e. the very high or low $I_I$ was not due to one of the effects, described above but due to statistics) or images of wrong ion species which fit the selection criteria were not rejected by the procedure and thus upset the result. The contribution to the relative error of $d_{pr}(y)$ due to this artefact is depending form the radial distance to the track core. We estimate the effect on the $y$-distribution to be less than 2%.

7. The electron collection efficiency in a parallel-plate ionization chamber is not 100% because of the initial recombination of the free electrons with the positive ions, left behind. Kanai et. al [Kan98] study the extent of the initial recombination in several different gases at atmospheric pressure. The extent of the recombination increasing with

decreasing angle between the propagation direction of the ion and the electric field (no data is shown for angles above 45° - this angle is 90° in the case of OPAC). Furthermore, higher LET of the ion or lower electric field in the chamber result in a higher initial recombination as well. E.g. in the case of 135 MeV/u carbon beam passing the chamber - filled with air; electric field: 400 V/cm - under an angle of 45° the ratio between the produced and the collected charge remains under 1,01. However, it is not possible to assess the recombination coefficient for TEA compared to that for air, we can assume, that the much lower gas pressure and the projection angle of 90° assure a very low initial recombination in the measurements with OPAC. Therefore, we neglect this effect in the uncertainty analysis.

The main uncertainties of the models and cross section tables applied by the Monte Carlo code, TRAX, were described in chapter 3.3.4.2 and chapter 3.3.5. Here we mention only some of the possible sources of uncertainty in the case of simulation of $^{12}$C tracks, without analyzing their effect on the simulation results:

1. No comprehensive set of cross section data is available for TEA; mainly semi-empirical cross section data for water vapor is applied.

2. The applied model for $\delta$-electron production due to ion impact is the BEA. The model simplifies the $\delta$-electron production process largely, neglecting e.g. the effect of Cusp- and Auger electrons and those from peripherical collisions. The Auger electrons and electrons from peripherical collisions have energies typically far below 1 keV and thus ranges in water of far below 100 nm (see Figure A1.2 in [X-r73]). Therefore, it can be expected, that TRAX slightly overestimates the relative ratio of $\delta$-electrons which are detected in the regions, where the diffusion is already negligible ($r > 100$ nm). This could partly explain the observed overestimate of simulations compared to measurements.

3. The central assumption of the BEA model is the treatment of primary $\delta$-electron emission process as an interaction of a pure Coulomb field with a quasi-free electron, originating from an unperturbed target shell. This assumption is fulfilled well by light ions, but is less valid for projectiles of larger $Z$. $^{12}$C ions are neither heavy nor light. The projectile is fully stripped at the measured energies but the perturbation of the electron cloud of the target due to the relative high charge state of the projectile is probably not negligible.

4. No comprehensive theory exists for the transport of low-energy electron transport in matter (see chapter 3.3.5). Only sparse, semi-empirical cross section data with relative large uncertainties are available (for e.g. water vapor). The errors due to the modeling of TEA with water vapor and the simple scaling with the ratio of densities, as described in chapter 4.1, can be significant.

There is a further error source that affects both the simulated and the measured $d_{pr}(y)$ distributions particularly at high $y$ (expressed in pixels); the interaction volume of OPAC is flat and not axially symmetric regarding the ion track as axis. This geometry and the very small number of $\delta$-electrons with large ranges result in relatively large statistical errors at large radial distances. Particularly, the number of $\delta$-electrons that have their end points in the region of 150 pixels $< y <$ 200 pixels is very low. The effect is illustrated with an example;

Figure 7.12 shows two selected tracks of $E = 92$ MeV/u carbon ions used for the derivation of the measured $d_{pr}(y)$ function at $p = 10$ hPa pressure (black symbols in Figure 7.10). The both lines in Figure 7.12 a) and b) are plotted at a radial distances of 190 pixels ($y = 1425$ nm in water at $p = 10$ hPa) from the center of the ion trajectories. Figure 7.12 a) contains the track of a sparsely ionizing and thus higher energetic $\delta$-electron. This $\delta$-electron track crosses the lower line at $y = 190$ pixels. Figure 7.12 b) contains a $\delta$-electron track with its endpoint exactly on the line. The endpoint delivers a high contribution to $d_{pr}(y)$ values between $y = 185$

and 195. The whole data set under consideration contains 1700 images of carbon ion tracks. Figure 7.12 a) and b) do not image typical tracks. The vast majority of the 1700 tracks do not contain $\delta$-electrons with a contribution to $d_{pr}(190)$ or in its neighborhood. Only about 5-10% of the images are similar to Figure 7.12 a) in that sense, that at least one faintly ionizing $\delta$-electron track crosses the line at $y = 190$. Furthermore, among the 1700 images only three were found, which contain a $\delta$-electron endpoint in the $y$-regime of [185,195] and they contain about 70 % of the dose in this radial distance range (the remaining 30 % is due to the images like Figure 7.12 a) with sparsely ionizing a $\delta$-electron tracks crossing the $y$‒range of interest). Since the $d_{pr}[185,195]$ dose is made up by only few stochastic events it is prone to strong fluctuations and thus large statistical uncertainty.
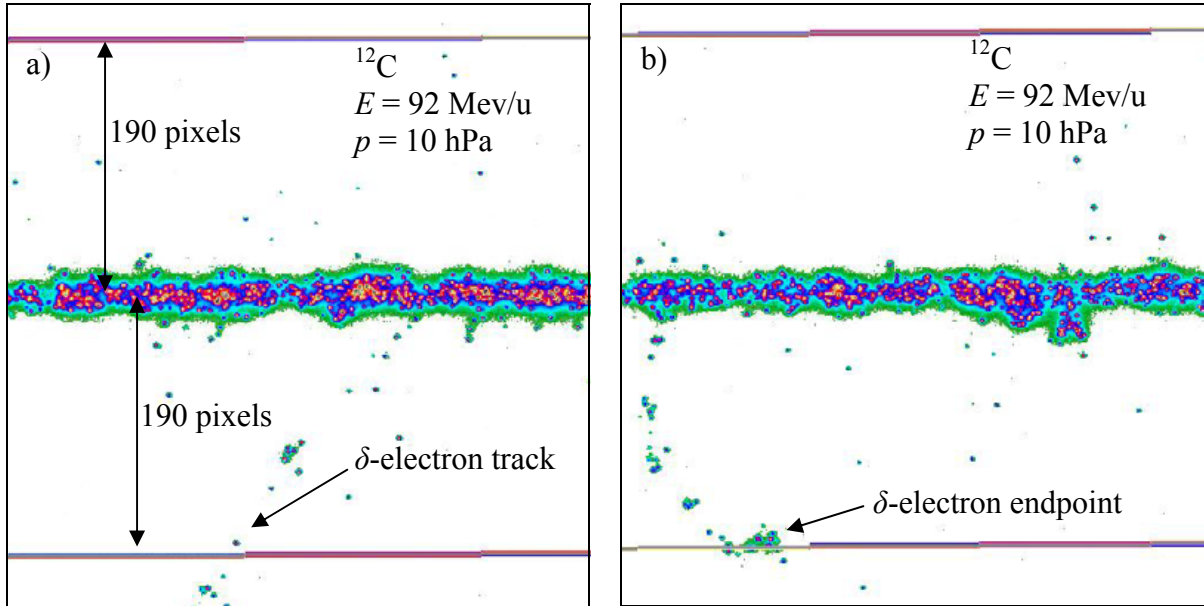


Figure 7.12: *Two selected tracks of E = 92 MeV/u $^{12}$C ions, measured at 10 hPa gas pressure. Each image contains two lines parallel to the ion track at a distance of 190 pixels from the track core. Image a) contains the track of a sparsely ionizing δ-electron which crosses the lower line. Image b) is very atypical, because the track contains a δ-electron with an endpoint at y = 190 pixels. Only three tracks were found among the 1700 images of the data set with this ion at this energy, which contain similar δ-electron tracks with endpoints in the neighborhood of y = 190 pixels.*

The relative measurement uncertainty due to stochastic fluctuations depends on many parameters, like ion type and energy or gas pressure. Nevertheless, the most important parameter that determines it is the number of available images in the data set under consideration. E.g. in the given example, the relative uncertainty due to stochastics is estimated to be:

2% for $y < 30$ pixels
3% for 30 pixels $< y < 70$ pixels
5% for 70 pixels $< y < 120$ pixels and
increasing linearly from 5% to 20% for 120 pixels $< y < 200$ pixels.

(7.3)

Not only the measured, but also the simulated $d_{pr}(y)$ distribution is affected by the described stochastics of $\delta$-electron tracks and particularly by that of the $\delta$-electron endpoints. In order to limit the computation time and the size of the data sets, the number of simulated tracks has to be restricted. E.g. the black line of Figure 7.10 (simulated $d_{pr}(y)$, corresponding to $p = 10$ hPa and $E = 92$ MeV/u) was derived from the simulation of 3000 tracks. Figure 7.13 shows the same $d_{pr}(y)$ distribution, derived from the first and the second half of the 3000 simulated tracks, respectively. If related to the average of the both curves (i.e. the black curve of Figure

7.10), the "red" value is 17% below and the blue is 17% above the "black" value at $y = 1450$ nm. This difference is due to the stochastics of such rare events far away from the track core as described before. The estimation of the relative uncertainties of the measured data due to stochastics, listed in (7.3), is based on the systematic study of the variation of the $d_{pr}(y)$ distribution when comparing the $d_{pr}(y)$ distributions of different simulated subsets of the whole simulated data set.
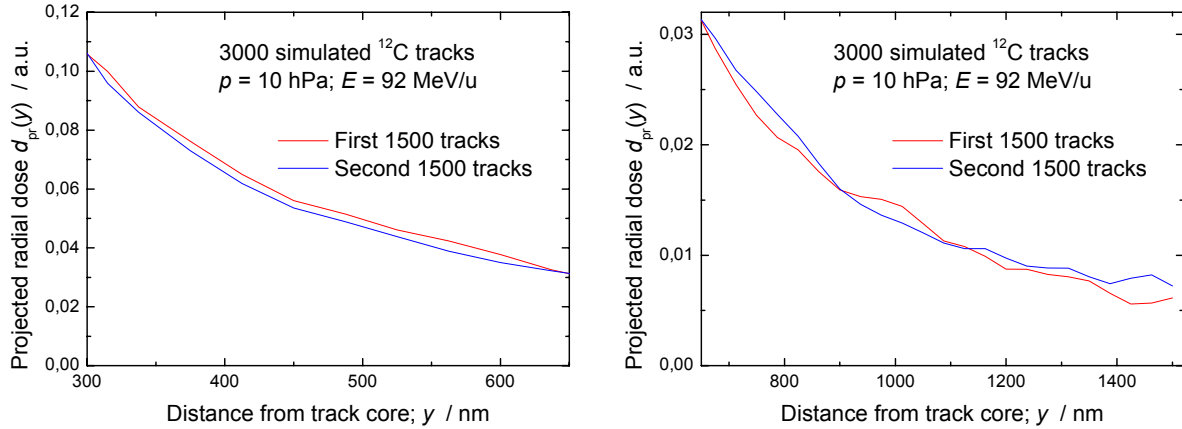


Figure 7.13: *Results for projected radial dose distribution ($d_{pr}(y)$) calculated from two different set of 1500 tracks. The discrepancy is due to the influence of very rare far-ranging δ-electrons (especially endpoints), which are present in only a very few tracks.*

Another source of uncertainty which affects both, the measured and the simulated $d_{pr}(y)$ distributions at large radial distance expressed in pixels is due to the limited size of the interaction volume of the measuring chamber. In tissue, e.g. the target region of energetic ions is situated deep in the body and is surrounded by a by matter of the same density. Under such circumstances, scattered δ-electrons have the chance to exit and re-enter the target volume in a predictable way. In the case of OPAC, the interaction volume is delimited by stainless steel meshes of - compared to the gas - "infinite" high density and a further gas volume adjacent to the meshes. The influence of these meshes on the backscattering of electrons is not included in the simulation. Modeling of this phenomenon is even more complicated by the effect of the electric field between the amplification electrodes (DA, $G_1$ and $G_2$, see Figure 5.1 and Figure 5.5) This field for example does not allow low energy electrons to re-enter the volume.

The full simulation of the whole geometry including the meshes, the stainless steel potential rings and the electric fields was not performed within this work (see also chapter 6.1). Due to the problematic modeling of their effects, only the interaction volume between DC and DA with the thickness of 3,2 cm was simulated (see chapter 7.2.1). On the other hand, the "real" radial distribution is simulated in a full, cylindrical symmetric geometry - up to a range of $r = 200$ pixels (see in the next chapter). It was already shown earlier (see Figure 6.4), that there is no significant difference between the directly simulated $d(r)$ and the unfolded $d_{pr}(y)$ functions. Nevertheless, a relative measurement uncertainty of up to 10% should be associated to this artefact for $y > 150$ pixels (linearly increasing with $y$)

Figure 7.14 summarizes the upper limits for the relative measurement uncertainty of the $d_{pr}(y)$ values as a function of $y$ for a few, arbitrary selected cases. The total uncertainty was obtained by calculating the RMS-sum of all uncertainty contributions discussed above. In summary it can be concluded, that the discrepancies of measured and simulated $d_{pr}(y)$ distributions, shown in the diagrams of chapter 7.2.1, are smaller, than the measurement errors in the case of $p = 40$ hPa in the whole $y$-regime. At lower gas pressures, there are ion energies and $y$-regimes, where the discrepancies between experiment and simulation are larger than the

relative measurement errors. The relative uncertainty of the simulations is not available. From the measurement results with their relatively small relative uncertainties we conclude those at large distances from the track core the projected radial dose $d_{pr}(y)$ is slightly overestimated by the simulations.

Nevertheless, the overall agreement between the measured and simulated $d_{pr}(y)$ distributions is very good. It proofs, that the numerous assumptions and simplifications behind both, the measurements and the simulations, are mostly justified and understood well. Note, that Figure 7.9, Figure 7.10 and Figure 7.11 present a detailed comparison on a lin-lin scale in four $y$-regimes over 3 decades of radial dose values. Due to the high complexity of the various physical processes which determine the heavy ion transport in matter, and due to the large variation of the radial dose from track center to the periphery, it is rather common to display such a function in log-log scale. To emphasize the main discrepancies between measurements and simulations and increase their visibility we have chosen this 4-fold segmented linear representation.
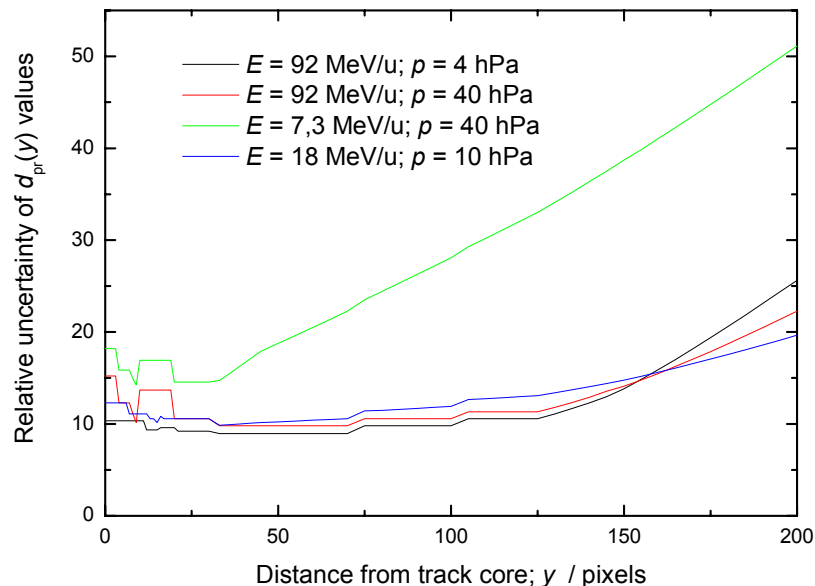


Figure 7.14: *Estimate for the relative uncertainties of the measured $d_{pr}(y)$ distributions as a function of y in few cases.*

# 7.3 Radial dose distributions around $^{12}$C ion tracks

It was shown in chapter 7.2.1, that very good agreement could be achieved between the measured and simulated projected radial dose distributions ($d_{pr}(y)$) for $^{12}$C ion trajectories. However, the quantity $d_{pr}(y)$ is very specific to the OPAC geometry; it was merely defined in order to be able to describe the images that are achieved after projecting the thermalized ionization electrons, which were generated in the interaction volume of OPAC. The method for unfolding the measured $d_{pr}(y)$ distributions in order to derive the desired radial dose functions, $d(r)$, was described in chapter 6.2. Figure 7.15 shows the measured ($p = 10$ hPa) and simulated $d(r)$ radial dose functions of $^{12}$C ions at two energies ($E = 92$ and 4,4 MeV/u). The curves were derived by simulating the trajectory of an ion traversing a cylindrical volume, where the cylinder axis is identical with the track core. (This is the same method which was used to derive the red $d(r)$ curve of Figure 6.3.) The simulations which include electron diffusion were performed according to the explanations in chapter 6.3.3. Both

calculation alternatives ($d\_d(r)$ and $d_{r\_d}(r)$), described in chapter 6.3.3, were tested. No significant differences could be observed, therefore the method resulting in lower uncertainties was selected ($d\_d(r)$, see black symbols in Figure 6.7)

The experimental radial dose values are based on the corresponding projected radial dose ($d_{pr}(y)$) distributions of Figure 7.10 (red and black symbols). OPAC can not easily be calibrated for absolute radial dose measurements. Therefore the unfolding method produces only a relative $d_r(r)$ distribution, i.e. "only" the shapes of the distributions are actually measured, and their absolute values require additional normalization. The absolute dose normalization is based on restricted stopping power values. From the regular stopping power, also called unrestricted LET or $LET_\infty$, and the restricted stopping power $LET_{200pixel}$ the ratio, $q_{200}$ is calculated, where the 200 refers to the LET, restricted to $r < 200$ pixels:

$$q_{200} = \frac{LET_{200\,picxels}}{LET_\infty} \tag{7.4}$$

The restriction to 200 pixels is based on the size of the OPAC interaction chamber and varies, in $r$ due to different filling pressures. The value of $q_{200}$ is calculated with TRAX by calculating restricted and unrestricted LETs by simulating the $d(r)$

a) in the $r$-regime, which was accessible by the measurements (i.e. $0 - 200$ pixels which corresponds e.g. at a gas pressure of $p = 10$ hPa to $0 < r < 1500$ nm), and

b) in the full relevant $r$-regime which is up to a, maximal range $r_{max}$ which is the range of the fastest $\delta$-electrons.

In the example of Figure 7.15 the values of $r_{max}$ and $q_{200}$ are the following:

| Specific energy, $E$ | $r_{max}$ | $q_{200}$ |
|---|---|---|
| 4,4 MeV/u | 15 µm | 99,8% |
| 92 MeV/u | 350 µm | 81,9% |

The table shows, that the slow ion deposits its whole dose within the interaction volume of OPAC while the fast ion this value drops to about 80 % due to its larger number of fast delta electrons. The $q_{200}$ values were taken into account for the normalization.

It has to be further emphasized that both, the simulated and the measured functions describe the spatial distribution of the electron stopping locations. Due to the initial kinetic energy of the electrons these locations are not identical with the places where the energy transfer by the fast ion has occurred. The real local dose is correlated to these energy transfers, which might be better represented by the distribution of the remaining positive ions. Furthermore, the measured dose distribution is distorted by diffusion in the low $r$-regime (till about 150 nm in the case of Figure 7.15). The extent of this effect is shown in chapter 6.3.3.

In order, to be able to show the tendency of the measured and simulated functions, and to achieve a more constant sampling distance on the logarithmic scale, the neighboring pixels were binned as follows:

no binning                          at $r < 15$ pixels (112,5 nm if $p = 10$ hPa)
binning of 3 neighboring pixels     at $15 < r < 50$ pixels
binning of 5 neighboring pixels     at $50 < r < 110$ pixels
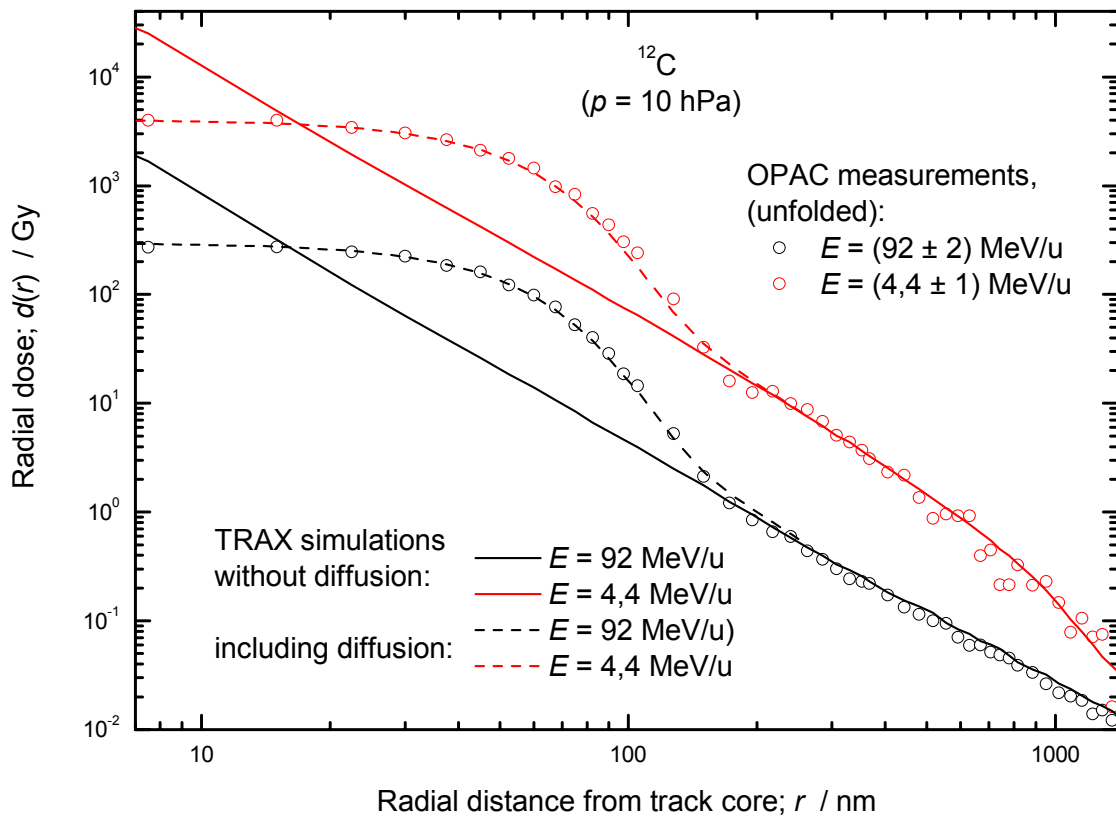binning of 9 neighboring pixels     at $110 < r < 200$ pixels

Figure 7.15: *Measured and simulated radial dose values at two carbon ion energies. The absolute dose normalization of the measured data was obtained by calculation (see text above for details.)*

In Figure 7.15, excellent agreement between the measured and simulated data above the diffusion range is observed. The discrepancies show the same tendencies which are described in chapter 7.2. E.g. large fluctuations due to stochastics of rare fast delta electron events. At low radial distances $d(r)$ is determined by the diffusion. If the diffusion is included into the simulation, the agreement between the measured and simulated data is very good in the whole displayed r-regime. Note, that the value of $\sigma$, used for the simulation is not the result of a fitting, but was derived from an independent measurement of the diffusion, see chapter 6.3. As a consequence, it can be stated, that the simulations without diffusion cannot deviate from the reality in a high extent for lower $r$ neither, otherwise, the reconstruction of the measured results via additionally simulated diffusion could not be as successful, as observed.

In order to compare the $d(r)$ functions at different ion energies, it is useful to normalize the dose values by the corresponding LETs. Note, that in the diagrams in chapter 7.2 the normalization was performed to a common yield of electrons in the interaction volume of OPAC. In contrary, for the normalization leading to Figure 7.16 the expectable ionization electron yield for $r > 200$ pixels is included. I.e. the total measured yield is divided by $q_{200}/100$ in both cases.

For $r < 250$ nm, the $d(r)$ functions at 4,4 and 92 MeV/u proceed parallel to each other on the log-log scale. The ratio is determined mainly by the difference in $q_{200}$ ($\approx 18\%$). For ions of $E = 4,4$ MeV/u, the shape of the $d(r)$ function starts to deviate strongly from the typical $\approx 1/r^2$ for $r > 250$ nm. This prediction of the BEA model (in conjunction with the $1/r^2$ characteristics for smaller $r$ or higher ion energy) is confirmed by the OPAC measurements. The intersection of the two functions is at $r_{eq} \approx 500$ nm for both, the measured and the simulated data. For

$r > 500$ nm, $d(r)$ drops rapidly in the case of $E = 4{,}4$ MeV/u. This characteristics is also confirmed well by the measurement. However, the measurement error at $r > 1000$ nm is rather high, the two last values at $r = 1290$ and $1360$ nm which are strongly higher and lower than the simulated data are not very reliable (for the reason see chapter 7.2).
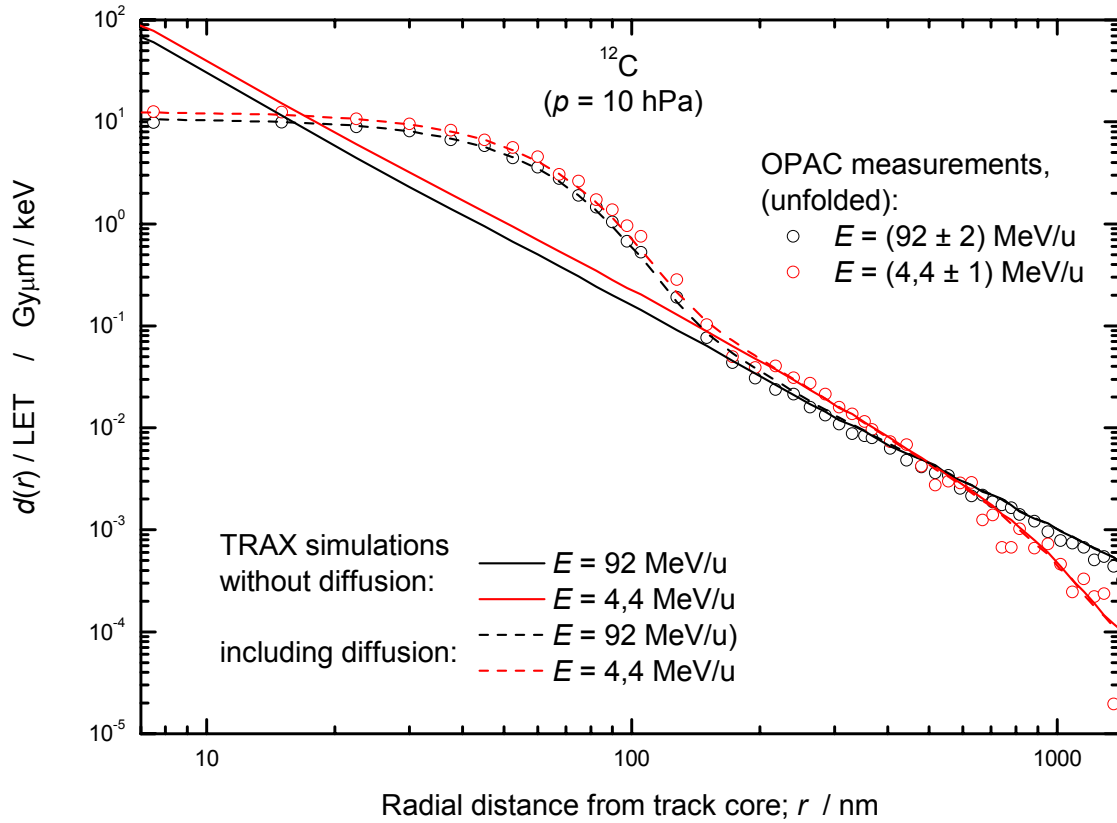


Figure 7.16: *Measured and simulated radial dose distributions at p = 10 hPa at two ion energies. The only difference compared to Figure 7.15 is the different normalization; the plots of Figure 7.16 are normalized to the same LET to emphasize the different shapes of d(r) at different ion energies.*

Figure 7.17 shows the comparison of $d(r)$ / LET data in the case of $p = 40$ hPa at two ion energies. The measured and simulated distributions there were derived in the same way as in Figure 7.16 applying the same unfolding, normalization and binning methods. The intersection of the $d(r)$ / LET distributions at the two different energies are found at a distance of $r_{eq} \approx 2$ μm from the track core in the simulated and the measured cases. If we compare the radial distance of this intersection point with the one in Figure 7.16 (carbon ion energies of $E = 4{,}4$ MeV/u and at 92 MeV/u) the corresponding $r_{eq}$ distance is higher by a factor of four if the energy of the slower ion is higher by a factor of 2,5 and that of the faster ion is the same.
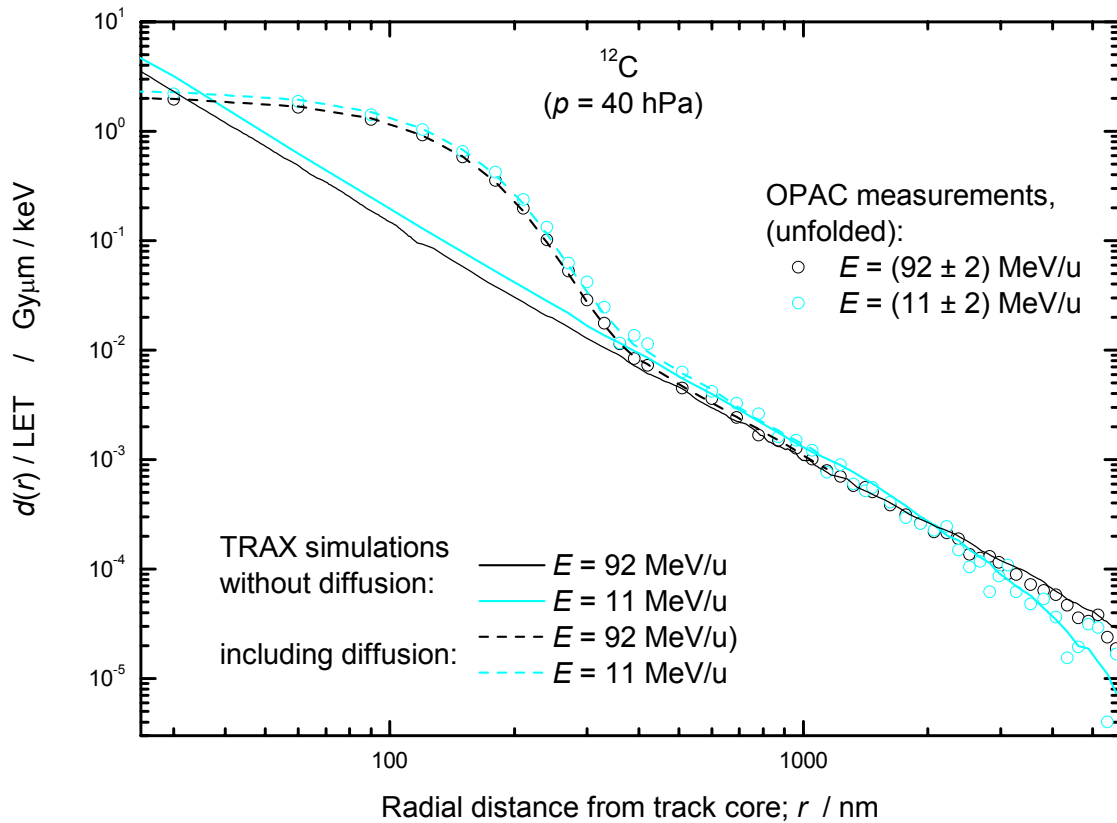
127

Figure 7.17: *Measured and simulated radial dose distributions at p = 40 hPa at two ion energies. The plots are normalized to the same LET to emphasize the different shapes of d(r) at different ion energies.*

Figure 7.18 demonstrates that the data derived from the measurements at three different pressures are not independent from each other but it is possible and useful to link them. Such a linkage is not possible based on the original, projected data, e.g. the $d_{pr}(y)$ distributions of chapter 7.2.1. But it is well feasible after the radial unfolding and the appropriate normalization is performed.

The black curve is the simulated $d(r)$ for $^{12}$C at $E = 92$ MeV/u. The simulation was performed in the whole range of $r$ up to the cutoff distance ($r_{max} \sim 300$ μm). At large radial distances (r > 100 μm) the statistical uncertainty of the simulation is very high, because only a limited number of primary particles were simulated. The effect of the gas pressure on the diffusion is nicely observable in Figure 7.18. For lower gas pressure the radial distance above which the role of diffusion is negligible decreases (i.e. the corresponding simulated curves including diffusion does not deviate significantly from the black curve). On the other hand the maximum radial range which can be measured with OPAC decreases with decreasing gas pressure. Hence, there is a certain optimal radial range accessible with each pressure selection. The three pressure values used in our measurements provide three optimal radial ranges which partly overlap. E.g. at $r = 500$ nm all three distributions deliver valuable results, which are not affected significantly by diffusion.
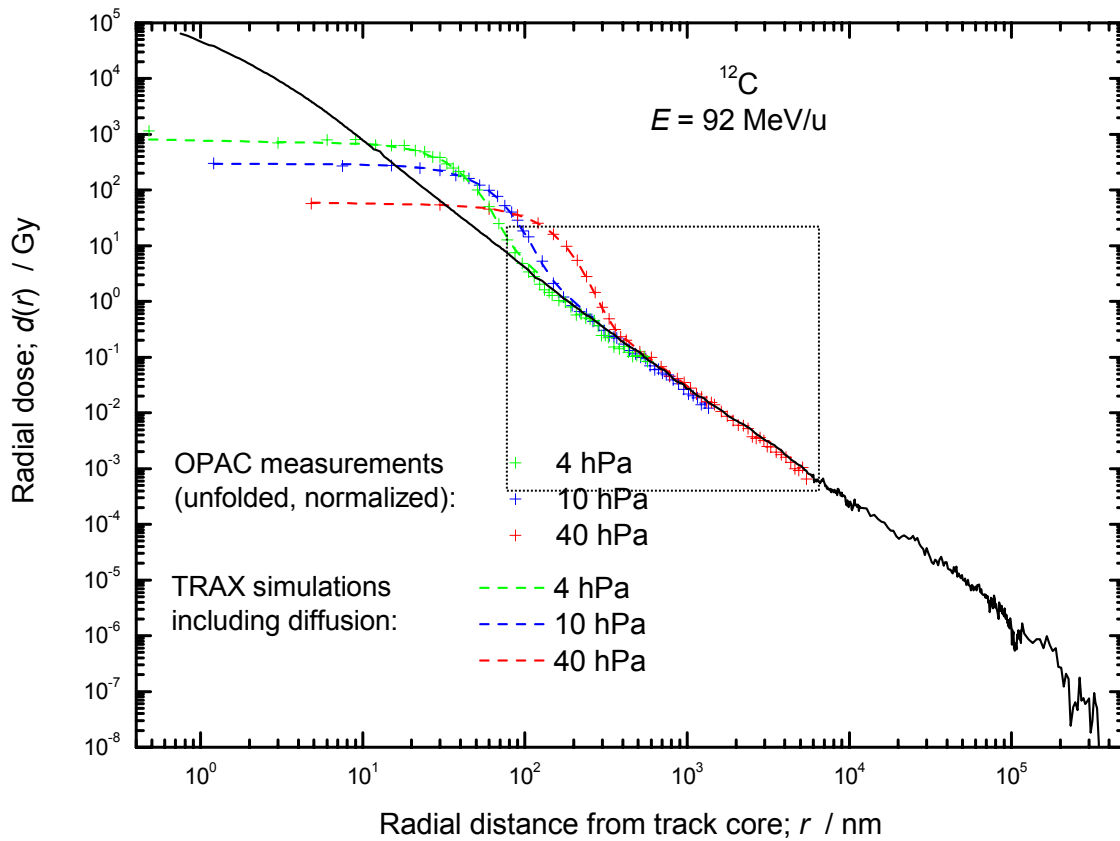
Figure 7.18: *Merging of unfolded d(r) functions for different pressures derived from the measurements of $^{12}C$ ions at 92 MeV/u. The marked window in the center is magnified in Figure 7.19.*

The excellent agreement between all three measured data sets and the corresponding simulations, visible in Figure 7.18 allows for a more detailed comparison. Figure 7.19 shows a section of Figure 7.18, where the combined measurement results are expected to match the radial dose distribution without the broadening effect of diffusion. The agreement between the three measured and the simulated data sets is indeed very good in the whole range of interest. However, a slight overestimation of $d(r)$ by TRAX is apparent. Its possible reasons were discussed in chapter 7.2.2. It is also observable, that the measured $d(r)$ at a given $r$ is slightly pressure-dependent. This latter observation has two main reasons:

1. The influence of the diffusion broadening extends to larger $r$ for higher pressure (if $r$ is expressed in nm in tissue density). The contribution of diffused electrons causes the $d(r)$ values for higher pressure to be slightly larger than the values at low pressure, where the diffusion range is shorter.

2. The boundary effect and the low probability of $\delta$-electron endpoints at high $r$ (see details in chapter 7.2.2) can result in an underestimation of $d(r)$, particularly if $r > 150$ pixels. (E.g. due to the lower re-entry probability in the case of OPAC compared to the simulations where the cylindrical sensitive volume is surrounded by matter of the same density.) As the wall of the chamber is located at a fixed distance from the track core (real distance in pixels - not simulated distance in unit density) independently from the gas pressure, for the boundary effect the distance is decisive in pixels rather than in nm. The course of the red dashed curve ($d_{r\_d}(r)$ distribution at 40 hPa) reflects this artefact as well. The simulation in this case was performed in OPAC-geometry and the achieved $d_{pr}(y)$ was than unfolded (see derivation of $d_{r\_d}(r)$ function in chapter 6.3.3). The resulting red dashed

curve - similarly to the measured data - has typically lower values and higher uncertainties than the black curve for high $r$ values. However, as shown in Figure 7.13, the statistical significance of the exact course of the dashed red line is limited (see also the dip of the dashed red line at $r \approx 4800$ nm.)
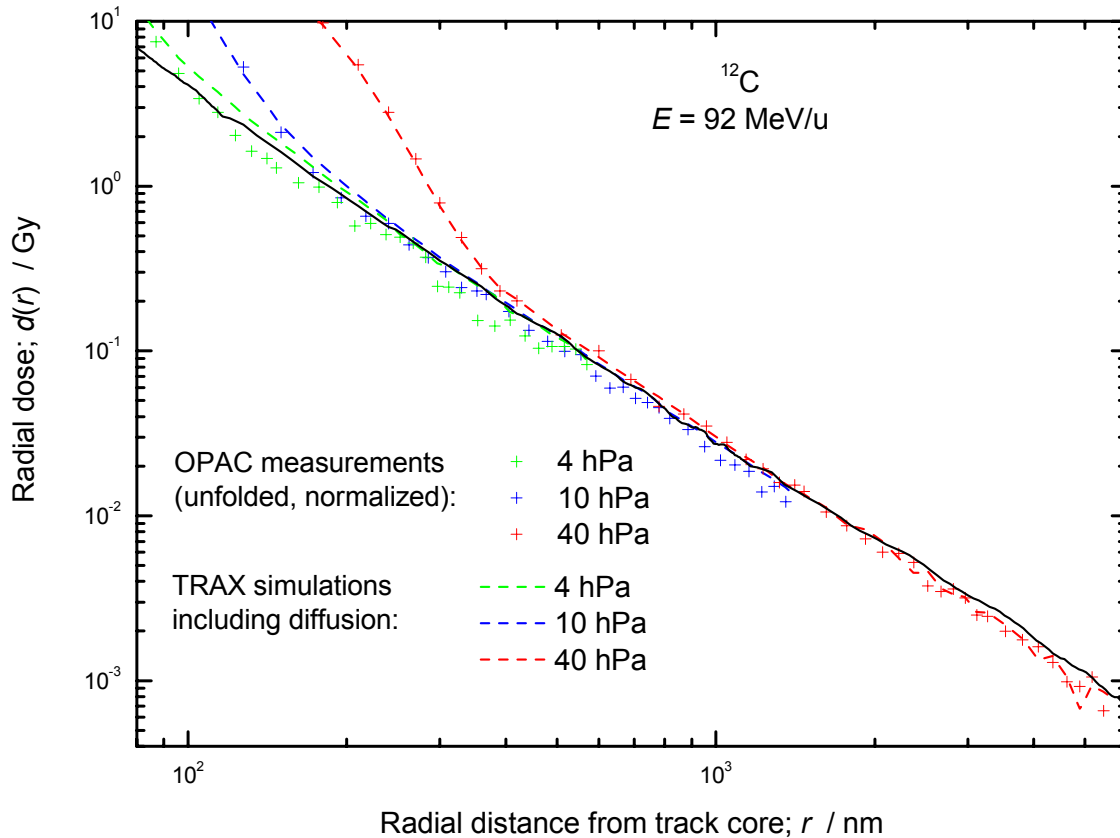


Figure 7.19: *The same diagram as Figure 7.18 plotted in the range of interest marked as box in Figure 7.18.*

## 7.4 Radial dose distribution around very heavy ion tracks

Figure 7.20 shows the measured and simulated $d(r)$ functions of uranium tracks. The normalization was performed similar to the procedure which led to Figure 7.16, i.e. the data are normalized to the same LET in order to emphasize the different shapes of $d(r)$ at the two ion energies. Only the differences in $q_{200}$ are taken into account (see equation (7.4)) for the normalization. Figure 7.20 shows the $d(r)$ in the $r$-range of 100 nm $< r < 5$ μm, where the measurement data of at least one pressure is applicable (i.e. measurable and not affected strongly by diffusion or the measurement statistics at very large $r$.) The simulated data which include diffusion are not plotted in this case to enhance clarity.
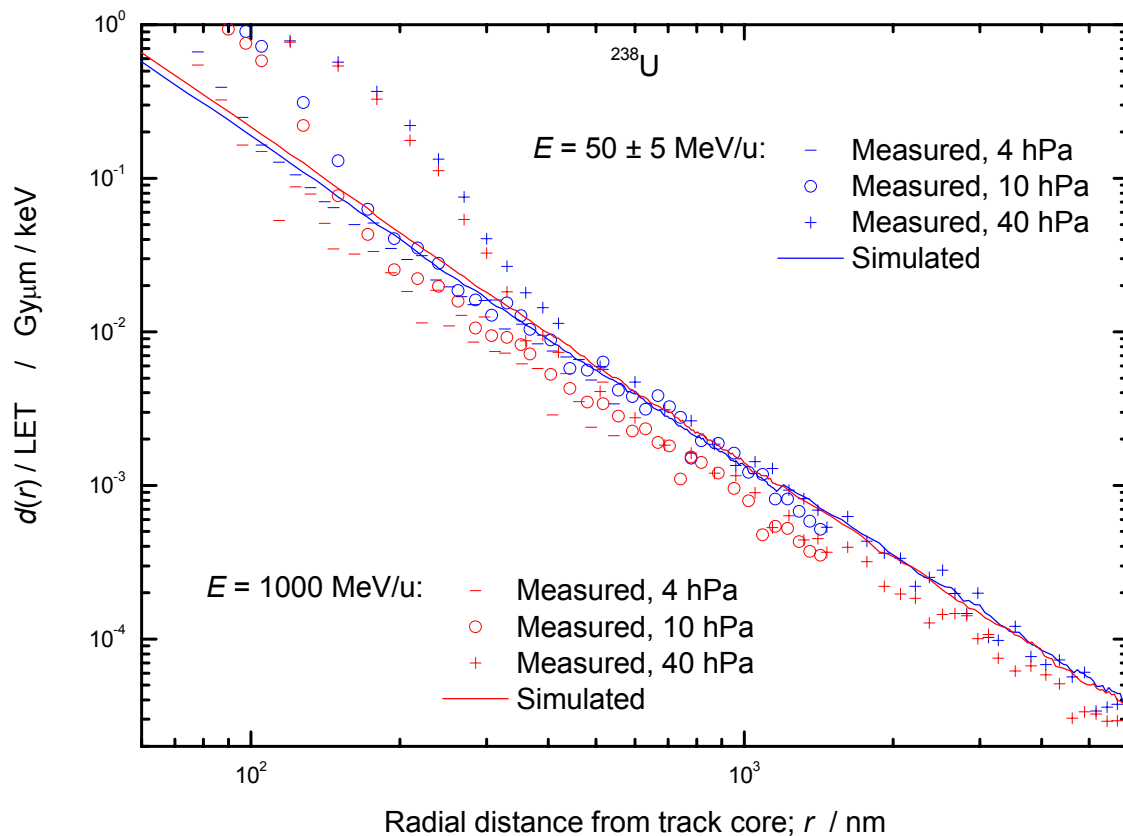
Figure 7.20: *Measured and simulated radial dose distributions around $^{238}U$ tracks. The energy of the tracked uranium ions was 50 (blue symbols) and 1000 MeV/u (red symbols). The diagram shows the measurement data of all three gas pressures.*

From Figure 7.20 it is visible, that the simulated $d(r)$ data of uranium at 50 and 1000 MeV/u, if normalized to the same LET, do not differ significantly. But on the other hand, the measured function corresponding to the 1000 MeV/u ions has significantly lower values, than the curve derived from the less energetic tracks. However, the differences between the measured values remain typically below 50%.

While there is a surprisingly good agreement between measurements and simulation in the case of $E = 50$ MeV/u, the simulated $d(r)$/LET values are typically higher by 50-100% than the corresponding measured values for the very energetic uranium ions. It was pointed out in chapter 3.3, that the BEA model, used in TRAX for the $\delta$-electron production, is not adequate for heavy projectiles [Krm94]. This is most probably the reason for the observed discrepancies here.

The statistical uncertainties of the measured $d_{pr}(y)$ distributions are expected to be smaller in the case of uranium, than in the case of carbon ions. The reason for this is the lower influence of stochastics at large $y$ distances around $^{238}U$ tracks. Due to their very high LET, the number of $\delta$-electron tracks - and particularly that of end points - in the case of $^{238}U$ ions is much higher than for carbon., which leads to much better event statistics in the track periphery. Though, for the high-Z ions the detection efficiency of single electrons is reduced due to the low gain operation of OPAC in these cases (see comments to Figure 6.19), the event statistics is not dominated so much by a very few rare $\delta$-electron endpoints, as we have shown for the case of $^{12}C$ in chapter 7.2.2. As a result, the relative uncertainty of the $d_{pr}(y)$ function for $^{238}U$ ions does not exceed 15%, if $y < 180$ pixels, at any gas pressure (compare to Figure 7.14 for carbon ions). Although no calculations were yet performed in order to determine the relative

errors of the resulting $d(r)$ values (only for $d_{pr}(y)$), the average differences between the measured data at the two energies studied in Figure 7.20 are definitely higher than the measurement errors.

# 7.5 Radial dose of ions of different *Z* but similar LET

The second series of measurements were performed in order to compare the radial dose distribution functions of different ions having similar LET values. Figure 7.21 shows the $d(r)$ function of $^{12}C$, $^{40}Ar$ and $^{84}Kr$. The energies were adjusted in such a way, that all three ions had the same LET of $315 \pm 10$ keV/μm in liquid water. The absolute dose-values of Figure 7.21 are results of an appropriate normalization as described in chapter 7.3. The diagram shows the simulated curves without diffusion (solid lines), the simulated curves including simulated diffusion (dashed lines) and the measured data (symbols). The measured data are signed by the same symbols according to the applied gas pressure, as introduced in the previous chapters ($p = 4$ hPa: dashes; $p = 10$ hPa: circles; $p = 40$ hPa: crosses; measured 4,4 MeV/u carbon data are available only at $p = 10$hpa pressure and 65 MeV/u argon data at 4 and 40 hPa pressure.)

The $d(r)$ results of the TRAX simulations - in agreement with the predictions of analytical models (see [Kat72], [Cha76], [Kie86] [Xap94] or [Scm95]) - show the typical $r^{-2}$ characteristics for the two heavier ions (Ar, Kr) in the whole range of Figure 7.21. The curve of the 4,4 MeV/u $^{12}C$ deviates from this behavior above a few hundreds of nm. The maximal radial range of $\delta$-electrons for the carbon ions is about $r_{max\_C} = 2$ μm (according to the equation (3.4) and the electron range table in [ICR96] and a steeper fall of the $^{12}C$-curve following the similar $r^{-2}$ shape is therefore expected for $r >$ few hundreds of nm. The simulation in Figure 7.21 reproduces this result. However, the simulated curve suffers from strong statistical uncertainty for $r > 1$ μm (for the reasons for this see chapter 7.2.1).

For radii, where the effect of diffusion is negligible, the measurement results are in good agreement with the simulations. Both, the $r^{-2}$ characteristics for the heavier ions and for carbon at low $r$, and the cut off of the $^{12}C$-curve of at high $r$ are reflected by the measurements very well. However, while the agreement of measurement and simulation is excellent for $^{12}C$, it deteriorates for the heavier ions, $^{40}Ar$, and even worse for $^{84}Kr$. The main reasons for the increasing discrepancies between simulations and measurements with increasing $Z$ is the decreasing capability of the BEA model, used in TRAX, to describe the process of the $\delta$-electron production correctly (see chapter 3.3.4.2 for more details on the limitations of the BEA model).

While the $d(r)$ curve of the $^{12}C$ differs strongly from that of the heavier ions, no strong differences can be observed between the measured $d(r)$ functions of $^{40}Ar$ and $^{84}Kr$. The main reason for the similar shapes of the $^{40}Ar$ and $^{84}Kr$ curves is the relatively small radial range, where the OPAC measurements can deliver precise information - typically in the region of $0,1$ μm $< r < 5$ μm. Due to the large range of energetic binary encounter electrons of the heavier ions, the radial range covered by the $^{40}Ar$ ion amounts to $r_{max\_Ar} \approx 300$ μm and for $^{84}Kr$ up to $r_{max\_Kr} \approx 6$ mm. (ranges refer to liquid water density). Therefore, we expect strong differences between the two curves only for $r > 100$ μm, where the Ar-induced electrons reaches their cut off range and the $d(r)$ starts to drop rapidly similar to the carbon-curve at $r > 0,5$ μm. To measure this range OPAC must be operated at atmospheric pressure which is not feasible with the present technique.
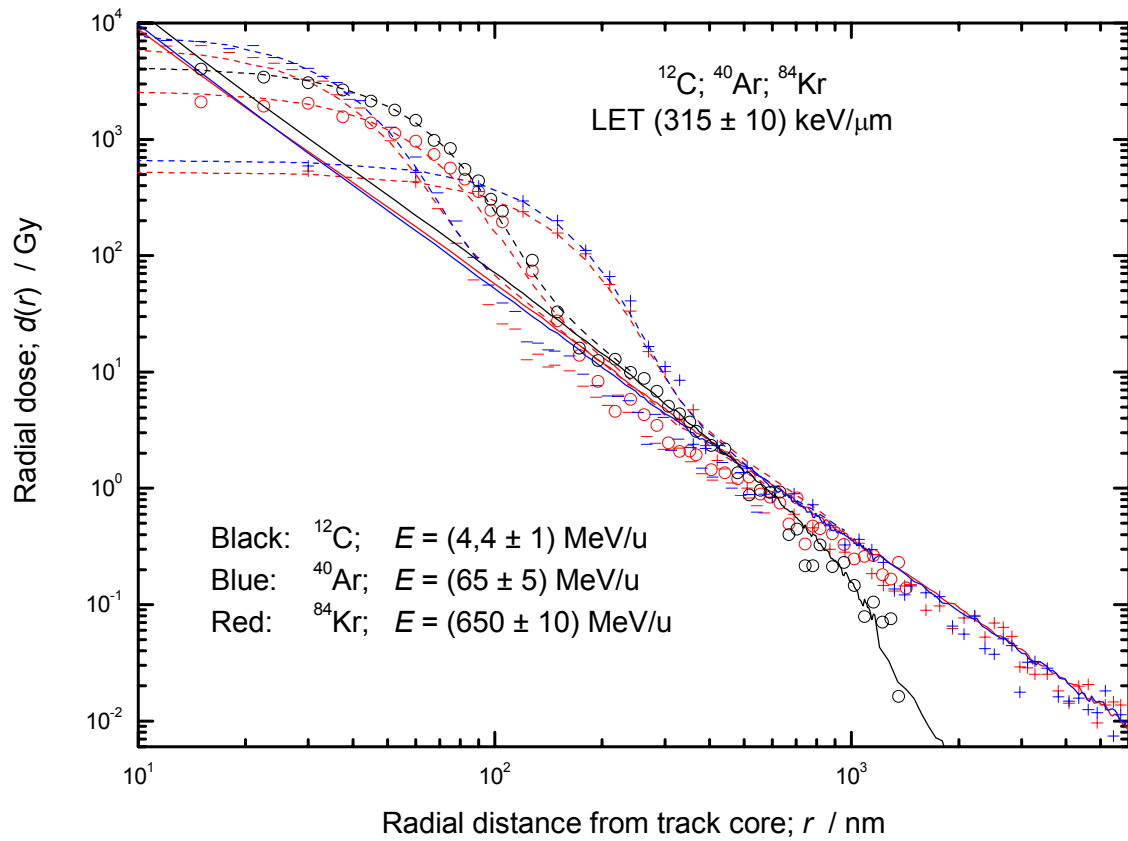
Figure 7.21: *Comparison of the radial dose distribution functions of ions with different Z but similar LET. The absolute values are results of an appropriate normalization as described in chapter 7.3. For more details see text above.*

# 8 Summary

In the present work we applied the Optically read out PArticle track Chamber, OPAC, for the measurement of radial dose distributions, $d(r)$, around tracks of heavy ions passing through the gas-filled sensitive volume of the chamber. The measured data were compared with $d(r)$ functions derived from data calculated with the Monte Carlo particle transport code, TRAX.

Direct measurements of $d(r)$ in dense materials like tissue or water in biologically relevant volumes (cells size and beyond) are not possible. The required resolution has to be of the order of nanometers up to several micrometers. This is not achievable with present technology. Instead, gas filled chambers or cloud chambers can be used to measure the corresponding quantity at much lower matter density. The length scale is then multiplied by the ratio of the densities of gas and tissue.

To measure this quantity we have used here an optically read out time projection chamber (OPAC) with a parallel-drift field and one or several electron and light amplification stages. The two dimensional projection of the three dimensional ionization pattern - caused by the ionizing particle passing through the chamber - is captured by an image intensified CCD camera. The pressure of the filling gas was adjusted to 4, 10 and 40 hPa in the measurements presented in this work. The gas pressure and the width of the drifting region determine the extent of electron diffusion in the chamber which is the major limiting parameter of the spatial resolution of OPAC. A resolution of 33 nm ($1 \cdot \sigma$ of electron diffusion) is achievable at a pressure of 4 hPa. With increasing gas pressure the spatial resolution decreases. On the other hand, a higher gas pressure enables the stopping of faster $\delta$—electrons, i.e. a broader neighborhood of the track core can be imaged.

The work is motivated by the role the radial dose distribution plays in the estimation of the relative biological effectiveness (RBE) of heavy ions, e.g. in radiation therapy and in radiation protection. Therefore, the work starts with a brief overview of the most important quantities and concepts of the radiation biophysics. Radiation biophysics is a rather heterogeneous field - similar effects are often explained with seemingly or principally different causes or arguments by different models. There is no closed, generally accepted, quantitative description that can explain the biological effect for any type of irradiation under all possible conditions. Nevertheless, many of the more sophisticated models are able to predict the response of some biological systems under certain circumstances and endpoint requirements to a certain radiation with satisfactory accuracy. The most successful model for high-dose irradiation with ions (applicable e.g. for heavy ion therapy) is found to be the local effect model (LEM). The present work intends to deliver measured data for one of the basic physical parameters which serve as input for the application of the local effect model: the radial dose distribution, $d(r)$.

After the biophysical introduction a brief description of the physical processes responsible for the formation of the ionization track structure in matter is provided. The track structure is the complex convolution of different physical processes – ion and electron interactions with atoms and molecules. Thus, the $d(r)$ distribution is a derived quantity that can only be investigated by simulations or measurements, if the physical processes - such as ionization, excitation and scattering of ions and electrons with all relevant atoms and molecules - are understood well. We have to point out that both measurements and simulations merely model the physical processes we are interested in. Therefore, in the central part of the work we described in detail the hardware and software improvements and extensive data analysis techniques (e.g. unfolding of the measured pure data with given detector response function), which were necessary to analyze, compare and interpret the results. We have performed

rigorous tests on the analysis methods - e.g. with successful reproduction of the measured data by successive back-folding of the unfolded data. Thus we can be sure that the data analysis and unfolding techniques, developed in this work, produce stable and reliable results from the measured raw data.

In the final part of this work we present results of the measurements in comparison with the corresponding simulation results. The previously described data analysis technique ensured the direct comparability of measured and simulated data. The first goal of our measurement program was the measurement of $d(r)$ distributions around carbon ions of different energies from 400 MeV/u down to the Bragg peak regions. We found an excellent agreement between the measured and simulated distributions at all carbon energies for the $r$–range in which the measurements deliver useful results. The lower limit of this range is about 100 nm and the upper limit is 6 μm at a resolution of down to 33 nm - if scaled to water density.

Note, that the comparison between the measured and the simulated distributions does not comprehend the comparison of the absolute dose values. Only the relative shape of the corresponding $d(r)$ functions is compared after a proper normalization. This is due to the fact, that OPAC is not capable for absolute dose measurements - only with relatively high uncertainty after extensive calibration efforts. Nevertheless, the very similar relative shape of the measured and simulated curves is a great evidence of the fact, that both approaches represent reasonably good models of the underlying physical processes. This is true despite the fact that the TRAX code uses partly simplified models (e.g. binary encounter theory for $\delta$-electron emission) or scaled cross sections for processes where no measured data are available for the molecules and ions used in the experiment.

Despite these deficits, the discrepancies between the simulated and measured $d(r)$ distributions are found to be lower than the measurement uncertainties at all measured carbon ion energies in the observed $r$-range. An exception from this is the case of carbon ions at an energy of 95 MeV/u (see Figure 7.19) in the $r$-range of 70 nm $< r <$ 400 nm, where the simulations overestimate the measured data by up to 25% (the measurement uncertainties amount to $10 - 15$%). Besides, at medium carbon energies (18 - 35 MeV/u) in the $r$-range of 80 nm $< r <$ 200 nm the simulations overestimate the measured data by an extent ($\approx$ 15%) which is comparable with the measurement uncertainties. As the simulated and measured $d(r)$ functions are normalized to the same LET, the overestimation in the above $r$-ranges imply an underestimation in another region. New measurements with a further-developed OPAC would be necessary in the $r$-ranges below 100 nm and above 6 μm, to determine the $r$-distance, where the simulations underestimate the measurements, and the extent of this deviation. Nevertheless, it can be assumed, that the simulation slightly underestimates the radial dose for $r <$ 10 nm, because it does not take account the low energetic Auger-electrons and the electrons from peripheric collisions. Fortunately, due to the very steep drop of the $d(r)$ function towards large $r$-values (i.e. the majority of all $\delta$-electrons get stopped within $r <$ 10 nm), an underestimation by a few % would compensate the overestimation by 10 - 25% in the limited range, described above. Nevertheless, it cannot be excluded that the RBE around very fast carbon ions - where the discrepancies are the highest and the overkill effect is negligible at the same time - is slightly underestimated according to the simulated $d(r)$ function. This is due to the possibly underestimated local dose in the $r <$ 10 nm region (the radiation is more densely ionizing in the reality, than indicated by the simulation). The verification of this hypothesis will be only possible, if precise measurements can be done for $r <$ 100 nm.

The slight discrepancies between the measured and simulated $d(r)$ distributions are, however, hardly observable in the log-log representation (see Figure 7.18). There are two main reasons, why the log-log representation is preferred in the literature to illustrate the radial dose

distribution: Firstly, the ranges of interest, both in radius and dose, amount to many (5 to 15) orders of magnitude. Secondly, the biophysical models, which use $d(r)$ as input parameter, are not very sensitive to slight variations in $d(r)$. E.g. the local effect model, that delivers the most precise results for the biological effective dose after heavy ion irradiation, applies further biological and atom physical assumptions (e.g. for the shape and radius of the cell core, for the X-ray survival curve or for the model building, itself) that are realistic, but have uncertainties with higher potential effects on the biological effective dose, than a slight variation in the shape of $d(r)$ of the order of up to 25%.

Hence, within the limitations of our measurements we can conclude that the precision of TRAX is sufficient to simulate the $d(r)$ distributions around carbon ions to serve as input parameter for therapy planning. However, this conclusion is only valid for larger radial distances ($r > 100$ nm). For smaller radial distances the measured data are dominated by the diffusion.

Apart from carbon ion tracks, tracks of very heavy ions ($^{40}$Ar, $^{84}$Kr and $^{238}$U) were also measured with OPAC. The simulated $d(r)$ values were typically slightly or significantly higher than the measured data in the $100$ nm $< r < 5$ μm region (see Figure 7.21). The experience has shown: the heavier or the faster the ion, the higher the discrepancies. On the one hand, we found a surprisingly good agreement between measurements and simulations if the ions had energies of around $50$ MeV/u (i.e. relatively low energy). On the other hand, at higher energies, simulated data underestimate the measured ones by up to a factor of two in the region of $100$ nm $< r < 1$ μm for $^{84}$Kr ($E = 650$ MeV/u) or in the region of $100$ nm $< r < 6$ μm for $^{238}$U ($E = 1$ GeV/u). A possible reason for these discrepancies is that the BEA model, used in TRAX for the $\delta$-electron production, is not adequate for very heavy projectiles.

The energy values of the very heavy ions were selected with the aim of comparing the track structures - and namely the $d(r)$ distributions - of ions with largely different atomic mass but similar LET values. From the $Z$-dependency of the stopping power we know that for heavier ions a higher specific ion energy (expressed in MeV/u) is required to provide the same LET. E.g. in the example of Figure 7.21 the common LET of $315$ keV/μm was achieved at largely different specific energy levels of 4,4 MeV/u for $^{12}$C, 65 MeV/u for $^{40}$Ar and 650 MeV/u for $^{84}$Kr ions. The difference in the track structures was expected mainly due to the different ion velocities and thus e.g. different ranges of $\delta$-electrons. This expectation could be confirmed by the measurements. The reason why - in line with the simulations - no strong differences could be observed in the $d(r)$ distributions of the argon and krypton ions is the relatively small difference in the velocities of the both ion types in conjunction with the limited range in $r$, where the data can be compared. In contrary, the $d(r)$ function of the carbon ion shows a qualitatively different behavior than the heavier ions inside the observable radius-range - in agreement with the simulations.

# 9 Outlook

We have shown, that the recent improvements of OPAC made it possible to derive quantitative results from particle tracks with a fairly high precision. However, there are significant possibilities to improve OPAC further in several aspects. In principle, consequences of all artifacts, which were described in chapter 6 and have negative effects on the measurement quality, can be reduced further with additional improvements of the instrument and of the data analysis methods. The shape of the image of a single photoelectron in OPAC is not a delta-function but a narrow peak with a very broad, though low halo around. Due to the superposition of many of these halos in the track core, an artificial ridge is observed in the image around the track core. Without corrections this would result in an artificial broadening of the radial dose distribution in the vicinity of the central track region. Though this effect of peak broadening could be eliminated efficiently by the described iterative unfolding method (see chapter 6.5), it is desirable to find the cause of this phenomenon and if it is possible, this cause should be eliminated and not its effects. Each detector part out of the image intensifier (II), the CCD camera and the fiber optical coupling between those (see Figure 5.2) can be responsible for the observed high extent of the peak halo.

In the future also the replacement of the CCD camera would be reasonable. Even if the camera is not the cause of the peak halo, the current CCD camera has a relatively low spatial resolution and a very limited dynamical range. The best solution would be to replace the CCD camera with one, having a window of the same size as the image intensifier (i.e. 25 mm in diameter). In this case a parallel fibre plate could be used to couple CCD camera and intensifier.

Another artifact that has a big contribution to the measurement uncertainty is the stray light in the detector, which hits the photocathode of the image intensifier "accidentally" after being scattered from internal structural elements from outside of the focus of the lens (see chapter 6.6). After difficult but successful efforts to minimize this effect we do not see further potential in instrumental developments that could further reduce the stray light. Instead, there is a possibility to make the statistical stray light subtraction method (see Appendix 10.2) more powerful. At present, $d(r)$ of tracks of $\alpha$-particles is used as reference distribution. This reference distribution that is supposed to contain - far away from the track core - only stray light but no $\delta$-electron tracks, is then subtracted from the measured $d(r)$ (of e.g. carbon ion) after the appropriate normalization. Though the method works well, the application of low energetic proton beams instead of the $\alpha$-particles as reference would be much more convenient for this purpose, as the above condition of very short $\delta$-electron tracks is even better fulfilled.

The row images taken with OPAC are 2 dimensional projections of the ion tracks. We have shown a mathematical method to unfold the "projected radial dose distribution" in order to achieve the real $d(r)$ function. Though this method works very well and the method itself does not cause any systematic error, it is of course not possible to regain the information, which is lost due to the narrow drifting field (see chapter 5.4.1). The narrow drifting field means a truncation of the space from which the information about the spatial ionization distribution is collected. And especially that subspace is truncated, where only the very few high energetic $\delta$-electrons can get to. This results in a bad sampling statistics among the sparse high energetic $\delta$-electrons for large distances from the track core - i.e. the random error for high $r$-values is high (see chapter 7.2.2). Furthermore, the narrow, delimited drifting chamber leads to a slight systematic error as well. This is due to the re-entering probability of the once (from

the sensitive volume) escaped $\delta$-electrons, which is different in a homogenous tissue and in the case of the drifting chamber.

To decrease the above random and systematic errors we propose, that the following measurement series should be performed not only in the present chamber arrangement. Additional measurements are proposed with a detector chamber that has a wider gap between the drifting anode and cathode (e.g. 10 cm). As the narrow drifting field has clear advantages for the results close to the track core (see chapter 5.4.1) the measurements in the narrow configuration are necessary as well. Furthermore, as the unfolding method can handle asymmetric space, is also not thinkable, that the ion beam passes the chamber close to the drifting anode (e.g. 1 cm) but far from the cathode (e.g. 5 cm), in order to avoid largely increasing diffusion due to the longer drifting length.

The most important effect which limits the resolution of OPAC is the diffusion of the thermalized $\delta$-electrons in the drift stage. As we pointed out in chapter 2, the most relevant sensitive volume size in the cell nucleus is two nm (distance of the both strands of the DNA) or slightly higher (maximal distance of single damages that can build a complex damage cluster). For instance, the local effect model also applies a nm-nodalization of the cell nucleus. I.e. though the spatial resolution of OPAC is already competitive with most similar detectors in the literature (see chapter 4), a further improvement in this aspect implies a real qualitative jump in the biophysical relevance of the experimental results.

An effort has been made to unfold the measured $d(r)$ distribution in order to achieve a $d_{nodiff}(r)$ distribution that is the original radial dose distribution arising in the chamber before the electrons are drifted. The unfolding was performed with the computer code, WinBUGS, which solves unfolding problems with the application of Bayes' theorem [Mac03]. The input data for the unfolding program were the measured $d(r)$ function, the parameters of the Gaussian broadening (i.e. the radial component of the diffusion distance in OPAC) and a prior estimate for the diffusion-free $d_{nodiff}(r)$ distribution (a $d_{nodiff\_0}(r) \sim 1/r^2$ dependency was presumed). Though the method itself worked well, we dismiss to present the results in this work, because no unambiguous and reliable results could be achieved. The instability of the result is due to the large dependence on the prior estimate and on the range of $r$, in which the measured $d(r)$ distribution was given for the program as input data to be unfolded.

Despite the first failures, it is possible that after deeper investigation the described procedure or another unfolding method that attempts to unfold each image individually before averaging could lead to some improvement in the resolution of OPAC. However, a serious breakthrough is not expected from such attempts. This is due to the extremely steep drop of the $d(r)$ distribution with increasing $r$. This behavior of the distribution results in a very low signal to noise ratio in the $r$-regime to be unfolded (up to an $r$-distance of $3 \cdot \sigma$ from the track core - where $\sigma$ is the diffusion parameter). Here signal is the contribution of the "real" radial dose distribution to the measured $d(r)$ function at a given $r$, while noise is the contribution of diffusion electrons originated from the very close neighbourhood of the track core to the measured $d(r)$ function at the same $r$. Very close to the track core (within an $r$-distance of $1 \cdot \sigma$) the noise dominates the measured $d(r)$ absolutely, while the signal is negligible. This fact makes any kind of unfolding to recover the undiffused $d(r)$ function very difficult. E.g. small deviations of the $d(r)$ function from a prior estimated $1/r^2$ function in the close neighborhood of the track core cannot be revealed by the unfolding method.

For the future some instrumental changes might improve the spatial resolution. The diffusion distance is proportional with the root of the gas pressure. We found, that a stable gas szintillation could not be reached in the amplification stage of OPAC at a gas pressure of 2 hPa. With a more efficient optics – which in turn require less gas amplification - and

optimized amplification geometries one can try to reduce the lowest operation pressures down to an expected limit of about 1 hPa.

However, a real breakthrough in the resolution (down to a few nm) would require a fundamental change in the working principle of OPAC. At present, OPAC uses the ionization electrons to reconstruct ionization profiles. The transport of the positive ions - instead of ionization electrons - would offer a far better solution. Firstly, heavy positive ions or molecule fragments suffer much less from diffusion than electrons when being drifted and secondly, the spatial distribution of the positive ions, left behind after the ionization by the incident ion, reflects the spatial distribution of the damages much better, than that of the thermalized $\delta$-electrons (see chapter 6.4). Unfortunately, we could not find a feasible concept for such a development within the original concept of OPAC (there exist ion counting detectors [Gro04], [Gar04] with very high spatial resolution but these are not capable for imaging - see chapter 4.3).

Another idea is the mixing of an electronegative gas into the gas filling of OPAC. Snowden et al. [Sno00] report about a negative ion time projection chamber (NITPC) used for astrophysical measurements. This detector is filled with a mixture of a target gas and an electronegative gas (e.g. $CS_2$). The gas pressure is between 10 and 40 hPa. Primary ionization electrons are rapidly and efficiently captured by the electronegative gas molecules (the capture distance is a few tenths of an mm). The resulting $CS_2^-$ ions drift to the anode wires (single-wire proportional counters are applied in this concept). The strong, inhomogeneous field around the wires causes field-ionization of the ions and thus induces free electrons. These electrons can trigger now an avalanche multiplication and, if a suitable gas is used, scintillation – like in the present OPAC. Though this latter concept is still based on the initial distribution of the ionization electrons (instead of the one of the ions) the diffusion can be reduced dramatically and such also the spatial resolution of the instrument will be much better. As first step for the further development of OPAC, the investigation of suitable gases or gas mixtures has to start, which is electronegative and still offers high charge multiplication and a large proportional scintillation light yield.

After analyzing the data of the present measurement program, we gained some experience on an optimal measurement plan for the following measurement program. As long as no special request arises and no major development of OPAC (e.g. significantly improved spatial resolution) is achieved, there is no need for further measurement of ions, heavier than carbon. We judge this part of the measurement program to be successful and completed.

While the measurement program of very fast carbon ions is completed, the amount and the quality of data for carbon ions with energies below 30 MeV/u is low. However, the data of these slower carbon ions show interesting features, because we can observe the fast decline of the $d(r)$ distribution for large distances from the track core, which are reached only by the fastest (and very sparse) $\delta$—electrons. (The $d(r)$ distribution for faster ions shows only slight discrepancies from the $1/r^2$ characteristic in the whole range accessible with OPAC). Furthermore, the $d(r)$ distributions for slow carbon ions are of particular interest from the biophysical point of view, because the tracks that contribute to the dose in the tumor and in the surrounding healthy tissue are caused by slower ions. The reason why the amount and quality of data of the slower carbon ions is inferior to the high energy ones is the fact, that all our measurements were made at the accelerator "SIS" at GSI, where only ions of energies above about 100 MeV/u can be produced directly by the accelerator. For the lower ion energies we had to use a water column as an energy degrader to slow down the ions to the desired energy level. However, the slow down in matter causes energy straggling, which becomes very prominent in the Bragg peak range (see chapter 7.2). Therefore, we plan to

perform more measurements at a smaller accelerator (e.g. UNILAC at GSI), where the lower carbon ion energies can be delivered directly by the accelerator.

A further plan at the smaller accelerator is to measure the $d(r)$ function around lighter ions, than carbon. Such measurements would be of particular interest for the therapy planning as well, because a big ratio of the incident carbon ions suffers from fragmentation during passing through the human body. The result is a mixed radiation filed, where all isotopes contribute to the dose, and thus the therapy planning (e.g. the local effect model) includes their contribution. Also the measurement and the comparison of ions of different atomic mass but similar LET should be extended to the lighter ions. We expect that the simulated results with TRAX are very good for the lighter ions; however, this must be confirmed experimentally.

The great success of the presented measurement program opens a wide range of possibilities for the further application of OPAC. Due to the expectable continuously increasing spread of the heavy ion therapy facilities, the further study of the spatial ionization distribution of ion tracks will remain in the focus of the experimental atom physics. However, with the high quality and flexibility of the information that OPAC delivers about a particle track a much wider application of the detector in the atom physics or in the nuclear astrophysics [Mos05], [Wei06] is possible.

# 10 Appendix

## 10.1 Peaks after subsequent unfolding and folding of the peak halos

Figure 10.1 a) shows the same measured, magnified track segment as Figure 6.13 a). Figure 10.1 b) is the same segment after unfolding and subsequent folding of the resulting $<n_{sp}>_i$ and $(x_i,y_i)$ data (see chapter 6.5.6) with experimental single electron response function (the same method as shown on the example of Figure 6.17 a) and b)). Due to the applied folding method, the shape of the peaks of Figure 10.1 b) is uniform (if normalized to the same peak integral). It is also obvious, that the original height of each single peak cannot be reconstructed exactly, especially if two or more local maxima were close to each other in the original image. However, the sum of pixel integrals of peaks inside one larger cluster of compound peaks is still nearly constant.
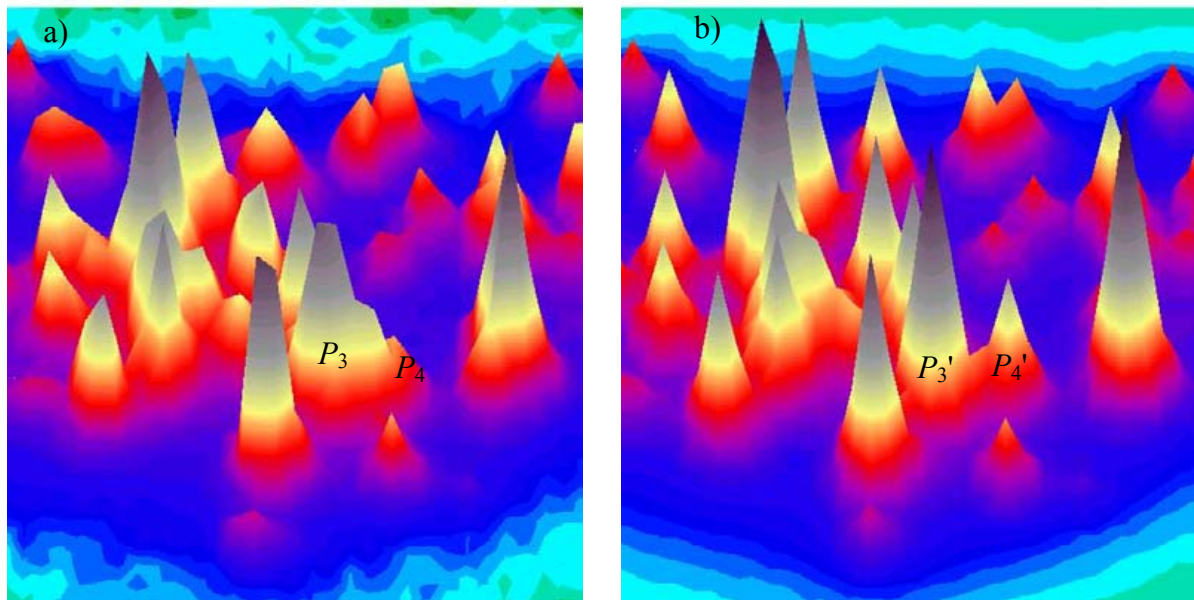


Figure 10.1: *a) original ion track segment; the same as in Figure 6.13 a) and b) the result of unfolding – refolding process (similarly to Figure 6.17, but with a magnified view to a smaller region. For this reconstruction only $<n_{sp}>_i$ and $(x_i,y_i)$ data of the resulting peaks and the shape of the average peaks are used as input parameters.*

Let us explain the phenomenon on a numerical example. The compound peak, marked with $P_3$ is a superposition of more single peaks (probably three or more). As the formation had only one local maximum, it was handled as one compound peak. (Note, that the expectable amount of average peaks below its contour, $<n_{sp}>$, is not one, but higher.) The small peak, marked with $P_4$ next to $P_3$ was caused probably by one single photoelectron of the photocathode. The distance between the both local maxima was found to be 4 pixels. After recognizing the both local maxima, the automatic peak searching algorithm orders each pixel between $P_3$ and $P_4$ (in Figure 10.1 a)) to one of the both peaks. As a result, 6,9 average peaks were attributed to $P_3$ and 3,9 average peaks to $P_4$:

$<n_{sp}>_{3\_original} = 6,9$

$<n_{sp}>_{4\_original} = 3,9$

Although the real difference between the both peaks is higher, this separation can be accepted as the very precise assignment of pixel hits is not of central importance (see simplification Nr. 5 in chapter 6.5.6). After subtracting the halo contributions of the surrounding peaks, i.e. the result of unfolding for the both selected peaks, the content in each peak is:

$<n_{sp}>_{3\_unfolded} = 5,5$
$<n_{sp}>_{4\_unfolded} = 2,1$

The smaller peak has lost more of its content in absolute numbers. The reason for this is simple: The closest neighbor of P4, which is $P_3$, is taller and thus has also a larger halo contribution in the $Q_1$ region of $P_4$, as $P_4$ in the $Q_1$ of $P_3$. After refolding the whole track with the expectable halo contributions, the original peak integrals are reconstructed correctly:

$<n_{sp}>_{3\_reconstructed} = 6,9$
$<n_{sp}>_{4\_reconstructed} = 3,9$

# 10.2 Detailed description of the method for stray light subtraction

This appendix explains the method that we chose to create a standard reference data set for the stray light contribution as a function of $y$ (projected radial distance from the track core) for a given total amount of light (see also chapter 6.6). This data is essential for the quantitative data analysis of the measurements; the standard distribution must be multiplied by the ratio of the total light in the observed to that in the reference case. The resulting stray light contribution must be subtracted from the unfolded measured $d_{pr}(y)$ data.

The most obvious method to derive the standard reference stray light function is to image ion tracks which can produce only low energetic $\delta$-electrons. If the range of the fastest $\delta$-electrons is $r_{range}$ and the maximal reasonably achievable overall one-dimensional root-mean-square diffusion distance is $y_{diff}$ (for example $y_{diff} = 3 \cdot \sigma$), then it is ensured that outside of a projected distance of $y_{max} = r_{range} + y_{diff}$ all (or practically all) observed single peaks are due to stray light. Hence, the ratio of light yield at a given $y > y_{max}$ to the overall light yield is the same, as the corresponding ratio of stray light contribution for ions with higher possible $\delta$-electron ranges. The main limitation of the method is the problematic stray light contribution estimation for $y < y_{max}$.

The maximal initial energy of $\delta$-electrons depends primarily on the velocity of the ion. 5,6 MeV (1,4 MeV/u) $\alpha$-particles from a [241]Am source induce $\delta$-electrons with a maximal energy of about 2,8 keV according to equation (3.4). Such electrons have a range of a few hundred nm in liquid water corresponding to about 10 pixels at a TEA pressure of 40 hPa. $\delta$-electrons with energies around this limit are extremely rare; in fact the probability of inducing a $\delta$-electron with an energy above 1 keV is still very low. The Am-source was placed inside the gas volume into the port, where the first trigger detector is mounted (Figure 5.1). In order to be sure that the method provides a reliable estimate under all circumstances, about 1000 tracks were imaged under many different measurement conditions (varied gas pressure and $A_{c\&l}$ gain). Figure 10.2 shows arbitrary selected examples of two tracks, measured at $p = 4$ hPa and $p = 32$ hPa. As the $\delta$-electron ranges are very low, the widths of the track cores are determined mainly by the electron diffusion. As $\sigma \propto 1/\sqrt{p}$ according to (6.9), the expected one-dimensional diffusion length is nearly three times lower in image b) compared to a) (if measured in pixels). The comparison of both images confirms this expectation.
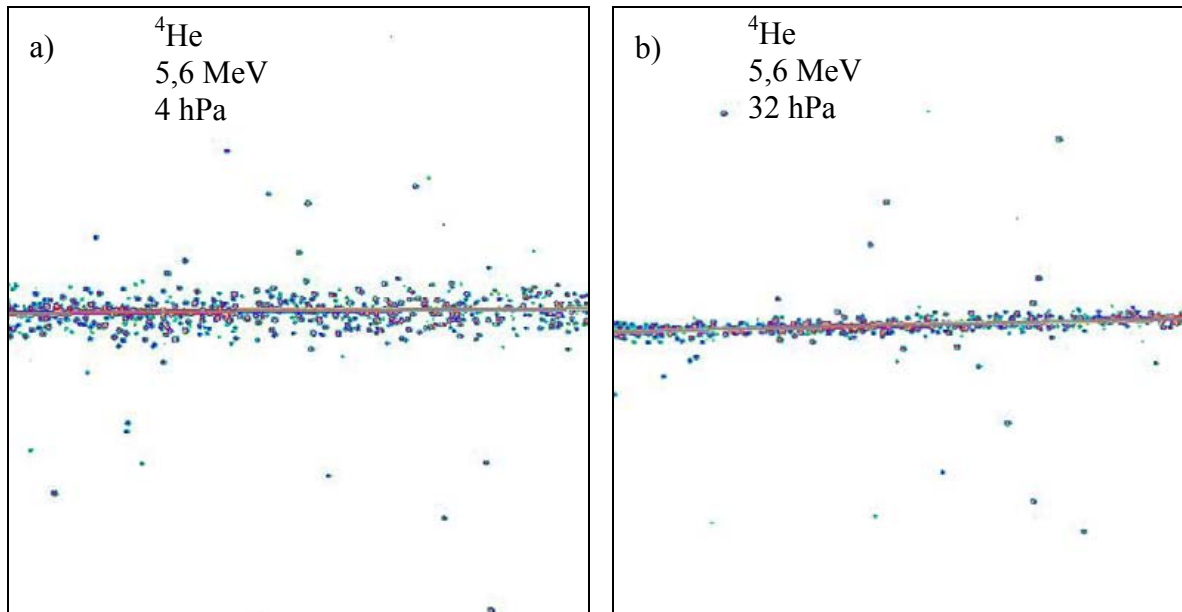
Figure 10.2: *Measured tracks of α-particles after peak-halo elimination. The ion trajectories have been found by the automatic algorithm and are plotted as gray lines. The isolated single peaks further away from the diffused track cores are due to stray light.*

The theoretical determination of the maximum (projected) radial range of the delta electrons ($y_{max}$) for each measurement condition is not trivial. Due to the relative high LET and low energy of the α-particles, their energy cannot be treated as constant inside the interaction volume at higher pressure. (This and the need that the alpha particle reaches the second trigger detector are the reason why the highest gas pressure applied was 32 hPa instead of 40 hPa.) The simulation of α-particle tracks with TRAX in order to determine the δ-electron ranges is not the best choice either, because relative high discrepancies were experienced between earlier measurements and TRAX simulations for radial dose distributions around the cutoff distance for α-particles (see Figure 8 in [Krm94]).

The selected method for the estimation of $y_{max}$ is based on its direct, experimental determination, performed by OPAC at the presence of stray light. Projected radial dose distributions, $d_{pr}(y)$, of α-particles are compared in Figure 10.3. The corresponding measurements were performed at different (4, 10, 20 and 32 hPa) gas pressures. The $d_{pr}(y)$ distributions are here termed as light yield distributions, because the stray light contributions are still included. For the determination of each distribution the data of 1000 to 5000 images are used after the peak halos were subtracted in each image. The resulting distributions were smoothed, according to the description in chapter 6.2, and normalized to the same total light yield.
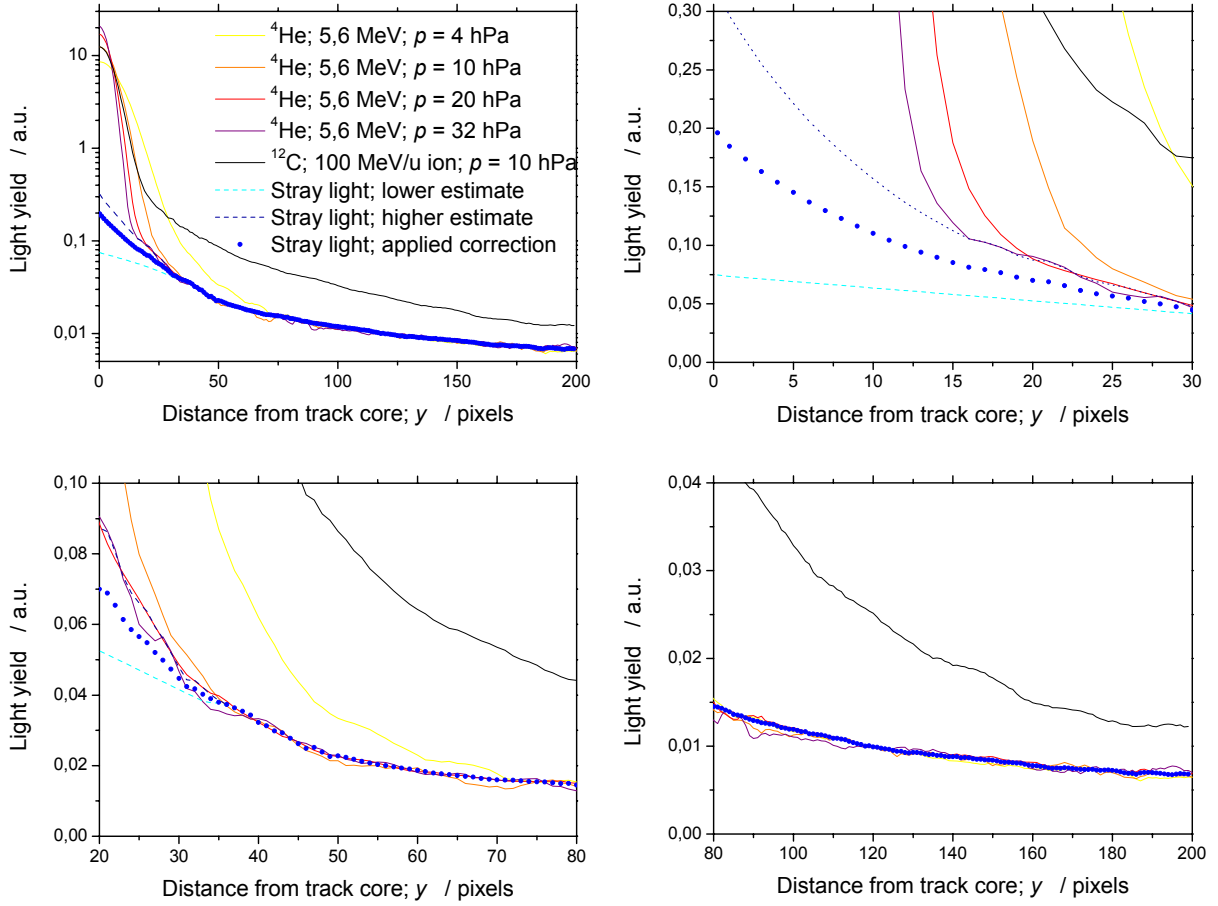
Figure 10.3: *The method for measuring the stray light contribution (blue symbols) to the measured projected radial light distributions is based on the comparison of the plotted distributions for a-particles. These distributions contain only the stray light contribution for projected distances from track core (y) above the max range of the $\delta$-electrons ($y_{max}$) ($y > y_{max}$,) where $y_{max}$ depends on the gas pressure. The black curve is the projected radial light distribution — still including the stray light contribution — of 100 MeV/u carbon ions. The stray light-free, measured $d_{pr}(y)$ can be derived by subtracting the stray light contribution values from the raw distribution (black line). All the curves are normalized to the same overall light yield; the four diagrams contain the same data in different regimes with different scalings.*

There are three facts, which help to interpret Figure 10.3. Firstly, the contribution of stray light is proportional to the total light yield but definitely independent of the gas pressure. Secondly, no $\delta$-electron can deliver a contribution for $y > 75$ pixels at a gas pressure of 32 hPa (maximal range of $\delta$-electrons is below 15 pixels and $3\sigma \approx 13$ pixels). Finally, it is well observable in Figure 10.3, that the measured light distribution of $\alpha$-particles is independent of the gas pressure for large radial distances ($y > 75$ pixels). From these facts we conclude that for $y > 75$ pixels no measurable contribution of ionization electrons is present at any of the four gas pressures, studied. Thus, in this region the average of the four curves can be considered as the projected radial distribution function of the stray light background. This stray light distribution (marked with blue symbols in Figure 10.3) is close to the distribution at $p = 20$ hPa, because the averaging was performed by weighting with the number of available images in order to achieve the best possible statistics. There are more, than 5000 images available at $p = 20$ hPa, because many different gain and drift voltage conditions were. The red curve in Figure 10.3 was achieved by averaging of these different data sets at $p = 20$ hPa. This averaging could be done easily, because the different gain or peak density

144

conditions did not influence the shape of the curve after tail-unfolding significantly. This latter observation is not relevant relating to the stray light reduction, but provides a further indication, that the algorithms for data analysis and peak tail subtraction work reliably and stable.

For the intermediate projected radial distance region (36 pixels > $y$ > 75 pixels) there are already some diffused electrons present among the stray light peaks at the lowest pressure of $p$ = 4 hPa. At higher pressure the diffusion does not play set a role and the three other curves are still in good agreement. Therefore, the weighted average of these three curves was used to determine the stray light contribution in this region of $y$. Similarly, in the region, 22 pixels > $y$ > 36 pixels, the average of measurements at 20 hPa and 32 hPa was applied to achieve the desired distribution of the blue symbols. For 16 pixels > $y$ > 22 pixels only the data of measurements at $p$ = 32 hPa were applied. The limiting values of $y$, where the images contain only stray light, were derived according to the diagrams in Figure 10.3. The values of 75 pixels for $p$ = 4 hPa, 36 pixels for $p$ = 10 hPa and 22 pixels for $p$ = 20 hPa are rather conservative estimates, because it is more important to exclude the whole contribution due to ionization electrons, than to increase the statistics slightly by including more data. Even more difficult is to find the best estimate for the threshold level for the measurement at $p$ = 32 hPa, because no reference curve at higher pressure levels exists. If a threshold level of $y_{min}$ = 21 is accepted for $p$ = 20 hPa, the threshold level at 32 hPa should be at

$$y_{min\_range} = 22\frac{20\text{hPa}}{32\text{hPa}} = 13,1 \quad \text{pixels if the range of } \delta\text{-electrons and at}$$

$$y_{min\_drift} = 22\sqrt{\frac{20\text{hPa}}{32\text{hPa}}} = 16,6 \text{ pixels if their diffusion dominates } y_{max} \text{ under the observed}$$

circumstances. The slope of the curve which corresponds to $p$ = 32 hPa increases for $y$ < 16-17 pixels. In this range the distribution is determined by electron diffusion rather than by the contribution of the fastest $\delta$-electrons. The distance of 16 pixels corresponds to about 3,7·$\sigma$ at $p$ = 32 hPa, if the value of $\sigma$ is calculated according to (6.9). As the diffusion is found to be dominating compared to the range of $\delta$-electrons, it is probable, that the contribution from diffused ionization electrons to the radial ionization distribution of $\alpha$-particles at $p$ = 32 hPa for radial distances above 16 pixels is very low.

To estimate the remaining effect of diffused electrons for projected radial distances above 16 pixels the shape of the stray light distribution for $y$ < 35 pixels is investigated. The light yield distribution function at $p$ = 32 hPa is an upper estimate for the stray light distribution at 16 pixels < $y$ < 22 pixels (dashed dark blue curve in Figure 10.3). A steeper than linear (if a line is fitted onto the curve in the interval of 16 pixels < $y$ < 22 pixels) increase is then extrapolated for $y$ ≤ 16 pixels. The lower estimate (dashed light blue line) assumes, that the steepness of the stray light contribution curve is constant below $y$ = 35 pixels (a line is extrapolated). As a compromise for the stray light contribution function (blue symbols), the average values of the upper and lower estimates are calculated for 0 < $y$ < 22 pixels.

The "projected radial" distribution, marked with blue symbols, was selected as an empirically derived estimate for the stray light contribution function. The black curve of Figure 10.3 shows the $d_{pr}(y)$ distribution for 100 MeV/u $^{12}$C ions before the stray light subtraction. The curve is the smoothed version of the (peak halo-) unfolded $d_{pr}(y)$ distribution in Figure 6.18 (black symbols there; differently normalized). The diagrams of Figure 10.3 make it clear, that the relative contribution of stray light to the overall light yield at a certain $y$ distance from the track core increases with $y$. For $y$ > 150 pixels even more single peaks are observable due to stray light than due to the ionization electrons; the signal to noise (due to stray light) ratio, $SNR_{SL}$, is below one. $SNR_{SL}$ reaches two at $y \approx 95$, three at $y \approx 60$, four at $y \approx 45$. The value of $SNR_{SL}$ at $y$ = 0 is 50 for the higher and 150 for the lower estimate. In order to achieve the

projected radial dose distribution of the ions under consideration -such as that of the 100 MeV/u $^{12}$C ions of the example- the stray light contribution has to be simply subtracted from the measured and unfolded light yield values at each $y$-distance. I.e., values of blue symbols have to be subtracted from the corresponding values, represented by the black curve.

The last important question regards the uncertainties of the subtracted stray light contributions. For $y > 40$ pixels the searched uncertainties are identical with the uncertainties of the light yield distribution values determined from the $\alpha$-particle images. In chapter 6.5.6 the upper limit for the uncertainty of the (normalized) projected radial dose values was estimated to be 5% due to the peak unfolding algorithm. Due to the stable measurement conditions and good statistics with $\alpha$-particles and limited peak densities the uncertainty should be significantly lower. The very good agreement of the four light distributions at $y > 75$ pixels also indicates, that the peak unfolding algorithm is reliable irrespective to the gas pressure. Thus, the overall uncertainties (including other error sources) of the stray light contribution values are estimated to be 5% for $y > 40$ pixels. This implies that e.g. at $y = 150$ pixels, where $SNR_{SL} = 1$, the relative uncertainty of $d_{pr}(y)$ has a component of 2,5% due to stray light.

For $y < 40$ pixels the uncertainty from the expected stray light contribution starts to be larger than the uncertainties of the relative light yield values from the $\alpha$-particle measurements. This is due to the additional uncertainties of $y_{max}$. These additional absolute uncertainties are estimated to amount to the difference between the lower and higher estimates (dashed curves in Figure 10.3). E.g. about $\Delta d_{pr}(20) = 0{,}015$ a.u. at $y = 20$ pixels. Although it corresponds to a relative error of about 15 % for the stray light contribution, but due to the largely increased signal level in the $^{12}$C measurements the relative error of the $d_{pr}(y)$ of carbon due to stray light is much lower. I.e. in the example above, the relative light yield for the 100 MeV/u $^{12}$C tracks at $y = 20$ pixels is about $d_{pr}(20) = 0{,}35$ a.u. Thus, the relative error due to stray light amounts to $\Delta d_{pr}(20)/d_{pr}(20) = 4{,}3\%$. For lower $y$ values the distance between the dashed curves is smaller and for higher $y$ values, the signal value increases rapidly. Therefore, an upper estimate for the contribution of stray light to the overall relative uncertainty of $d_{pr}(y)$ can be summarized as follows:
2% for $y \leq 15$
5% for 15 pixels $< y < 30$ pixels
2% for 30 pixels $< y < 100$ pixels
4% for 100 pixels $< y < 200$ pixels.

The given values are valid for the presented example of 100 MeV/u $^{12}$C ions at $p = 10$ hPa. In a measurement where $p = 40$ hPa the signal values in the region of 10 pixels $< y < 20$ pixels are significantly lower due to the lower diffusion distances (if expressed in pixels). Thus, the relative role of stray light uncertainties is increased and if a generally (for $p = 40$ hPa) valid upper estimate is desired, 10% has to be given for 10 pixels $< y < 20$ pixels and 5% for 20 pixels $< y < 30$ pixels. On the other hand, at $p = 4$ hPa a typical upper estimate is not higher than 3% in the entire 10 pixels $< y < 30$ pixels regime due to the high signal values.

In a future measurement campaign it is suggested to determine the stray light contribution function with protons from an accelerator instead with the $^{241}$Am $\alpha$-source. Due to the lower LET of protons compared to the $\alpha$-particles at the same reduced energy, the gas pressure could be increased up to the TEA-specific limitation of about 80 hPa, if 1 MeV protons were used instead of $^{241}$Am $\alpha$-particles. The lower specific energy and higher possible gas pressure would allow for a more precise determination of stray light contribution down to about 10-15 pixels.

# 11 References

[Ang67] G.M. Angleton, *Health Phys.* 13 (1967) 45

[Ash82] J.C. Ashley, Energy losses and inelastic mean free paths of low-energy electrons in polyethylen, *Rad. Res.* 90 (1982) 433-436

[Azz04] E.I. Azzam EI and J.B. Little, The radiation-induced bystander effect: evidence and significance, *Hum. Exp. Toxicol.* 23(2) (02. 2004) 61-5

[Bar63] G.W. Barendsen, H.M. Walter, J.P. Fowler, D.D. Bewley, Effects of different ionizing radiation on human cells in tissue cultures, *Radiat. Res.* 15 (1963) 106-119

[Ang67] G.M. Angleton, *Health Phys.* 13 (1967) 45

[Ash82] J.C. Ashley, Energy losses and inelastic mean free paths of low-energy electrons in polyethylen, *Rad. Res.* 90 (1982) 433-436

[Azz04] E.I. Azzam EI and J.B. Little, The radiation-induced bystander effect: evidence and significance, *Hum. Exp. Toxicol.* 23(2) (02. 2004) 61-5

[Bar63] G.W. Barendsen, H.M. Walter, J.P. Fowler, D.D. Bewley, Effects of different ionizing radiation on human cells in tissue cultures, *Radiat. Res.* 15 (1963) 106-119

[Bar90] G.W. Barendsen, LET dependence of linear and quadratic terms in dose-response relationships for cellular damage: correlations with the dimensions and structures of biological targets, *Raditat. Prot. Dosim.* 31 (1990) 235-239

[Bau74] J.W. Baum, M.N. Warma, C.L. Wingate, H.G. Paretzke and A.V. Kuehner, Nanometer dosimetry of heavy ion tracks, In *Proceedings of the 4th Symposium of Microdosimetry, Verbania Pallanz, Italy* (Editors: J. Booz, H.G. Ebert, R. Eickel and A. Waker) Euratom, Brussels, Vol. 1, (1974) 93-112

[Bec96] Uwe Bechthold, Elektronenemission aus Stössen schneller Schwerionen mit komplexen Targets, *Dissertation zur Erlangung des Doktorgrades der Naturwissenschaften*, Frankfurt am Mein (1996)

[Bec97] U. Bechtold, S. Hagmann, J. Ullrich, B. Bathelt, A. Bohris, R. Moshammer, U. Ramm, C. Bhalla, G. Kraft, H. Schmidt-Böcking, Intra-atomic double scattering of binary encounter electrons in collisions of fast heavy ions with atoms and molecules, *Phys. Rev. Lett.* 79 (1997) 2034-2037

[Bel89] M. Belli, R. Cherubini, S. Finotto, G. Moschini, O. Sapara, G. Simone and M.A. Tabocchini, RBE-LET relationship of the survival of V79 cells irradiated with low-energy protons, *Int. J. Radiat. Biol.* 53 (1989) 93-104

[Ben62] M.A. Bender, and P.C. Gooth, *Int. J. Radiat. Biol.* 5 (1962) 133

[Ber63] M.J. Berger, Monte Carlo calculation of the penetration and diffusion of fast charged particles, *Methods Comp. Phys.* 1 (1963) 135-215

[Bet30] H. Bethe, Zur Theorie des Durchgangs schneller Korpuskularstrahlung durch Materie, *Ann. Phys.*, 5 1930 325-400

[Bew68] D.K. Bewely, and S. Hornsey, *Biophysical Aspects of Radiation Quality, Second Panel Report, Vienna, I.A.E.A.*, 1968, 65

[Bia63] M.H. Biavati, W. Rosenzweig, H.H. Rossi and I. Miyagana, The dependence of RBE on the energy of fast neutrons. III. evaluations of radiation quality, *Rad. Res.* 19 (1963) 512

[Bla79] E. A. Blakley, C.A. Tobias, T.C.H. Yang, K.C. Smith and J.T. Lyman, Inactivation of human kidney cells by high-energy monoenergetic heavy-ion beams, *Rad. Res*. 80 (1979) 122-160

[Blo33] F. Bloch, Zur Bremsung rasch bewegter Teilchen beim Durchgang durch Materie, *Ann. Phys.* 6 1933 285-321

[Bon70] T.F.M. Bonsen, L. Virens, Angular distribution of electrons ejected by charged particles, *Physica* 47 (1970) 307-319

[Bre88] A. Breskin, R. Chechik, Z. Fraenkel, D. Sauvage, V. Steiner, I. Tserruya, G. Charpak, W. Dominik, J.P. Fabre, J. Gaudean, F. Sauli, M. Suzuki. P. Fischer, P. Glässel, H. Ries, and H.J.Specht, A highly efficient low-pressure UV-RICH detector with optical avalanche recording *Nucl. Instr. and Methods A* 273 (1988) 798

[Bre89] New developments in optical imaging detectors, Invited talk at the Quark Matter Conf. Lenox Mass. Sept., 1988, *Nucl. Phys.* A498 (1989) 457

[Bre90] A. Breskin, R. Chechik and D. Sauvage, A 3-stage gated UV-photon optical imaging gaseous detector, *Nucl. Instrum. Meth. A* 286 (1990) 251

[Bre95] A. Breskin, R. Chechik, P. Colautti, V. Conte, L. De Nardo, A. Pansky, S. Shchemelinin, G. Talpo, G. Tornielli, A single-electron counter for nanodosimetry, *Radiat. Prot. Dosim.* 61 (1995) 199-204

[Bro03] S. Brons, G. Taucher-Scholz, M. Scholz, G. Kraft, A track structure model for simulation of strand breaks in plasmid DNA after heavy ion irradiation, *Radiat. Environ. Biophys.* 42 (2003) 63-72

[Bud81] T. Budd, M. Marshall and C.S. Kwok, Advances in cloud-chamber techniques and measurements of W value in a tissue-equivalent gas, *Rad.Res.* 88 (1981) 228-239

[Bud83a] T. Budd and M. Marshall, Microdismetric properties of electron tracks measured in low-pressure cloud chamber, *Rad. Res.* 93 (1983) 19-32

[Bud83b] T. Budd, C.S. Kwok, M. Marshall and S. Lythe, Microdosimetric properties of alpha-particle tracks measured in a low-pressure cloud chamber, *Rad. Res.* 95 (1983) 217-230

[But67] J.J. Butts, R. Katz, Theory of RBE for heavy-ion bombardment of dry enzymes and viruses, *Rad. Res.* 30 (1967) 855-871

[Cha73] K.H. Chadwick and H.P. Leenhouts, A molecular theory of cell survival, *Phys. Med. Biol.* 13 (1973) 78-87

[Cha76] A. Chatterje and H. J. Schaefer, Microdosimetric structure of heavy ion tracks in tissue, *Rad. Environ. Biophys.* 13 (1976) 215-227

[Cha81] K.H. Chadwick and H.P. Leenhouts, The molecular model for cell survival following radiation, In *The molecularTheory of radiation biology* New York: Springer Verlag (1981) 25-50

[Dan01] V. Dangendorf, H. Schumacher, M. Kraemer, D. Schardt, Measurement of ionization topology of heavy ions in low pressure TE-gas, Presentation as a beam time proposal at GSI, Darmstadt, (2001)

[Des64] F. Dessauer, K. Sommermeyer (editor), *Quantenbiologie: Einführung in einen neuen Wissensszweig*, Spronger Verlag, Berlin, 1964

[Dou76] B.G. Douglas and J.F. Fowler, The effect of multiple small doses of X rays on skin reactions in the mouse and a basic interpretation, *Rad. Res.* 66 (1976) 401-426

[Egu96] K. Eguchi-Kasai, M. Murakami, H. Itsukaichi, K. Fukutsu, T. Kanai, Y. Furusawa, K. Sato, H. Ohara, F. Yatagi, The role of the DNA repair on cell killing by charged particles, *Adv. Space res.* 18 (1996) 109-118

[Eng81] H.A. Engelhardt, Novel charged particle analyzer for momentum determination in the multichanneling mode: Part I and II Rev, *Sci. Instr.* 52 (1981) 835 and 1161

[Far04] M. Farahmand, A novel tissue-equivalent proportional counter based on a gas electron multiplier, (2004) TU Delft

[Feh83] J. Fehlmann, G. Viertel, Compilation of data for drift chamber operation, ETH, Zürich (1983)

[Fon89] P. Fonte, A. Breskin, G. Charpak, W. Dominik and F. Sauli, First beam tests of an imaging high density projection chamber. *Nucl. Instrum. Met. A* 283 (1989) 658

[Gar02] G. Garty, S. Shchemelinin, A. Breskin, R. Chechik, G. Assaf, I. Orion, V. Bashkirov, R. Schulte, B. Grosswendt, The performance of a novel ion-counting nanodosimeter, *Nucl. Instr. Meth. Phys. Res. A.*, 492, N.1,2 (2002) 212-235

[Gar04] G.Y. Garty, Development of ion-counting nanodosimetry and evaluation of its relevance to radiation biology, Thesis for the degree of Doctor of Philosophy (2004), Submitted to the Scient. Council of the Weizmann Institut of Science, Rehovot, Israel

[Goo79] D.T. Goodhead, J. Thacker and R. Cox., Effectiveness of 0,3 keV carbon ultrasoft *X*-rays for the inactivation and mutation of cultured mammalian cells, *Inter. Journal of Radiat. Biol.* 36 (1979) 101-114

[Goo85] D.T. Goodhead, Saturable repair models of radiation action in mammalian cells, *Radiat. Res.* Suppl. 8, 104 (1985) S-58-S-67

[Grc69] J.D. Garcia, Ejected electron distributions, *Phys. Rev.* 177 (1969) 223-229

[Grn80] K-O. Groneneveld, E. Schopper and S. Schumann, edited by H. Francois et al., Solid state nuclear track detectors, Oxford and New York, (1980)

[Gro02a] B. Grosswendt and S. Pszona, The track structure of $\alpha$-particles from the point of view of ionization-cluster formation in "nanometric" volumes of nitrogen, *Radiat. Environ. Biophys.* 41 (2002) 91-102

[Gro02b] B. Grosswendt, Formation of ionization clusters of propane-based tissue-equivalent gas or liquid water by electrons and $\alpha$-particles, *Radiat. Environ. Biophys.* 41 (2002) 103-112

[Gro04] B. Grosswendt, Recent advaces of nanodosimetry, *Rad. Prot. Dosim.* 110 (2004) 789-799

[Gro78] B. Grosswendt and E. Waibel, Transport of low energy electrons in nitrogen and air, *Nucl. Instrum. Methods* 155 (1978) 145-156

[Gry59] M. Gryzinski, Classicla theory of electronic and ionic inelastic collisions, *Phys. Rev.* 115 (1959) 374-383

[Gun77] K. Guenther, W. Schultz and W.Leistner, Microdosimetric approach to cell survival curves in dependence on radiation quality, *Stud. Biophys.* 61 (1977) 163-209

[Gun83] K. Guenther and W. Schulz, *Biophysical theory of radiation action*, Akademie-Verlag, Berlin, (DDR) 1983

[Hag93] S. Hagmann, GSI-intern

[Hag06] S. Hagmann, Private communication

[Hec60] H.H. Heckmann, B.L. Perkins, W.G. Simon, F.M. Smith and W.H. Barkas, Ranges and energy-loss classical processes of heavy ion emulsion, *Phys. Rev.*, 117 (1960) 544-556

[Hod77] D.C. Hodges and M. Marshall, A low-pressure cloud chamber to study the spatial distribution of ionizations, *J. Phys. E* 10 (1977) 342-350

[Hug66] O. Hug, A. M. Kellerer, *Stochastik der Strahlenwirkung* (Berlin, Heidelberg, New York: Springer), 1966

[ICR66] ICRP, 1966, Recommendations of the International Commission on Radiation Protection 1965. *ICRP Publication 9*, Pergamon Press, Oxford

[ICR83] Microdosimetry, *ICRU Report 36*, Bethesda, USA (1983)

[ICR84] Stopping powers for electrons and positrons, *ICRU Report 37*, ICRU, Washington DC, 1984

[ICR96] Secondary Electron Spectra from Charged Particle Interactions, *ICRU report 55*, Maryland, USA (1996)

[Kan98] T. Kanai, M. Sudo, N. Matsufuji and Y. Futami, Initial recombination in a parallel-plate ionization chamber exposed to heavy ions, *Phys. Med. Biol.* 43 (1998) 3549-3558

[Kap72] A. Kappos, W. Pohlit, A cybernetic model for radiation reactions in living cells. I. Sparsely-ionizing radiations; stationary cells, *Int. J. Radiat. Biol.* 22 (1972) 51-65

[Kat03] R. Katz, Commentary, The parmeter-free structure model of Scholz and Kraft for heavy-ion cross sections, *Rad. Res.* 160 (2003) 724-728

[Kat71] R. Katz, B. Ackerson, M. Homayoonfar, S.C. Shrama, Inactivation of cells by heavy-ion bombardment, *Rad. Res.* 47 (1971) 402-425

[Kat72] R. Katz, S.C. Sharma and M. Homayoonfar, F.H.Attix (editor) The structure of particle tracks, in topics in radiation disimetry, supp1, Academic Press New York and London (1972) 317-384

[Kat85] R. Katz, Thindown in radiobiology, *Rad. Prot. Dos.* 13 (1985) 281-284

[Kel71] A.M. Kellerer, An assessment of wall effects in microdosimetric measurements, *Rad. Res.* 47 (1971) 377

[Kel72] A.M. Kellerer and H.H. Rossi, The theory of dual radiation action, *Curr. Top. Radiat. Res.* Q8 1972 85-158

[Kel75] A.M. Kellerer, and D. Chmelevsky, Concept of microdosimetry. III: Mean values of the microdosimetric distributions, *Radiat. Environ. Biophys.* 12 (1975) 321

[Kel78] A.M. Kellerer, H.H. Rossi, A generalized formulation of dual radiation action, *Curr. Top. Rad. Res.* 97 (1978) 471-488

[Kel80] A.M. Kellerer, Concepts of geometrical probability relevant to microdosimetry, in J. Booz, H.G. Ebert and H.D.Hartfiel (editors): *Seventh Symposium on Microdosimetry, EUR 7147*, Haword, London: Academic Publishers, 1049-1062

[Kie86] J. Kiefer and H. Straaten, A model of ion track structure based on classical collision dynamics, *Phys. Med. Biol.* 31 (1986) 1201-1209

[Kif71] L. Kieffer, Low-energy electron-collision cross-section data, *Atomic Data* 2 (1971) 293

[Kli90] P. Kliauga, Measurement of single event energy deposition spectra at 5 nm to 250 nm simulated site size, *Radiat. Prot. Dosim.* 31 (1990) 119

[Kon04] K. Gunzert-Marx, Nachweis leichter Fragmente aus Schwerionenreaktionen mit einem $BaF_2$-Teleskop-Detektor

[Kra00] G. Kraft, Tumor therapy with heavy charged particles, *Progress in Particle and Nuclear Physics* 45 (2000) S473-S544

[Kra87] G. Kraft, Radiobiological effects of very heavy ions, *Nucl. Sci. Appl.* 3 (1987) 1-28

[Kra99a] G. Kraft, M. Scholz, U. Bechthold, Tumor therapy and track structure, *Radiat. Environ. Biophys.* 38 (1999) 229-237

[Kra99b] G. Kraft, RBE and ist interpretation, *Strahlenther. Onkol. 2Suppl 2, 175 (1999) 44-7*

[Krm00a] M. Kraemer, O. Jaekel, T. Haberer, G. Kraft, D. Schardt and U. Weber, Treatment planning for heavy-ion radiotherapy: physical beam model and dose optimization, *Phys. Med. Biol.* 45 (2000) 3299-3317

[Krm00b] M. Kraemer and M. Scholz, Treatment planning for heavy-ion radiotherapy: calculation and optimization of biologically effective dose, *Phys. Med. Biol.* 45 (2000) 3319-3330

[Krm04] M. Kraemer, Heinrich, Data sheet "dEdx" containing LET and ion range values for different ions as a function of specific energy, GSI, (2004)

[Krm91] M. Kraemer and G. Kraft, Heavy ion track structure calculations, In: K.H. Chadwick, G. Moschini and M.N. Varma (editors), *Biophysical Modelling of Radiation Effects*, Adam Hilger, Bristol, (1991) 61-76

[Krm94] M.Kraemer and G. Kraft, Calculations of heavy-ion track structure, *Radiat. Environ. Biophys.* 33 (1994) 91-109

[Krm98] M. Kraemer, Keynote lecture: Heavy ion track structure models, (1998), source: http://www-aix.gsi.de/~bio/PUBS/1998/pubs1998.html

[Lan00] D. Landau, K. Binder, A guide to Monte Carlo simulations in statistical physics, Cambridge Univesity Press, Cambridge (2000)

[Lea56] D.E. Lea, Actions of radiations on living cells, Camridge University press, 1956

[Mac03] MacKay D.J.C. Information Theory, Interference and Learning Algorithms, Chapter 3, More about Interference, Cambride University Press, 2003

[Mar70] M. Marshall, J.A.B. Gibson and P.D. holt, An analysis of the target theory of Lea with modern data, *Int. J. Radiat. Biol.* 18 (1970) 127-138

[Met88] N.F. Metting, H.H. Rossi, L.A. Braby, P.J. Kliauga, J. Howard, M. Zaider, W. Schimmerling, M. Wong and M. Rapkin, Microdosimetry near the trajectory of high-energy heavy ions, *Rad. Res.* 116 (1988) 183-195

[Mir03] W. Mirande, Measurement of light reflection of different surfaces after private discussions PTB, (2003)

[Mol48] G. Molière, Theie der Streuung geladener Teilchen, *Z. Naturforsch* 3A (1948) 78-97

[Mos05] G. Moshe, A. Breskin, R. Chechik, V. Dangendorf and H.R. Weller, Optical Readout Time Projection Chamber (O-TPC) for a Study of Oxygen Formation In Stellar Helium Burning, *Proceedings 21st Winter Workshop on Nuclear Dynamics*, Breckenridge, CO, February 5-12 (2005)

[Nag92] H. Nagasawa and J.B. Little, Induction of sister chromatid exchanges by extremely low doses of alpha particles, *Cancer Res.* 52, (1992) 6394–6396

[Nak67] S. Nakai and R. Mortimer, *Radiat. Res. Suppl.* 7 (1967) 172

[Nar02a] L. De Nardo, P. Colautti, V. Conte, W.Y.Baek, B. Grosswendt, G. Tornielli, Ionization-cluster distributions of $\alpha$-particles in nanometric volumes of propane: measurement and calculation, *Radiat. Environ. Biophys.* 41 (2002) 235-256

[Nar02b] L. De Nardo, A. Alkaa, C. Kahamphan, V. Conte, P. Colautti, P. Segur, G. Tornielli, A detectro for track-nanodosimetry, *Nucl. Instrum. Methods Phys. Res. A* 484 (2002) 312-326

[Oak99] Copyright: Oak Ridge Associated Universities, (1999), Donated by Columbia University, *http://www.orau.org/ptp/collection/proportional%20counters/rossi.htm*

[Opa72] J.B. Opal, E.C. Beaty and W.K. Peterson, Tables of secondary-electron-production cross sections, *Atomic Data* 4 (1972) 209-253

[Pag01] H. Paganetti and M. Goitein, Biophysical modelling of proton radiation effects based on amorphous track models, *Int. J. Radiat. Biol.* 77 (2001) 911-928

[Par74] H.G. Paretzke, Comparison of track stucture calculations with experimental results, *Proc. Fourth Symposium on Microdosimetry Verbania Pallanz, Italy* (Editors: J. Booz, H.G. Ebert, R. Eickel and A. Waker) Comission of the European Communities, Luxembourgh, (1974) 141-165

[Par78] H.G. Paretzke and M.J. Berger, Stopping power and energy degradation for electrons in water vapor, In: J. Booz, H.G. Ebert (editors*), Proceedings of the 6th Symposium on Microdosimetry*, Harwood Academic Publishers Ltd., Brussels (1978) 749-758

[Par88] H.G. Paretzke, Simulation von elektronenspuren im energiebereich 0,01-10 keV im Wasserdampf, *GSF_Bericht* (1988) 24-88

[Pei84] A. Peisert, F. Sauli, Drift and diffusion of electrons in gases, a compilation, *CERN report 84-08* (1984)

[Psz02] S. Pszona and J. Kula, Ionization clusters at DNA level: Experimental modeling, *Radiat. Prot. Dosim.* 99 (2002) 387-390

[Ram94] Ulla Ramm, Systematische Untersuchung der $\delta$-Elektronenemission in Stoessen schneller, schwerer Ionen mit Atomen und einfachen Molekuelen: eine Grundlage zur Dosisberechnung von Schwerionen in Materie, *Dissertation zur Erlangung des Doktorgrades der Naturwissenschaften*, Frankfurt am Main (1994)

[Rei98] C.O. Reinold, D.R: Schultz, U. Brechthold, G. Kraft, S. Hagmann, H. Schmidt-Böcking, Ternary Ridge of ejected electrons from fast ion-atom collisions, *Phys. Rev. A* 58(3) (1998) 2611-2614

[Ric90] P. Richard, D.H. Lee, T.J.M. Zouros, J.M. Sanders and J. Shinpaugh, Anomalous $q$ dependence of 0° binary encounter electron production in energetic collision of $F^{q+}$ (q = 3-9) with He and $H_2$ targets, *J. Phys. Soc.*, 88 (1990) 213-218

[Ric98] R.C. Miller, S.G. Martin, W.R. Hanson, S.A. Marino and E.J. Hall, Heavy-Ion Induced Oncogenic Transformation, Center for Radiological Research, Annual report, 1998

[Ros59] H.H. Rossi, Specification of radiation quality, *Rad. Res.* 10 (1959) 522

[Ros60] H.H. Rossi, Spatial distribution of energy deposition by ionizing radiation, *Radiat. Res. Suppl.* 2 (1960) 290

[Ros64] H. H. Rossi, Annals of the New York Academy of Sciences, 114 (1964) Art 1, 4.

[Ros67] H.H. Rossi, Energy distribution in the absorption of radiation, page 27 in *Advances in Biological and Medical Physics*, Vol. 11 (1967) Academic Press, New York

[Ros68] H.H. Rossi; F.H. Attix and W.C. Roesch (editors) Microscopic Energy distribution in irradiated matter, *Radiation Dosimetry, Vol. I*, Academic Press, New York

[Ros70] H. H. Rossi, The effects of Small Doses of Ionizing radiation, *Radiation Phys. Med. Biol.* 15 (1970) 255-262

[Ros92] H.H. Rossi, M. Zaider, Compound dual radiation action. I. General aspects, *Rad. Res.* 132 (1992) 178-183

[Ros96] H.H. Rossi, M. Zaider, Microdosimetry and Its Applications, 1996

[Rud85] M.E. Rudd, Y.K. Kim, D.H. Madison, J.W. Gallagher, Electron production in proton collisions: total cross sections, *Rev. Mod. Phys.* 57 (1985) 965-994

[Sau89] D. Sauvage, A. Breskin and R. Chechik, A systematic study of the emission of the light from electron avalanches in low-pressure TEA and TMAE gas mixtures, *Nucl. Instrum. Methods A* 275, (1989) 351

[Sau97] F. Sauli, *Nucl. Instrum. and Meth. A* 386 (1997) 531

[Saw01] S.G. Sawant, G. Randers-Pehrson, N.F. Metting and E.J. Hall, Adaptive response and the bystander effect induced by radiation in C3H 10T1/2 cells in culture, *Radiat. Res.* 156 (2001) 177–180

[Sch04] M. Scholz and G. Kraft, The physical and radiobiological basis of the local effect model: a response to the commentary by R. Katz, *Rad. Res.* 161 (2004) 612-620

[Sch94] M. Scholz, G. Kraft, Calculation of heavy ion inactivation probabilities based on track structure, X-ray sensitivity and target size, *Radiat. Prot. Dosim.* 52 (1994) 29-33

[Sch96] M. Scholz and G. Kraft, Track structure and the calcualtion of biological effects of heavy charged particles, *Adv. Space. Res.* 18 (1996) 5-14

[Sch97] M. Scholz, A.M. Kellerer, W. Kraft-Weyrather and G. Kraft, Computation of cell survival in heavy ion beams for therapy; The model and ist approximation, *Radiat. Environ. Biophys.* 36 (1977) 59-66

[Scl03] R. Schulte, V. Bashkirov, G. Garty, C. Leloup, S. Shchemelinin, A. Breskin, R. Chechik, J. Milligan, B. Grosswendt, Ion-counting nanodosimetry: current status and future applications, *Australas Phys. Eng. Sci. Med.* 26(4) 2003 149-155

[Scm95] J.U. Schmollack, Radiale mikroskopische Energieverteilungen um Bahnen leichter Ionen im Energiebereich von 20 MeV/u, PHD Thesis, Giessen, (1995)

[Scn66] J. Schutten, F.J. deHeer, H.R. Moustafa, A.J.H. Boerboom, J. Kistemaker, Gross- and potential-ionization cross sections for electrons on water vapor in the energy range 0,1-20 keV, *J. Chem. Phys.* 44/10 (1966) 3924-3928

[Scw91] T. Schwab, Transport von schwerionen durch materie innerhalb ionenoptischer systeme, GSI 1991, Report 91-10, Ph.D Thesis Gießen, 1991

[Scz04] D. Schulz-Ertner, A. Nikoghosyan, C. Thilmann, Th. Haberer, O. Jäkel, C. Karger, G. Kraft, M. Wannenmacher, J. Debus, Results of carbon ion radiotherapy in 152 patients, *Int. J. Rad. Oncol. Biol. Phys.* 58/2, (2004) 631-640

[Sdt87] S. Schmidt, Energie- und Winkelabhaengigkeit der $\delta$-Elektronen in Stoessen schneller Uranionen mit Edelgasatomen, *Masters's thesis*, Universitaet Frankfurt am Main, (1987)

[Sdt96] D. Schardt, I. Schall, H. Geissel, H. Irnich, G. Kraft, A. Magel, M.F. Mohar, G. Munzenberg, F. Nickel, C. Scheidenberger, W. Schwab, L. Sihver, Nuclear fragmentation of high-energy heavy-ion beams in water, *Adv. Space Res.* 17(2) (1996) 87-94

[Sim99] J.A. Simmons and D.E. Watt, Radiation Protection Dosimetry: A Radical Reappraisal, Medical Physics Publishing, Madison, WI, (1999) ISBN 0-944838-87-1

[Sla60] J.C. Slater, *Theory of Atomic structure, Vol. !,* McGraw Hill, New York, (1960)

[Sno00] D.P. Snowden-Ifft, C.J. Martoff and J.M. Burwell, Low pressure negative ion time projection chamber for dark matter search, *Phys. Rev. D*, 61 (2000) 101301(R)

[Sto93a] G.P. Stonell, M. Marshall and J.A. Simmons, Track studies in water vapor using a low-pressure cloud chamber I. Macroscopic measuremnts, *Rad. Res.* 136 (1993) 353-360

[Sto93b] G.P. Stonell, M. Marshall and J.A. Simmons, Track studies in water vapor using a low-pressure cloud chamber II. Microdosimetric measuremnts, *Rad. Res.* 136 (1993) 353-360

[Tau96] G. Taucher-Scholz, J. Heilmann and Gerhard Kraft, Induction of DNA strand breaks by heavy ions, *Nucl. Inst. and Meth. B* 107 (1996) 318-322

[Tho12] J.J. Thomas, Ionization by moving electrified particles, *Phil. Mag.* 23 (1912) 449-457

[Tit98] U. Titt, A. Brskin, R. Chechik, V. Dangendorf, H. Schmidt-Böcking, H. Schumacher, A time projection chamber with optical readout for charged particles track structure imaging, *Nucl. Instr. and Methods in Phys. Res. A* 416 (1998) 85-99

[Tit99] U. Titt, Entwicklung einer optisch ausgelesenen Teilchenspurkammer für dosimetrische und mikrodosimetrische Anwendungen, *Physikalisch-Technische Bundesanstalt Lavorbericht*, 1999

[Tob79] C.A. Tobias, E.A. Alpen, E.A. Blakely, J.R. Castro, A. Chatterjee, G.T.Y. Chen, S.B. Curtis, J. Howard, J.T. Lyman, F.Q.H. Ngo, Radiobiological basis for heavy-ion therapy in: Treatment of radioresistant cancers, editors: M. Abe, K. Sakamoto, T.J. Phillips, Elsevier (1979) 159

[Tob85] C.A. Tobias, The repair-misrepair model in Radiobiology: comparison of other models, *Rad. Res.* 104 (1985) S-77-S-95

[Tod65] P.W. Todd, Heavy-ion irradiation of human and chinese-hamster cells, *Radiat. Res.*, 61 1965 288-297

[Ton77] L.H. Toburen and W.E. Wilson, Energy and angular distributions of electrons ejected from water vapor by 0,3-1,5 MeV protons, *J. Chem. Phys.* 66 (1977) 5202-5213

[Ton80] L.H. Toburen, W.E. Wilson and R.J. Popovich, Secondary electron emission from ionization of water vapor by 0,3 to 2 MeV He$^+$ and He$^{2+}$ ions, *Rad. Res.* 82 (1980) 27-44

[Tra83] S. Trajmar, D.F. Register, A. Chutijan, Electron scattering by molecules II, Experimental methods and data, *Phys Rep.* 97/5 (1983) 219-356

[Tur89] J.E. Turner, S.R. Hunter, R.N. Hamm, H.A. Wright, G.S. Hurst and W.A. Gibson, Development of an optical digital ionization chamber, *Radiat. Prot. Dosim.* 29 1/2 (1989) 9-14

[Var75] M.N. Varma, J.W. Baum and A.V. Kuener, Energy deposition by heavy ions in a "tissue equivalent" gas, *Rd. Res.* 62 (1975) 1-11

[Var77] M.N. Varma, J.W. Baum and A.V. Kuehner, Radial dose, LET, and W for $^{16}$O ions in N$_2$ and tissue-equivalent gases, *Rad. Res.* 70 (1977) 511-518

[Var80] M.N. Varma, J.W. Baum, A.V. Kuehner, Stopping power and radial dose distribution for 42 MeV bromine ions, *Phys. Med. Biol.* 25/4 (1980) 651-656

[Var90] M.N. Varma and M. Zaider, The radial dose distribution as a microdosimetric tool, *Radat. Prot. Dosim.* 31, 1/4 (1990) 155-160

[Web90] W. Webber, J. Kish, D. Scherier, Individual isotopic fragmentation cross sections of relativistic nuclei in hydrogen, helium and carbon targets, *Phys. rev.* 41(2) (1990) 520-532

[Wei06] L. Weissmann, M. Gai, A. Breskin, R. Chechik, V. Dangendorf, K. Tittelmeier and H.R. Weller, Amplification and Scintillation Properties of Oxygen-Rich Gas Mixtures for Optical - TPC Applications, Submitted for publication in *JINST*

[Win76] C.L. Wingate and J.W. Baum, Measured radial distributions of dose and LET for alpha and proton beams in hydrogen and tissue-equivalent gas. *Rad. Res*. 65 (1976) 1-19

[Wul85] H. Wulf, W. Kraft-Weyrather and H.G. Miltenburger, Heavy-ion effects on mammalian cells: inactivation measurements with different cell lines, *Rad. Res*. 104 (1985) 122-134

[Xap94] M.A. Xapsos, E. A. Burke, P. Hapiro and G.P. Summers, Energy deposition and ionization fluctuations induced by ions in small sites - an analytical approach, *Rad. Res.* 137 (1994) 152-161

[X-r73] N.A. Dyson, X-rays in atomic and nuclear physics, Longman Group Limited, London (1973)

[Zae02] T. Zaepfel, S. Hagmann, H. Rothard, J. Ullrich, G. Kraft, H. Schmidt-Böcking and K.O. Groeneveld, Experimental studyy of electron ejection by heavy ion irradiation of solids: Observation of forward and backward emitted electron jets, *Nucl. Insrt. and Meth.* 193 (2002) 651-655

[Zai88a] M. Zaider and G.N. Minerbo, On the possibility of obtaining non-diffused proximity functions from cloud chamber data. I. Fourier deconvolution, *Phys Med. Biol.* 33 (1988) 1261-1272

[Zai88b] M. Zaider and G.N. Minerbo, On the possibility of obtaining non-diffused proximity functions from cloud chamber data. II. Maximum entropy and Bayesian methods, *Phys Med. Biol.* 33 (1988) 1273-1284

[Zir53] R.E. Zirkle, D.F. Marchbank and K.D. Kuck, Exponential and sigmoidal survival curves resulting from α and X-irradiation of Aspergillus spores, *J. Cell. Comp. Physiol.* 39/Supl. 1 (1953) 75-85

# 12 Zusammenfassung

Schwere geladene Teilchen wie Protonen oder schwerere Ionen sind eine erfolgsversprechende Alternative für die Therapie tief liegender Tumoren verglichen mit konventionellen Photonenstrahlen. Ionenstrahlen haben ein invertiertes Dosisprofil: Im Gegensatz zur exponentiell abfallenden Tiefendosisverteilung von Photonenstrahlen steigt die absorbierte Dosis bei Ionen mit der Eindringtiefe an, weist ein scharfes Maximum (den Bragg Peak) auf und fällt dann dahinter sehr steil ab. Damit lassen sich Tumore die dicht neben besonders strahlenempfindlichem Gewebe liegen (wie z.B. dem Rückenmark) besonders schonend therapieren. Darüber hinaus ist die relative biologische Wirksamkeit, RBW (s. Gleichung (2.1)), von schweren Ionen höher als die von locker ionisierenden Strahlen – vor allem in der Abbremsungsregion des Bragg Peaks. Demzufolge hat die vom Strahl deponierte Dosis und – noch ausgeprägter wegen der höheren RBW – die Strahlenwirkung ihr Maxima nicht auf der Haut sondern in einer über die kinetische Energie der Ionen präzise einstellbaren Tiefe im Körper. Diese Eigenschaft der Ionen ermöglicht eine überragende Genauigkeit und Effektivität der verabreichten Dosis sofern adäquate Technologien der Strahlenanwendung und der Therapieplanung eingesetzt werden.

Bei der GSI, an der eine der fortschrittlichsten experimentellen Ionentherapieanlagen betrieben wird, werden kollimierte Strahlen (s.g. Pencilbeams) von Kohlenstoffionen mit schnell variierbarer Energie und Intensität für eine tumorkonforme Bestrahlung bereitgestellt. Dieses s.g. aktive Bestrahlungssystem ermöglicht es, die vorgeschriebene Dosis in einem ausgedehnten Zielvolumen (typischerweise $100 - 200$ cm$^3$) durch die Überlagerung von vielen (tausenden oder zehntausenden) eng kollimierten Nadelstrahlen appliziert wird. Dabei wird das Tumorvolumen entlang der Strahlrichtung in verschiedene dazu senkrecht stehende Schichten zerlegt. Jede Schicht wird vom Strahl rasterförmig abgetastet und dabei wird jedes Voxel des Tumors so lange bestrahlt, bis der vorab berechnete Sollwert erreicht wird. Zur lateralen Ablenkung des Strahls dienen Ablenkungsmagnete. Die Schichttiefe selbst wird durch die Eindringtiefe der Ionen und damit von der Strahlenenergie bestimmt die direkt vom Beschleuniger definiert wird – also nicht wie in manchen anderen Anlagen durch passive s.g. "Rangeshifter". Mit diesem Verfahren kann man die Dosisverteilung exakt dem Zielvolumen bzw. dem Bestrahlungsplan anpassen.

Die geringe laterale Streuung von Schwerionen (das sind hier Ionen die schwerer als Protonen sind) und die steile Abnahme der Dosis hinter dem Bragg Peak sind entscheidende Voraussetzungen für den Erfolg des "intensitätsgesteuerten Rasterscan" Verfahrens. Die Auswahl des Kohlenstoffions für die Therapie ist das Ergebnis einer Optimierung: Kohlenstoff Ionen haben einen höhere RBW (s. Abschnitt 2.7) bei gleichzeitig niedrigerer laterale- und Tiefenstreuung, als z.B. Protonen [Tob79]. Auf der anderen Seite wäre nach der Bestrahlung mit Ionen, die noch schwerer als Kohlenstoff sind, die Ionisationsdichte im zentralen Spurbereich höher als nötig (s. "overkill" Effekt im Abschnitt 2.7). Dazu ist bei Schwerionen der Dosisbeitrag von Fragmenten hinter des Bragg Peaks auch beträchtlich. Fragmente sind Neutronen sowie leichtere Ionen als das Projektil, die durch Kernreaktionen des Projektils auf dem Weg durch das Körpergewebe entstehen können (s. Abschnitt 3.1). Im Falle vom relativ leichten Kohlenstoff wird jedoch die Strahlenqualität vom Phänomen der Fragmentierung nicht so stark beeinträchtigt. Gleichwohl ermöglicht Kohlenstoff, eine PET (Positronen Emissions Tomografie) - Analyse der räumlichen Verteilung der Positron-emittierenden $^{11}$C Fragmente im Patienten während der Bestrahlung durchzuführen [Eng81]. Diese Isotope haben vom $^{12}$C-Projektil kaum abweichende Reichweiten. Deshalb kann man von der durch PET messbaren Verteilung dieser Isotope auf die tatsächlich durch die C12 Ionen applizierte Dosisverteilung Rückschlüsse ziehen und damit die vorberechnete

Verteilung verifizieren. Für eine ausführliche Beschreibung des Therapieverfahrens siehe [Kra00], und für eine Zusammenfassung der therapeutischen Ergebnisse nach den ersten 152 durchgeführten Behandlungen siehe [Scz04].

Die Grundvoraussetzung einer erfolgreichen Tumortherapie ist eine starke und einheitliche Bestrahlung des Tumors mit gleichzeitiger Schonung des umliegenden gesunden Gewebes. Die mit Protonen und Schwerionen erzielbare Dosisverteilung ist zwar tumorkonformer als mit Photonen (s. oben), diesen Vorteil kann man aber nur in dem Fall optimal nutzen, wenn eine aufwändige, auf Radiobiologie basierende Bestrahlungsplanung zuvor durchgeführt wird. Die Bestrahlungsplanung muss, im Falle von Schwerionen, mit einem komplexen, gemischten Strahlenfeld umgehen können, da, wie oben beschrieben, im Körper ein Teil der originalen Kohlenstoffionen fragmentiert wird und die Fragmente über die verschiedensten Ordnungszahlen, Energien und Eindringtiefen verfügen. Darüber hinaus muss die Bestrahlungsplanung nicht nur die Energiedosis sondern auch die energie- und teilchenabhängige relative biologischen Effizienz der Strahlung mit berücksichtigen. Dieser Unterschied wird auf der Abb. 1.1 deutlich gemacht. Die Bilder zeigen die simulierte Dosisverteilung (rechts) und die daraus berechnete biologisch effektive Dosisverteilung (links) als Folge der Bestrahlung eines Schädelbasistumors mit Kohlenstoff. Die einheitliche biologisch wirksame Dosisverteilung resultiert aus einer deutlich niedrigeren Energiedosis auf der rechten Tumorseite, wo der Großteil der Dosis von Kohlenstoffionen Nahe ihres Bragg Maximums (d.h. mit den höchsten RBWs) geliefert wird.

Das Beispiel von Abb. 1.1 demonstriert, dass die Energiedosis alleine nicht ausreicht um den biologischen Effekt von Strahlung zu beschreiben. Ionisierende Strahlung deponiert die Energie in kleinen, diskreten Paketen, die sich im bestrahlten Volumen inhomogen verteilen. Dabei ist Ionisation die relevanteste Form der Energiedeposition im Hinblick auf die biologischen Effekte. Die räumliche Verteilung der Ionisation bei einer gegebenen Dosis beeinflusst den Effekt der Strahlung auf biologische Strukturen maßgebend. Im Allgemeinen kann man feststellen, dass locker ionisierende Strahlung (wie z.B. Photonenstrahlung) hauptsächlich Einfachstrangbrüche bei der DNA verursacht, welche durch biochemische und zelluläre Reparaturmechanismen mit einer hohen Wahrscheinlichkeit korrekt repariert werden können. Im Gegensatz dazu kann dicht ionisierende Strahlung (z.B. Kohlenstoffionen im Bragg Peak Bereich) Häufungen von Ionisationen in kleinen Volumina von einige Kubiknanometern verursachen (s.g. Ionisationscluster). Diese Cluster führen mit einer relativ hohen Wahrscheinlichkeit zu irreparablen Schädigungen (Läsionen) der DNA, die wiederum zu einer Mutation, Fehlfunktion oder Absterben der betroffenen Zelle führen können.

Um den biologischen Effekt von Schwerionen für die Zelltötung relativ zu dem der von Photonen zu quantifizieren, wurde bei der GSI das "Local Effect Model" (LEM) entwickelt [Sch94], [Sch96]. Das LEM antizipiert, dass der zu erwartende biologische Effekt der Bestrahlung auf eine Zelle nicht direkt mit der über den Zellkern gemittelten makroskopischen Dosis zusammenhängt. Stattdessen kann man einen "lokalen Effekt" aus der "lokalen Dosis" in einem sehr kleinen, biologisch relevanten Volumen (z.B. einige $nm^3$) ableiten. Aus dieser Denkweise folgt, dass die Art der Strahlung keine Rolle in der Entstehung des lokalen Effekts spielt, falls die Größe der lokalen Dosis festgelegt ist. D.h., die Ionenstrahlung kann auf dem nm-Maßstab von Röntgenstrahlung ersetzt werden, um den zu erwartenden lokalen Effekt mit Hilfe der wohlbekannten Überlebenskurve der Röntgenstrahlung zu ermitteln. Die eigentliche Strahlenwirkung auf die Zelle lässt sich anschließend vom einfachen Integral der lokalen Effekte über den gesamten Zellkern nachvollziehen. Hier wird die Annahme impliziert, dass lokale Effekte nicht über größere Abstände miteinander wechselwirken.

Die Annahmen des Modells können von theoretischen und experimentellen Ergebnissen gerechtfertigt werden. Das LEM hat sich als bisher erfolgreichstes biophysikalisches Modell in der Vorhersage der Überlebenskurven nach einer Bestrahlung mit Schwerionen erwiesen. Die erfolgreiche praktische Anwendung des LEM in der Bestrahlungsplanung der Schwerionentherapie bei der GSI [Scz04] ist ein eindeutiger Nachweis für dessen Potential. Nichtsdestotrotz kann die erwartete Präzision des Modells nur in dem Fall garantiert werden, in dem die verwendeten Eingabeparameter der Realität entsprechen. Die Vorhersagen des LEM basieren auf zwei biologischen (1. und 2. unten) und zwei physikalischen (3. und 4.) Parametern:

1. Größe und Form des Kern des bestrahlten Zelltyps
2. Röntgen-Überlebenskurve des bestrahlten Zelltyps
3. Mittelwert von Menge (abgeleitet z.B. vom Integral über Teilchenflussdichte) und Typ (Ordnungszahl, Energie) der Ionen, die in einer zufällig ausgewählten Zelle des bestrahlten Volumens Energie deponieren
4. Radiale Dosisverteilung, $d(r)$, d.h. der radiale Dosisverlauf um die Spur eines Teilchens, das das Volumen durchdringt.

Der vierte Parameter, $d(r)$, ist eine deterministische Größe, und sie beschreibt den Erwartungswert der Dosis, $d(r) = dE / dm$ in einem kleinen Volumen mit einer Masse von $dm$ in einer Entfernung von $r$ von der Spurmitte des Ions. Basierend auf den $d(r)$ – Beiträgen der Ionen, deren Spuren mit den Atomen des ausgewählten kleinen Volumens wechselwirken, kann man die lokale Dosis und daraus den lokalen Effekt in diesem Volumen berechnen. Aus den entsprechenden Ergebnissen aller nanometrischen Volumina des Zellkerns kann man dann die Überlebenswahrscheinlichkeit oder die RBW für die Zelle bestimmen. Eine ausführliche Beschreibung des LEM und ein kurzer Überblick über andere biophysikalische Modelle folgt im Abschnitt 2. Die vorliegende Arbeit fokussiert auf die experimentelle Bestimmung der Funktion, $d(r)$.

Außer Experimenten gibt es im Wesentlichen zwei Möglichkeiten für die Bestimmung der $d(r)$ Funktion von Ionenspuren: Verwendung analytischer Modelle oder Monte Carlo (MC) Simulationen. Die analytischen Modelle, wie das Spurstruktur-Modell von Katz et al. [Kat72], das Core-Penumbra Modell von Chatterjee und Schäfer [Cha76], und die Modelle von Kiefer et al. [Kie86] und Xapsos et al. [Xap94] leiten geschlossene Gleichungen für $d(r)$, basierend auf verschiedenen Annahmen und Vereinfachungen der Stoßprozesse, ab. Ein Überblick der wichtigsten analytischen Modelle findet sich in den Doktorarbeiten von Ramm [Ram94] und Schmollack [Scm95]. Den Modellen ist gemeinsam dass eine $1/r^2$ - Abhängigkeit eine gute Näherung für $d(r)$ über einen weiten Bereich von $r$ ist (s. Abb. 2.3). Es gibt jedoch signifikante Abweichungen unter den verschieden Modellen was die Feinstruktur der $d(r)$ Funktion betrifft – insbesondere für sehr kleine und sehr große Werte von $r$.

Wegen der Fähigkeit von MC-Simulationen, den Teilchentransport in Materie in ihrer vollständigen Komplexität und Stochastik zu beschreiben, wird diese Methode in der Praxis zur Bestimmung der $d(r)$ Funktion am häufigsten verwendet. Allerdings kann die Genauigkeit der MC Simulationen nie besser sein als die der Rechnung zu Grunde liegenden Wirkungsquerschnitte. Eine Tabelle mit einem Überblick über die verschiedenen MC Codes befindet sich in [Krm95]. Die Motivation der vorliegenden Arbeit ergibt sich aus dem Bedarf eines experimentellen Benchmarktests für die Ergebnisse und Vorhersagen dieser MC Simulationen. In dieser Arbeit werden die gemessenen Daten mit dem Code „TRAX" verglichen, der für die Simulation und Untersuchung der Struktur von Ionenspuren bei der GSI von Krämer und Kraft [Krm94] entwickelt wurde. Der Code wird seit Jahren sehr erfolgreich eingesetzt, um für die Therapieplanung mit Schwerionen erforderliche Daten zu

erzeugen. Aus der Zahl der existierenden MC Codes haben wir TRAX als zu validierenden Code gewählt, da TRAX für die Fälle optimiert wurde, die für die Strahlentherapie relevant sind (leichte bis mittelschwere Ionen von mittlerer Energie) – im Einklang mit unserer Motivation und unserem Messprogramm. Eine ausführliche Beschreibung der physikalischen Prozesse, die von TRAX berücksichtigt bzw. vernachlässigt werden, folgt im Abschnitt 3.

Messungen von $d(r)$ direkt in biologisch relevanter kondensierter Materie (wie Gewebe oder Wasser), sind nicht möglich: die benötigte räumliche Auflösung in der Größenordnung von nm bis einige µm ist nicht erreichbar mit den zur Verfügung stehenden Meßmethoden. Stattdessen versucht man, die erforderlichen Auflösungen durch Messungen in einem wesentlich größeren gasgefüllten Volumen zu erreichen. Die Längenskala wird dann entsprechend dem Verhältnis der Dichten vom Gas und kondensierter Materie skaliert. Dabei werden allerdings spezifische Unterschiede zwischen den Teilchenspurstrukturen in Gas und in kondensierter Materie [Zae02] vernachlässigt. Die wichtigsten dichteabhängigen Effekte und deren möglicher Konsequenzen werden im Abschnitt 4.1 beschrieben. Einige der wenigen existierenden Meßsysteme, die in der Lage sind, $d(r)$ Funktionen mit einer räumlichen Auflösung deutlich unterhalb der Größenordnung von einem µm zu messen ([Met88], [Win76] oder [Var77] – alle Messungen im Gas; Längenangaben auf Wasserdichte skaliert), sind im Abschnitt 4 kurz beschrieben. Die experimentellen Untersuchungen in dieser Arbeit wurden mit der optisch ausgelesenen Teilchenspurkammer, OPAC, durchgeführt. Über die Funktionsweise der Kammer wird in den Arbeiten von Titt umfangreich berichtet [Tit98] und [Tit99]. Basierend auf den Arbeiten von Titt und auf dem Proposal von Dangendorf [Dan01] wurde das Projekt im Rahmen dieser Doktorarbeit fortgeführt.

OPAC ist eine optisch ausgelesene Zeitprojektionskammer (TPC) mit einem parallelen Driftfeld und mit einer oder mehreren Ladungs- und Lichtverstärkungsstufen. Die zweidimensionale Abbildung der dreidimensionalen Verteilung der Ionisationselektronen, das nach dem Durchdringen des ionisierenden Teilchens durch das Gas der Kammer entstanden ist, wird von einer CCD Kamera mit gegatetem Bildverstärker ausgelesen. Im Rahmen der durchgeführten Messungen wurde der Gasdruck in der Kammer zwischen 4, und 40 hPa variiert. Der Gasdruck und die Driftlänge eines Elektrons im elektrischen Feld bestimmen das Ausmaß der Diffusion der driftenden Elektronen. Die Elektronendiffusion ist der wichtigste unter den Faktoren, die die räumliche Auflösung von OPAC bestimmen. Die untere Grenze der radialen Dosisverteilung ab der die gemessene Verteilung nicht mehr signifikant von der Diffusion beeinflusst wird, liegt bei etwa 100 nm (bei einem Gasdruck von 4 hPa). Mit steigendem Gasdruck verschlechtert sich die räumliche Auflösung. Gleichwohl ermöglicht der höhere Gasdruck dass $\delta$-Elektronen mit höherer Energie in der Kammer gestoppt werden, d.h. bei höherem Druck kann eine größere Umgebung der Spur abgebildet werden. Die obere Grenze der durch OPAC experimentell zugänglichen radialen Entfernung liegt bei ca. 6 µm (bei einem Gasdruck von 40 hPa). Zwischen diesen beiden Begrenzungen ist eine räumliche Auflösung von bis 33 nm erreichbar (alle Längenangaben sind auf die Dichte von Wasser skaliert). Eine ausführliche Beschreibung des Detektors und seiner weiteren Entwicklung ausgehend vom bereits beschriebenen Status (in Titt et al [Tit98]) ist im Abschnitt 5 zu finden.

Die von der OPAC-Kamera aufgenommen Rohbilder illustrieren die qualitativen Eigenschaften der Spuren von ionisierenden Teilchen sehr gut. Eine extensive Datenanalyse ist jedoch erforderlich, um quantitative Informationen, z.B. die erwähnten $d(r)$ Funktionen, zu erhalten. Z.B. ist das Bild lediglich eine zweidimensionale Projektion der Elektronenspur, d.h. der Abstand eines bestimmten Ionisationsereignisses von der Spurmitte (ein einzelnes Ionisationsereignis (Elektron) ist z.B. sichtbar als eine kleine Spitze in Abbildung 7.1) entspricht nicht direkt dem messbaren Abstand in dem projizierten Bild, da die relative dritte Dimension in Projektionsrichtung, die "Tiefe", nicht bekannt ist. Deshalb ist eine

Entfaltungsmethode notwendig, um von den Bildern die gesuchte originale $d(r)$ Funktion abzuleiten. Dies ist aber nur ein Beispiel dafür, dass eine von OPAC gemessene Spur eine komplexe Konvolution von verschiedenen physikalischen Prozessen ist. Neben den zu messenden Ionisationen und Streuungen von Ionen und $\delta$-Elektronen spielen für die Bildentstehung auch die physikalischen Vorgänge beim Detektionsprozess (wie Transport und Diffusion von Elektronen) und die Detektoreigenschaften (wie z.B. Auflösung des optischen Erfassungssystems) eine wichtige Rolle. Es muss betont werden, dass die Messungen – aber auch die Simulationen – die gesuchten physikalischen Prozesse lediglich modellieren. Die Methoden und Algorithmen der Datenauswertung zur Gewinnung der gewünschten Informationen und zum Vergleich mit den Simulationen sind im Abschnitt 6 beschrieben. Die angewandten Auswertungsmethoden wurden rigoros getestet – z.B. durch erfolgreiches Wiederherstellen der gemessenen Daten, indem die entfalteten Daten wieder mit der Detektorfunktion gefaltet wurden. Somit kann man sicher sein, dass die Entfaltungs- und Analysemethoden, die für diese Arbeit entwickelt wurden, aus den Rohdaten zuverlässige und von den Detektoreigenschaften bereinigte Ergebnisse liefern.

Schließlich werden im Abschnitt 7 die Ergebnisse der Messungen mit OPAC bei der GSI im Vergleich mit den entsprechenden simulierten Daten gezeigt. Die im Abschnitt 6 gezeigten Datenauswertungsmethoden bzw. ein den Detektorgegebenheiten angepasstes Simulationsverfahren (auch beschrieben im Abschnitt 6) stellen sicher, dass die gemessenen und simulierten Daten miteinander direkt vergleichbar sind. Die erste Zielstellung des Messprogramms war die Durchführung systematischer Messungen von Spuren von Kohlenstoffionen mit Energien von 400 MeV/u bis hinunter zu Bragg Peak Energien. Der Vergleich der gemessenen Ergebnisse (d.h. $d(r)$ Funktionen im aktuellen Messprogramm) mit den entsprechenden simulierten Daten zeigt eine sehr gute Übereinstimmung bei allen Kohlenstoff – Energien über den gesamten sinnvoll messbaren Bereich der radialen Entfernung (ausgehend von der Spurmitte), für den die Messungen nutzbare Daten liefern (d.h. im Bereich von 100 nm $< r <$ 6 μm; Längen skaliert auf die Dichte des Wassers).

Es muss betont werden, dass der Vergleich der gemessenen und simulierten Daten kein Vergleich der absoluten Dosiswerte erfasst. Stattdessen werden die relativen Verläufe der einander entsprechenden $d(r)$ Funktionen nach adäquaten Normalisierungen verglichen. Die Ursache dafür liegt darin, dass OPAC nicht in der Lage ist, absolute Dosiswerte zu messen (nur mit relativ hohen Unsicherheiten nach extensiven Kalibrierungsmaßnahmen). Nichtsdestoweniger repräsentieren die sehr ähnlich verlaufenden normierten Kurven der methodisch unabhängigen gemessenen und simulierten $d(r)$ Funktionen, dass die beiden Ansätze sehr erfolgreiche Modelle der unterliegenden physikalischen Prozesse sind. Diese Aussage zu obwohl der Simulationscode TRAX teilweise stark vereinfachte Modelle anwendet (z.B. das "Binary Encounter Approximation (BEA)" s. Abschnitt 3.2.), sowie mit skalierten Wirkungsquerschnitten arbeitet wenn keine gemessenen Wirkungsquerschnittstabellen existieren.

Trotz dieser Vereinfachungen in der Simulation sind die Abweichungen zwischen den gemessenen und simulierten $d(r)$ Funktionen für jede Ionenenergie kleiner, als die geschätzten Messunsicherheiten in dem gesamten gemessenen $r$-Bereich. Eine Ausnahme davon ist im Fall der Kohlenstoffionen bei einer Energie von 95 MeV/u der $r$-Bereich von 70 nm $< r <$ 400 nm (s. Abb. 7.19). Hier überschätzen die simulierten Daten die gemessenen um bis zu 25 %. Die Messunsicherheiten belaufen sich auf 10 - 15 %. Außerdem überschätzen die simulierten Daten die gemessenen bei mittleren Energien (18 – 35 Mev/u) im $r$-Bereich von 80 nm $< r <$ 200 nm um ca. 15 %. Diese Abweichung ist mit den Messunsicherheiten vergleichbar. Da die gemessenen und die simulierten $d(r)$ Funktionen auf das gleiche LET (für Definition s. Gleichung (2.4)) normiert sind, muss die Überschätzung in den oben genannten $r$-Bereichen mit einer Unterschätzung in anderen Regionen einhergehen die mit

OPAC nicht messbar sind. Um das Verhalten der $d(r)$ Funktion außerhalb der derzeit zugänglichen radialen Abstände zu klären wären neue Messungen mit einem weiterentwickelten OPAC in den $r$-Bereichen $r < 100$ nm und $r > 6$ µm notwendig.

Es kann jedoch vermutet werden, dass die simulierten $d(r)$ Daten die tatsächlichen Werte für $r < 10$ nm unterschätzen, da die Simulationen (d.h. der TRAX Code) die niederenergetischen Auger-Elektonen und Elektronen aus peripheren Stößen nicht berücksichtigt. Wegen der sehr raschen Abnahme der $d(r)$ Funktion mit steigendem $r$ ($d(r) \approx 1/r^2$), könnte glücklicherweise eine Unterschätzung der $d(r)$ Funktion für $r < 10$ nm um einige weinige Prozente die Überschätzung von 10-25 % im oben genannten limitierten Bereich kompensieren. Falls die Simulation die $d(r)$ Funktionen für $r < 10$ nm tatsächlich signifikant unterschätzen würde, könnte dies auch zu einer Unterschätzung der RBW-Werte führen, falls deren Bestimmung auf simulierten $d(r)$ Funktionen basiert. Die Ionisationsdichte der Strahlung wäre in der Wirklichkeit höher als von den Simulationen erwartet. Dies könnte vor allem für schnelle Kohlenstoff Ionen der Fall sein, wo die Abweichungen zwischen Messungen und Simulationen am höchsten, und gleichzeitig die "overkill" Effekte am niedrigsten sind. Um diese Hypothese zu verifizieren, sind jedoch präzise Messungen im Bereich von $r < 100$ nm oder sogar bei $r < 10$ nm, notwendig.

Die leichten Abweichungen zwischen den gemessenen und simulierten $d(r)$ Funktionen sind allerdings in der log-log Repräsentation kaum erkennbar (s. Abb. 7.18). Es gibt zwei Gründe, warum die log-log Repräsentation in der Literatur für die Darstellung der radialen Dosisverteilungen bevorzugt wird: Erstens verlaufen die interessanten Bereiche sowohl der Radien, als auch der Dosen über viele Größenordnungen (5 bis 15). Zweitens sind die biophysikalischen Modelle, die $d(r)$ als Eingabeparameter benutzen, nicht sehr sensitiv auf leichte Variationen der $d(r)$ Funktion. Das LEM z.B. braucht neben der $d(r)$ Funktion biologische Eingabedaten (Röntgen-Überlebenskurve bzw. Größe und Form des bestrahlten Zelltyps), deren deutlich größere Unsicherheiten jedenfalls größere mögliche Auswirkungen auf die RBW haben können, als die leichte Variationen im Verlauf der $d(r)$ Funktionen in der Größenordnung von bis zu 25 %.

Zusammenfassend können wir feststellen, dass die Präzision von TRAX ausreicht, um $d(r)$ Funktionen für Kohlenstoffionen zu simulieren die dann auch mit in die Therapieplanung einfließen. Diese Konklusion gilt allerdings für radialen Entfernungen von $r < 100$ nm von der Spurmitte nur bedingt. Für kleinere Entfernungen werden die Messdaten zu stark von der Elektronendiffusion dominiert um aus dem Experiment eine eindeutige Aussage über die Präzision der Simulation zu treffen.

Abgesehen von den Kohlenstoffionen wurden auch Spuren von schwereren Ionen ($^{40}$Ar, $^{84}$Kr und $^{238}$U) im Rahmen des aktuellen Messprogramms mit OPAC gemessen. Die simulierten $d(r)$ Daten liegen im gesamten $r$-Bereich von 100 nm $< r < 5$ µm typischerweise etwas (teils auch signifikant) über den entsprechenden gemessenen Daten (s. Abb. 7.21). Die Erfahrung hat gezeigt: je schwerer oder schneller ein Ion ist, desto größer sind die Abweichungen. Einerseits haben wir eine überraschend gute Übereinstimmung zwischen den Messungen und Simulationen für Ionen mit Energien um etwa 50 MeV/u (d.h. relativ niedrige Energien). Anderseits Unterschätzen die simulierten Daten die gemessenen um einen Faktor zwei in der Region von 100 nm $< r < 1$ µm im Falle von $^{84}$Kr ($E = 650$ MeV/u) oder in der gesamten gemessenen Region von 100 nm $< r < 6$ µm im Falle von $^{238}$U ($E = 1$ GeV/u). Eine mögliche Erklärung für diese Abweichungen ist, dass das im TRAX angewande BEA Modell für die Simulation der $\delta$-Elektronen Produktion bei sehr schweren Projektilen zu starke Vereinfachungen enthält.

Die kinetische Energie der gemessenen sehr schweren Ionen wurde so ausgewählt, dass die Ionen trotz stark unterschiedlichen Ordnungszahlen ähnliche LET-Werte in der Kammer

aufwiesen. Ziel war dabei der Vergleich der Spurstruktur (und zwar anhand der $d(r)$ Funktionen). Schwerere Ionen benötigen eine größere spezifische Energie (ausgedrückt in MeV/u) und damit Geschwindigkeit um den gleichen LET-Wert wie leichtere Ionen aufzuweisen (s. dazu Abschnitt 2.7.1). Im Beispiel von Abb. 7.21 wird der gleiche LET von 315 keV/μm (im Wasser) bei Energien von 4,4 MeV/u für $^{12}$C, 65 MeV/u für $^{40}$Ar und 650 MeV/u für $^{84}$Kr erreicht. Die Abweichung in den Spurstrukturen wird hauptsächlich wegen der sehr unterschiedlichen Geschwindigkeiten der Projektile erwartet, die die mittlere δ-Elektronenenergie beeinflusst. So erwartet man bei den schwereren Ionen relativ mehr hochenergetische und weniger langsame δ-Elektronen als bei leichteren Ionen gleichen LETs. Folglich sind die mittleren Reichweiten der entstehenden δ-Elektronen auch unterschiedlich für unterschiedliche Ionen. Diese Erwartung konnte von den Messungen bestätigt werden. Es konnten jedoch – in Übereinstimmung mit den Simulationen – keine starken Unterschiede zwischen den d(r) Funktionen um Argon und Kryptonionen gemessen werden. Die Ursache dafür liegt darin, dass einerseits der Unterschied in den Geschwindigkeiten der beiden Ionen vergleichsweise gering ist (2 Größenordnungen) und zweitens ist der abgebildete Bereich von $r$ verglichen mit den in Betracht kommenden Reichweiten der δ-Elektronen klein. Gleichwohl weist die $d(r)$ Funktion der Kohlenstoffionen bereits in dem abgebildeten $r$-Bereich einen qualitativ anderen Verlauf auf als bei den genannten schwereren Ionen – wieder in Übereinstimmung mit den Simulationen.

Mit den präsentierten Ergebnissen ist das Messprogramm für die Bestimmung der $d(r)$ Funktion für sehr schwerere Ionen und die sehr schnellen Kohlenstoffionen vorerst als beendet. Sollten jedoch signifikante Verbesserungen am Messverfahren möglich sein (insbesondere eine weitere deutliche Verbesserung der räumlichen Auflösung – s. Abschnitt 9), wäre eine Weiterführung dieser Messungen sinnvoll. Im Gegensatz zu den genannten Fällen sind für langsamere Kohlenstoff Ionen ($E < 30$ MeV/u) nur wenige Messungen von niedriger Qualität vorhanden, da in unseren Messungen die langsamen Ionen nicht direkt vom Beschleuniger bereitgestellt, sondern aus schnelleren Ionen durch Abbremsung in einer Wassersäule hergestellt wurden. Wegen des damit unvermeidbaren Energiestragglings waren die Energien der detektierten Ionen in einem breiten Energiebereich verteilt und innerhalb eines sinnvoll definierten engen Energiefensters wurden zu wenige Ionen nachgewiesen um statistisch haltbare Aussagen zu machen. In Zukunft sollten deshalb noch Messungen mit langsameren Kohlenstoffionen durchgeführt werden, die direkt mit der benötigten Energie von einem kleineren Beschleuniger (z.B. UNILAC bei der GSI) bereitgestellt werden. Diese Daten wären aus Sicht der Biophysik von besonderem Interesse, da im Bereich des Tumors und des direkt umgebenden Gewebes die Dosis hauptsächlich von diesen langsameren Ionen deponiert wird. Des Weiteren sollten die Messungen auch auf leichtere Ionen ausgeweitet werden, da diese durch Fragmentation von Kohlenstoffionen entstehen und bei der Dosimetrie eine wichtige Rolle spielen. Man kann nach den vorliegenden Ergebnissen vermuten, dass der TRAX Code die radiale Ionisationsverteilung um die leichteren Ionen herum sehr gut beschreibt; diese Vermutung sollte allerdings von Experimenten untermauert werden.

Der Erfolg des präsentierten Messprogramms eröffnet eine breite Palette für die weiteren Einsatzmöglichkeiten von OPAC. Wegen der erwartungsgemäß stetig zunehmenden Ausbreitung der Anlagen für Ionentherapie wird die weitere Forschung der räumlichen Ionisationsmechanismen von Ionen im Fokus der experimentalen Atomphysik bleiben. Es liegt auf der Hand, dass die Anwendungsmöglichkeiten von OPAC nicht auf die Bestimmung von radialen Dosisverteilungen beschränkt sind. Dank der sehr detaillierten Information, die OPAC über das Ionisationsmuster verschiedener Teilchen liefern kann, können die bereits (oder in der Zukunft) aufgenommen Bilder für die Bestimmung verschiedenster Größen der Mikro- oder Nanodosimetrie benutzt werden. Diese Größen dürfen nicht nur von

deterministischer, sondern auch von stochastischer Natur sein (z.B. Proximity Funktionen, Clustergößenverteilungen – für Definitionen s. Abschnitt 2). Über der Biophysik hinaus kann OPAC natürlich auch in anderen Gebieten der Strahlenphysik oder Atomphysik verwendet werden. Jüngst wurde eine Messmethode mit OPAC für eine Anwendung im Bereich der nuklearen Astrophysik vorgeschlagen [Mos05], [Wei06].

# Danksagung